Shaping Ultrasmall Peptide-Based Supramolecular Hydrogel into Robust, Reusable, and Multifunctional Core–Shell Beads

A Thesis Submitted in Partial Fulfilment of the Requirements for the Degree of

Doctor of Philosophy

in

Chemistry

by

Tanushree Das

Roll No.: 206122035

Supervisor

Prof. Debapratim Das

Department of Chemistry

Indian Institute of Technology Guwahati

Guwahati – 781039, Assam (India)

Dedicated with all my heart to my **mom**, **dad**, and **sister**, who have been the wind beneath my wings, the calm in my chaos, and the foundation upon which I stand.

Declaration

I hereby declare that the matter embodied in this thesis is the result of investigations carried out by me in the Department of Chemistry, Indian Institute of Technology Guwahati, India, under the guidance of Dr. Debapratim Das. In keeping with the general practice of reporting scientific observations, due acknowledgements have been made wherever the work described is based on the findings of other investigators.

Tanushree Das

(Tanushree Das)

भारतीय प्रौद्योगिकी संस्थान गुवाहाटी
INDIAN INSTITUTE OF TECHNOLOGY GUWAHATI

Dr. Debapratim Das
Professor
Department of Chemistry
Ph: + 91 361 258 3301
Fax: + 91 361 258 2349
E-mail: ddas@iitg.ac.in

16th Oct, 2025

To whom it may concern.

This is to certify that the thesis entitled **"Shaping Ultrasmall Peptide-Based Supramolecular Hydrogel into Robust, Reusable, and Multifunctional Core–Shell Beads"** submitted by Tanushree Das (Roll No. 206122035) for the award of PhD degree to IIT Guwahati, is absolutely based on her own research work and that neither this thesis nor any part of it has been submitted for any degree/diploma or any academic award anywhere before.

(Dr. Debapratim Das)

Contents

Abstract

The thesis "**Shaping Ultrasmall Peptide-Based Supramolecular Hydrogel into Robust, Reusable, and Multifunctional Core–Shell Beads**" explores the design, fabrication, and functional applications of peptide-based core–shell hydrogel beads, focusing on how small molecular systems can be engineered into robust, multifunctional platforms. By combining supramolecular assembly, surface engineering, and nanocatalyst integration, the thesis develops innovative materials addressing challenges in catalysis, sensing, and environmental remediation.

Chapter 1 provides an introduction to hydrogels, explaining their classification, crosslinking mechanisms, and structural properties that enable diverse applications. It also describes the preparation methods for hydrogel beads and reviews their roles in drug delivery, catalysis, sensing, and water purification.

Chapter 2 presents the fabrication of core–shell hydrogel beads and hollow capsules using the low molecular weight peptide PyKC through a simple extrusion technique without external cross-linkers. It demonstrates how the chemically tunable surfaces of these beads allow versatile functionalization and the preparation of hollow capsules via selective removal of the hydrogel core.

Chapter 3 describes the functional surface engineering of the core–shell beads to enable host–guest interactions, covalent biocatalyst immobilization, and the in situ, reducing-agent-free synthesis of gold nanoparticles within the polymeric shell. It highlights the catalytic applications of the AuNP-embedded beads, demonstrating efficient reduction of nitroaromatic compounds and azo dyes with excellent reusability and stability.

Chapter 4 discusses the development of gold nanostar-coated hydrogel beads as photo-oxidase mimics that exhibit light-induced, peroxide-free catalytic oxidation. It details their application in the sensitive and selective colorimetric detection of uric acid and successful integration into a smartphone-based point-of-care testing system.

Chapter 5 presents the design of sulfonate-functionalized hydrogel beads embedded with gold nanoparticles that display non-plasmonic, light- and chemical oxidant-free oxidase-like activity for broad-spectrum water decontamination. It demonstrates the system's effectiveness in degrading phenolic pollutants, azo dyes, and catecholamines, as well as its antibacterial activity, mechanical robustness, and reusability.

Indian Institute of Technology Guwahati

Acknowledgements

With deepest humility and immense gratitude, I extend my heartfelt thanks to everyone who has been a part of this journey. What began as a collection of uncertain ideas slowly took shape into this body of work, shaped and nurtured by the constant support, guidance, and encouragement of so many wonderful people. This journey was not a straight path; it was filled with doubts, detours, and moments of struggle. But through it all, it was equally filled with discovery, resilience, and growth. Every challenge taught me something meaningful, and every small success gave me strength to keep moving forward. This experience has transformed me not just as a researcher but as a person.

I offer my deepest respect and sincere thanks to my mentor, Prof Debapratim Das. His wisdom, patience, and unwavering support were the pillars on which I built this work. He did not just guide me in research; he taught me how to think, how to question, and how to believe in myself. His encouragement extended far beyond academics and often arrived in the form of a kind word, a thoughtful suggestion, or a much-needed moment of levity. Working under his mentorship has been one of the greatest privileges of my life, and I will carry his lessons with me always.

I am truly grateful to my Doctoral Committee members, Dr Dipankar Srimani, Dr Kalyan Raidongia, and Professor Tapas Kumar Mandal, for their insightful suggestions, constructive feedback, and consistent encouragement. Their involvement added depth and direction to this work. I owe special thanks to Dr Sunanda Chatterjee, whose thoughtful feedback and graceful presence brought clarity not just to my research but also to my voice as a scholar. She is a source of inspiration, and I feel fortunate to have crossed paths with her.

To my senior lab mates, Dr Saurav Das, Dr Payel Dowari, Dr Basab Kanti Das, and Dr Sumit Chowdhuri, thank you for welcoming me, guiding me, and helping me find my footing in the early days. I will always cherish the patience, wisdom, and kindness you showed me. I am equally grateful to Priyam Das, Malay Kumar Baroi, Ritvika Kushwaha, Sampurna Routray, and Rakesh Routh for being my companions on this journey, for sharing ideas, laughter, and motivation, and for creating a warm and supportive space that helped me grow.

A very special note of gratitude goes to Saurav, my senior in the lab and my greatest source of strength. Your unwavering love, quiet encouragement, and selfless guidance gave me the courage to keep going even when things felt impossible. You lifted me through my worst moments and reminded me of my potential when I had forgotten it. Your belief in me was often the light that kept

me moving. This journey would not have been possible without you, and I will forever be grateful for your presence beside me.

I would also like to thank everyone in the Department of Chemistry at IIT Guwahati, including friends, fellow researchers, faculty members, and technical staff, for their invaluable support and assistance throughout this time. I am especially thankful to Maitery Yadav, Ankit Jana, Rahul Maurya, and Sudeshna Mukherjee for their important help during various project tasks. I also appreciate the anonymous reviewers whose constructive feedback improved the quality of my research publications. I am grateful to the Central Instruments Facility and the Department of Chemistry for access to essential resources, and to IIT Guwahati for the financial support that made this work possible.

To my beloved family, my mother, Mrs Popy Das, my father, Mr Nitish Kumar Das, and my sister, Mrs Alpana Das, there are no words that can fully express what your love and sacrifices mean to me. You have been my strength in every sense. Your faith in me never wavered, even when I doubted myself. You stood by me in silence and in storm, and every achievement of mine is rooted in your patience, your prayers, and your endless love. I am who I am because of you.

I also extend heartfelt thanks to my mother-in-law, Mrs Shipon Rani Das, my father-in-law, Mr Sanjay Kumar Das, and my sister-in-law, Mrs Sushmita Das for their warmth, understanding, and unwavering support. Your care and presence brought comfort and reassurance during difficult moments.

Finally, I thank God for giving me the strength to endure, the courage to persist, and the grace to complete this remarkable journey. It has been one of the most beautiful and transformative chapters of my life, and I am thankful for every moment of it.

List of Abbreviations

Abbreviations

NMR	Nuclear Magnetic Resonance
ESI-MS	Electrospray Ionization
MALDI	Matrix Assisted Laser Desorption/Ionization
FESEM	Field Emission Scanning Electron Microscopy
FETEM	Field Emission Transmission Electron Microscopy
HRTEM	High Resolution Transmission Electron Microscopy
SAED	Selected Area Electron Diffraction
EDX	Energy Dispersive X-ray
XRD	X-Ray Diffraction
XPS	X-Ray Photoelectron Spectroscopy
FTIR	Fourier-Transform Infrared Spectroscopy
DLS	Dynamic Light Scattering
HPLC	High-Performance Liquid Chromatography
TGA	Thermogravimetric Analysis
UV-Vis	Ultraviolet–Visible Spectroscopy
FL	Fluorescence
λ_{max}	The wavelength in the absorption spectrum where the absorbance is maximum
λ_{em}	The wavelength in the emission spectrum where the emission is maximum
ε	Molar Extinction Coefficient
G′	Storage Modulus
G″	Loss Modulus
γ	Strain
CA	Contact Angle
k_{app}	Apparent Rate Constant
V_{max}	Maximum Reaction Rate
K_m	Michaelis Constant
TLC	Thin Layer Chromatography
ITC	Isothermal Titration Calorimetry
FCC	Face-Centered-Cubic
MeOH	Methanol
EtOH	Ethanol
ACN	Acetonitrile
DMSO	Dimethyl Sulfoxide
DMF	N,N-Dimethylformamide
IPA	Isopropyl Alcohol
t-BuOH	Tert-butyl Alcohol
DIPEA	N,N-Diisopropylethylamine
TFA	Trifluoroacetic Acid
TES	Triethylsilane

TEA	Triethylamine
DMAP	4-Dimethylaminopyridine
HBTU	Hexafluorophosphate Benzotriazole Tetramethyl Uronium
MY	Metanil Yellow
SDB	Solochrome Dark Blue
MG	Malachite Green
EBT	Eriochrome Black T
NR	Nile Red
CR	Congo Red
MB	Methylene Blue
MO	Methylene Orange
MR	Methyl Red
FITC	Fluorescein isothiocyanate
RhB	Rhodamine B
POCT	Point-of-Care Testing
TMB	3,3',5,5'-Tetramethylbenzidine
OPD	Ortho-phenylenediamine
ABTS	2,2'-Azino-bis(3-ethylbenzothiazoline-6-sulfonic acid)
TRIS	Tris(hydroxymethyl) aminomethane
HEPES	N-(2-Ethanesulfonic hydroxyethyl)piperazine-N'-(2-ethanesulfonic acid)
BSA	Bovine Serum Albumin
HRP	Horseradish Peroxidase
SOD	Superoxide Dismutase
TCEP	Tris(2-carboxyethyl)phosphine
DTT	Dithiothreitol
EDC	1-Ethyl-3-(3-dimethylaminopropyl)carbodiimide
NHS	N-hydroxy succinimide
BQ	Benzoquinone
EDTA	Ethylenediaminetetraacetic acid
AuNP	Gold Nanoparticle
AuNS	Gold Nanostars
LSPR	Localized Surface Plasmon Resonance
DNA	Deoxyribonucleic acid
CAC	Critical Aggregation Concentration
SPA	Supramolecular Peptide Amphiphile
CB[n]	Cucurbit[n]uril (n = 5, 6, 7, 8, 10)
CT	Charge Transfer
pNP	p-Nitrophenol
pAP	p-Aminophenol
DNP	2,4-Dinitrophenol
p-NO	p-Nitrosophenol
MV	Viologen Derivative
PyCHO	Pyrene-1-carboxaldehyde
$PyCH_2NH_2$	1-pyrenemethylamine

PyC	Pyrene-Cysteine
TsO-CD	Mono-6-tosyl-β-cyclodextrin
Ada-RhB	Adamantyl appended rhodamine B derivative
4-NBA	4-Nitrobenzaldehyde
TA	Terephthalic Acid
DAB	3,3′-Diaminobenzidine
5ACl	Dipentaerythritol penta-/Hexa-acrylate
BPEI	Branched Polyethylene Imine
PEI	Polyethyleneimine
DA	Dopamine
EP	Epinephrine
LMWG	Low molecular weight gelators
MGC	Minimum Gelation Concentration
LOD	Limit of Detection
SPPS	Solid Phase Peptide Synthesis
Tyr	L-tyrosine
Glu	L-glutamic acid
Gln	L-glutamine
Gly	L-glycine
Lys	L-lysine
Leu	L-leucine
Thr	L-threonine
Arg	L-arginine
Asn	L-aspargine
Cys	L-cysteine

Chapter 1

Introduction

Indian Institute of Technology Guwahati

1.1 From Molecules to Materials: An Introduction to Hydrogels

Hydrogels are a fascinating class of materials characterized by their three-dimensional crosslinked polymeric networks that can absorb and retain substantial amounts of water or biological fluids while maintaining structural integrity. The concept of hydrophilic polymeric gels is not entirely modern. Naturally derived hydrogels such as gelatin and agar have been utilized for centuries in food, medicinal, and cosmetic applications. Gelatin, obtained from collagen, was used in Europe as early as the Middle Ages for culinary and medicinal purposes, while agar, extracted from red algae, has been employed in East Asia for over 500 years as a gelling agent in traditional foods and remedies. These examples demonstrate that the practical use of hydrophilic polymeric networks predates the formal chemical and material characterization that defines modern hydrogel research. The term "hydrogel" was first introduced in 1894 to describe colloidal inorganic salts, but its modern relevance began with the pioneering work of Wichterle and Lim in 1960, who synthesised poly(2-hydroxyethyl methacrylate) (PHEMA) for use in contact lenses.[1-3] This breakthrough laid the foundation for decades of hydrogel research, leading to the development of materials valued for their unique properties and adaptability across scientific and industrial domains. Hydrogels derive their functionality from hydrophilic polymer chains that form a porous matrix via physical or chemical crosslinking, allowing them to swell in aqueous environments without dissolving.[4] The interplay among polymer composition, crosslinking density, and synthesis methods governs their mechanical strength, biocompatibility, and responsiveness to environmental stimuli, making them suitable for a wide range of applications.

The structural complexity of hydrogels arises from their biphasic nature, comprising a solid polymeric network and a permeating aqueous phase. The polymer network can be sourced from natural or synthetic materials and is stabilized either by covalent bonds or by non-covalent interactions such as hydrogen bonding, hydrophobic forces, or ionic associations. Crosslinking density is a major factor influencing hydrogel properties. Higher crosslinking enhances mechanical robustness but limits swelling, whereas lower crosslinking improves water absorption at the expense of structural stability.[5] The choice of polymer type also influences performance. Natural polymers like alginate, chitosan, and collagen offer excellent biocompatibility and biodegradability, making them highly suitable for biomedical use.[6] Synthetic polymers such as polyethylene glycol (PEG) and polyacrylamide (PAAm) provide greater tunability in mechanical behaviour and long-term stability. Hybrid hydrogels that combine natural and synthetic polymers are particularly attractive, as they integrate the strengths of both systems to produce materials customized for specific functions.

Hydrogel development has historically progressed through three distinct generations, each marked by specific innovations (Figure 1.1).[7] The first generation, emerging in the mid-twentieth century, focused on chemically crosslinked hydrogels like PHEMA and polyvinyl alcohol (PVA), valued for their swelling capacity and mechanical stability.[8-13] These materials found early applications in contact lenses and wound dressings but lacked dynamic responsiveness. The second generation, appearing later in the century, introduced stimuli-responsive "smart" hydrogels capable of altering their properties in response to pH, temperature, or ionic changes.[14-17] Examples include PEG-polyester copolymers and acrylamide derivatives, which enabled applications in controlled drug release and adaptive tissue scaffolds.[18] The third generation, still evolving, emphasizes physically crosslinked and stereocomplex hydrogels that rely on non-covalent interactions for features like self-healing and injectability.[19-21] This progression reflects a growing interest in multifunctional hydrogels that mimic natural extracellular matrices for advanced biomedical applications such as regenerative medicine and biosensing.

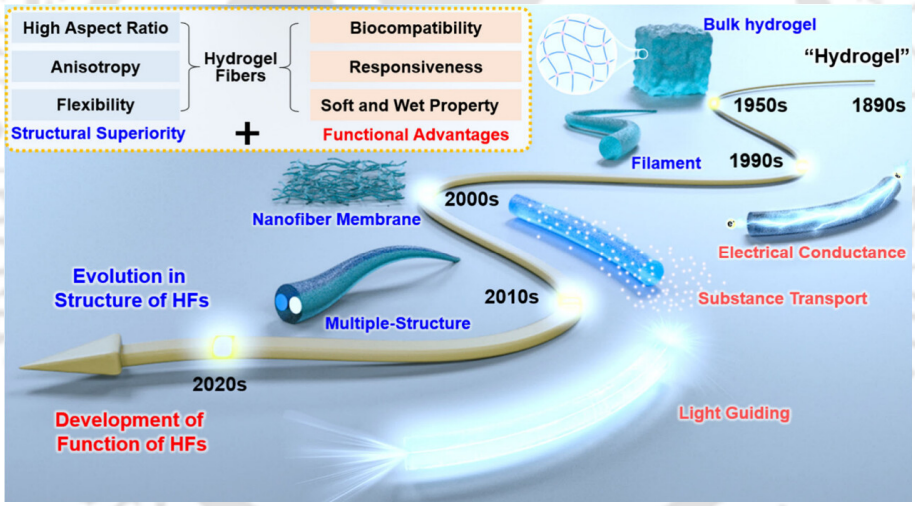

Figure 1.1 Evolution of hydrogels and hydrogel fibres through the decades. Reproduced with permission from Ref. 7.

The defining properties of hydrogels underpin their wide applicability. Their remarkable water absorption capacity, often exceeding 90%of their weight, imparts softness, porosity, and flexibility, making them structurally similar to biological tissues. Mechanical properties can vary widely, from soft gels to durable scaffolds, depending on polymer composition and crosslinking. Hydrogels also exhibit stimulus-responsive behaviour, dynamically adapting to environmental changes such as pH, temperature, and ionic strength. For example, temperature-sensitive hydrogels like poly(N-isopropylacrylamide) (PNIPAM) undergo reversible phase transitions near their lower critical solution temperature, making them suitable for controlled drug release.[22] Similarly, pH-responsive

hydrogels formed from chitosan or poly(methacrylic acid) can swell or shrink in response to the surrounding pH, enabling targeted drug delivery.[23, 24]

Owing to their unique properties, hydrogels have found applications across a broad spectrum of fields. In biomedicine, they are widely employed in drug delivery systems to encapsulate and release therapeutic agents in a controlled manner, often in response to specific physiological triggers.[25] In tissue engineering, hydrogels act as scaffolds that mimic the extracellular matrix, supporting cell adhesion, growth, and differentiation.[26] Their biocompatibility and customizable mechanical properties make them ideal for wound dressings that maintain a moist environment conducive to healing.[27] Beyond biomedical applications, hydrogels are used in agriculture to retain water in arid soils and in food technology to modify texture or encapsulate flavours and nutrients.[28] In environmental science, hydrogels function as adsorbents for water purification.[29] Specialized hydrogels are also integral to advanced technologies such as biosensors, where molecularly responsive hydrogels detect analytes like glucose or antigens, and actuators for soft robotics.[30] Injectable hydrogels with reversible bonding chemistry offer minimally invasive platforms for drug delivery and tissue repair.[20] In energy-related applications, hydrogels have been investigated as electrolytes in energy storage devices due to their ion-conductive nature.[31] These wide-ranging applications underscore the adaptability and functionality of hydrogels as engineered materials.

1.2 Hydrogel Architectures

The structural architecture of hydrogels plays a fundamental role in determining their physicochemical properties, mechanical stability, and functional performance. These soft materials can be engineered by varying the nature of their building blocks and the interactions that hold them together. Hydrogels are broadly classified based on the molecular weight of the gel-forming agents, which may be either high molecular weight polymers or low molecular weight gelators. They can also be categorized according to the type of crosslinking mechanism involved, such as covalent chemical interactions or non-covalent physical interactions. Each category imparts distinct characteristics to the hydrogel network, influencing its suitability for applications in biomedicine, environmental remediation, and smart material design.

1.2.1 Polymeric vs. Low Molecular Weight Supramolecular Hydrogels

Among the diverse classes of hydrogels, supramolecular and polymeric systems stand out due to their distinct structural architectures, assembly mechanisms, and functional characteristics. These two types differ fundamentally in their design principles, each offering unique advantages and limitations that make them suitable for different applications. Low molecular weight supramolecular hydrogels form through the self-assembly of small molecules or oligomers, known

as hydrogelators, via non-covalent interactions such as hydrogen bonding, π-π stacking, ionic interactions, hydrophobic forces, and host–guest chemistry (Figure 1.2A).[32] These weak but highly dynamic forces facilitate the formation of nanostructured networks that encapsulate water within a gel matrix. Their assembly is reversible and highly sensitive to external stimuli, including pH variations, temperature shifts, and ionic strength changes. For example, amino acid-based hydrogelators can self-organize into nanofibrous networks under specific conditions, creating hydrogels that exhibit reversible gel–sol transitions.[33] This dynamic behaviour makes supramolecular hydrogels particularly valuable for applications requiring adaptability, such as drug delivery and tissue engineering. In contrast, polymeric hydrogels can form through covalent crosslinking of polymer chains during polymerization or chemical modification, or through physical interactions such as hydrogen bonding, chain entanglements, or ionic associations, as observed in agarose and gelatin (Figure 1.2B).[34] Even physically crosslinked polymer gels differ from low molecular weight supramolecular hydrogels in their disassembly dynamics, because the polymer chains must first unentangle before the network can break down. Covalently crosslinked polymer networks offer permanent mechanical robustness and maintain stability under prolonged stress or extreme conditions. While generally less responsive to environmental stimuli than supramolecular hydrogels, polymeric systems provide superior structural integrity suitable for load-bearing applications and long-term biomedical use. Despite their differences, both types of hydrogels share key attributes. Their hydrophilic nature enables high water retention, and they can be engineered for biocompatibility. Additionally, both can be designed to respond to external stimuli such as pH or temperature changes, although supramolecular hydrogels generally exhibit greater responsiveness due to their dynamic, reversible interactions.

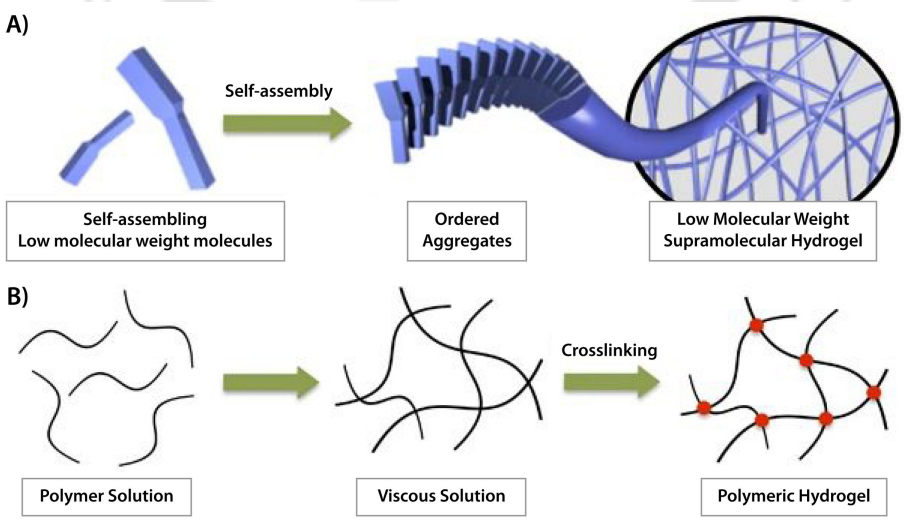

Figure 1.2 Schematic representation depicting the formation of A) a low molecular weight supramolecular hydrogel, and B) a polymeric hydrogel. Reproduced with permission from Ref. 35.

The primary distinction between these two hydrogel architectures lies in their structural behaviour. Low molecular weight supramolecular hydrogels, due to their non-covalent assembly, are highly dynamic, enabling rapid gel-sol transitions and self-healing properties. However, this reliance on weak interactions results in lower mechanical strength. Conversely, polymeric hydrogels achieve greater mechanical stability through covalent crosslinking but lack the flexibility and adaptability of supramolecular systems. This trade-off makes each hydrogel type ideal for specific applications: supramolecular hydrogels are advantageous for scenarios requiring responsiveness and biodegradability, whereas polymeric hydrogels excel in applications demanding durability and structural resilience.

In nutshell, supramolecular and polymeric hydrogels represent two complementary paradigms in hydrogel design. Supramolecular systems emphasize dynamic behaviour but sacrifice mechanical robustness, while polymeric systems prioritize stability at the cost of adaptability. The choice between these architectures depends on the specific requirements of the intended application. Future research in hybrid hydrogels that integrate features from both systems holds great potential for overcoming current limitations and expanding the possibilities of hydrogel-based materials in biomedical and industrial applications.

1.2.2 Chemical vs Physical Crosslinking

Hydrogels, being three dimensional polymeric networks capable of absorbing significant amounts of water, are widely used across various fields due to their tunable physicochemical properties. One of the primary determinants of a hydrogel's structure and function is the method of crosslinking employed, either chemical or physical. Chemically crosslinked hydrogels are formed via covalent bonds between polymer chains, offering long term stability and mechanical robustness. Four major types of chemical crosslinking methods exist.

(1) Bifunctional crosslinkers like glutaraldehyde react with amine groups on polymer chains to form Schiff base linkages, leading to the formation of stable and interconnected network structures (Figure 1.3A).[36]

(2) Polymer-polymer conjugation, either through the coupling of pre-functionalized groups on the polymer chains, such as amine-thiol Michael-type additions, or through strong electrostatic interactions between oppositely charged components, as demonstrated by the robust binding between positively charged amino groups in chitosan and negatively charged carboxyl groups in oxidized alginate (Figure 1.3B).[37]

(3) Photocrosslinking, involving the use of photosensitive moieties to form covalent bonds upon light exposure, enabling the creation of spatially defined hydrogel structures.

However, this approach typically requires photosensitizers and ultraviolet light, which can raise concerns regarding cytotoxicity (Figure 1.3C).[38]

(4) Enzymatic crosslinking, such as the transglutaminase-catalyzed bonding of hyaluronic acid chains, allows for rapid gelation under mild conditions and offers excellent biocompatibility, supporting the formation of functional neuronal synapses (Figure 1.3D).[39]

These methods allow for the incorporation of biofunctional molecules, tailoring of mechanical stiffness, and controlled degradation, which are critical for long term in vitro culture or implantation scenarios. In contrast, physically crosslinked hydrogels rely on noncovalent interactions such as hydrogen bonding, ionic interactions, hydrophobic interactions, and crystalline domain formation. While these interactions typically occur under milder and more physiologically relevant conditions, they generally result in weaker mechanical properties and limited structural longevity. For instance, peptide based hydrogels formed via hydrophobic interactions are excellent for promoting neurite outgrowth and synaptic connectivity but often suffer from mechanical fragility (Figure 1.3E).[40] Ionic crosslinking, such as that between alginate and chitosan, can yield polyelectrolyte complexes supporting olfactory ensheathing cells and neural stem cell proliferation, although their ionic nature makes them vulnerable to environmental fluctuations (Figure 1.3F).[41] Hydrogen bonding, utilized in polyvinyl alcohol and polyacrylic acid systems, results in tougher hydrogels suitable for electrode coatings (Figure 1.3G),[42] whereas crystallinity based hydrogels like cellulose microfibrils enable mechanical enhancement and porosity tuning (Figure 1.3H).[43]

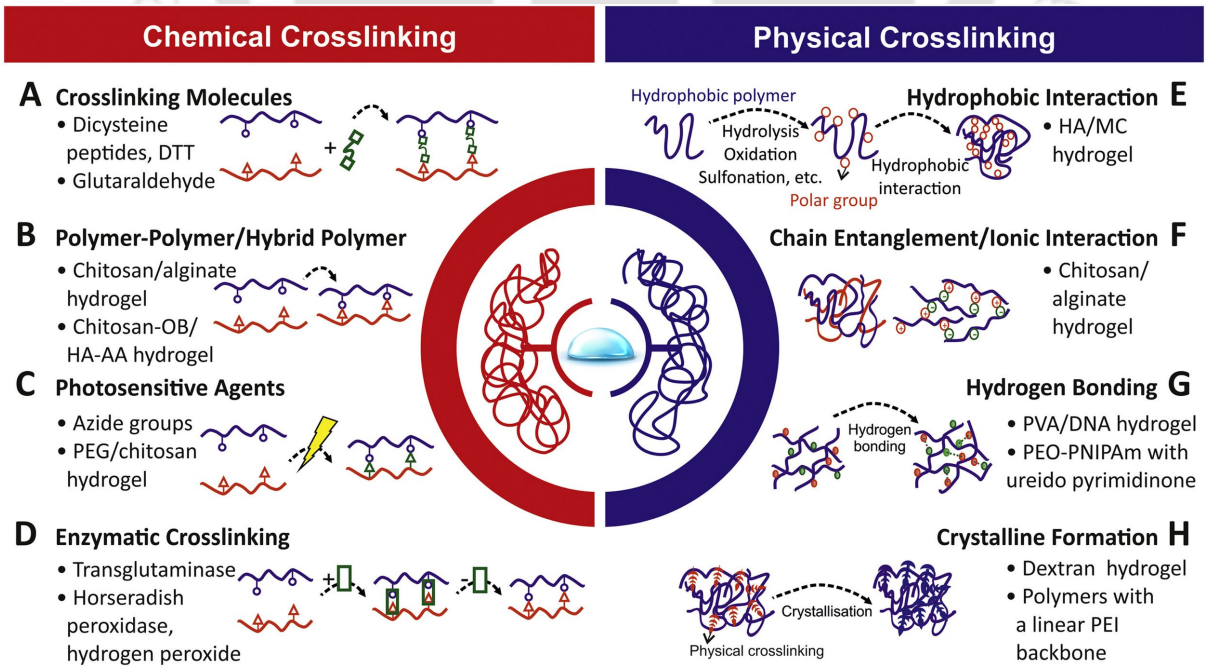

Figure 1.3 Schematic representation of chemical and physical crosslinking methods for hydrogel formation. Chemical crosslinking involves covalent bond formation between polymer chains through: A) Crosslinkers like

dicysteine peptides, DTT, or glutaraldehyde, B) Polymer–polymer interactions via reactive groups, C) Photocrosslinking using light-activated reactions, D) Enzymatic crosslinking catalysed by specific enzymes. Physical crosslinking relies on non-covalent interactions, including: E) Hydrophobic aggregation of polymer segments, F) Chain entanglement and ionic interactions, G) Reversible hydrogen bonding, H) Crystalline domain formation acting as physical crosslink points. Reproduced with permission from Ref. 44.

The choice between chemical and physical crosslinking often depends on the application-specific requirements for mechanical strength, degradation profile, and cell compatibility. Chemical crosslinking offers high tunability and durability, making it ideal for load-bearing or long-term scaffolds, whereas physical crosslinking, due to its reversibility and cytocompatibility, is often preferred for applications like injectable systems or dynamic cultures. Despite these trade-offs, hybrid strategies combining both crosslinking methods are gaining interest for balancing mechanical integrity with biological functionality.[45, 46]

1.3 Challenges Associated with Traditional Hydrogels

Traditional hydrogels, while widely utilized in biomedical, catalytic, and industrial applications, face significant challenges that limit their functionality and versatility. One significant issue is their inherent difficulty in handling due to their soft, fragile, and often amorphous nature. Hydrogels are often mechanically weak, which makes them prone to tearing or deformation when subjected to external forces.[47] This fragility complicates their processing, storage, and application, especially in scenarios requiring robust mechanical properties, such as tissue engineering or structural supports in regenerative medicine.[48] Furthermore, their high water content and gel-like consistency make them slippery and challenging to manipulate without specialized tools or techniques.

Another critical limitation lies in the use of hydrogels as reusable catalysts or catalytic supports. Hydrogels have been explored as matrices for immobilizing catalytic species due to their porous structure and high water content, which can facilitate mass transport and reaction kinetics. However, the weak mechanical properties of many traditional hydrogels make them prone to deformation or collapse during catalytic processes, particularly under harsh reaction conditions such as high temperatures or pressures.[49] This limits their reusability and operational lifespan. Moreover, the chemical stability of hydrogels can be compromised by the catalytic reactions themselves or by the solvents used, leading to degradation of the hydrogel matrix and loss of catalytic activity over time. Even chemically crosslinked hydrogels, which are more robust than their physically crosslinked counterparts, may suffer from leaching of immobilized catalysts due to insufficient binding strength between the hydrogel network and the catalytic species. These limitations necessitate the development of advanced hydrogel systems with enhanced mechanical strength, chemical stability, and binding affinity for catalytic applications.

Moreover, traditional hydrogels often lack the adaptability required for specific applications. Their synthesis typically results in bulk forms that may not be optimal for precise tasks. For example, in drug delivery or tissue scaffolding, the shape and size of the hydrogel significantly influence its performance.[26] Bulk hydrogels may not provide the desired spatial control or mechanical properties needed for these purposes. To address these limitations, advancements in hydrogel fabrication techniques have introduced innovative solutions. By shaping hydrogels into specific geometries such as films, fibres, beads, or 3D-printed structures, they can be made more user-friendly and suitable for targeted applications. These tailored shapes enhance their mechanical stability and ease of handling while ensuring compatibility with the operational requirements of various processes.

1.4 Structured Hydrogels: Designing Shape-Defined Soft Materials

Macrodimensional hydrogel objects capable of forming specific shapes hold great potential across a wide range of applications due to their tunable properties and structural versatility. These hydrogels, typically ranging from millimetres to centimetres in size, can be fabricated into well-defined geometries such as tubes, grids, filaments, pillars, hemispheres, and lattices using advanced techniques that ensure high structural precision. The ability to engineer distinct shapes enhances their functional utility and enables the integration of spatial heterogeneity, mechanical gradients, and internal architectures tailored for specific applications, such as controlled release, selective permeability, or structural support. Among the various fabrication strategies, direct-write assembly, three-dimensional bioprinting, replica moulding, and coaxial extrusion printing are the most prominent for generating structurally precise hydrogel constructs.

Direct-write assembly is a programmable fabrication technique that enables the deposition of hydrogel precursor inks into designed geometries with high resolution. Barry et al. utilized ultraviolet-assisted direct-write assembly to fabricate hydrogel scaffolds composed of acrylamide-based inks (Figure 1.4A).[50] These structures included one-dimensional filaments and three-dimensional lattice frameworks with controlled filament diameters and interfilament spacing. The printed scaffolds successfully supported the alignment and proliferation of NIH 3T3 fibroblasts, demonstrating the relevance of spatially organized shapes in guiding cellular behaviour. The ability to form grid-like structures with micron-level control made this technique suitable for replicating the fibrous microarchitecture of soft connective tissues such as muscle and tendon.

Three-dimensional bioprinting is another pivotal technique for shaping hydrogels into anatomically and functionally relevant forms. Hong et al. developed tough hybrid hydrogels comprising polyethylene glycol and alginate, which were printed into complex forms such as human ears and noses (Figure 1.4C).[51] These constructs exhibited excellent mechanical stability and supported high

cell viability. The dual crosslinking mechanism allowed the printed objects to retain their shape under physiological conditions. This ability to fabricate macroscopic hydrogel constructs with defined external geometries makes three-dimensional bioprinting indispensable in organ modelling and facial reconstructive engineering. Moreover, these printed shapes were mechanically robust and could be tuned by altering polymer concentration and crosslinking parameters.

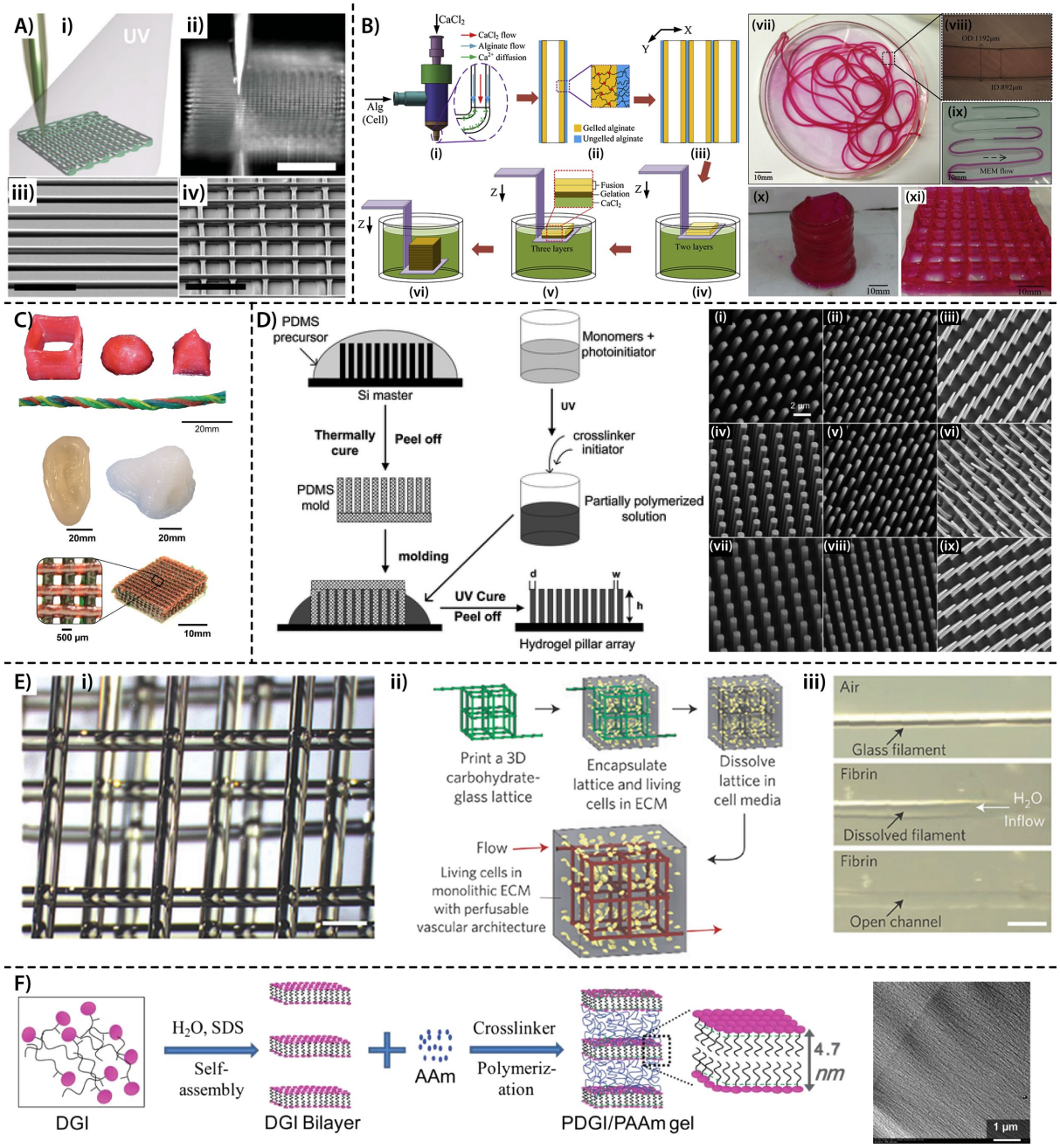

Figure 1.4 A) Direct ink writing of hydrogel scaffolds: (i) Schematic of UV-assisted extrusion through a gold-coated micro-nozzle, (ii) optical image of printed 3D scaffold, Scale bar: 200 µm. (iii) SEM of 1D filament array, Scale bar: 50 µm, (iv) SEM of four-layered microperiodic scaffold, Scale bar: 50 µm. B) Fabrication of 3D alginate constructs with internal microchannels: (i–vi) Schematic of the printing process, (vii–viii) images of hollow filaments, (ix) medium perfusion, (x–xi) printed structures with embedded channels. C) 3D hydrogel-printed

structures including a cube, hemisphere, pyramid, twisted bundle, ear, and nose. D) Schematic of hydrogel pillar array fabrication and SEM images of PHEMA hydrogel arrays with varying pillar sizes and spacing. E) Fabrication of vascularized hydrogel constructs: (i) Photopolymerized carbohydrate glass lattices with high spatial precision. (ii) Schematic of hydrogel vascular network formation with embedded cells. (iii) Sacrificial lattice embedded in ECM, dissolved to form perfusable 3D vascular architecture. F) Formation of a hybrid polymeric-DGI/PAAm hydrogel via self-assembly of DGI in SDS and subsequent polymerization within an acrylamide matrix, and TEM image showing uniaxial bilayer alignment within the hydrogel cross-section. Reproduced with permission from Ref. 50-55.

Coaxial nozzle-based extrusion printing provides a facile method for fabricating hydrogel tubes with hollow interiors, thereby enabling the generation of vascular-like constructs. Gao et al. implemented a coaxial printing strategy where sodium alginate and calcium chloride were simultaneously extruded to form hydrogel tubes with controlled outer diameter and wall thickness (Figure 1.4B).[52] These tubular structures could be stacked to create three-dimensional networks, facilitating their use in vascular tissue engineering. The method provided precise control over the geometry of the hollow channels, and the resultant structures exhibited good mechanical strength after secondary crosslinking. Such constructs are particularly valuable for building perfusable systems required in artificial vasculature and organ-on-chip devices.

Compared to techniques that require complex patterning or templating, extrusion-based fabrication allows the direct formation of shape-stable hydrogel structures using minimal processing steps. Smith et al. demonstrated that the low molecular weight gelator DBS-$CONHNH_2$ forms stable filaments upon extrusion into aqueous media, while co-extrusion with calcium alginate yields core–shell tubular constructs.[56] These structures are generated via a solvent-switch mechanism and retain their shape without the need for external moulds. Additionally, the gels enable in situ formation of gold nanoparticles within the matrix, imparting antimicrobial properties while maintaining high biocompatibility. Human mesenchymal stem cells cultured on these constructs exhibited enhanced viability and metabolic activity, highlighting their potential in the development of simple yet multifunctional hydrogel scaffolds.

Replica moulding has also been extensively used to fabricate hydrogels in specific shapes by casting prepolymer solutions into patterned moulds. Chandra et al. demonstrated the use of replica moulding to produce arrays of hydrogel pillars with uniform geometry (Figure 1.4D).[53] Using poly(hydroxyethyl methacrylate) and polydimethylsiloxane moulds, they fabricated cylindrical and conical hydrogel structures with feature sizes in the submicron to micrometre range. These structures maintained their shape upon demoulding and could be programmed to deform in response to environmental stimuli, making them useful for constructing mechanically responsive surfaces and soft tactile sensors. The regular shape and spatial arrangement of these pillars also provided a platform for studying cell-surface interactions at the microscale.

Sacrificial moulding is a technique that enables the fabrication of hydrogel constructs with internal channels and complex geometries. Miller et al. used this method to fabricate perfusable hydrogel scaffolds with vascular-like networks (Figure 1.4E).[54] Carbohydrate glass was printed into a three-dimensional lattice that served as a removable template embedded within a polyethylene glycol hydrogel matrix. Upon dissolution of the template, a hydrogel with precisely shaped internal channels remained. The spatial geometry of the channels could be customized by altering the template design, providing a versatile method for generating macroscopic constructs that mimic the hierarchical structure of blood vessels. These constructs were used to maintain high cell viability by enabling nutrient transport across thick hydrogel matrices, highlighting the significance of shape-specific design in large tissue engineering scaffolds.

Another example of specific shape formation is seen in the fabrication of lamellar hydrogels with anisotropic properties. Gong et al. synthesized sandwich-like laminar hydrogels through the self-assembly of amphiphilic monomers such as dodecyl glyceryl itaconate in the presence of acrylamide and crosslinkers (Figure 1.4F).[55] The resulting hydrogels exhibited a layered internal structure with parallel bilayers, leading to direction-dependent mechanical properties. The hydrogels maintained a slab-like rectangular shape and displayed distinct elastic modulus values depending on the direction of applied stress. These lamellar hydrogels demonstrated potential in soft actuators and as responsive substrates for strain sensing applications. The ability to fabricate rectangular prisms with internal alignment further extends the design space for macrodimensional hydrogel objects.

In addition to lamellar and vascular structures, hydrogel cubes and hemispheres have been fabricated using mould-based strategies. For example, hydrogel microspheres and hemispherical domes can be created using well plates or concave moulds where photopolymerization is initiated through a defined interface.[57] These structures are employed in drug delivery, diagnostics, and as simplified models for tumour spheroids. Their symmetrical and reproducible shape is critical for consistent experimental outcomes, especially in high-throughput biological assays.

Taken together, these examples underscore the versatility of macrodimensional hydrogels in forming specific shapes with functional relevance. The integration of advanced fabrication techniques such as direct-write assembly, three-dimensional bioprinting, coaxial extrusion, replica moulding, and sacrificial templating has enabled precise control over hydrogel geometry, internal architecture, and spatial functionality. These shaped hydrogels can be engineered to mimic the native organization of tissues, support cell growth and differentiation, and facilitate the development of responsive or perfusable systems. Future advancements are likely to focus on enhancing the resolution, scalability, and multifunctionality of these fabrication methods, thereby

expanding the range of applications for shape-specific macrodimensional hydrogel objects in regenerative medicine, soft robotics, and organ-on-chip technologies.

1.5 The Concept of Hydrogel Beads

Among the various macrodimensional hydrogel architectures developed for specific applications, hydrogel beads represent a particularly versatile and widely studied form. These bead-shaped hydrogels combine the advantages of macroscopic size with well-defined spherical geometry, enabling efficient handling, uniform diffusion profiles, and scalable fabrication. Unlike bulk hydrogels with irregular or slab-like forms, hydrogel beads possess discrete, reproducible dimensions that make them highly compatible with both batch and continuous processing systems. Typically, hydrogel beads are produced by dispersing a hydrogel precursor solution into an immiscible continuous phase through techniques such as droplet extrusion, microfluidics, or emulsion polymerization, followed by gelation via physical or chemical crosslinking.[58] The resulting beads comprise a soft, hydrated, three-dimensional polymeric network capable of retaining large volumes of water while maintaining mechanical integrity. This structure enables hydrogel beads to function as microreactors, cell carriers, adsorbent particles, or controlled release systems in a wide array of biomedical and environmental applications.

One of the core advantages of hydrogel beads over bulk hydrogels lies in their macrodimensional yet discrete structure, which offers a high surface-area-to-volume ratio, improved diffusivity, ease of handling, and enhanced reusability. Their spherical shape ensures consistent diffusion kinetics, which is especially critical in drug delivery or biosensing applications where uniform release or signal response is necessary. Moreover, hydrogel beads can be functionalized with various active components such as nanoparticles, enzymes, or ligands to impart catalytic, bioactive, or responsive functionalities.[59-62] For instance, beads composed of alginate, a naturally derived polysaccharide, can be ionically crosslinked using calcium ions to encapsulate living cells or drugs, offering a gentle and biocompatible environment for biomedical use.[63, 64] In environmental science, synthetic hydrogel beads made from polyacrylamide or polyvinyl alcohol have been employed to entrap catalysts or adsorbents for the removal of pollutants like heavy metals, dyes, and phenolic compounds. Furthermore, hydrogel beads have been integrated into controlled release systems, where their swelling and degradation profiles are tailored to release encapsulated agents in a time- or environment-dependent manner. The modular design of hydrogel beads also facilitates their incorporation into flow-through systems, such as packed bed reactors or column setups, where the flow of liquids across the bead matrix enables continuous processes. This makes them particularly attractive for reusable biocatalysts or in vitro cell culture models. Structurally, hydrogel beads can

be engineered to possess core–shell architectures, anisotropic domains, or gradient compositions by manipulating fabrication parameters, including solvent exchange, crosslinking time, or precursor composition. Such structural diversity allows tuning of mechanical strength, permeability, and responsiveness to external stimuli such as pH, temperature, or light. While their physical dimensions typically range from a few micrometres to several millimetres, their size distribution can be tightly controlled through microfluidic or nozzle-based generation techniques. In recent years, hybrid hydrogel beads incorporating inorganic nanomaterials or responsive polymers have demonstrated enhanced functionalities, including stimuli-induced colour change, catalytic activity, or antibacterial effects, thus expanding their applicability in advanced sensing and therapeutic platforms.

Overall, the concept of hydrogel beads lies at the intersection of material science and functional design, offering a versatile and tunable platform that bridges fundamental research and practical application in biomedical, environmental, and industrial domains. Their discrete, reproducible shape, combined with the inherent advantages of hydrogel materials, make them an essential tool in the development of next-generation soft materials and multifunctional devices.

1.6 Fabricating Hydrogel Beads: Techniques and Approaches

Spherical hydrogel beads, typically ranging from tens of nanometres to a few millimetres in diameter, are fabricated using various techniques that allow precise control over their size, shape, internal architecture, and functional properties. These beads are generally synthesized by inducing gelation in confined domains through either physical or chemical crosslinking. Depending on the desired characteristics and applications, fabrication techniques can be broadly classified into six main categories: injection-based methods, templating techniques, polymer phase separation, antisolvent precipitation, top-down particle reduction, and polymerization-based approaches (Figure 1.5). Each of these techniques offers distinct advantages and is selected based on the polymer type, bead size requirements, scalability, and intended application.

Injection-based methods are among the most common techniques used to prepare hydrogel beads, especially in the millimetre to sub-millimetre range. In the simplest form, hydrogel precursor solutions are dropped into a crosslinking bath, usually containing multivalent cations or a chemical initiator.[65] The most well-known example is the formation of calcium alginate beads by extruding sodium alginate into a calcium chloride solution, where ionic crosslinking occurs at the droplet interface. This technique benefits from simplicity, biocompatibility, and mild gelation conditions. However, droplet sizes tend to be polydisperse. To overcome this limitation, microfluidic devices have been developed that allow generation of highly monodisperse hydrogel droplets.[63] In microfluidic flow-focusing geometries, a hydrogel precursor is sheared into uniform droplets within

an immiscible oil phase. These droplets are then gelled either within the chip or downstream. Cha et al. fabricated core–shell microgels composed of methacrylated gelatin and silica nanoparticles using a microfluidic device, achieving uniform sizes in the range of 35 to 150 micrometres.[66] Similarly, Kim et al. developed a dual flow-focusing microfluidic system to encapsulate cells within gelatin-based microgels, yielding beads between 30 and 120 micrometres in diameter while preserving high cell viability.[67] Another advanced variant of this approach is electrospraying, where a high-voltage electric field breaks a hydrogel solution into micron-sized droplets that are collected in a crosslinking bath.[68] Electrospraying allows for the generation of small beads with narrow size distribution and is suitable for core–shell bead production using coaxial nozzle configurations.

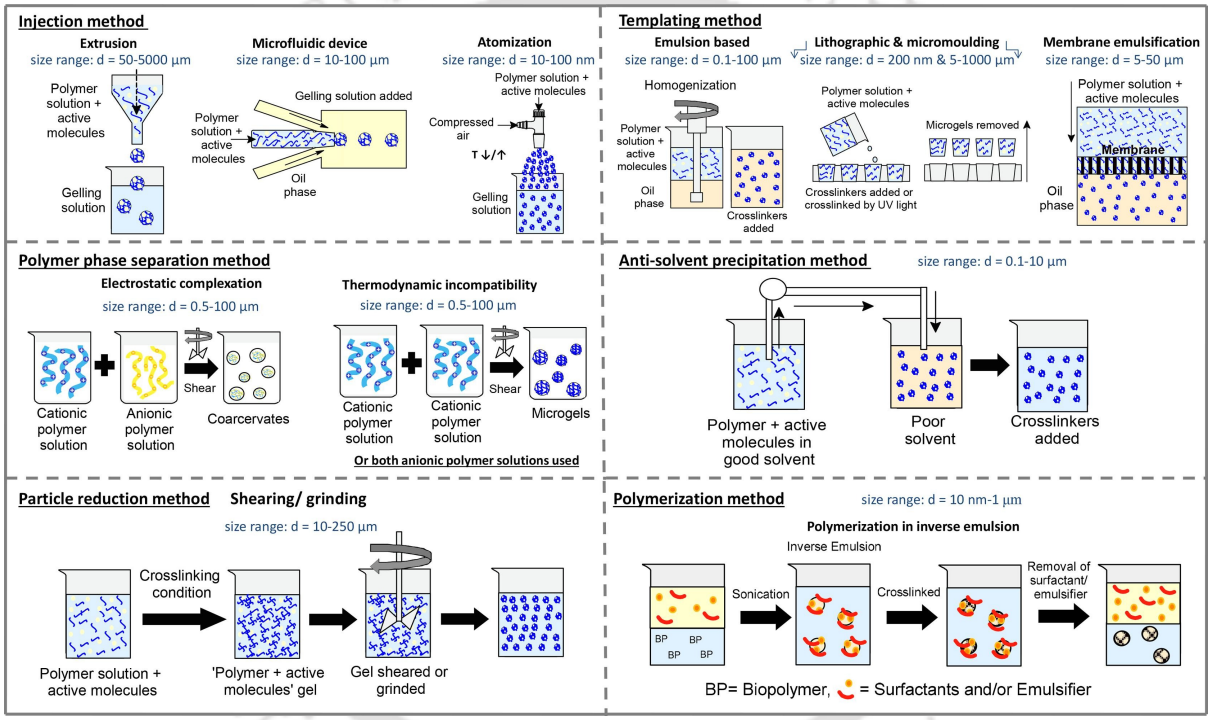

Figure 1.5 Schematic representations of different techniques used for the fabrication of micro- and macro-dimensional hydrogel beads. Reproduced with permission from Ref. 69.

Templating techniques provide another robust strategy for hydrogel bead fabrication by using physical templates to define droplet size and shape. In emulsion-based templating, an aqueous hydrogel precursor is dispersed into an oil phase under high shear, forming water-in-oil droplets that act as templates.[70] These droplets are then crosslinked thermally, photochemically, or ionically to yield spherical hydrogel particles. Emulsion polymerization is particularly useful for preparing beads from synthetic monomers such as acrylamide, N-isopropylacrylamide (NIPAm), or polyethylene glycol diacrylate (PEGDA). After polymerization, beads are recovered via centrifugation and solvent washing. Inverse emulsion techniques are especially suited for nanogel synthesis, where droplet diameters are in the range of 50 to 500 nanometres. Microemulsion

polymerization further refines this approach by producing nanogels with diameters under 100 nanometres. These methods offer high reproducibility and scalability, although they often require surfactant removal steps. Another templating method involves membrane emulsification, where a hydrogel solution is forced through a membrane with defined pore size into a crosslinking bath or immiscible phase, forming droplets of controlled size.[71] Photolithographic and micromoulding techniques are also employed for fabricating uniform hydrogel spheres, particularly when high precision and pattern fidelity are required for applications in diagnostics or drug screening.[70]

Polymer phase separation is another strategy used for bead formation, relying on the thermodynamic incompatibility of polymer mixtures.[70] When two aqueous polymers, such as gelatin and maltodextrin, are mixed under shear conditions, they phase separate into discrete domains.[72] These domains can be crosslinked using biocompatible agents such as genipin to form stable microgels. This method is particularly attractive for creating water-in-water emulsions that are free from organic solvents or surfactants. Another phase separation approach involves electrostatic complexation, where polyelectrolyte complexes are formed between oppositely charged polymers such as chitosan and gum arabic.[73] The resulting coacervate droplets are spherical and can be stabilized by chemical or thermal crosslinking. This technique enables the formation of multi-compartmental beads, which are useful for co-delivery of incompatible drugs or sequential release applications.

Antisolvent precipitation, also known as solvent displacement, is particularly effective for the fabrication of spherical beads from hydrophilic biopolymers.[70] In this technique, a polymer dissolved in a good solvent (such as ethanol or acetone) is introduced into a non-solvent like water. The sudden change in solvent environment leads to the rapid precipitation of the polymer into small, often spherical aggregates. These aggregates can then be stabilized by crosslinking. Zou et al. used this approach to fabricate core–shell microgels composed of zein and whey protein, which were employed for oral drug delivery.[74] Beads formed by this method typically have diameters under one micrometre, and the approach is well suited for creating porous or nanostructured hydrogel particles.

Top-down methods involve the mechanical breakdown of bulk hydrogel materials into smaller particles, which are then rounded and stabilized to form microgels. For example, shear-induced grinding can be used to fragment large hydrogel blocks into microspheres. These particles can be further processed by sonication, sieving, or crosslinking to improve sphericity and uniformity. Although this method lacks the size precision of bottom-up techniques, it is scalable and particularly useful for biodegradable polymers like pectin, gelatin, or agarose. It is often employed when high-throughput or low-cost production is prioritized over exact size control.

Polymerization-based techniques, including suspension and inverse emulsion polymerization, are highly versatile for synthesizing uniform hydrogel beads from synthetic polymers. In suspension polymerization, the monomer solution is dispersed in a continuous phase (usually oil) with the help of stabilizers, and polymerization is initiated thermally or photochemically. In inverse emulsion polymerization, the aqueous monomer phase is emulsified in an organic phase and polymerized within nanodroplets to yield nanogels. These methods allow for incorporation of functional comonomers, crosslinkers, and initiators, enabling precise control over network density and functional group distribution. Zheng et al. synthesized guar gum-based microgels by inverse emulsion polymerization, using epichlorohydrin as a crosslinker in a system stabilized by Span 80 and Tween 60.[75] Similarly, κ-carrageenan nanogels have been prepared using reverse microemulsions stabilized by cetrimonium bromide in n-heptane.[76] These polymerization methods offer a high degree of tunability and are particularly suitable for creating responsive or stimuli-sensitive microgels for applications in biosensing and targeted drug delivery.

1.7 Applications of Hydrogel Beads: A Multidisciplinary Perspective

Hydrogel beads have garnered significant attention as multifunctional platforms due to their tunable physicochemical properties, high water retention capacity, and compatibility with a wide range of functional materials. Their ability to encapsulate active agents, respond to external stimuli, and maintain structural integrity under diverse conditions has positioned them as promising candidates across numerous fields. This section provides a comprehensive overview of recent advances in the design and application of hydrogel beads, highlighting their roles in adsorption, catalysis, biosensing, environmental remediation, agriculture, and controlled substance delivery. In biomedical sciences, they are used for drug delivery, cell immobilization, and tissue engineering. Functionalized beads act as reusable catalytic microreactors, while in environmental systems they serve as efficient adsorbents for pollutant removal. In agriculture, hydrogel beads improve soil moisture retention and nutrient release, reflecting their versatility across disciplines.

1.7.1 Hydrogel Beads as Adsorbents for Ion and Molecule Capture

Hydrogel beads have emerged as potent and multifunctional adsorbents for ion and molecule capture, owing to their hydrophilic networks, high surface area, tunable functionality, and environmentally benign nature. Their structural versatility has allowed researchers to engineer these materials for a wide range of applications in water purification, toxic metal removal, and clinical detoxification. Recent advancements focus on the rational modification of bead composition and architecture to maximize adsorption capacity, selectivity, and reusability under real-world conditions.

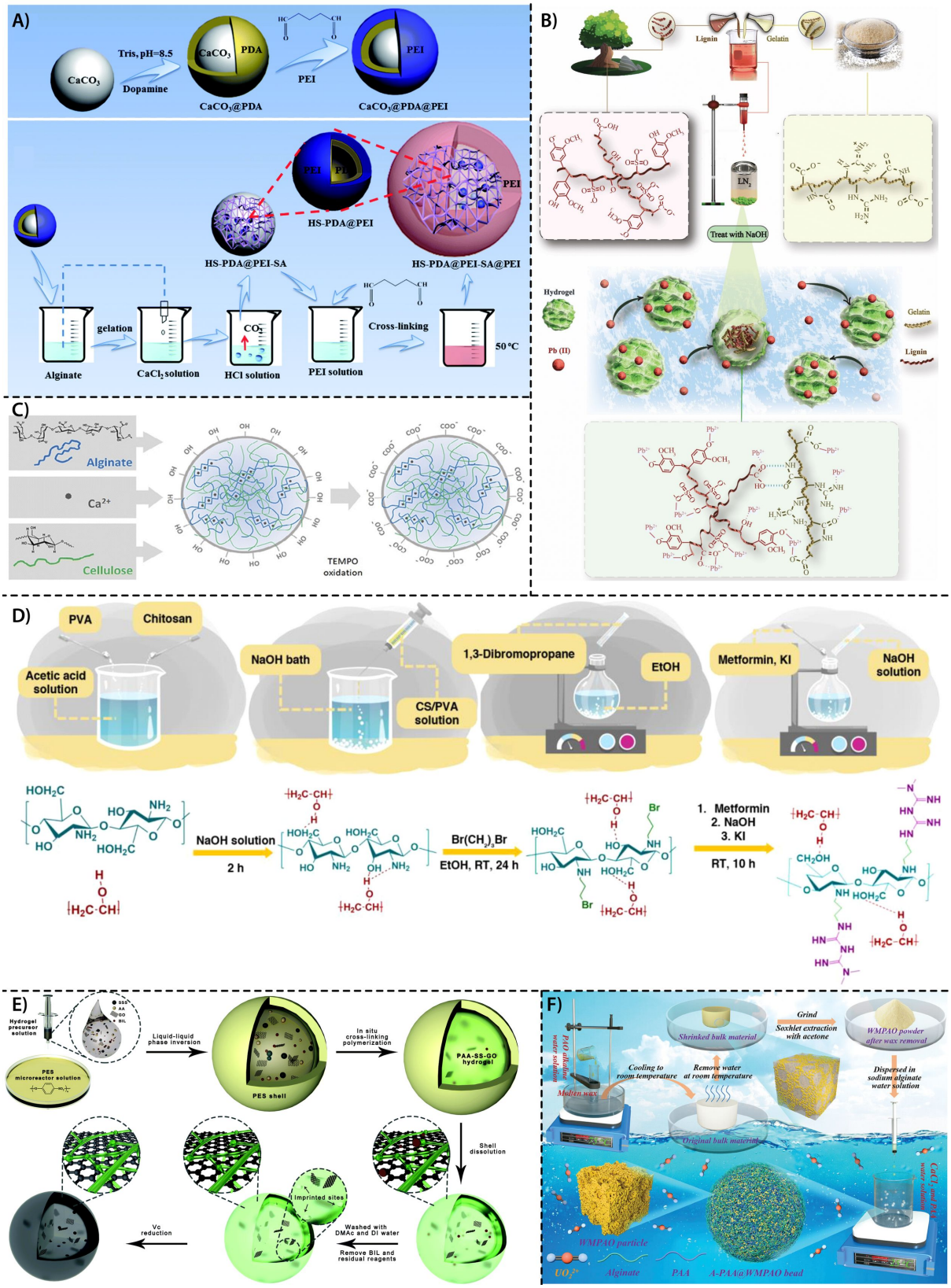

Figure 1.6 Schematic illustrations of various hydrogel bead fabrication strategies: A) Preparation of $CaCO_3$@PDA@PEI and HS-PDA@PEI-SA@PEI beads, B) SKLGE bead synthesis and Pb(II) adsorption mechanism, C) Cellulose-SA bead formation via Ca^{2+} complexation and TEMPO oxidation, D) Synthesis of CS/PVA-based bead variants, E) Bead formation using self-sacrificing micro-reactors, and F) Fabrication of WMPAO hydrogel

particles and A-PAA@WMPAO beads for uranium extraction from seawater. Reproduced with permission from Ref. 77-82.

A representative example of structural optimization was demonstrated by Yan et al., who developed functional alginate beads constructed using polydopamine-polyethylenimine (PDA–PEI)-modified $CaCO_3$ particles as solid porogens, where PEI served as both an interior and surface modifier (Figure 1.6A).[77] The removal of $CaCO_3$ created hollow cavities enriched with immobilized reactive amine sites, while additional PEI was grafted onto the bead surface via crosslinking. This dual-functional architecture provided accessible PEI both internally and externally, enabling highly efficient Cr(VI) adsorption from aqueous solutions. The composite beads performed well under both batch and continuous flow conditions, supported by kinetic modelling that followed pseudo-second-order behaviour. Their ability to be regenerated over multiple cycles with negligible performance loss highlighted their suitability for scalable water remediation technologies.

In another study, Georgouvelas et al. introduced a nanocellulose/alginate composite bead system, where surface oxidation via TEMPO-mediated chemistry enriched the bead matrix with carboxyl groups (Figure 1.6C).[79] These beads achieved high efficiency in removing cationic species like Cd^{2+} and dyes such as methylene blue. Their porosity reached approximately 99%, resulting in high water throughput without significant pressure drop, and enabling high-flux treatment processes. Importantly, the modified beads retained structural integrity and adsorption performance under operational conditions, emphasizing their practical utility for industrial wastewater treatment.

To broaden the pollutant spectrum, Ramsheh et al. devised hydrogel beads composed of chitosan and poly(vinyl alcohol) (CS/PVA), further functionalized with metformin to introduce nitrogen-rich active sites (Figure 1.6D).[80] The resulting CS/PVA-Pr-Met beads exhibited dual adsorption functionality, effectively capturing both Pb(II) ions (313 mg g^{-1}) and pharmaceutical contaminants like levofloxacin (2872 mg g^{-1}). The enhanced adsorption was attributed to coordination interactions involving –NH, $–NH_2$, and imidazole groups in metformin, and the system adhered well to the Langmuir isotherm and pseudo-second-order kinetics. The beads showed excellent reusability, retaining their adsorption capacity over multiple cycles, making them promising for use in complex wastewater streams containing both metal ions and pharmaceuticals.

To promote sustainable material design, Hu et al. developed hydrogel beads from industrial waste-derived sulfonated kraft lignin (SKL) blended with gelatin (Figure 1.6B).[78] A green and rapid fabrication method involving liquid nitrogen-assisted cooling was employed to form highly porous beads. These lignin–gelatin (SKLGE) beads showed excellent Pb(II) ion adsorption capacity, reaching up to 155 mg g^{-1}. Their performance was further enhanced by covalent crosslinking with EDC, which improved both structural stability and adsorption efficiency. Notably, the beads maintained

integrity and functionality across ten regeneration cycles in both acidic and basic conditions, highlighting their practical applicability and alignment with circular economy goals.

For biosorption-based approaches, Gokhale et al. encapsulated yeast cells within hollow hydrogel capsules to develop a scalable solution for lead removal from trace-contaminated water.[83] The biosorptive activity of the yeast was preserved, while the hydrogel matrix provided mechanical strength and ease of separation from treated water. These yeast-laden capsules achieved rapid uptake of Pb(II) ions, reaching equilibrium within minutes, and were successfully integrated into a continuous flow-packed bed system capable of meeting stringent regulatory standards. The system demonstrated robustness over extended operational periods, suggesting its potential for low-cost decentralized water treatment applications.

Beyond environmental remediation, hydrogel beads have found important applications in clinical detoxification. Yin et al. proposed a molecularly imprinted hydrogel bead system to selectively adsorb bilirubin (BIL), a toxic metabolite accumulated in patients with liver dysfunction (Figure 1.6E).[81] Using self-sacrificing micro-reactors, the team synthesized PAA–SS–rGO hydrogel beads imprinted with BIL, enabling high selectivity through template-driven recognition and π–π/hydrophobic interactions. These beads also incorporated sulfonated and carboxylated groups that mimic heparin, thereby ensuring excellent blood compatibility. In vitro assays demonstrated their ability to reduce bilirubin to safe levels within hours, indicating strong promise for blood purification and hemoperfusion therapies.

A particularly high-impact development in the area of nuclear resource recovery was introduced by Yang et al., who designed macroporous polyamidoxime (PAO) hydrogel particles using a wax-casting method (Figure 1.6F).[82] These PAO particles were encapsulated in alginate–polyacrylic acid (A-PAA) beads to create A-PAA@WMPAO composites for uranium extraction from seawater. The amidoxime groups provided multiple coordination sites for uranyl ion capture, and the macroporous structure facilitated fast mass transport. These composite beads demonstrated exceptional uranium uptake, reaching up to 687 mg g^{-1} in laboratory settings and maintaining their performance over five regeneration cycles. The simplicity, scalability, and efficacy of this approach position it as a leading candidate for sustainable uranium recovery from marine sources.

These studies highlight that hydrogel beads have emerged as versatile and efficient materials for pollutant removal from aqueous systems. Their tunable structures, functional group diversity, and adaptability to different treatment conditions make them promising candidates for sustainable water purification technologies. Ongoing research continues to focus on enhancing their regeneration efficiency and scalability to enable practical deployment in real-world remediation processes.

1.7.2 Hydrogel Beads in Sustainable Agriculture and Soil Conditioning

Hydrogel beads have gained increasing attention in sustainable agriculture due to their multifunctionality in nutrient delivery, soil conditioning, water retention, and environmental protection. Various studies have explored their potential to enhance agricultural productivity while addressing issues such as fertilizer inefficiency, water scarcity, and soil degradation. Karunarathna et al. demonstrated that Fe(III)–polysaccharide hydrogel beads could be employed to capture valuable nutrients such as phosphate, ammonium, and nitrate from animal waste (Figure 1.7B).[84] These beads effectively absorbed up to 0.7 mg g^{-1} ammonium from raw manure and released nutrients in a controlled manner. In greenhouse trials using tomato plants, the nutrient-loaded hydrogels supported comparable growth and fruit production relative to conventional fertilizers, while significantly minimizing nutrient leaching and environmental runoff. Moreover, the photoresponsive nature of the Fe(III)–carboxylate complex enabled sunlight-triggered nutrient release, offering potential for light-mediated fertilization strategies. The system also preserved soil microbial diversity, making it a sustainable choice for integrated nutrient management in agriculture.

Chang et al. advanced the utility of hydrogel beads by addressing agricultural water demands. They fabricated double-network hydrogel beads (cl-SP beads) from marine biomass-derived sodium alginate and thermoresponsive PNIPAM, incorporating hygroscopic calcium chloride and photothermal dyes (Figure 1.7A).[85] These beads captured atmospheric moisture during nighttime and released it during daytime through temperature- and light-induced phase transitions. A solar-powered seed propagator integrated with these beads successfully sustained plant germination and growth in the absence of direct water supply. With a water uptake capacity exceeding 5 g g^{-1} under 90% relative humidity and efficient solar-triggered desorption, this system demonstrated how hydrogel beads can provide clean irrigation water in off-grid and arid regions, supporting resilient and energy-efficient agriculture.

In another significant development, Baruah et al. engineered biodegradable hydrogel beads composed of carboxymethyl cellulose (CMC), zinc oxide (ZnO), and nickel ions (Ni^{2+}) for simultaneous nutrient delivery and soil improvement (Figure 1.7C).[86] These beads were loaded with urea and dipotassium hydrogen phosphate to create slow-release formulations (UHB and UPHB). The urea release in soil extended up to 15 days, demonstrating sustained nutrient availability. Importantly, the presence of nickel supported urease enzyme activity in soil, facilitating the conversion of urea to ammonium for plant uptake. Trials using rice as a model crop showed that 0.5 wt% UHB in soil significantly enhanced plant growth, root development, and nitrogen assimilation, particularly under water-stress conditions. Additionally, the hydrogel beads improved the water

holding and retention capacity of sandy soils and increased parameters like cation exchange capacity and electrical conductivity during biodegradation. This multifunctional design not only improved nutrient use efficiency but also addressed the common challenges of Ni deficiency and nitrogen loss in flooded paddy fields.

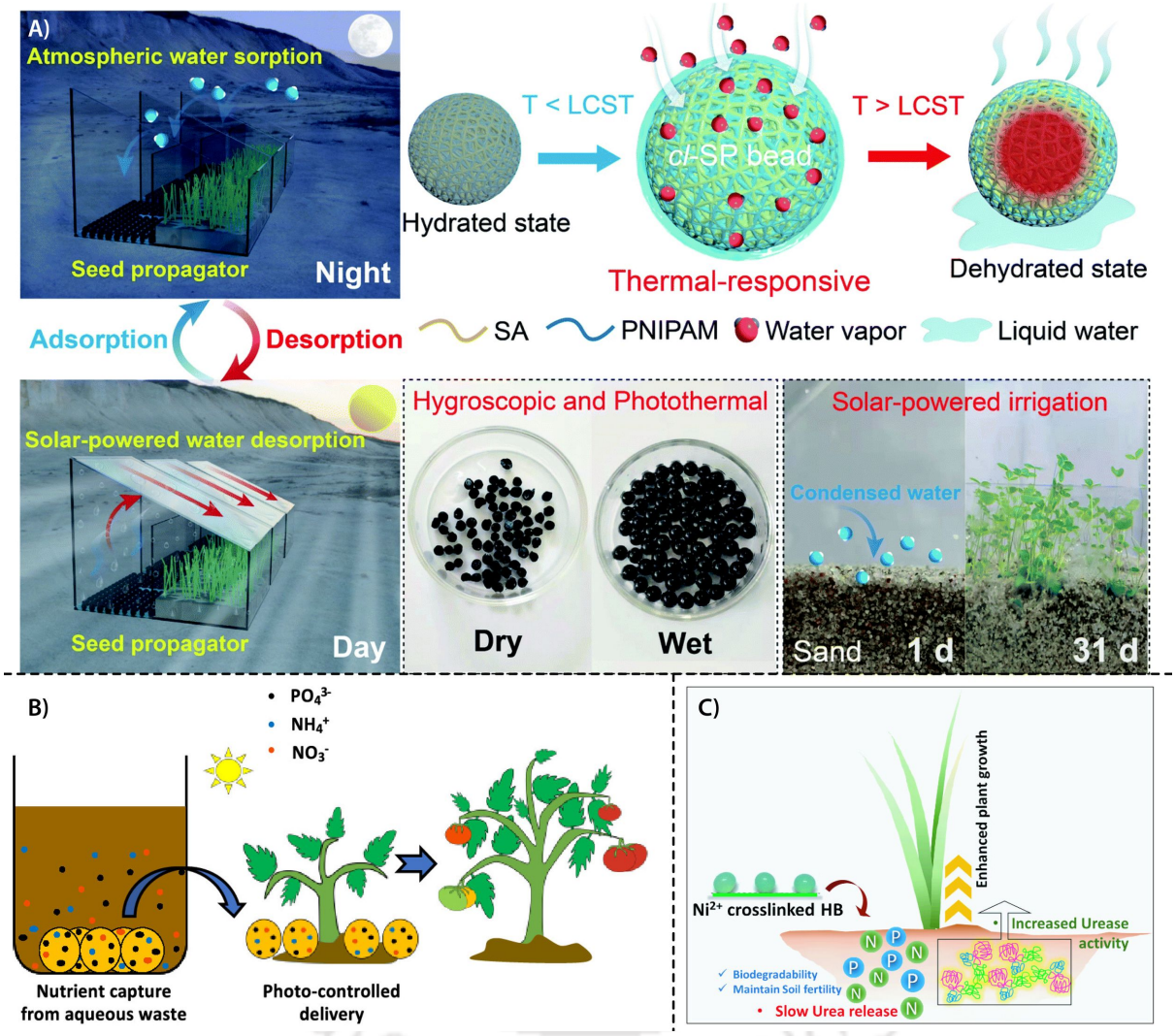

Figure 1.7 Schematic illustrations of hydrogel bead applications: A) cl-SP beads with hygroscopic, photothermal, and temperature-responsive properties for water harvesting and solar irrigation, B) Fe(III)–polysaccharide hydrogels for nutrient capture and photo-controlled fertilizer delivery, C) Biodegradable CMC/ZnO/Ni hydrogel beads for promoting plant growth and soil urease activity. Reproduced with permission from Ref. 84-86.

Together, these studies demonstrate the versatility of hydrogel beads in sustainable agriculture through applications such as nutrient recovery, controlled fertilizer release, water harvesting, and soil improvement. Their responsive features allow precise control over water and nutrient availability, while the use of biodegradable and low-cost materials ensures environmental

sustainability. These multifunctional systems offer promising solutions for enhancing crop productivity and resilience in the face of growing agricultural challenges.

1.7.3 Hydrogel Beads for Pollutant Degradation and Environmental Clean-Up

Hydrogel beads have progressively evolved as advanced functional materials for environmental remediation, showcasing remarkable versatility in pollutant degradation and clean-up. Xu et al. pioneered the use of buoyant calcium alginate beads encapsulating carbonic anhydrase (CA) for enhancing atmospheric CO_2 capture in microalgal systems (Figure 1.8A).[62] Through glutaraldehyde crosslinking, CA was immobilized within the bead matrix, retaining enzymatic activity over repeated cycles and significantly improving microalgal productivity. These enzyme-stabilized hydrogel systems demonstrated effective CO_2 mass transfer at the air–culture interface, offering a sustainable solution to carbon biofixation constraints in large-scale algal cultivation.

In a parallel effort to address water pollution, Shaheen et al. reported hybrid ionotropic hydrogel beads formed by electrostatic interaction between ammonium metavanadate (AMV) and chitosan-based biopolymers (Figure 1.8B).[87] These AMV–polymer composites exhibited a unique combination of luminescence, self-healing, and mechanical robustness. The beads demonstrated high swelling capacity (up to 432%) and an outstanding Congo red adsorption capacity of 539 mg/g, surpassing many natural biosorbents. Their multifunctionality extended to ascorbic acid sensing and antimicrobial activity, with significant inhibition zones against pathogenic bacteria. The incorporation of polyoxometalate clusters endowed the beads with redox and coordination-driven functionalities, enhancing environmental applicability across dye adsorption, sensing, and microbial control.

Continuing the innovation, Yang et al. developed CS-Ca@PEI/$CuMnO_2$ hydrogel beads capable of activating peroxymonosulfate (PMS) for the degradation of Congo red (Figure 1.8C).[88] Utilizing a bimetallic oxide catalyst embedded within a cellulose nanofiber–alginate–polyethylenimine matrix, the beads achieved over 90% dye degradation at neutral pH, retaining catalytic efficiency across multiple cycles. Reactive oxygen species, including singlet oxygen and superoxide radicals, were identified as key oxidative agents, underscoring the beads' advanced oxidation process (AOP) performance. Their structural integrity, reusability, and heterogeneous configuration ensured minimal secondary pollution, making them apt for industrial wastewater treatment.

Subsequently, Harris et al. engineered PVA-alginate hydrogel beads encapsulating *Rhodococcus rhodochrous* ATCC 21198 bacterial strain and tetrabutoxysilane for aerobic cometabolism of cis-1,2-dichloroethylene (Figure 1.8D).[89] Employing a design of experiments approach, optimal bead formulations were developed to support microbial viability and mechanical resilience under field-

mimicking conditions. The beads enabled sustained pollutant degradation in low-permeability aquifers, offering a robust, passive remediation strategy for chlorinated solvent-contaminated groundwater. The slow-release substrate ensured steady microbial metabolism, while the bead matrix preserved oxygen diffusion and mechanical integrity over extended deployment.

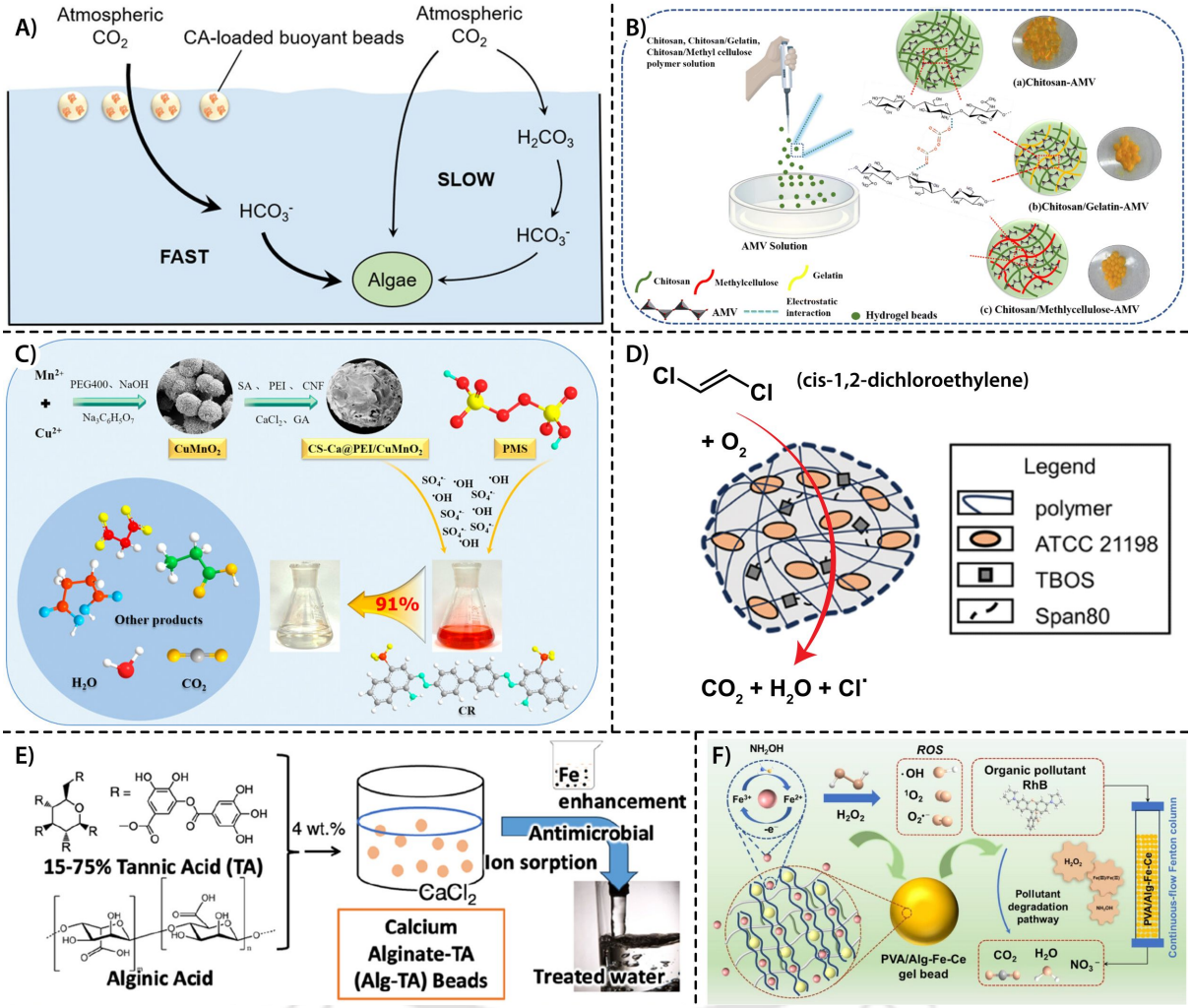

Figure 1.8 Schematic illustrations of diverse hydrogel bead applications: A) CO_2 capture using carbonic anhydrase-encapsulated buoyant hydrogel beads, B) Programmable chitosan-based bead formation via ammonium metavanadate (AMV) interactions, C) Reusable CS-Ca@PEI/$CuMnO_2$ beads for Congo Red degradation, D) PVA–alginate beads with slow-release agents for chlorinated hydrocarbon co-metabolism, E) Polyphenol-based beads for metal ion adsorption and antimicrobial water treatment, F) Double-metal-cross-linked beads as Fenton catalysts for organic wastewater degradation. Reproduced with permission from Ref. 62, 87-91.

Jawed et al. then advanced polyphenol-based hydrogel design by incorporating tannic acid (TA) and alginate to develop Alg-TA beads with enhanced metal ion sorption and antimicrobial capabilities (Figure 1.8E).[90] With TA content reaching 75%, the beads demonstrated superior swelling, high Cr(VI) and Pb(II) uptake, and antimicrobial performance, particularly when iron was incorporated to form TA–Fe complexes. Their ambient-temperature gelation and rehydratable

format provided logistical benefits for decentralized water treatment in low-resource settings. These systems exemplified how natural, multifunctional components could be harnessed for eco-friendly pollutant remediation.

Further refining catalytic hydrogel platforms, Li et al. introduced double-metal cross-linked PVA/Alg-Fe-Ce hydrogel beads serving as stable heterogeneous Fenton catalysts (Figure 1.8F).[91] These beads rapidly degraded rhodamine B in both batch and continuous flow settings, demonstrating high catalytic turnover, minimal Fe leaching, and compressive strength up to 0.8 MPa. The incorporation of cerium enhanced coordination stability and reinforced the hydrogel framework, while PVA contributed to water transport and mechanical durability. The system's dual-network architecture facilitated effective hydroxyl radical generation and pollutant oxidation with sustained performance. Collectively, these studies underscore the advancing role of hydrogel beads in pollutant degradation and environmental clean-up.

1.7.4 Hydrogel Beads in Chemical and Biosensing Applications

Hydrogel beads have steadily evolved into highly efficient platforms for chemical and biosensing applications, driven by their intrinsic properties such as high water content, tunable porosity, biocompatibility, and capacity for functionalization. Early developments emphasized colorimetric and fluorometric detection of toxic metal ions, particularly lead. Wang et al. introduced polydiacetylene (PDA) liposome-encapsulated alginate hydrogel beads as dual-mode sensors capable of detecting Pb^{2+} ions through distinct colorimetric and fluorometric signals (Figure 1.9A).[92] The sensor is based on a custom-designed monomer (PCDA–DA) functionalized with dopamine, whose catechol groups strongly bind Pb^{2+}. Upon binding Pb^{2+}, the PDA undergoes a conformational change, triggering a distinct colour shift (blue to red) and fluorescence enhancement. These hydrogel beads addressed issues of liposome aggregation and signal instability commonly seen in solution-based systems. By immobilizing PDA–DA liposomes within alginate matrices via microfluidic droplet methods, they achieved improved sensitivity and reusability, demonstrating strong potential for trace-level heavy metal sensing in environmental applications.

Advancing this direction, Tam and Pradeep et al. designed alginate hydrogel beads embedded with bovine serum albumin-protected gold nanoclusters (Au@BSA NCs) and cellulose nanocrystals for simultaneous sensing and scavenging of mercury ions (Figure 1.9B).[93] The system allowed real-time, fluorescence-based monitoring of mercury binding, facilitated by the unique quenching behaviour of the gold nanoclusters upon metal interaction. Notably, they introduced a novel method to visualize analyte diffusion into hydrogel matrices by correlating it with fluorescence decay kinetics, allowing both quantitative sensing and dynamic diffusion modelling. This work marked a significant

step forward by combining sensing with contaminant removal, leveraging the multifunctionality of the hydrogel matrix.

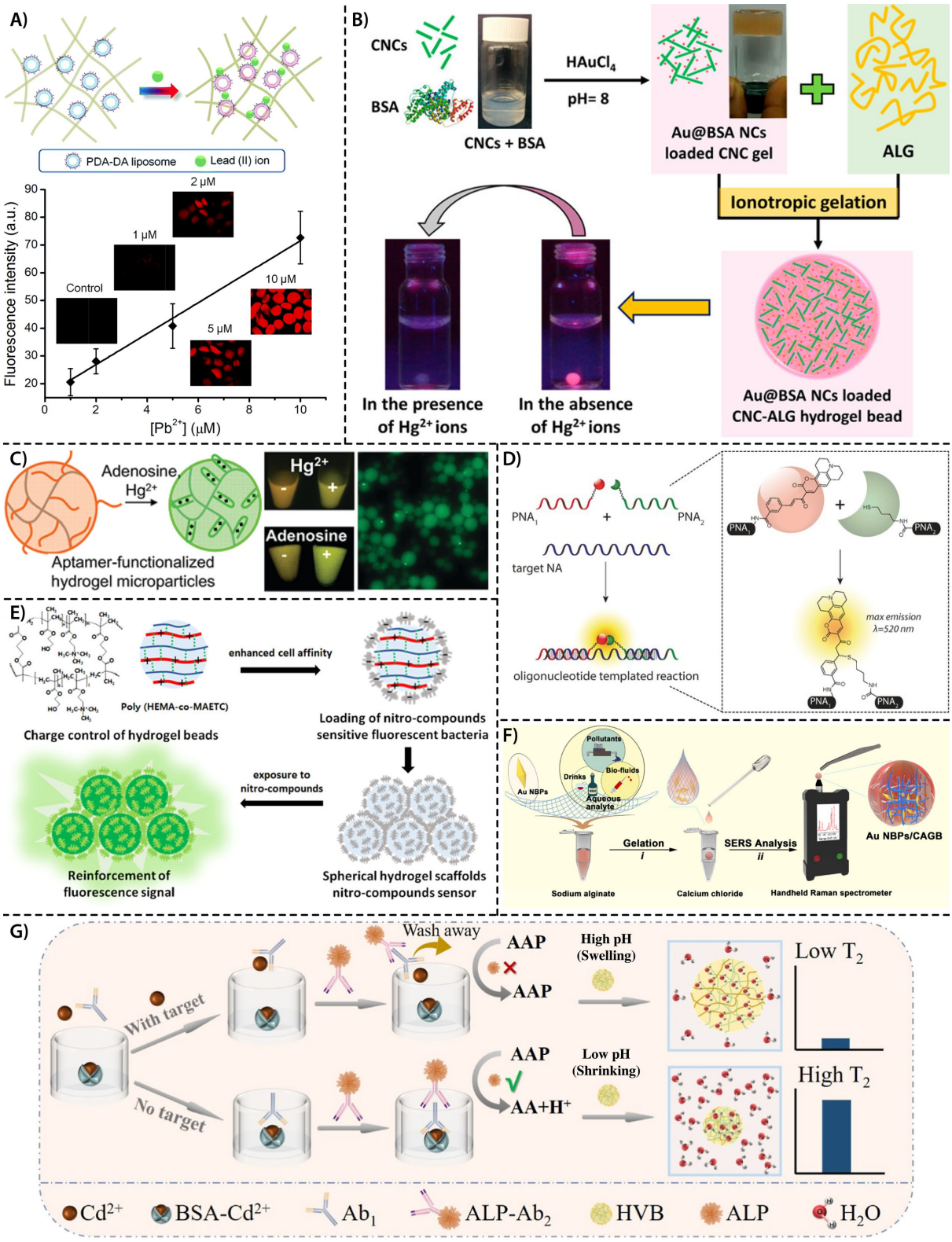

Figure 1.9 Schematic representations of hydrogel-based systems for sensing and detection applications: A) Colorimetric and fluorometric detection of Pb^{2+} using PDA–DA liposome-encapsulated hydrogel microbeads,

B) Diffusion-controlled sensing and scavenging of heavy metals using cluster–cellulose nanocrystal composites, C) Aptamer-functionalized hydrogel microparticles for rapid visual detection of Hg^{2+} and adenosine, D) Subnanomolar oligonucleotide detection via templated fluorogenic reactions in hydrogels, E) Fluorescence enhancement from nitro-compound-sensitive bacteria embedded in hydrogel spheres, F) Calcium alginate gel beads with gold nanobipyramids for SERS-based detection in aqueous media, and G) Gel-MRS immunosensor for Cd^{2+} detection. Reproduced with permission from Ref. 92-98.

In another significant contribution, Helwa et al. explored DNA-functionalized hydrogel microparticles for the optical detection of Hg^{2+} and adenosine (Figure 1.9C).[94] Using emulsion polymerization, they produced polyacrylamide beads incorporating aptamers that enabled rapid, visual detection of metal ions and nucleotides. These beads exhibited superior response kinetics compared to bulk monolithic gels, reducing detection time to just two minutes. This improvement was attributed to the shorter diffusion distances in microparticle geometry and effective analyte enrichment within the hydrogel network. The platform also underscored the critical role of aptamer affinity in defining sensing performance, as sensitivity to adenosine remained limited due to weaker target binding. Expanding the scope to nucleic acid detection, Al Sulaiman et al. implemented templated fluorogenic reactions within agarose and alginate hydrogels to detect oligonucleotides with subnanomolar sensitivity (Figure 1.9D).[95] By immobilizing peptide nucleic acid (PNA) probes in the hydrogel matrix, they achieved enhanced specificity and reduced background noise due to restricted molecular diffusion, which suppressed non-specific probe interactions. The hydrogel environment created confined reaction zones that improved the effective concentration of reactants and amplified the signal-to-noise ratio. This strategy, based on a fluorogenic Michael addition catalysed by the presence of target nucleic acids, was capable of detecting circulating microRNAs with high precision, making it well-suited for clinical biosensing applications.

Parallel to these developments, Kim et al. designed a biosensor using hydrogel scaffolds loaded with genetically engineered *Escherichia coli* expressing green fluorescent protein in response to nitroaromatic compounds such as trinitrotoluene (TNT) (Figure 1.9E).[96] The hydrogel beads, synthesized from poly(HEMA-co-MAETC), were surface-charge-modified to enhance bacterial loading through electrostatic attraction. These beads amplified the fluorescence signal upon exposure to TNT vapours, facilitating remote and long-distance detection. This work highlighted the utility of hydrogels as protective and signal-amplifying environments for living cell-based sensors, offering a safe and scalable alternative for explosive detection.

Building on material enhancement and signal transduction, Chen et al. introduced calcium alginate gel beads containing gold nanobipyramids (Au NBPs) as surface-enhanced Raman scattering (SERS) substrates (Figure 1.9F).[97] These beads addressed challenges in conventional SERS detection such as analyte-nanoparticle affinity and aggregation-induced signal variability. The 3D network of Au NBP-decorated alginate fibres formed uniform “hotspot” regions capable of capturing analytes

directly from aqueous samples. This system provided reproducible and rapid detection of rhodamine 6G and uric acid, achieving sub-nanomolar detection limits and strong correlation with ELISA results. Its portability, low cost, and evaporation-free detection made it suitable for point-of-care diagnostics and environmental monitoring.

Complementing optical and fluorescence strategies, Yang et al. developed a magnetic relaxation switch (MRS) sensor using pH-responsive hydrogel beads for cadmium detection (Figure 1.9G).[98] Unlike conventional MRS sensors that depend on nanoparticle dispersion or aggregation, their system modulated the transverse relaxation time (T2) of water protons via swelling-induced pH changes within the hydrogel. Sodium alginate and carboxymethyl chitosan formed the hydrogel matrix, and cadmium ions selectively trigger a pH change through an immunoassay-based enzymatic reaction. Without Cd^{2+}, antibodies bind to immobilized Cd^{2+} antigens, allowing alkaline phosphatase (ALP)-labelled secondary antibodies to catalyse ascorbic acid 2-phosphate (AAP) into ascorbic acid, releasing H^+ ions and lowering the pH. This acidic condition prevents hydrogel swelling, keeping water free and resulting in a high T_2 relaxation signal. When Cd^{2+} is present, it binds to the antibodies, preventing ALP retention and thus the reaction, keeping the pH higher. This higher pH causes hydrogel swelling, trapping water and lowering T_2, enabling sensitive Cd^{2+} detection. This design not only improved signal stability against magnetic field interference but also achieved a remarkably low detection limit of 0.009 ng/mL. The hydrogel-based MRS platform exhibited superior anti-interference capacity, making it highly suitable for food safety and environmental surveillance.

Altogether, these advancements illustrate versatility of hydrogel beads as robust platforms for chemical and biosensing applications. Their tunable structure and ability to integrate diverse sensing mechanisms make them highly effective for rapid, sensitive, and multiplexed detection across environmental and biomedical fields.

1.7.5 Catalytically Active Hydrogel Beads for Heterogeneous Catalysis

Catalytically active hydrogel beads have gained considerable attention in heterogeneous catalysis due to their ability to combine structural versatility, high surface area, and the confinement of catalytic species within a reusable and eco-friendly matrix. Among the earliest examples, Huang et al. developed silver nanoparticle-loaded calcium alginate hydrogel beads, further stabilized by glutaraldehyde crosslinking (Ag/CA\@GTA), to catalyse the reduction of 4-nitrophenol to 4-aminophenol (Figure 1.10A).[99] These beads demonstrated impressive durability and reusability, maintaining over 97% conversion through ten cycles. The enhanced mechanical strength imparted by crosslinking ensured stability in aqueous media, while nanoparticle characterization confirmed

uniform dispersion and limited aggregation. This system set an early benchmark for metal-loaded hydrogel catalysts by balancing catalytic efficiency with structural integrity.

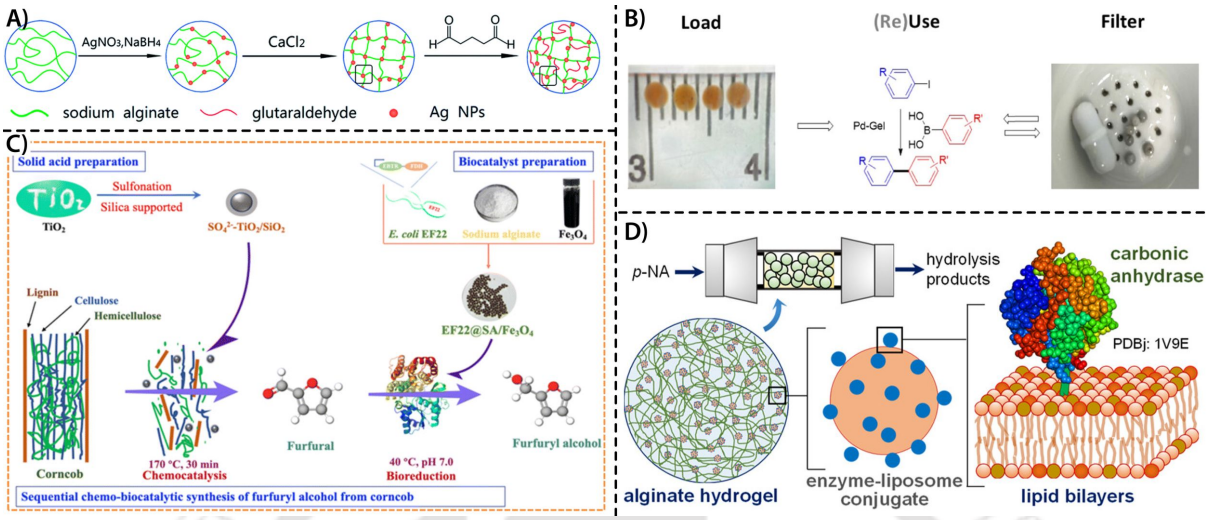

Figure 1.10 Schematic representations of hydrogel bead-based catalytic systems: (A) Preparation of Ag/CA@GTA catalytic hydrogel beads, (B) Palladium-loaded hybrid gel beads for reusable Suzuki–Miyaura catalysis, (C) Sequential chemo-biocatalytic conversion of corncob to furfuryl alcohol, (D) Liposome-assisted entrapment of carbonic anhydrase in alginate beads for continuous-flow catalysis. Reproduced with permission from Ref. 49, 99-101.

Subsequent developments explored hybrid hydrogel systems that combined the mechanical benefits of polymer gelators with the functional responsiveness of supramolecular networks. Piras et al. introduced a hybrid bead system by co-assembling calcium alginate with a low-molecular-weight gelator (LMWG), DBS-$CONHNH_2$.[65] These core–shell beads uniquely preserved the supramolecular characteristics of the LMWG within a structurally defined alginate shell. Importantly, the LMWG served as both a reductant and stabilizer for palladium, allowing in situ formation of catalytically active Pd^0 nanoparticles without the use of ligands or external reducing agents. A single Pd-loaded bead was sufficient to drive the Suzuki–Miyaura cross-coupling reaction, demonstrating that these beads could serve as discrete, ready-to-use catalytic units with precise dosing capabilities. The work highlighted how supramolecular assembly could be effectively translated into structured hydrogel forms for practical catalytic applications.

Building upon this concept, the same research group, led by Albino et al., refined the bead architecture by replacing alginate with agarose to improve mechanical resilience and eliminate the limitations encountered with earlier formulations (Figure 1.10B).[49] The resulting agarose–DBS-$CONHNH_2$ hybrid beads addressed key challenges such as Pd leaching, poor durability under stirring, and inefficient mass transfer. With enhanced thermal stability and mechanical stiffness, these beads enabled sustained catalytic activity under continuous stirring while maintaining bead integrity. Rheological and spectroscopic analyses confirmed the interpenetrating nature of the two

gel networks, and the in situ reduction of Pd^{2+} again produced "naked" Pd^0 nanoparticles that catalyzed Suzuki–Miyaura reactions under green conditions. The uniformity in bead size allowed for accurate catalyst dosing and scalability, making the system well-suited for modular synthesis and potential "reaction kit" deployment. By systematically evolving from core–shell alginate structures to robust interpenetrating agarose gels, this body of work established a comprehensive framework for the design of reusable, ligand-free palladium catalysts within hydrogel matrices.

From a biocatalytic perspective, Moriyama and Yoshimoto demonstrated that the entrapment of carbonic anhydrase-liposome conjugates in calcium alginate beads significantly enhanced enzyme retention and operational stability (Figure 1.10D).[101] Liposome-assisted encapsulation increased the effective molecular size of the catalyst complex, limiting enzyme leakage and maintaining catalytic activity under continuous-flow operation. These beads enabled efficient hydrolysis of p-nitrophenyl acetate, serving as a model for potential applications in enzymatic CO_2 hydration or other continuous bioprocesses. Their approach revealed how rational design at the molecular and colloidal scale could improve catalyst loading efficiency and mechanical performance within hydrogel matrices.

Extending hydrogel bead applications to integrated chemo–biocatalysis, Li et al. proposed a dual-function system using silica-supported SO_4^{2-}–TiO_2 for the chemocatalytic conversion of corncob biomass to furfural, followed by bioreduction to furfuryl alcohol using recombinant *E. coli* immobilized in Fe_3O_4-loaded calcium alginate beads (Figure 1.10C).[100] The hydrogel beads facilitated magnetic separation and reuse of whole-cell biocatalysts, contributing to enhanced productivity and selectivity in the two-step process. This strategy demonstrated the synergistic integration of solid acid catalysis and biotransformation within structured hydrogel matrices, highlighting the role of hydrogels in bridging biochemical and chemical catalysis for biomass valorization.

Collectively, these studies demonstrate the evolution of hydrogel beads into robust platforms for heterogeneous catalysis. Through strategic integration of nanoparticles, supramolecular gelators, and biocatalysts, these systems offer high efficiency, reusability, and adaptability for diverse catalytic applications.

1.7.6 Hydrogel Beads for Controlled Payload Release

Hydrogel beads have emerged as dynamic platforms for controlled payload release, offering structural tunability, responsiveness to physiological stimuli, and biocompatibility, traits that make them ideal for therapeutic delivery systems. Early efforts demonstrated the potential of supramolecular cross-linking strategies. Xu et al. fabricated monodisperse hydrogel beads using

droplet-based microfluidics by combining functional polymers with cucurbit[8]uril (CB[8]) (Figure 1.11A).[102] The host–guest interaction mediated bead formation allowed for both sustained and triggered release of fluorescein-labeled dextran. Release profiles followed an anomalous (non-Fickian) diffusion mechanism and could be accelerated by competitive guest-induced network disassembly. This system showcased the advantage of non-covalent assembly in responsive, programmable cargo release.

Building upon material diversity, Wu et al. developed dual cross-linked chitosan/sodium alginate (CS/SALG) beads for colon-targeted delivery of doxorubicin hydrochloride (DOX) (Figure 1.11B).[103] These beads demonstrated enhanced mechanical integrity to endure the gastrointestinal tract and a pH-sensitive release behaviour, minimal drug release in acidic and neutral environments and rapid release in simulated colonic conditions. In vitro cytotoxicity and in vivo assays affirmed their therapeutic efficacy and safety. The incorporation of polysaccharides ensured bioadhesion and mucosal compatibility, reinforcing the utility of natural polymer matrices in targeted drug delivery.

Advancements in gelator integration were achieved by Piras et al., who introduced hybrid beads formed by combining calcium alginate with two distinct low-molecular-weight gelators (LMWGs): pH-sensitive DBS-COOH and thermally responsive DBS-$CONHNH_2$ (Figure 1.11C).[104] These multi-component networks enabled tunable and pH-responsive delivery of rosuvastatin, a statin drug. Notably, the composition of the beads significantly influenced the drug release profile. While DBS-COOH/alginate systems allowed rapid release at intestinal pH, the three-component hybrid systems slowed drug diffusion, highlighting how multi-gelator systems enable precise modulation of payload kinetics via environmental triggers.

Miniaturization and injectability were addressed in subsequent work by Piras et al., who developed injectable microgel beads based on the same LMWG/alginate system.[105] Using an emulsion-based method, they achieved sub-millimeter spherical gel particles that retained heparin, a bioactive polysaccharide used to promote tissue regeneration. These microgels maintained shape fidelity and responsiveness after injection, demonstrating their capacity to support cell growth and therapeutic delivery in regenerative applications. This innovation illustrated the transition from macro-scale oral formulations to minimally invasive injectable delivery systems, broadening the clinical utility of hydrogel beads.

Further leveraging environmental responsiveness, Chen et al. designed insulin-loaded porous starch–alginate hydrogel beads exhibiting dual sensitivity to pH and α-amylase (Figure 1.11D).[106] These beads protected insulin from gastric degradation and enabled targeted release in the intestine. The degree of release could be fine-tuned by adjusting the thickness of an added high-amylose starch film, achieving a graded release profile tailored to postprandial glycemic

fluctuations. Their porous microstructure enhanced drug entrapment, while enzymatic degradation of starch offered a second trigger beyond pH, demonstrating the advantages of multistage responsiveness in controlled insulin delivery.

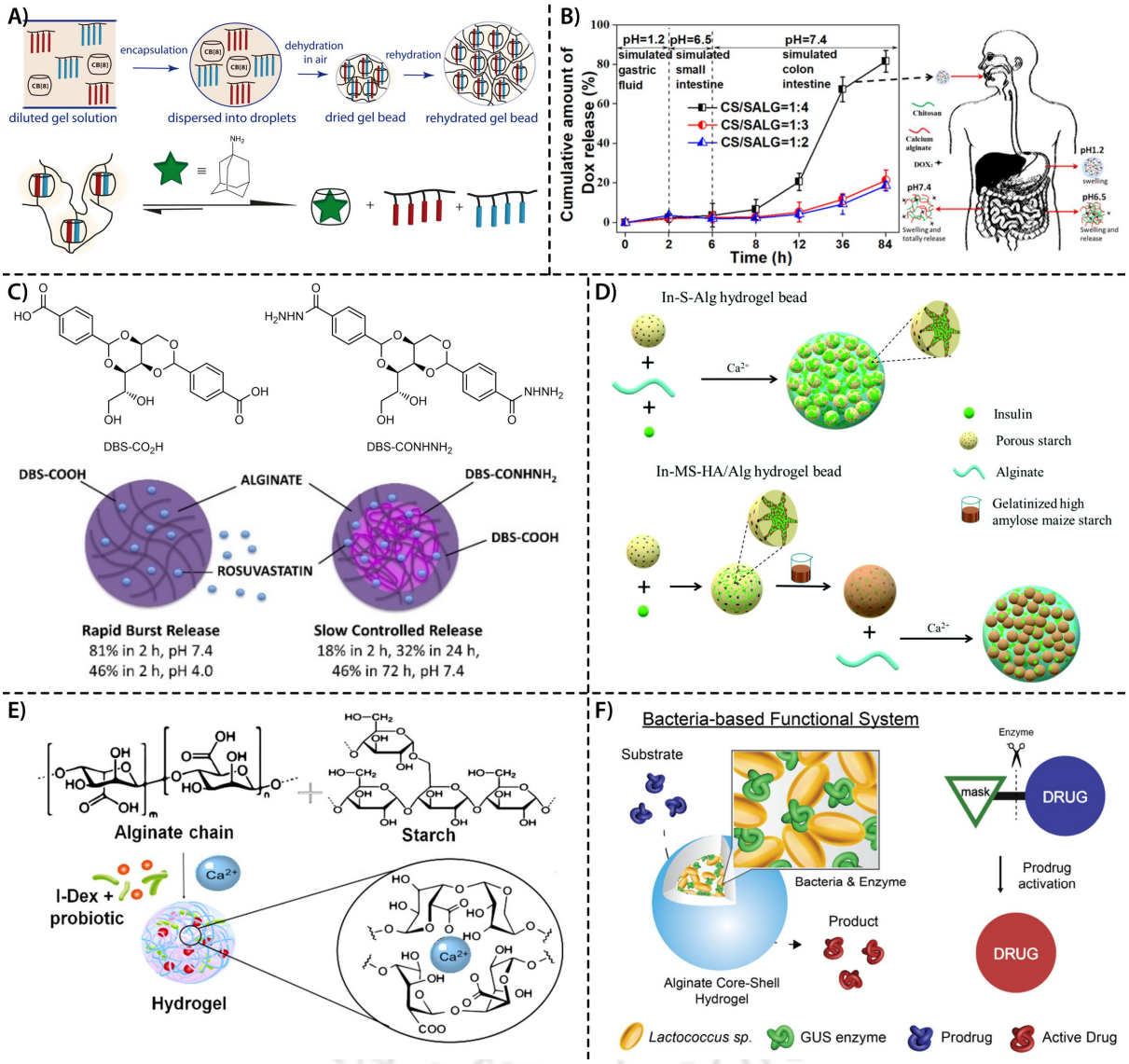

Figure 1.11 Schematic illustrations of hydrogel bead systems for controlled drug delivery and biocatalysis: A) Formation of cucurbit[8]uril-based beads with ADA-triggered release, B) Doxorubicin release from dual cross-linked chitosan/alginate beads, C) Rosuvastatin release profiles from beads of varying composition, D) Preparation of In-S-Alg and In-MS-HA/Alg hydrogel beads, E) Synbiotic bead formation via Ca^{2+}-induced ionic crosslinking of alginate, F) Bacteria-loaded hydrogel-shell beads as bioreactors for prodrug activation. Reproduced with permission from Ref. 102-104, 106-108.

In a similar vein, Sagar et al. formulated synbiotic hydrogel beads by encapsulating iron dextran along with probiotic *Bifidobacterium breve* in a starch–alginate matrix (Figure 1.11E).[107] Designed to treat iron deficiency anaemia, these pH-responsive beads released their payload specifically at intestinal pH. Their co-delivery of iron and probiotic bacteria not only improved iron bioavailability

but also reduced inflammation, offering a holistic approach to therapy. FESEM analysis confirmed their porous architecture, and in vivo studies validated both bioavailability and reduced inflammatory response, exemplifying the synergy of nutrient and microbiome modulation in functional bead design.

More recently, Jeong et al. introduced a hydrogel bead platform for localized prodrug activation in cancer therapy. They encapsulated genetically engineered *Lactococcus lactis* expressing β-glucuronidase in hydrogel compartments to enzymatically activate the prodrug glycyrrhizin (Figure 1.11F).[108] These beads supported microbial viability and localized enzymatic conversion in dynamic coculture models, including 2D cancer cells and 3D tumour spheroids. The system demonstrated enhanced therapeutic efficacy by spatially confining prodrug activation at the tumour site, bridging microbial engineering with hydrogel-based drug delivery for precision oncology.

Together, these studies highlight the versatility of hydrogel beads as responsive and tunable systems for controlled payload release. The examples outlined in the preceding sections illustrate only a fraction of the extensive potential of hydrogel beads. With continued innovation, hydrogel beads are poised to impact a wide range of fields, from healthcare and biotechnology to environmental and industrial applications.

1.8 Challenges and Limitations in Hydrogel Bead Research

Despite the growing interest in hydrogel bead systems for various biomedical, environmental, and catalytic applications, several challenges persist that limit their broader utility and scalability. One of the primary limitations in hydrogel bead research lies in the overwhelming reliance on polymeric gelators. Polymeric hydrogels such as those derived from alginate, chitosan, polyethylene glycol, and polyacrylamide are widely used due to their rapid gelation kinetics, robust mechanical strength, and long-term structural stability. These properties make them highly favourable for forming spherical or core–shell bead architectures, especially when shape retention, durability, and ease of processing are crucial. However, their synthetic or semi-synthetic origin and slow or incomplete degradation often raise concerns regarding biocompatibility, environmental safety, and regulatory acceptance in biomedical applications.

In contrast, low molecular weight gelators (LMWGs), which self-assemble via non-covalent interactions such as hydrogen bonding, π–π stacking, van der Waals forces, and metal–ligand coordination, offer significant advantages in terms of biocompatibility, biodegradability, and molecular tunability. These supramolecular hydrogels often mimic the natural extracellular matrix more closely than polymeric hydrogels, making them attractive candidates for cell encapsulation, tissue engineering, and drug delivery. However, the practical realization of LMWG-based hydrogel

beads remains extremely limited due to inherent material drawbacks. One major challenge is their generally poor mechanical integrity. Unlike polymeric chains that can entangle and form a stable network under stress, LMWGs often form fragile networks that collapse or dissolve under minimal perturbation. Additionally, LMWGs typically exhibit slow gelation kinetics, often requiring long induction times or specific environmental triggers such as pH, ions, or enzymes to initiate and complete gelation. These requirements are difficult to synchronize with the rapid processes used for bead generation, such as dripping, spraying, or microfluidic approaches, where rapid gelation is essential for maintaining shape fidelity and structural integrity.

Nevertheless, several studies have convincingly demonstrated that purely LMWG-based particulate systems can be realized through careful control of assembly conditions. The works of Miravet and co-workers provide clear evidence that dipeptidic and naphthalimide-based gelators can self-assemble into stable nano- and microparticles through solvent displacement or interfacial self-assembly, yielding size-tunable structures with excellent thermal and temporal stability.[109, 110] Similarly, Ulijn and co-workers demonstrated that enzyme-triggered self-assembly of short peptide gelators within microfluidic droplets can produce monodisperse peptide microgels, while related systems form fibrous interfacial shells or nanogels when the gelator concentration and confinement parameters are finely tuned.[111, 112] Complementing these reports, Smith and co-workers have emphasized that LMWG-based gels, though highly tunable and biocompatible, often lack shape control because they simply occupy the vessel in which they form.[113] However, they also highlighted emerging fabrication methods such as moulding, photopatterning, diffusion control, and 3D printing, that can impose defined geometries and patterns within supramolecular gels, improving their structural integrity and potential for application.

Collectively, these examples underscore that while LMWG-based beads are difficult to obtain compared to polymeric systems, their fabrication is not impossible. Rather, it requires tailored design approaches that harmonize gelation kinetics with fabrication dynamics. Unlocking the potential of LMWG-based hydrogels for bead fabrication will require a transition toward innovative design strategies that accommodate their distinct self-assembly mechanisms and physicochemical properties. By adapting fabrication techniques to their dynamic and fragile nature, it may become possible to fully exploit their inherent biocompatibility and biodegradability for advanced biomedical and environmental applications.

1.9 Thesis Objectives: Engineering Peptide Hydrogel Beads for Advanced Applications

To address the critical challenges associated with low molecular weight gelator (LMWG)-based hydrogel bead fabrication, particularly their poor mechanical strength, slow gelation kinetics, and

incompatibility with rapid processing techniques, this thesis explores a fundamentally new design strategy centered around an ultrasmall peptide gelator. Traditional approaches to hydrogel bead formation have overwhelmingly relied on polymeric systems due to their robustness and ease of processing. However, these polymeric beads often lack the molecular precision, tunability, and inherent biocompatibility offered by LMWG-based supramolecular materials. Despite the significant advantages of LMWGs, their application in bead fabrication has remained largely underdeveloped, primarily because they form fragile and dilute networks that are difficult to handle under the mechanical stresses involved in bead formation methods such as extrusion, dripping, or spraying.

This thesis aims to bridge that gap by utilizing PyKC, an ultrasmall tripeptide composed of pyrene, lysine, and cysteine, as a self-assembling LMWG capable of forming structurally stable hydrogel beads.[114] PyKC exhibits a suite of properties that make it uniquely suited to this challenge. It forms water-insoluble, thixotropic hydrogels with rapid recovery after shear, and undergoes redox-responsive gelation via disulfide bond formation. These features enable PyKC to form a cohesive gel network that can be easily shaped into beads using simple extrusion techniques, without the need for any polymeric additives or complex crosslinking strategies. More importantly, the insolubility of the PyKC gel in water and organic solvents imparts structural integrity to the beads, allowing them to maintain their shape and functionality in diverse environments.

The core objective of this thesis is to exploit the unique physicochemical characteristics of PyKC to establish a robust and versatile platform for peptide-based hydrogel beads. These beads are envisioned not just as structural materials, but as dynamic, modifiable scaffolds capable of hosting functional molecules, catalytic entities, or sensing elements. By systematically developing methods for bead fabrication, surface engineering, and application-specific modification, this work seeks to demonstrate how a single LMWG-based material can transcend the conventional limitations of supramolecular systems and support diverse applications across catalysis, biosensing, and environmental remediation. The following chapters of the thesis detail the progression of this research, from the initial development of the beads to their deployment in advanced functional contexts.

Chapter 2: Development of Peptide-Based Hydrogel Beads and Core Shell Architectures

This chapter focuses on shaping the PyKC hydrogel into spherical beads through an extrusion process, leveraging the peptide's unique material properties. The resulting beads are structurally robust and remain stable in aqueous conditions. Through orthogonal surface functionalization using Michael addition chemistry, the beads are further developed into core shell architectures. In addition, hollow capsules are generated by selective removal of the PyKC core. These systems are

evaluated for their physical stability and chemical adaptability, establishing the foundational methodology for creating standalone LMWG-based hydrogel beads.

Chapter 3: Surface Engineering of Hydrogel Beads for Functional and Catalytic Applications

Building on the structural platform established in Chapter 2, this chapter explores post-synthetic surface modifications that expand the application scope of the beads. Functional groups such as viologen moieties and hydrophobic chains are introduced to enable host guest chemistry and surface wettability control. Enzymes like horseradish peroxidase are immobilized to create reusable biocatalytic systems. Additionally, gold nanoparticles are grown in situ on the bead surface to form hybrid catalytic materials for pollutant degradation, demonstrating the potential of these beads in heterogeneous catalysis.

Chapter 4: Gold Nanostar Embedded Beads for Plasmon Enhanced Biosensing

This chapter transitions the bead platform toward biosensing applications. Gold nanostars are immobilized onto the bead surface to produce photocatalytically active systems capable of mimicking oxidase-like behavior. These beads are applied in the colorimetric detection of uric acid under visible light, showing high sensitivity and operational stability. The study highlights how plasmonic enhancement, combined with the structural features of the hydrogel beads, can be utilized for point of care diagnostic applications.

Chapter 5: Non Plasmonic Gold Catalysts on Beads for Environmental Remediation

The final chapter explores the use of non-plasmonic gold nanoparticles anchored to the bead surface for the oxidase like degradation of a wide range of organic pollutants. These systems function under ambient conditions without the need for external oxidants or light sources. The beads demonstrate excellent reusability and catalytic performance, reinforcing their practicality for water purification and environmental remediation.

Chapter 2

Ultrasmall Peptide Hydrogel-Based Core-Shell Beads and Hollow Capsules with Chemically Tunable Surface

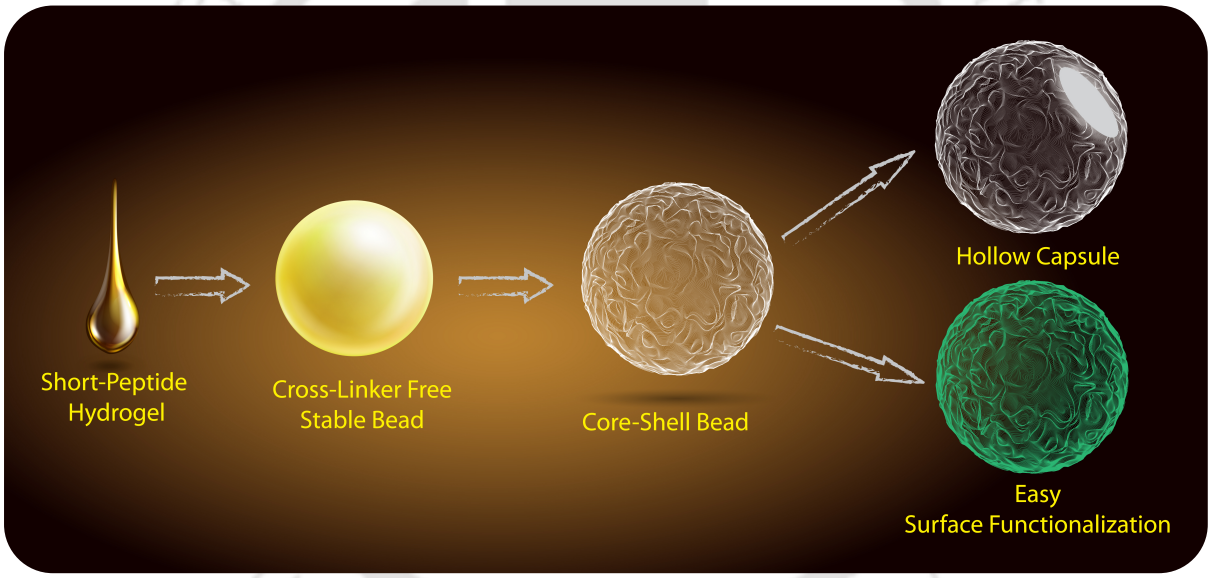

Indian Institute of Technology Guwahati

2.1 Introduction

The ability to contain a huge amount of water in a three-dimensional fibrillar entanglement, resulting in a phase intermediate to a solid and liquid, makes hydrogel an intriguing soft material. Due to the simplicity with which the mechanical rigidity/stiffness, porosity, and stimuli responsiveness can be tuned, and because of their resemblance to extracellular matrix (ECM), hydrogels are used in numerous sectors, from food and personal care items to tissue engineering and drug delivery to name a few.[33] Micro/nano-sized spherical colloidal gel networks have garnered considerable attention in recent years because they retain gel-like traits such as high solvent content, configurable porosity, and the capacity to trap molecular cargo while also introducing features like large surface area, customizable dimensions, and rapid responsiveness to various stimuli.[115] Many studies have shown that even macro-dimensional hydrogels can be tuned into specific shapes and sizes that will retain their inherent properties and can serve as a platform for specific applications such as ion and molecular recognition, oral drug delivery, tissue engineering, encapsulation of cells/proteins, and catalysis.[60, 105, 116]

Extrusion, emulsification, microfluidic, molding, and phase separation are some methods used to create hydrogel beads.[117] Extrusion-gelation is the most common, simple, and effective approach for producing hydrogel beads. It includes injecting small droplets of gelator solution into a "cross-linker" solution, where rapid cross-linking of the macromolecular gelator causes the droplets to gel into hydrogel beads. This method, however, is feasible for only macromolecular (i.e. polymeric) hydrogels as they are extremely robust and can be programmed to undergo instantaneous gelation. Low molecular weight gelators (LMWG), on the contrary, gel in a slow hierarchical pattern and so cannot be used to generate beads through extrusion technique.[116, 118] Although, LMWG can be programmed to assemble into spherical nano/micro-gel through specialized techniques such as micro-fluidic and water-in-oil emulsification,[119-123] LMWG-based hydrogels are difficult to be shaped into beads as they are significantly softer and have lower mechanical strength than polymeric hydrogels. LMWG, especially peptide gelators, have promising features such as high biocompatibility and biodegradability, improved tissue and cell adhesion, and excellent responsiveness.[33, 116, 124] Therefore, developing methods for producing small peptide-based hydrogel beads may expand the scope of peptide hydrogels for biomedical as well as many other applications. In recent years, Smith and coworkers have devised a strategy to incorporate LMWG in hydrogel beads. [60, 105, 125] However, in their approach, they combined a LMWG with a polymeric gelator, such as calcium alginate/agarose in a hybrid hydrogel system, and produced core-shell gel beads by utilizing the varied gelation kinetics of supramolecular and polymeric gelators.[49, 65, 104, 126, 127] Consequently, inventing methods to shape peptide hydrogels into beads and capsules without

employing polymeric gelators is a fascinating endeavor. Moreover, fabricating hydrogel beads with a customizable surface that may be functionalized with any molecule of choice would open up new horizons for LMWGs.

In order to extrude bulk hydrogel into stable hydrogel beads, the hydrogels need to show, a) injectability; b) optimum mechanical strength, and c) stability in bulk solvents where the droplets are immersed. A major obstacle toward creating stable beads with LMWG hydrogels is their easy dissolution in bulk solvents.[128] This is because supramolecular hydrogels are prepared from water soluble small molecules through non-covalent interactions and when such hydrogels are dispersed into bulk water, they get easily dissolved in it due to gain in entropy. In contrary to typical LMWGs, our group recently reported a dipeptide hydrogelator, PyKC (Scheme 2.1), that not only forms a redox-responsive hydrogel in aqueous medium but also exhibits a unique property of insolubility in bulk water as well as many other organic solvents.[114, 129-131] During hydrogelation, the non-aggregating PyKC monomers initially form dimers through intermolecular disulfide bond, and on account of reduced hydrophilicity and enhanced hydrophobicity, the dimers self-assemble hierarchically to generate supramolecular fibres that further intertwine into a water-impermeable hydrogel network. The strong $\pi-\pi$ interaction of pyrene units and hydrogen bonding between the PyKC dimers are the key supramolecular interactions behind the self-assembly. The unique confinement ability of the hydrogel is attributed to the slow dynamics of water which remains confined in the core region of PyKC via hydrogen bonds.[114] We observed that the PyKC hydrogel also exhibits injectability and thus it can easily be converted into water insoluble droplets by forcing it through syringe needles. To the best of our knowledge, apart from the PyKC peptide, another KC series peptide, Azo-KC [132], also exhibits the property of insolubility and injectability, and therefore might have the ability to form peptide hydrogel beads. This indicates the presence of the KC unit for in situ dimerization and a hydrophobic domain at the N-terminus is a prime design requirement to achieve the insolubility property.

Taking advantage of the unique insoluble nature and injectability of PyKC hydrogel,[114] herein we have demonstrated an extremely facile approach to create macro-sized gel beads using a simple extrusion method (Scheme 2.1). Unlike traditional extrusion techniques, the extruded PyKC gel droplets do not need any additional cross-linker treatment to retain their spherical swollen form. The beads made from PyKC hydrogel, owing to their high compartmentalization efficiency [114] and biocompatibility[133], can be used as carriers to deliver drugs and proteins in a redox-responsive fashion. However, for certain applications that may require vigorous agitation, the PyKC hydrogel beads may break down into smaller fragments. This may be avoided by coating the beads with a polymeric shell through surface cross-linking after bead fabrication. The free amine groups in

Lysine side chains exposed to the surface of the beads can easily be functionalized with acrylate derivatives through versatile Michael addition reaction.[134-136] Therefore, for surface cross-linking, initially the amine groups on the surface of the droplets were functionalized with dipentaerythritol penta-/Hexa-acrylate (5ACl), which were then further cross-linked by attachment of branched polyethylene imine (BPEI) . This yielded peptide-based hydrogel beads encased in a thin polymeric shell (core-shell). Depending on the final step of the polymeric surface cross-linking, the surface of the core-shell beads can be modified to have either free acrylate or amine groups and allow for further surface functionalization with numerous functional groups utilizing simple organic reactions. Furthermore, the inner core of the beads (PyKC hydrogel) was sacrificed using an appropriate solvent to create hollow organic capsules.[137, 138]

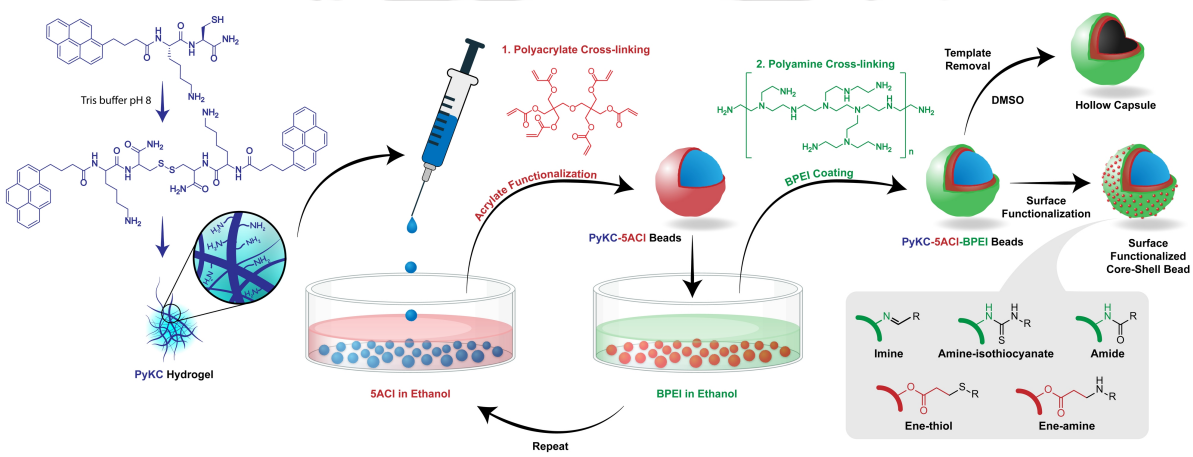

Scheme 2.1 Graphical illustration depicting the fabrication of low molecular weight peptide-based core–shell hydrogel beads, their surface functionalization via various covalent ligation strategies, and the preparation of hollow capsules through hydrogel template removal.

2.2 Results and Discussion

2.2.1 Rheology and injectability

PyKC can form a self-supporting hydrogel in TRIS buffer (pH 8, 20 mM) with a minimum gelation concentration (MGC) of 1 wt% (w/v).[114] However, to determine the optimal concentration of the gelator required for producing stable beads, a comprehensive rheological analysis of the hydrogel using varied concentrations of PyKC was performed. Frequency sweep of hydrogels produced with 1, 3, and 5 wt% PyKC revealed that the storage modulus (G′) was greater than the loss modulus (G″) in all cases, confirming the gel state of the samples (Figure 2.1A). Furthermore, as expected, amplitude sweep experiments showed that with increase in PyKC concentration, both the linear viscoelastic area as well as the yield strain of the hydrogel increased (Figure 2.1B). Thus, it was anticipated that a higher concentration of PyKC will be ideal for producing a strong and stiff hydrogel capable of generating stable beads. It is worth noting that the pH of the gelation media

plays an important role in determining hydrogelation kinetics. Faster gelation rates were seen as the pH of the gelation media increased from neutral to basic. Gelation time determined by vial inversion test revealed that the hydrogel in pH 9 buffer was formed in 10 h, whereas those in pH 8 and 7 buffers took 12 and 20 h respectively. This could be explained by the faster kinetics of disulphide bond formation at higher pH, which results in a rapid formation of the active dimeric PyKC gelator. However, hydrogels prepared at the varied pH levels were found to have identical mechanical properties (Figure 2.1C).

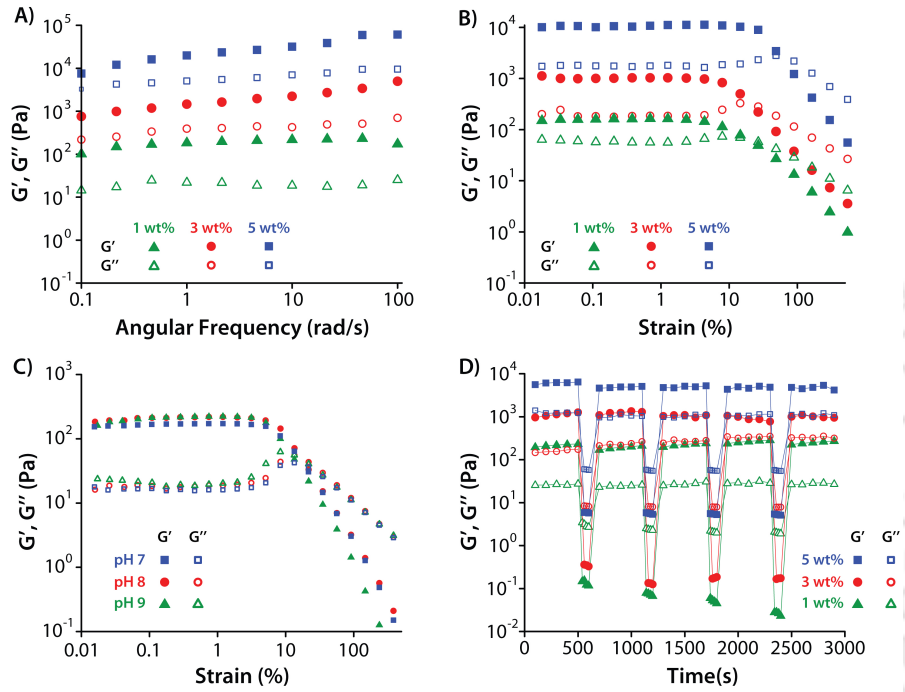

Figure 2.1 Rheological Analysis A) Frequency sweep profile, B) amplitude sweep profile, C) amplitude sweep profile of PyKC hydrogels (1 wt%) prepared in pH 7, 8 and 9 buffers, and D) time dependent step-strain rheological data of the bulk hydrogels prepared using 1, 3 and 5 wt% of PyKC.

In order to extrude hydrogel into stable beads, the hydrogel must also possess shear thinning/injectability properties.[132, 139] A cyclic strain-time sweep experiment was performed on PyKC hydrogels (1, 3, and 5 wt%) for thixotropic analysis (Figure 2.1D). Typically, when strain is applied to a thixotropic hydrogel, it transforms to sol, and upon removal of the applied strain, the sol returns to its original gel state.[20, 140, 141] This property of the hydrogel is crucial for the creation of hydrogel beads using the extrusion process, and all the samples demonstrated good shear thinning. However, visual inspection revealed that a gel containing at least 3 wt% PyKC is necessary to form stable and stiff droplets when injected from a syringe. Below this concentration, the droplets formed by the extrusion process were mechanically weak because the sol to gel transformation was relatively slower and therefore the beads gradually disrupted into smaller pieces in the bulk solvent even with minimal agitation. As a result, unless otherwise specified,

hydrogel containing 5 wt% PyKC was employed for the bead preparation. Higher concentration of PyKC also presumably provide a greater number of amine groups (from lysine side chains) on the bead surface that can be cross-linked in the subsequent steps.

2.2.2 Fabrication and characterization of hydrogel beads

The thixotropic and insoluble nature of PyKC hydrogel has been used for shaping the hydrogel into spherical beads. Upon extruding the hydrogel through a syringe, the hydrogel initially gets converted to sol droplets owing to temporary breakdown or rearrangement of the fibrillar networks under the influence of the applied stress. Thereafter, when the stress is withdrawn, the fibrillar structure within the sol droplet re-establishes itself as the molecular interactions and self-assembly processes resume and the sol droplet solidifies into a bead. Thus, the gel-sol-gel transition allows the formation of the peptide hydrogel beads. A step-by-step process of preparing PyKC hydrogel beads is outlined in Scheme 2.1 and experimental section.

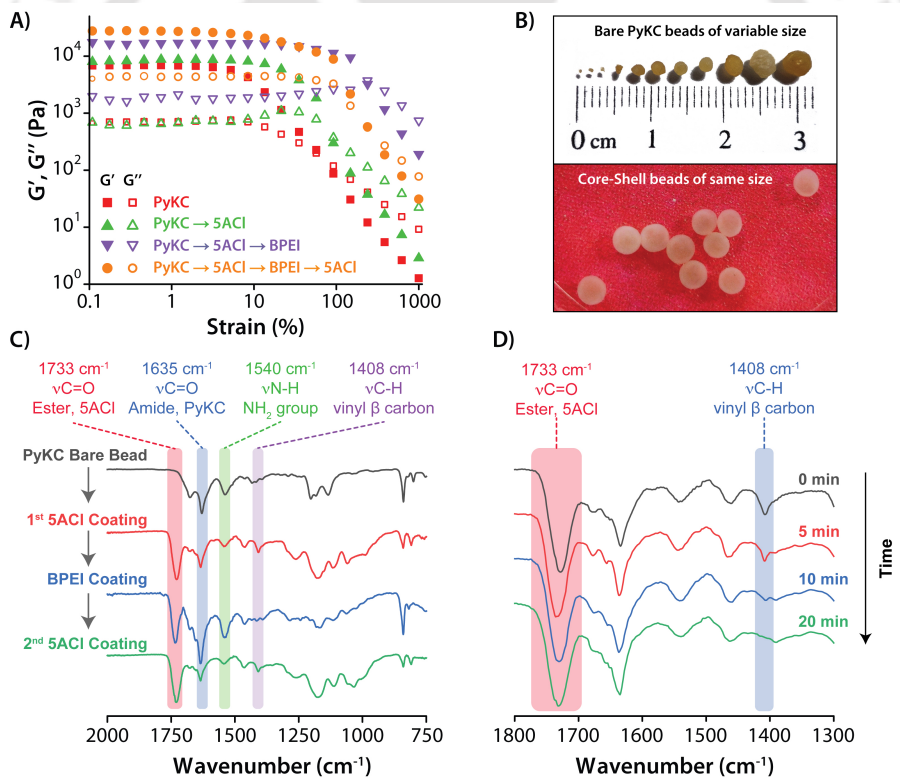

Figure 2.2 Characterization of surface cross-linked beads. A) Amplitude sweep profile of the hydrogel beads after successive surface modification steps, B) photographic images of bare PyKC hydrogel beads of variable sizes and core-shell beads of similar sizes, C) FTIR spectra of the beads after each successive surface modification step, and D) FTIR spectra at regular time intervals to track the progression of the Michael addition reaction on the surface of the beads.

Enhancement in mechanical strength of the beads upon surface modification was corroborated by rheological experiments which showed that both the G′ and G″ values of the beads increased

significantly upon application of each surface coating (Figure 2.2 A). Furthermore, the beads obtained after 5ACl-BPEI as well as 5ACl-BPEI-5ACl coating displayed markedly high yield strain in comparison to the bare PyKC beads. However, the rheological property of the 5ACl functionalized beads remained almost unaltered to that of bare PyKC beads as mere 5ACl functionalization did not result into significant surface cross-linking. By simply altering the needle diameter and the applied pressure, the volume of the droplets can be easily controlled. As can be seen from Figure 2.2B, we were able to produce hydrogel beads that were uniform in size and had tuneable diameters in the size range of 0.5 to 5 mm, with the bead size controlled by varying the needle diameter and the pressure applied on the syringe.

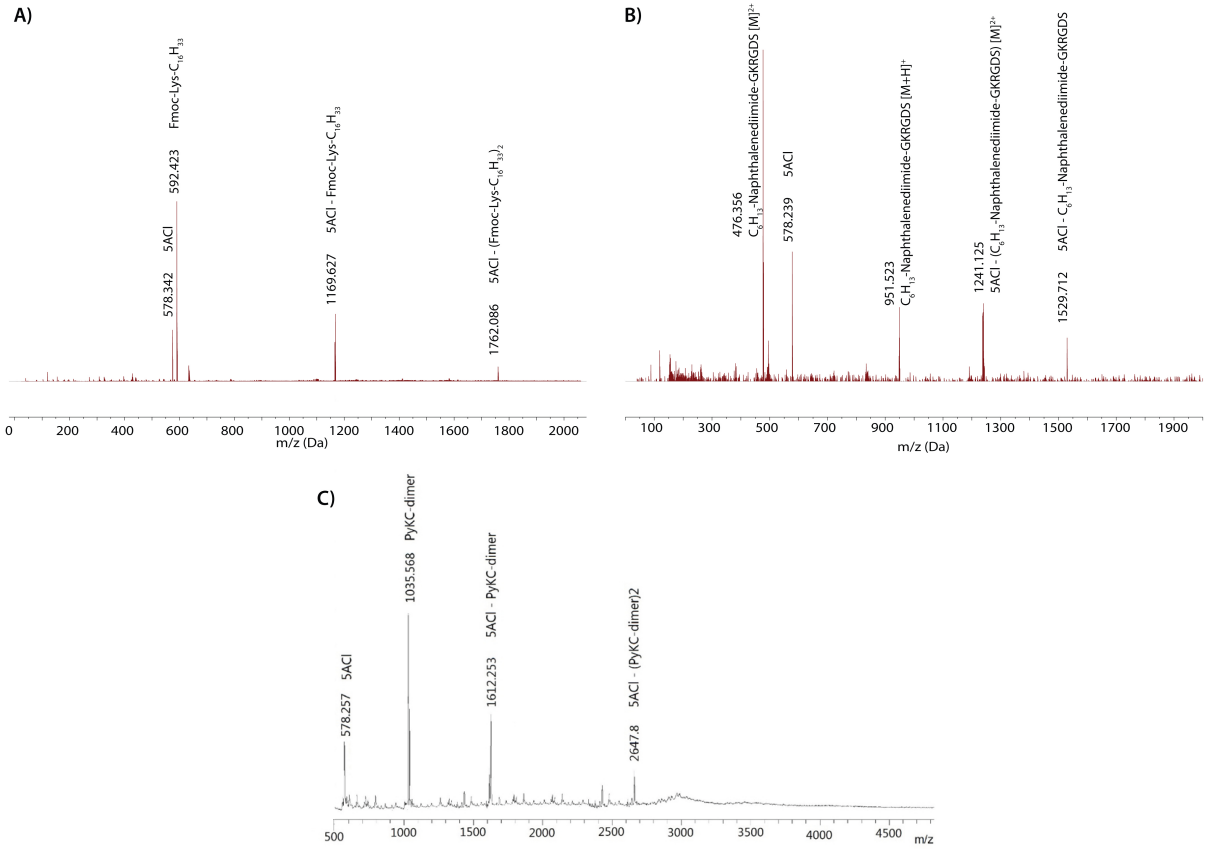

Figure 2.3 MALDI-TOF spectra of 5ACl treated A) Fmoc-Lys-$C_{16}H_{33}$, and B) C_6H_{13}-Naphthalenediimide-GKRGDS hydrogels, and C) 5ACl coated PyKC hydrogel beads.

The insolubility of the PyKC hydrogel in ethanol[114] allowed the beads to retain its shape and structure during the surface functionalization. Two previously reported Lysine containing short peptide-based hydrogels from our group (Fmoc-Lys-$C_{16}H_{33}$[142] and C_6H_{13}-Naphthalenediimide-GKRGDS[143]) were subjected to similar procedure. However, within 5 minutes both the hydrogels dissolved in the bulk ethanolic solution of 5ACl. Nevertheless, MALDI-TOF analyses of these solutions confirmed the attachment of 5ACl to the gelator peptides (Figure 2.3A-B). The 5ACl

functionalized PyKC beads were dissolved in dimethyl sulfoxide (DMSO, as the hydrogel is soluble only in DMSO or dimethyl formamide) and the MALDI-TOF analyses showed the attachment of one or two PyKC-dimers to 5ACl (PyKC remains in disulfide-linked dimer form in the hydrogel) (Figure 2.3C). This underscores the fact that, due to its insoluble nature, the PyKC hydrogel can be utilised to manufacture peptide hydrogel beads, and that the polymeric coating is required only to increase the durability of the insoluble beads. The attachment of 5ACl and subsequent crosslinking with BPEI on the surface were confirmed by FTIR spectroscopy using freeze-dried beads after every step (Figure 2.2C). The FTIR spectrum of bare PyKC bead (before any surface modification) displayed a prominent band at 1635 cm^{-1} characteristic of the stretching vibration of amide carbonyl groups present in the peptide.[144] In the case of 5ACl functionalised beads (PyKC-5ACl), peaks at 1408 and 1733 cm^{-1} corresponding to the asymmetric stretching vibration of the vinyl group and stretching vibration of ester carbonyl groups, respectively, revealed the presence of residual acrylate groups on the bead surface.[134, 145] As these signals are absent in the bare PyKC beads, acrylate functionalization of the bead surface was confirmed. The residual free acrylate groups on the PyKC-5ACl bead surface were then used for further modification with BPEI. The hybridization of the carbon atoms for the vinyl moiety shifted from sp^2 (C=C) to sp^3 (C-C) as a result of the Michael addition reaction between the acrylate and amine groups. The carbonyl moiety, on the other hand, was unaffected and served as an internal reference to track the reaction's development. Thus, the effective Michael addition of BPEI to 5ACl was demonstrated by a decrease in the peak intensity at 1408 cm^{-1} for C-H stretching of the vinyl groups relative to the normalised IR peak intensity for carbonyl groups at 1735 cm^{-1}. Furthermore, time dependent FTIR analysis demonstrated that the Michael addition occurs rapidly on the bead surface, with the majority of the surface exposed acrylate groups being consumed in less than 20 minutes (Figure 2.2D).[146]

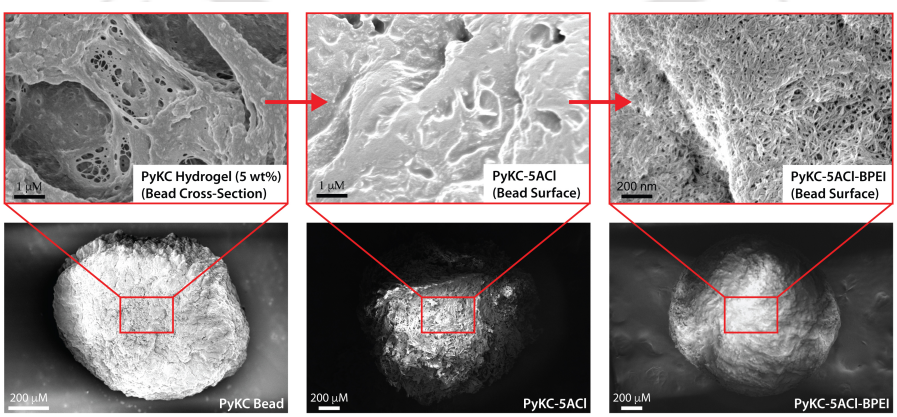

Figure 2.4 FESEM images of the bead surface after each successive surface modification step.

Microscopic analysis of the beads through FESEM shed light on the surface and cross-sectional morphologies of beads at the nanoscale. FESEM analysis of the beads prior to surface

functionalization revealed that the bare hydrogel beads had the same morphology throughout (Figure 2.4). Upon surface functionalization with 5ACl, the PyKC-5ACl beads presented a smooth surface with some intermittent cavities (Figure 2.4). This surface morphology is strikingly different from the dense fibrous network structure of the PyKC hydrogel in the bead's cross-section, indicating 5ACl functionalization over the bead surface.[114] After BPEI coating, the resulting PyKC-5ACl-BPEI beads exhibited a homogeneous and finely interwoven nanofibrillar network structure. After coating with the polymeric bilayer, no distinguishable morphology or shell-like structure could be identified at the periphery of the bead's cross-section through FESEM analysis. This may be because the polymeric coating on the surface of the core-shell beads collapses and becomes extremely thin when the beads are freeze-dried for FESEM analysis. Different surface morphologies of PyKC- 5ACl and PyKC-5ACl-BPEI beads, however, indicated that the PyKC hydrogel beads effectively underwent two subsequent Michael addition reactions with 5ACl and BPEI to generate a surface cross-linked core-shell structure.

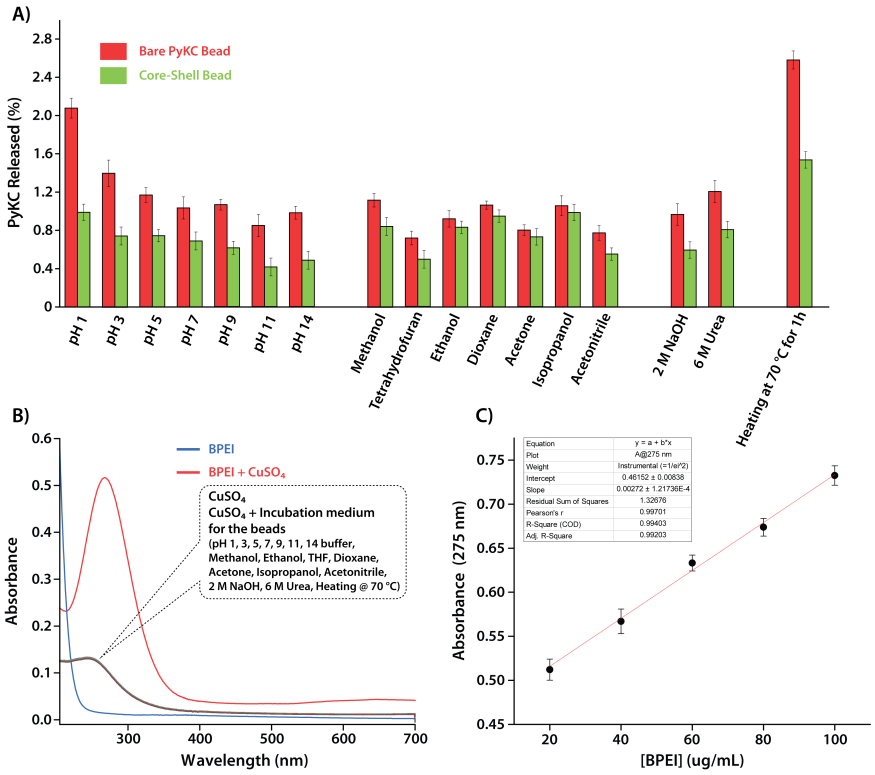

Figure 2.5 A) Release of PyKC from the bare as well as core-shell beads after incubating/treatment with various solvents and conditions. B) UV-Visible spectra for free BPEI (20 µg/mL), $CuSO_4$ (300 µM), and different incubation mediums treated with 300 µM $CuSO_4$, C) Calibration plot for the quantification of BPEI through copper(II)/BPEI complexation.

Next, the stability of the bare as well as core-shell beads was tested under different chemical environments. In order to assess the stability, the beads (10 beads of similar diameter) were dispersed into the corresponding medium and incubated for a specified time. After the incubation

period, the solutions were tested for any leakage of PyKC using UV-Visible spectroscopy. First, the beads were immersed in buffers of different pH values (1-14) and organic solvents (methanol, ethanol, tetrahydrofuran, dioxane, isopropanol, acetone, and acetonitrile) for 6 h. As expected, only a trace amount (>1%) of PyKC was found in the bulk medium (Figure 2.5A).[114] The beads were also tested under various harsh conditions like, 2M NaOH or 6M urea solutions, and no prominent leakages were observed under such conditions.

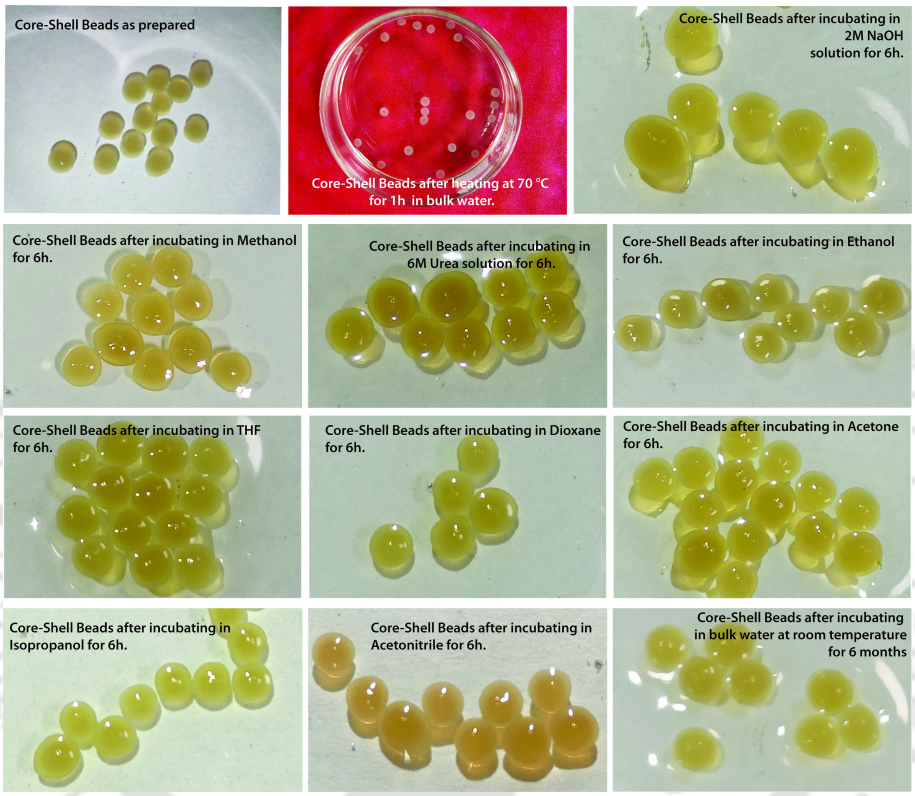

Figure 2.6 Photographs of the core-shell beads before and after various treatments.

Finally, the beads were incubated in water while the system was heated to 70 °C for an hour. A minor leakage of PyKC (>1.5 %) was observed. The degradation and leaching of the outer polymeric shell were also monitored through a copper(II)/BPEI complexation analysis (Figure 2.5B-C). The appearance of a characteristic absorption band at 275 nm owing to the formation of copper(II)/BPEI complex allows for the quantitative determination of free BPEI in the incubation medium. Hydrolysis of the ester bonds of the 5ACl units is expected to result in the release of BPEI from the surface of the beads, resulting in a loss of stability. Under different chemical environments, however, no noticeable BPEI leaching was observed (Figure 2.5B). This may be ascribed to the fact that 5ACl and BPEI are linked by an extensive network of ester bond cross-links. As a result, even if some ester linkages get hydrolysed, the polymeric coating demonstrates remarkable resistance to leaching when exposed to aqueous medium. Furthermore, as the pH of the medium rises, deprotonation of the amine groups of the outer BPEI polymeric shell increases their hydrophobic

character, protecting the inner localised ester bonds from the solvent's hydrolytic action.[147] Moreover, the shape and size of the beads were analysed visually and under optical microscope and the average diameters were checked after every experiment. Importantly, no noticeable change in the average diameter or the shape of the core-shell beads were observed in any case (Figure 2.6). Remarkably, the core-shell beads retained their stability for more than six months when stored in bulk water.

2.2.3 Various chemical conjugation reactions on the core-shell bead surface

In the last decade, facile and controlled functionalization of core-shell beads and hollow capsules emerged as a key tool for a wide range of applications.[137, 138, 148] Functionalization of various molecules (like, polymer, supramolecular hosts, nano-particles, enzymes and other biomolecules) on the surface of these core-shell beads or hollow capsules allowed one to control the physicochemical and mechanical properties, facilitating a variety of applications.[137] In this regard, development of a versatile surface that can easily be functionalized through various organic chemical transformations is critical.

Substrate	Bead Surface Functionality	Bead Surface Functionalization	Reaction Medium / Temperature	Extent of Functionalization
PyCHO			(Imine Coupling) Methanol, 50° C, 12 hr	0.142 pmol/μm² (33.4 %)
FITC			(Amine-Isothiocyanate Coupling) pH 9 Carbonate Buffer, RT, 3 hr	0.110 pmol/μm² (26 %)
RhB			(Amide Coupling) EDC/NHS, Water, RT, 10 hr	0.16 pmol/μm² (37.6 %)
$PyCH_2NH_2$			(Ene-Amine Coupling) Methanol, RT, 24 hr	0.247 pmol/μm²
PyC			(Ene-Thiol Coupling) Tetrahydrofuran, RT, 12 hr	0.234 pmol/μm²

Table 2.1 List of different chemical conjugation reactions performed on the core-shell beads.

In the current study, surface functionalization was achieved by exploiting the terminal chemistry of the polymeric shell of the beads. Depending on the final coating step, the bead surfaces

presented either free amine or acrylate functional groups, allowing orthogonal chemical modifications. The robustness of the core-shell architecture against variations in temperature, pH, and solvent polarity enabled the successful implementation of several organic conjugation reactions (as summarized in Table 2.1). To standardize the procedure, all conjugation reactions were carried out using identically sized beads (diameter: 900–950 μm), with an average surface area of 2.6×10^6 μm^2 per bead, determined from optical microscopy images of ten representative beads.

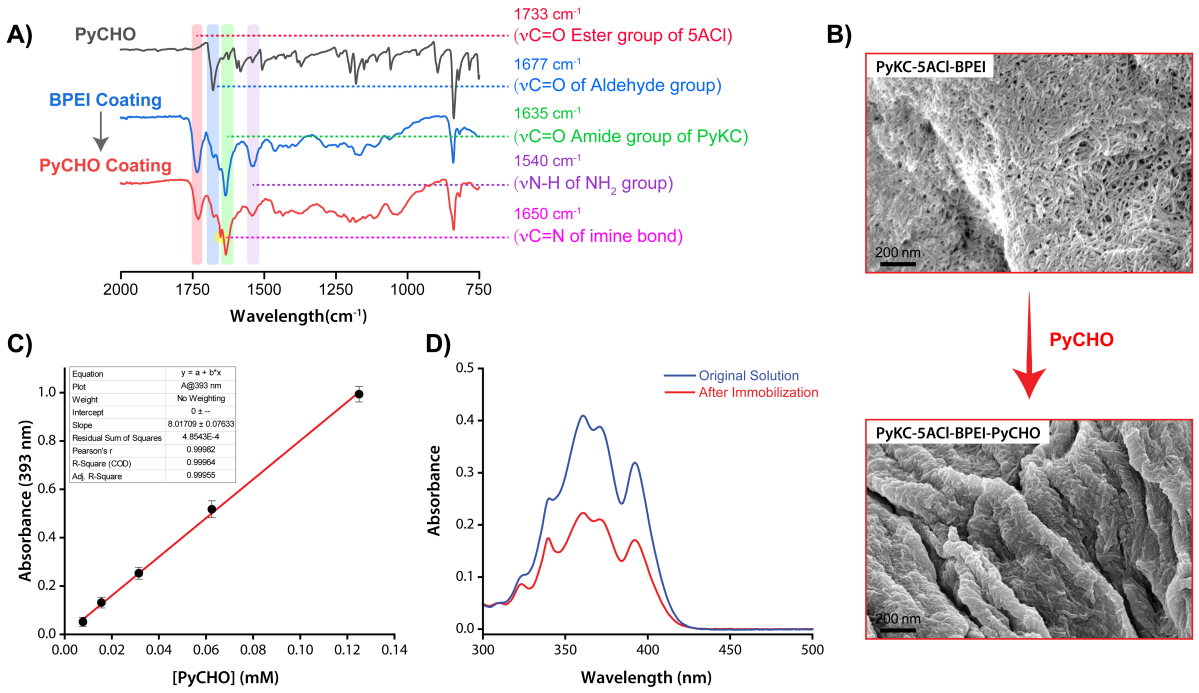

Figure 2.7 A) FTIR spectra of PyCHO, BPEI coated beads and PyCHO functionalised beads, B) FESEM images of the BPEI coated beads before and after the immobilization of PyCHO, C) Calibration plot for PyCHO in methanol, and D) Absorption spectra of PyCHO in methanol before and after the functionalization reaction with the beads.

Polyamine-coated beads were subjected to various nucleophilic coupling reactions. For instance, surface immobilization of pyrene-1-carboxaldehyde (PyCHO) was carried out in methanol through imine formation between the aldehyde moiety of PyCHO and surface-exposed amine groups (2.7A-D). Beads (10 numbers) were incubated with 4 mM PyCHO in methanol at 45 °C for 12 hours. Post-reaction, beads were washed thoroughly until the wash solvent was free from residual dye, as confirmed by UV spectroscopy. FTIR analysis revealed the appearance of a characteristic C=N stretching band at 1650 cm^{-1} and a decrease in the N–H bending vibration around 1540 cm^{-1}, confirming the success of the reaction (Figure 2.7A). FESEM imaging showed clear morphological changes to the bead surface, and the immobilization of PyCHO was quantitatively estimated using its molar absorptivity at 393 nm (ε = 8.02 mM^{-1}·cm^{-1}) (Figure 2.7B-D). Notably, acrylate-coated

control beads lacking amine groups showed no detectable immobilization, validating the chemical selectivity of the conjugation process.

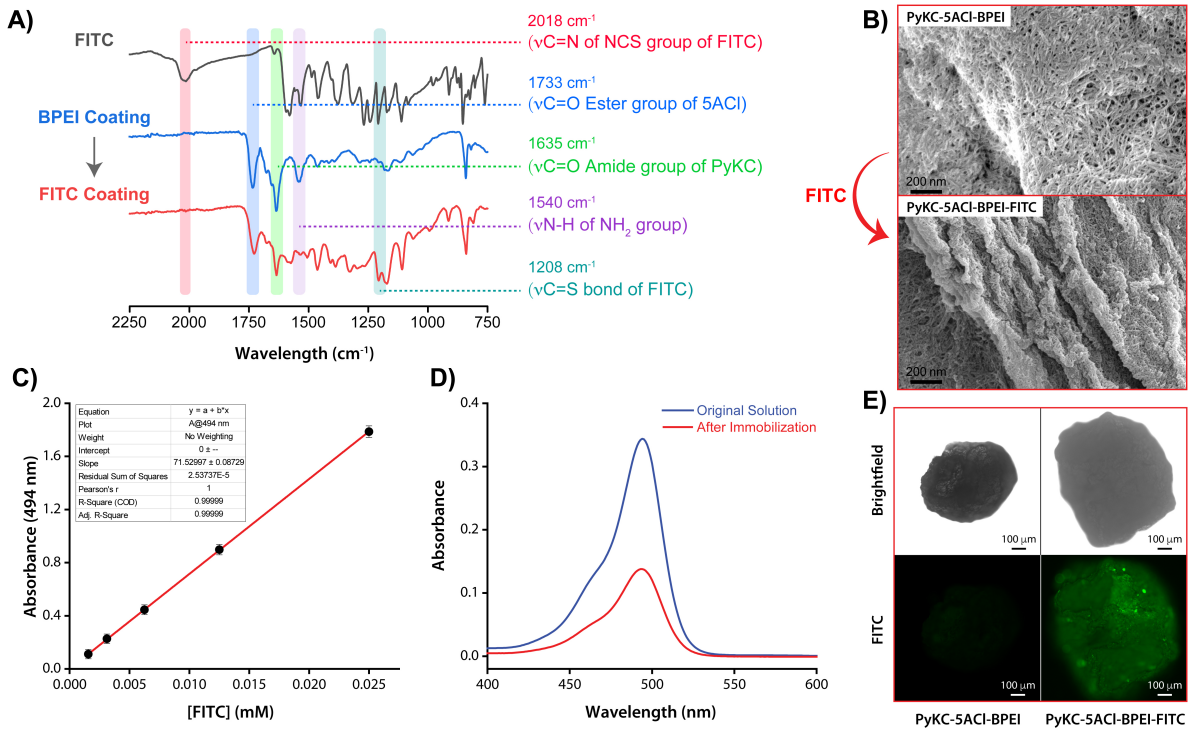

Figure 2.8 A) FTIR spectra of FITC, BPEI coated beads and FITC functionalised beads, B) FESEM images of the BPEI coated beads before and after the immobilization of FITC, C) calibration plot for FITC in carbonate buffer, D) absorption spectra of FITC in carbonate buffer before and after the functionalization reaction with the beads, and E) Optical images of the bare and FITC functionalised beads.

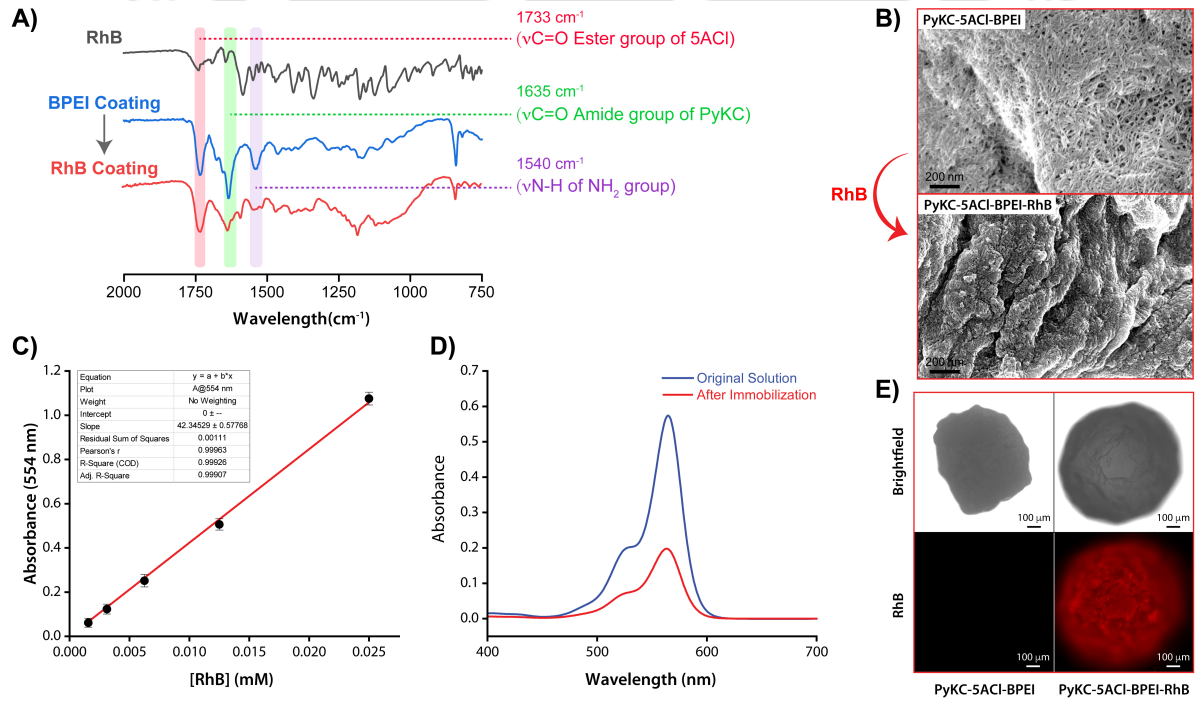

Figure 2.9 A) FTIR spectra of RhB, BPEI coated beads and RhB functionalised beads, B) FESEM images of the BPEI coated beads before and after the immobilization of RhB, C) calibration plot for RhB in water, D)

absorption spectra of RhB in water before and after the functionalization reaction with the beads, and E) Optical images of the bare and RhB functionalised beads.

In a similar fashion, fluorescein isothiocyanate (FITC), which contains an electrophilic isothiocyanate group, was covalently immobilized onto amine-functionalized beads via the formation of thiourea linkages (Figure 2.8A-D). The reaction was carried out in carbonate buffer (pH 9) with FITC (2.4 mM) at room temperature in the dark for three hours. FTIR spectra displayed a new C=S stretching vibration at ~1208 cm^{-1} along with the disappearance of the characteristic N=C=S band from unreacted FITC near 2018 cm^{-1} (Figure 2.8A) .[149, 150] A significant reduction in the N–H bending signal further indicated the consumption of surface amines. The immobilized dye was quantified using UV–vis absorption at 494 nm (ε = 71.53 $mM^{-1}·cm^{-1}$), and FESEM imaging revealed pronounced surface topographical modifications (Figure 2.8B-D). Optical images of the beads before and after FITC treatment also confirmed successful FITC immobilization on the bead surface(Figure 2.8E). Control beads with acrylate-only surfaces showed negligible binding, reinforcing the necessity of free amine groups for this ligation route.

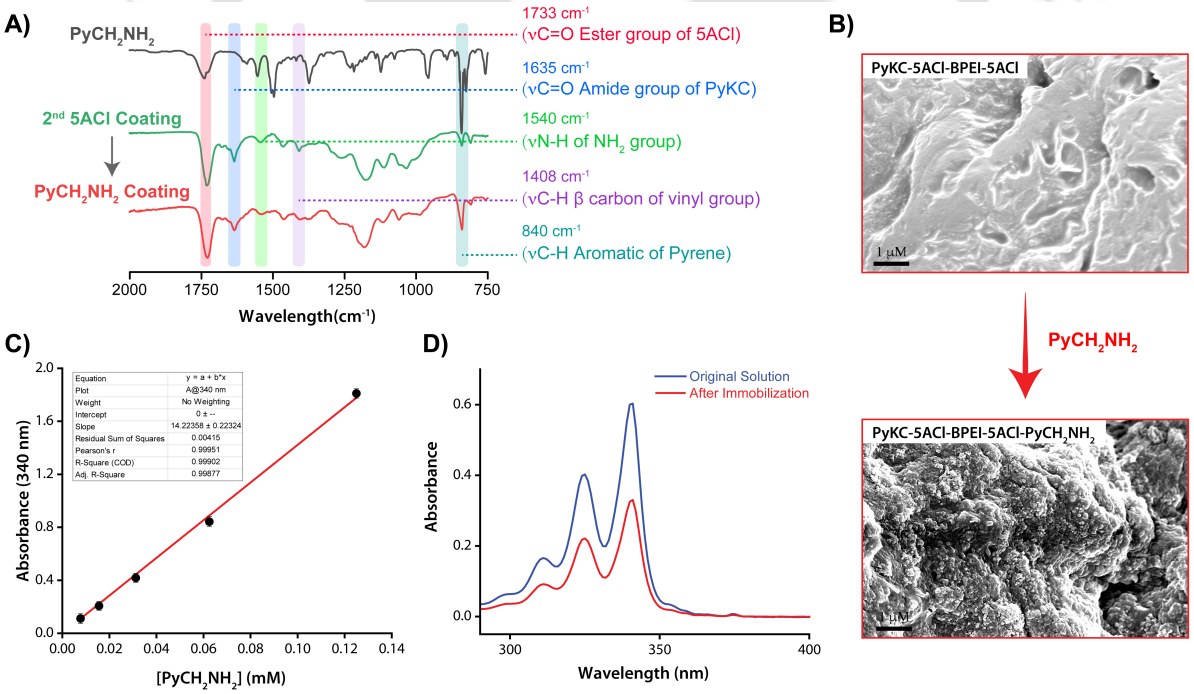

Figure 2.10 A) FTIR spectra of $PyCH_2NH_2$, 5ACl coated beads and $PyCH_2NH_2$ functionalised beads, B) FESEM images of the 5ACl coated beads before and after the immobilization of $PyCH_2NH_2$, C) Calibration plot for $PyCH_2NH_2$ in methanol, and D) Absorption spectra of $PyCH_2NH_2$ in methanol before and after the functionalization reaction with the beads.

The amine-rich bead surface was also subjected to classical amide coupling using Rhodamine B (RhB), which possesses a free carboxylic acid group (Figure 2.9A-D). The coupling was performed using EDC/NHS activation in aqueous medium for ten hours in the dark. FTIR analysis showed the

disappearance of N–H bending vibrations and formation of amide linkages (Figure 2.9A). UV–vis spectroscopy at 554 nm (ε = 42.34 $mM^{-1}·cm^{-1}$) confirmed significant dye loading, and FESEM imaging provided further evidence of successful surface modification (Figure 2.9B-D). The successful immobilization of RhB on the bead surface was further confirmed by optical images of the beads taken before and after the RhB treatment (Figure 2.9E). As in previous cases, beads lacking surface amines did not show any detectable conjugation, attesting to the selectivity and reliability of the reaction.

The chemical reactivity of acrylate-functionalized bead surfaces was next exploited through Michael addition reactions. In this reaction, 1-pyrenemethylamine ($PyCH_2NH_2$) was used as a nucleophile to attack the electrophilic acrylate groups on the bead shell in methanol under gentle agitation for 24 hours (Figure 2.10A-D). FTIR spectra of the modified beads displayed decreased β-vinyl C–H stretching near 1408 cm^{-1} and enhanced aromatic C–H bending around 840 cm^{-1}, consistent with successful Michael addition (Figure 2.10A). The loading of $PyCH_2NH_2$ was quantified using its UV–vis absorption at 340 nm (ε = 14.22 $mM^{-1}·cm^{-1}$). Notably, no dye binding was observed on amine-functionalized control beads, indicating that the reaction proceeded specifically through acrylate–amine addition (Figure 2.10C-D).

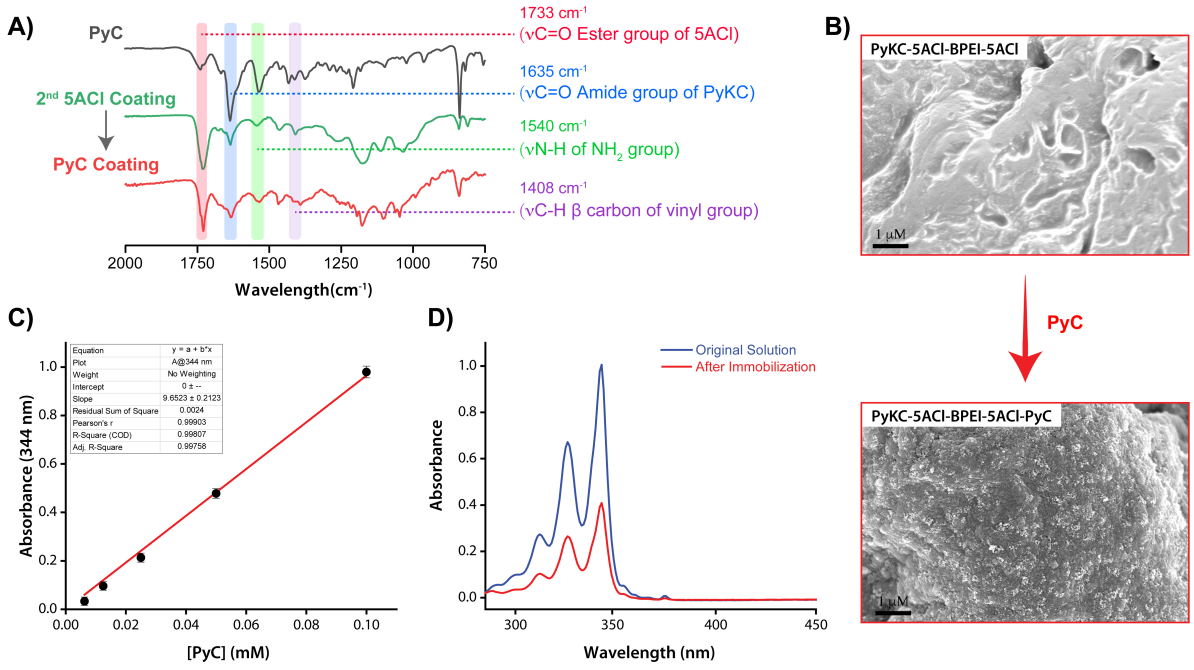

Figure 2.11 A) FTIR spectra of PyC, 5ACl coated beads and PyC functionalised beads, B) FESEM images of the 5ACl coated beads before and after the immobilization of PyC, C) calibration plot for PyC in THF, and D) absorption spectra of PyC in THF before and after the functionalization reaction with the beads.

To further demonstrate the versatility of acrylate surface chemistry, thiol–ene coupling was performed using pyrene-cysteine (PyC), a thiol-bearing conjugate (Figure 2.11A-D) The reaction

proceeded in THF with a catalytic amount of triethylamine for 12 hours at ambient conditions. The disappearance of β-vinyl C–H signals in the FTIR spectra and distinct alterations in surface morphology observed via FESEM supported successful thioether bond formation (Figure 2.11A-B). The amount of PyC immobilized was determined using UV–vis spectroscopy at 344 nm (ε = 9.65 $mM^{-1}·cm^{-1}$). Control experiments on amine-coated beads showed no coupling, highlighting the specificity of thiol–ene reactivity towards acrylate groups (Figure 2.11C-D).

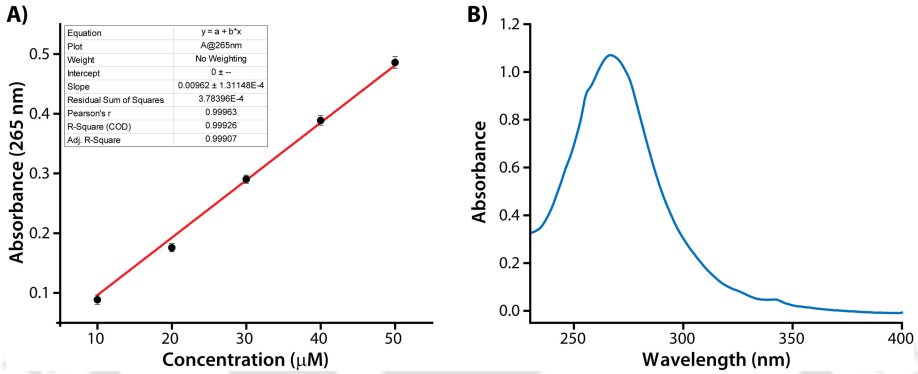

Figure 2.12. A) Calibration plot for p-nitrobenzaldehyde in 1:1 methanol/water, and B) Absorption spectrum of 4-NBA liberated from the bead surface through hydrolysis in 1:1 methanol/water.

In all cases, UV-visible spectrophotometric analysis served as the primary method for quantifying probe immobilization by comparing absorbance values of the chromophoric solutions before and after bead treatment. A decrease in absorbance directly correlated with the amount of probe immobilized. Furthermore, to determine the density of reactive sites on the polyamine bead surface, the exposed free amine groups were quantified using a 4-nitrobenzaldehyde assay and found to be 0.425 pmol/$μm^2$ (1.105 mmol per bead) (Figure 2.12A-B).[151] This high surface loading allowed for efficient and reproducible conjugation, as demonstrated by the high dye immobilization yields across reactions. In all functionalization experiments, the absence of coupling on non-complementary bead surfaces consistently validated the orthogonality of the reactions employed. Furthermore, it is worth mentioning that the list of conjugation reactions is not limited to the performed ones, many other types of organic transformations involving primary amine or acrylate can presumably be performed on the surface.

2.2.4 Preparation of hollow organic capsules

Hollow organic capsules are very useful as micro-reactors, in catalysis, as sensors, in energy storage materials, for drug delivery etc.[137, 152] Fabrication of such capsules involves silica, surfactants, microemulsions, and other colloidal templates that are sacrificed after the organic shells are prepared.[137, 152-156] However, to the best of our knowledge, there is no report on using LMWG-based hydrogels as the sacrificial template for the preparation of hollow capsules. Although PyKC

hydrogel is extremely stable under a wide range of stringent conditions,[114] it undergoes disassembly and dissolution when treated with disulphide breaking agents such as DTT/TCEP/GSH, or when taken in solvents like DMF and DMSO.[114] We anticipated that subjecting the core-shell beads to these solubilising agents might help in washing out the PyKC hydrogel core to produce hollow polymeric capsules. Initially, the beads (with single 5ACl-BPEI coating) were immersed in these solutions and incubated for 24 h. The amount of PyKC released was tested using UV-Visible spectrophotometric analyses. Interestingly, GSH triggered only ~ 10 % release of PyKC while DTT and TCEP resulted in ~33 and ~14 % release respectively (Figure 2.13A). DMF and DMSO, however, resulted in 53% and 76 % release of PyKC respectively. To check the effect of number of coatings, we prepared core-shell beads with varying number of polymeric bilayers (5ACl + BPEI) and checked the amount of PyKC released under the influence of different solubilising agent/medium. As expected, the amount of PyKC released decreased substantially with the increase in the number of bilayers. Since DMSO was found to be most effective in releasing PyKC, beads with a single polymeric bilayer and DMSO as the solubilizing medium were chosen to create the hollow beads.

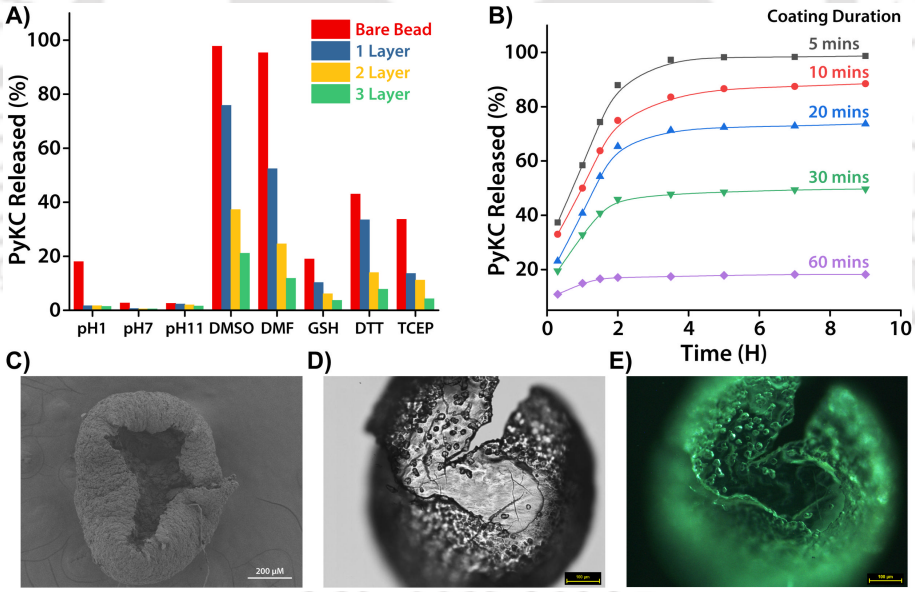

Figure 2.13 Making hollow capsules. A) PyKC release profile in different medium with varying number of polymeric bilayers, B) time dependent release of PyKC from core-shell beads where a single polymeric coating was applied, but for different time intervals. C-E) Microscopic images of the hollow polymeric capsules observed using C) FESEM, D) Bright field optical microscopy, and E) Fluorescence optical microscopy.

It is worth noting that the time spent during the polymeric coating has a major impact on the rigidity and porosity of the polymeric mesh, which in turn affects the extent of PyKC released (in DMSO) from the core. Coating applied for 5-10 minutes resulted in an extremely weak polymeric shell that spontaneously ruptured in DMSO, even with minor shaking, releasing 80-95% of PyKC

(Figure 2.13B). However, coating for an extended period of time (60 minutes) resulted in a compact shell that effectively prevented the bead from collapsing but limited the leaching of PyKC out of the shell in the presence of DMSO. A 20-minute coating time was found to be ideal as it resulted in the release of a considerable amount of PyKC from the bead in DMSO (~70% in 3 hours) while maintaining the stiffness of the polymeric shell. FESEM and optical images of the manually dissected capsules also confirmed the formation of hollow capsules having a central cavity surrounded by a polymeric shell (Figure 2.13C-E). The hollow capsules, like the core-shell beads, were found to be extremely stable over a wide pH range as no BPEI leaching was detected using copper(II)/BPEI complexation studies. Due to the presence of a central cavity and porous shell, the hollow polymeric capsules may serve as versatile tools, finding utility in drug delivery as well as functioning as macro-reactors for catalysing diverse reactions within their confined cavities.

2.3 Conclusion

To summarise, we established a simple and easy method for producing stable macro-sized beads from an LMW ultrashort peptide hydrogel without the need for mixing with any polymeric unit. Further, the PyKC hydrogel is used to make a thin polymer coated core-shell bead with an easily tunable surface where a variety of chemical reactions can be performed to conjugate a wide range of molecules. The core-shell beads were found to be extremely robust and stable under various extreme conditions. Owing to the dissolution of PyKC hydrogel in certain specific solvents, the core (PyKC hydrogel) of the core-shell beads can readily and selectively be sacrificed to make hollow capsules.

2.4 Experimental Section

2.4.1 Materials and Methods

Dipentaerythritol penta-/hexa-acrylate (5ACl), branched polyethylenimine (BPEI), 1-pyrenemethylamine hydrochloride, 1-pyrenecarboxyaldehyde, 1-pyrenemethylamine hydrochloride, Fluorescein isothiocyanate isomer I (FITC), 4-nitrobenzaldehyde, DL-Dithiothreitol (DTT), and Tris(2-carboxyethyl) phosphine (TCEP), were purchased from Sigma-Aldrich (USA). Rhodamine B and Glutathione reduced form was purchased from TCI, Japan. Rink amide MBHA resin, protected amino acids and coupling reagents were purchased from Novabiochem. HPLC-grade dimethylformamide (DMF), dichloromethane (DCM) and acetonitrile (ACN) were procured from Spectrochem (India) and Fisher Scientific (India). Solvents were dried whenever required according to the reported procedures. Milli-Q water with a conductivity of less than 2 μScm^{-1} was used for all sample preparations. 60-120 mesh silica gel (SRL, India) was used for column chromatography. ^{1}H NMR and ^{13}C NMR spectra were recorded using a Bruker Ascend 600 MHz (Bruker, Coventry, UK) spectrometer.

UV-Visible spectra were recorded on a PerkinElmer Lambda 365+ spectrophotometer, while fluorescence measurements were performed on a Fluoromax 4 Plus spectrophotometer. Bright-field and fluorescence microscopic images were obtained using a ZEISS Axio Vert.A1 inverted microscope with 10X objective. FESEM imaging of freeze-dried samples of different surface functionalised beads were performed on a Gemini SEM 300 (Sigma Zeiss) instrument. FTIR spectra for freeze dried samples of different surface functionalised beads were obtained on a PerkinElmer instrument under ambient conditions.

2.4.2 General synthesis of peptides (PyKC and PyC)

The peptides were synthesized on Rink amide MBHA resin using standard Fmoc (9-fluorenylmethoxycarbonyl) solid phase peptide synthesis (SPPS) protocol. In a typical coupling, 3 equiv. of a protected amino acid (with respect to the loading of the resin), 3 equiv. of HBTU, and 6 equiv. of DIPEA were taken in 5 mL of DMF (for 0.1 mmol scale with respect to the resin loading) and stirred for 5 minutes prior to the addition of the mixture to the swelled and deprotected resin. The reaction mixture was shaken for 60 min, and the resin was washed several times with DMF. The Fmoc-deprotection was achieved by treatment of the resin three times with 5 ml of 20% piperidine in DMF for 5 minutes, followed by a thorough washing of the resin with DMF and DCM. The Fmoc-deprotection and coupling steps were repeated until the desired peptide sequence was obtained. The resin with the loaded peptide was washed several times with DMF and DCM and dried. The dried resin was then treated with a mixture of freshly prepared mixture of 8.5:1:0.5 (trifluoroacetic

acid (TFA)/tetraethylsilane (TES)/H_2O) and stirred for 1 h. The resin was finally washed with DCM several times. The cleavage cocktail and the washings combined were concentrated to a minimum volume on a rotary evaporator. The cleaved peptide was then precipitated from cold dry ether, centrifuged and lyophilized to get the crude peptide. Purification was done in Dionex Ultimate 3000 HPLC using a Luna 5 μm (C18) column (Phenomenex) and using acetonitrile and water (containing 0.1% TFA each) as the mobile phase.

PyKC: ^{1}H-NMR (DMSO-d_6, 400 MHz): δ (ppm) 8.39 (d, 1H), 8.28 (m, 2H), 8.23 (m, 2H), 8.14 (d, 2H), 8.07 (t, 1H), 7.97 (t, 2H), 7.66 (s, 3H), 7.29 (s, 1H), 7.20 (s,1H), 4.39 – 4.21 (m, 2H), 2.90 – 2.66 (m, 4H), 2.29 (m, 3H), 2.03 (p, 2H), 1.69 (m, 1H),1.55 (m, 3H), 1.35 (d, 2H). MALDI-TOF: m/z calculated for $C_{29}H_{34}N_4O_3S$ $[M+H]^+$: 519.24, found: 519.24

HPLC R_T = 12.8 min (HPLC Program= 5% Acetonitrile/Water to 100% Acetonitrile in 20 minutes.)

PyC: MALDI-TOF: m/z calculated for $C_{23}H_{23}N_2O_2S^+$ $[M+H]^+$: 391.147, found 391.296. HPLC R_T = 18.1 min. (HPLC Program= 5% Acetonitrile/Water to 100% Acetonitrile in 25 minutes.)

2.4.3 Preparation of core-shell beads

There are two consecutive steps involved (Scheme 2.1).

Step 1: typically, a 5 wt% solution of PyKC (20 mM Tris buffer, pH 8) was prepared in a 1 mL syringe fitted with a 26 G needle and was left undisturbed at room temperature for a period of 24 h to allow the formation of the hydrogel. The hydrogel in the syringe was then forced out through the fine needle orifice using gentle mechanical pressure. Owing to the shear thinning property of PyKC hydrogel, the sol emerging out of the needle immediately hardened into small spherical hydrogel droplets which were dropped into an ethanolic solution of 5ACl (1 g/mL) for surface functionalization. The beads were allowed to react with 5ACl for 15 minutes with gentle shaking and subsequently washed several times with copious amount of ethanol to remove the unreacted and loosely bound 5ACl molecules from the surface.

Step 2: the beads, surface-functionalized with acrylate groups, were then treated with an ethanolic solution of BPEI (20 mg/ml) over a shaker for 15 minutes, followed by washing with ethanol to remove any unreacted BPEI. This led to the cross-linking of the surface of the beads and generated an amine functionalized surface.

2.4.4 Preparation of hollow capsules

For the preparation of hollow capsules, beads containing a single polymeric bilayer (PyKC -5ACl-BPEI) were prepared using a coating duration of 20 minutes. The beads were then suspended in 2 ml DMSO and shaken at 180 rpm. After 1 h, the beads were removed from the solvent and agitated in fresh DMSO for another 1 h. This step was repeated 3 times to ensure the effective removal of

PyKC template from the core. Finally, the hollow beads were washed with copious amounts of ethanol and dried.

2.4.5 Rheology

The viscoelastic properties of the hydrogels and coated hydrogel beads were analysed using an Anton Paar MCR 102 rheometer equipped with a 20 mm parallel plate (with 0.3 mm zero gap) measuring system at 25 °C. Appropriate amounts of peptides were dissolved in Tris buffer of pH 8 to make 1,3,5 wt% gel and kept undisturbed at room temperature for 12 h to get the hydrogels. Appropriate amounts of hydrogels are taken very carefully with the help of a spatula to avoid any damage to the hydrogel samples and placed on the lower plate of the rheometer. The measuring system is then lowered until it reaches the position where the gap between the two plates is 0.3 mm. Then the respective rheological measurements were performed. All the experiments were performed in triplicate. Strain sweep tests were performed to identify the linear viscoelastic region (LVR) over a range from 0.01 to 1000% strain at a fixed oscillatory frequency of 1 rad/s. The LVR can be defined as the range where strain has no impact upon G' and G''. Frequency sweep tests were carried out under an appropriate strain ($\gamma = 0.1\%$) selected from the LVR with the frequency ranging from 0.1 to 1000 rad/s at 25 °C. To investigate the thixotropic property of the gels (1,3 5 wt %), cyclic dynamic strain sweep experiment was performed at a constant angular frequency of 1 rad/s by altering the applied strain from 0.1 to 100%. In this experiment, a higher strain ($\gamma = 100\%$) and a lower strain ($\gamma = 0.1\%$) are applied on the gel alternatively over a period of 2300 s and four successive cycles. For the amplitude sweep experiment of hydrogel beads, 10 beads of each coating were taken.

2.4.6 Time-dependent FTIR analysis of 5ACl coating

Time dependent FTIR analysis was used to track the progress of the Michael addition reaction on the surface of 5ACl coated hydrogel beads with BPEI. The consumption of the acrylate groups via Michael addition reaction was indicated by a decrease in the intensity of the C-H stretching band of the vinyl moiety at 1408 cm^{-1} with respect to the internal standard, i.e. the IR peak for carbonyl stretching at 1733 cm^{-1} (Figure 2.2D). After five and ten minutes, respectively, 27% and 63% of the acrylate groups had been consumed. At 20 minutes, the intensity of the vinylic peak had almost vanished, suggesting that the acrylate groups had been nearly completely consumed.

2.4.7 Surface area calculation

10 spherical hydrogel beads prepared through the application of a bilayer of 5ACl and BPEI over PyKC beads were observed through an optical microscope, and their size was analysed with the

help of ImageJ software. The mean radius of the beads was found to be 910 ± 22.4 μm. Assuming the beads to be spherical, the surface area of the beads was calculated using the formula $4\pi r^2$ where r is the average radius as obtained from the analyses. The average surface area per bead was thus found to be $2.6 \times 10^6 \pm 1.2 \times 10^5$ μm^2. All subsequent surface functionalization experiments were performed using these beads.

2.4.8 Quantification of free amine of BPEI coated beads (4-Nitrobenzaldehyde assay)

The amount of free amine present on the surface of the core-shell beads were calculated following a literature protocol.[151] BPEI functionalised beads (10 numbers) were taken in 1 mL methanol containing 50 mg of 4-Nitrobenzaldehyde (4-NBA) and heated overnight at 45 °C with gentle stirring. The bead was then removed from the solution and washed thoroughly with copious amounts of methanol to remove unreacted 4-NBA. The washing step was repeated five times. The 4-NBA functionalized bead was then transferred to a hydrolysis solution, (1:1 methanol/H_2O), and stirred at 45°C for 24 hours. The hydrolytic wash was saved and diluted for measurement of optical density at 275 nm. Monitoring of hydrolysis solution indicated that 4-NBA was removed quantitatively with hydrolysis step. The amount of 4-NBA released provided an estimate of surface-accessible amines. The total amine content of the beads was therefore determined with the help of calibration curves prepared using 4-NBA in the hydrolysis solution and was found to be 0.425 pmol/μm^2 (1.105 μmol per bead) (Figure 2.12B).

2.4.9 Copper(II)/BPEI complexation assay

Ten identically sized core-shell beads or hollow capsules were incubated for an hour each in various buffer solutions or solvents in 5 mL round bottom flasks. The beads/capsules were then separated, and the solvents were evaporated. Aqueous $CuSO_4$ solution (300 μM, pH 7 buffer) was then added to each round bottom flask and the solution was incubated for 30 minutes. The solutions were then analysed through UV-Visible spectrophotometry to detect the presence of copper(II)/BPEI complex, which exhibits a prominent absorption peak at 275 nm (Figure 2.5B).[157] For quantification, a calibration plot was prepared by treating known concentrations with BPEI with $CuSO_4$.

2.4.10 Surface functionalization and other experimental procedures

2.4.10.1 Immobilization of 1-Pyrenecarboxaldehyde (PyCHO) via imine coupling

BPEI coated beads (10 numbers) were taken in 1 mL methanol containing 4 mM of PyCHO and were allowed to react at 45 °C for 12 hours. After cooling to room temperature, the dye solution was removed and the beads were washed thoroughly with methanol until the washing solvent was free from the unreacted aldehyde (confirmed through UV).

The molar extinction coefficient of PyCHO in methanol was determined by plotting the absorbance of known concentrations of PyCHO in methanol at 393 nm. The slope of the linearly fitted concentration vs absorbance plot yielded the value ε_{393nm} = 8.02 $mM^{-1}.cm^{-1}$. The amount of PyCHO immobilised on the surface of the beads was then assessed by comparing the change in absorption of PyCHO solution (in methanol) after treatment with the beads. All measurements were performed in triplicate.

2.4.10.2 Immobilization of FITC via amine-isothiocyanate coupling

BPEI coated beads (10 numbers) were taken in 1 mL of pH 9 carbonate buffer (10 mM) containing 2.4 mM FITC and were gently shaken over a shaker plate in the dark at room temperature for 3 h. After incubation, the dye solution was removed, and the beads were washed thoroughly with bicarbonate buffer several times until the washing solvent was free from the dye (confirmed through UV). The beads were then washed with water three times to remove any remaining salt.

The molar extinction coefficient of FITC in pH 9 carbonate buffer (10 mM) was determined by plotting the absorbance of known concentrations of FITC in carbonate buffer at 494 nm and was found to be ε_{494nm} = 71.53 $mM^{-1}.cm^{-1}$ (Figure 2.8C). The amount of FITC immobilised on the surface of the beads was then determined by comparing the decrease in absorption of the FITC solution after treatment with the beads. All measurements were performed in triplicate.

2.4.10.3 Immobilization of rhodamine B (RhB) via amide coupling

BPEI-coated beads (10 numbers) were taken in 1 mL water along with 5 mg RhB, 7 mg N-hydroxysuccinimide (NHS) and 15 mg EDC. The beads were then gently shaken over a shaker plate in dark at room temperature for 10 hours. After immobilization, the residual dye solution was removed and the beads were washed thoroughly with water until the washing solvent was free from the dye (confirmed through UV).

The molar extinction coefficient of RhB in water was determined by plotting the absorbance of known concentrations of RhB in water at 554 nm and was found to be ε_{554nm} = 42.34 $mM^{-1}.cm^{-1}$ (Figure 2.10C). Next, the difference in the absorption of the RhB solution after the treatment with the beads was used to calculate the amount of RhB immobilised on the bead surface. All measurements were performed in triplicate.

2.4.10.4 Immobilization of 1-Pyrenemethylamine ($PyCH_2NH_2$) via Michael addition

5ACl coated beads (10 numbers) were taken in 1 mL methanol containing 21.62 mM $PyCH_2NH_2$ and allowed to shake gently over a shaker plate at room temperature for 24 hours. Later, the remaining

solution was removed, and the beads were washed thoroughly with methanol until residual $PyCH_2NH_2$ was completely washed away (confirmed through UV).

The molar extinction coefficient of $PyCH_2NH_2$ in methanol was determined by plotting the absorbance of known concentrations of $PyCH_2NH_2$ in methanol at 340 nm and was found to be $\varepsilon_{340nm} = 14.22\ mM^{-1}.cm^{-1}$ (Figure 2.11C).The amount of $PyCH_2NH_2$ immobilised on the surface of the beads was then assessed from the decrease in absorption of $PyCH_2NH_2$ solution after the treatment with beads. All measurements were performed in triplicate.

2.4.10.5 Immobilization of PyC via thiol-ene coupling

5ACl coated beads (10 numbers) were taken in 1 mL solution of 9.22 mM PyC in THF (also added one drop of Et_3N) and subjected to gentle shaking at room temperature for 12 hours. The THF solution was then removed, and the beads were washed thoroughly with THF until free PyC molecules were completely washed away (confirmed through UV).

The molar extinction coefficient of PyC in THF was determined by plotting the absorbance of known concentrations of PyC in THF at 344 nm and was found to be $\varepsilon_{344nm} = 9.65\ mM^{-1}.cm^{-1}$ (Figure 2.12C). The amount of PyC immobilised on the surface of the beads was then determined by comparing the decrease in absorption iof PyC solution after the treatment with beads. All experiments were performed in triplicate.

2.4.11 Dissolution of the PyKC core from the core-shell beads

In a typical experiment, the core-shell beads were immersed in different solutions (different buffers, solvents as mentioned in the main text or in aqueous solutions of DTT, TCEP, GSH). The samples were incubated at room temperature with slow shaking (180 rpm). Aliquots of the bulk solvent/solution were taken from time to time and replaced with the same amounts of fresh bulk solvent/solution to keep the overall volume intact. The aliquots were diluted with the same bulk solvent/solution before recording their absorption spectra. Absorbance spectra of varying concentrations of freshly prepared solutions of PyKC-dimer/monomer in the respective bulk solvent/solution were recorded to get the calibration curve to determine the concentrations of PyKC-dimer in the aliquots. The % dissolutions were calculated using these calibration curves following the cumulative absorbance at 352 nm.

Chapter 3

Functional Surface Engineering of Core-Shell Hydrogel Beads: Host-Guest Chemistry, Biocatalysis, and AuNP-Assisted Catalysis

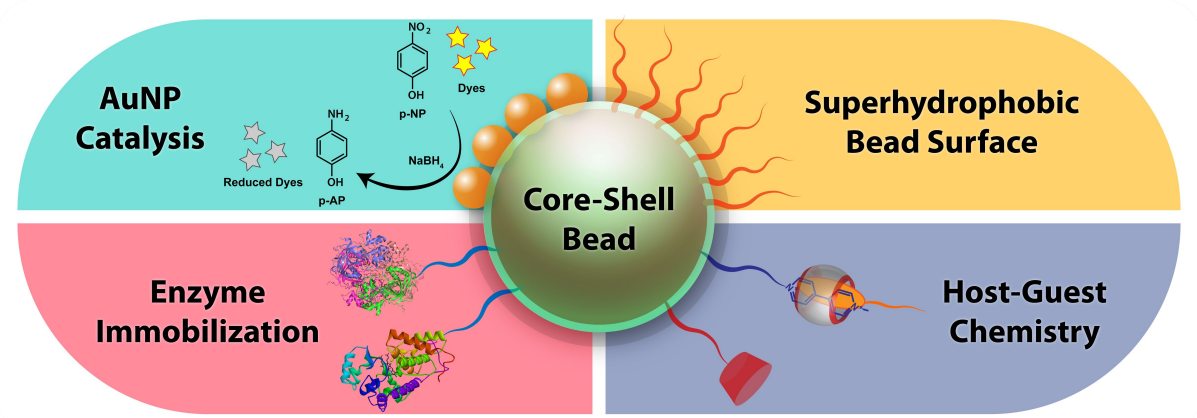

Indian Institute of Technology Guwahati

3.1 Introduction

Heterogeneous support materials play a pivotal role in diverse fields such as catalysis, biosensing, molecular separations, and environmental remediation.[158] These materials facilitate the immobilization of functional entities such as catalysts, enzymes, and molecular recognition elements onto solid or semi-solid platforms, thereby enabling improved operational stability, reusability, and simplified separation from reaction environments. Conventional heterogeneous supports such as silica particles, synthetic polymers, and magnetic nanocomposites, while widely used, often suffer from limitations including poor biocompatibility, inadequate aqueous compatibility, and restricted tunability at the molecular level.[159-161] These shortcomings can be especially detrimental in applications that require precise structural and chemical adaptability under biologically or environmentally relevant conditions. To overcome these limitations, significant attention has shifted toward hydrogel-based support materials, which combine the benefits of soft matter, such as flexibility, high water content, and permeability, with the potential for diverse chemical functionalization.[162-164] Hydrogels, composed of crosslinked hydrophilic polymer networks, are intrinsically porous and water-swollen, making them ideal scaffolds for hosting bioactive molecules, nanoparticles, and reactive intermediates. Their chemically modifiable matrix allows for tailored surface functionalities, enabling applications in enzyme immobilization, affinity separation, stimuli-responsive systems, and soft catalysis.[77, 79, 81, 83] However, traditional hydrogel systems suffer from several key drawbacks. First, their bulk diffusion characteristics can severely limit the kinetics of internal reactions and recognition processes, especially for large, charged, or hydrophobic substrates. Second, handling, recovering, and reusing hydrogel monoliths or films is often operationally challenging, particularly under flow or batch conditions, due to their mechanical fragility, lack of defined boundaries, and tendency to swell or deform. These practical limitations reduce their scalability and reproducibility in real-world applications.

To mitigate these issues, hydrogels have been increasingly engineered into discrete particulate formats such as beads, capsules, and microspheres.[61] This transformation improves mechanical stability, simplifies recovery and reuse, and enhances compatibility with flow-based or modular systems. Among these formats, the core–shell hydrogel beads described in Chapter 2 represent a particularly effective design, wherein the inner core imparts structural integrity while the outer shell serves as a chemically tunable interface for surface functionalization. Importantly, the core–shell hydrogel beads developed in this study differ fundamentally from conventional hydrogel supports: they are mechanically robust and impermeable to a wide range of solvent and solute molecules.[58] This unique property restricts all functional interactions, such as catalytic transformations, host–guest complexation, and biomolecular binding to the outer surface of the bead, eliminating the

complications associated with diffusion into the bulk matrix. Such a surface-confined functionalization strategy offers several critical advantages. The discrete bead format enables easy collection, washing, and redeployment over multiple cycles. Also, by eliminating the reliance on diffusion into the gel interior, the platform circumvents limitations like poor substrate accessibility, slow kinetics, and inefficient turnover. All interactions occur at a chemically defined, highly accessible interface, enabling rapid response, enhanced catalytic activity, and efficient molecular recognition. This redefines the role of hydrogel beads from passive carriers to active, interface-confined heterogeneous platforms suitable for advanced chemical and biological functions.

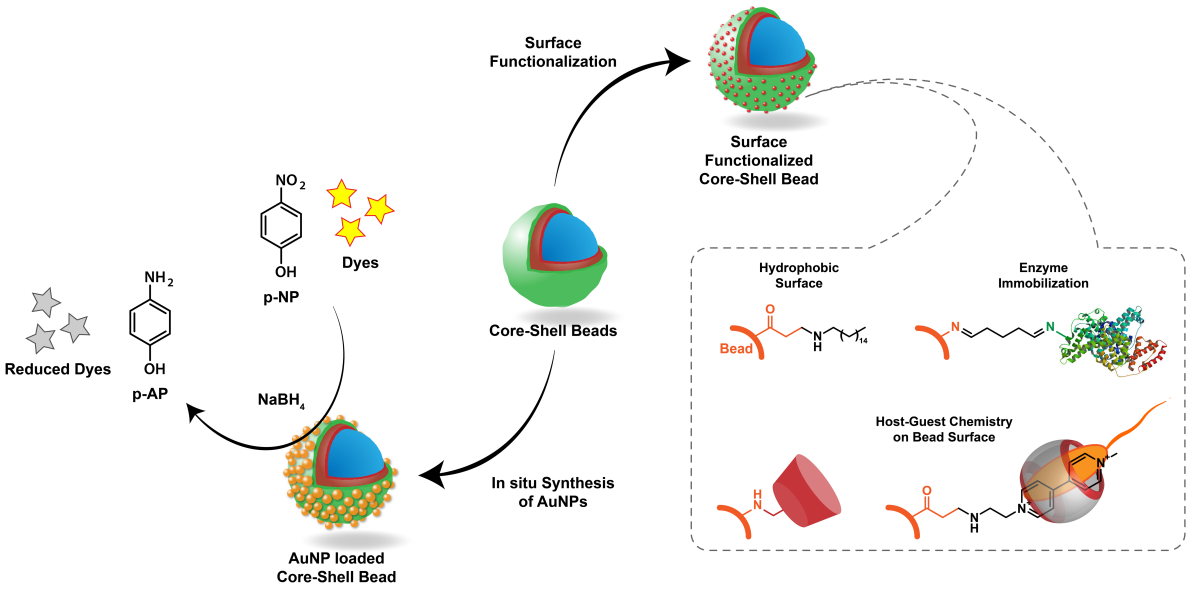

Scheme 3.1 Schematic representation of the functional surface engineering of core–shell hydrogel beads for diverse applications, including hydrophobic surface generation, host–guest interactions on the bead surface, enzyme immobilization for sustainable and reusable biocatalysis, and in situ growth of gold nanoparticles for catalytic purposes.

In this work, we leverage this platform to develop a series of multifunctional hydrogel beads with tailored surface properties (Scheme 3.1). Using diverse post-synthetic chemical modifications, we construct superhydrophobic beads by attaching long-chain alkylamines, enabling water-repellent surfaces. We also demonstrate efficient immobilization of proteins and enzymes, producing recyclable and reusable catalytic systems with retained activity across multiple reaction cycles. In addition, the bead surface is employed for host–guest complexation, facilitating selective molecular recognition and potential applications in affinity separations or biosensing. Furthermore, the beads functionalized with branched polyethyleneimine (BPEI) demonstrated a dual functionality: BPEI not only facilitated the in situ reduction of Au(III) ions to gold nanoparticles (AuNPs) but also served as a stabilizing scaffold, effectively anchoring the nanoparticles within the polymeric shell. The resulting AuNP@Beads, obtained by directly growing AuNPs on the bead surface, exhibited

remarkable catalytic efficiency in the reductive degradation of hazardous nitroaromatic pollutants and industrial azo dyes. The uniform dispersion of AuNPs within the BPEI layer, coupled with their strong retention, endowed the system with excellent catalytic longevity, allowing multiple reuse cycles without any noticeable loss of activity or evidence of nanoparticle leaching or aggregation. Collectively, this work presents a modular, chemically versatile, and operationally robust hydrogel bead platform that overcomes the key limitations of conventional hydrogel-based heterogeneous systems. Its surface-localized activity, reusability, and adaptability position it as a powerful tool for a broad range of applications in catalysis, molecular recognition, and environmental remediation.

3.2 Results and Discussion

3.2.1 Core-Shell beads with superhydrophobic surface

As a proof of concept, to tune the surface wettability of the beads, initially, hydrogel beads with free acrylate groups on the polymeric shell were functionalized with hexadecyl amine ($C_{16}NH_2$) employing the Michael addition (ene-amine) reaction. Attachment of the amine was ascertained through FTIR spectroscopy wherein the signal intensity at 1408 cm^{-1} for C-H stretching of the β-carbon of the vinyl groups decreased substantially relative to the normalised signal intensity for carbonyl groups at 1735 cm^{-1} (Figure 3.1A).[165]

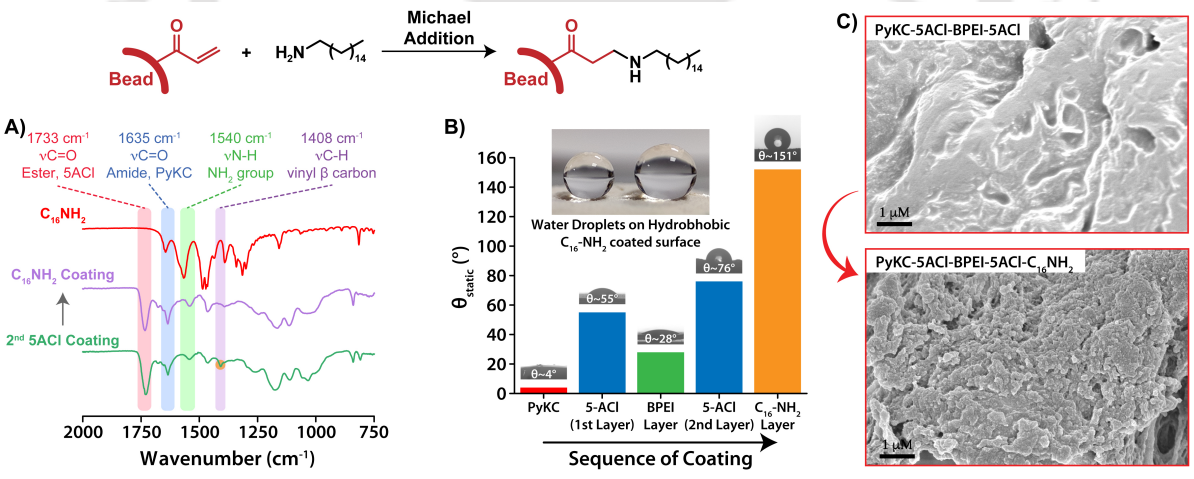

Figure 3.1 Fabricating superhydrophobic beads A) FTIR spectra showing immobilization of $C_{16}NH_2$ on the surface of 5ACl coated beads through Michael addition reaction, B) Changes in the water contact angle after each successive surface modification performed on a plane surface of a silicon wafer, and C) FESEM images of the 5ACl coated beads before and after the immobilisation of $C_{16}NH_2$.

As the small spherical beads cannot be used for contact angle (CA) measurements, the hydrophobic surface of the $C_{16}NH_2$ functionalized beads were replicated on the plane surface of an activated silicon wafer through layer-by-layer deposition of PyKC hydrogel followed by 5ACl and then BPEI (See the experimental section). As expected, the PyKC hydrogel surface, on account of surface exposed Lysine groups, was found to be hydrophilic in nature with a very low water CA of 4° (Figure

3.1B). Deposition of a layer of 5ACl over the PyKC hydrogel significantly lowered the hydrophilicity of the layer and the water CA increased to 55°. Coating the 5ACl surface with a layer of BPEI increased the hydrophilic character of the resulting polymeric bilayer and the water CA dropped to 28°. A second coating of 5ACl over the polymeric bilayer resulted in a water CA of 76°. Finally, upon treating the acrylate functionalized surface with $C_{16}NH_2$, the water CA jumped to 151°, indicating a superhydrophobic surface. FESEM analysis of the hydrophobic beads revealed an irregular surface morphology which is substantially different from the smooth surface observed in the case of the acrylate-coated beads (Figure 3.1C). This further confirmed effective conjugation of $C_{16}NH_2$ chains on the bead's surface.

3.2.2 Surface functionalization with guests for Cucurbit[8]uril

Next, we anticipated that if the surface of the hydrogel can be functionalized with an appropriate guest molecule for a specific macromolecular host, host-guest chemistry can be performed on the surface. Such modification can provide ample opportunity to utilize them as a smart functional material for various applications. For this purpose, we chose Cucurbit[8]uril assisted ternary complexation between viologen and an electron rich guest.[166-169] To create core-shell beads functionalized with viologen on the surface, an amine appended viologen derivative, MV, (Figure 3.2A) was selected as the guest molecule that can be attached on the bead surface. The viologen derivative was affixed to the surface of the acrylate functionalised beads through Michael addition reaction. The attachment of viologen to the bead surface was assessed through FTIR analysis (Figure 3.2B). Similar to the earlier cases, a decrease in the signal intensity at 1408 cm^{-1} for C-H stretching of the β-carbon of the vinyl groups of 5ACl relative to the normalised signal intensity for carbonyl groups at 1735 cm^{-1} confirmed the effective Michael addition of amine functionalised viologen to 5-ACl surface. Moreover, a strong IR signal for PF_6^- vibration at 836 cm^{-1} appeared in the MV-unfunctionalized beads, giving an evidence of successful conjugation of aromatic viologen unit.[170, 171] Next, it was observed that, the viologen functionalised beads turned blue when immersed in 1N NaOH solution owing to the base-mediated reduction of colourless dicationic viologen units to intense blue coloured viologen radical cations (Figure 3.2C).[172, 173] Furthermore, FESEM analysis revealed that the surface architecture differs from the fibrous network structure found in the BPEI functionalised surface to which viologen is attached, providing further evidence for viologen attachment (Figure 3.2D). The amount of viologen attached to the bead surface was found to be 0.644 µmol/bead or 0.255 pmol/$µm^2$.

Electron deficient molecules such as viologens are known to undergo CB[8] assisted heteroternary complexation with electron-rich guest molecules such as naphthalene, pyrene, tryptophan, etc.[166,

[174] Tryptophan has been known to act as a good second guest for MV@CB[8] binary complex especially when situated at the N-terminal of a peptide.[175] Therefore, to assess the formation of host-guest complex on the surface of the beads, the MV-functionalized beads were shaken with a 1:1 solution of CB[8] and tryptophan containing peptide WG_4K(Fluorescein)G (**Pep-1**) for 1 h at room temperature. As complexation on the bead surface cannot be assessed through techniques such as Isothermal Titration Calorimetry (ITC), a fluorescein group was attached to the aforementioned peptide to enable spectrophotometric quantification of the complexation process. A decrease in the absorption of the peptide solution after treatment with the MV-coated beads indicated that 52.22% of the peptide was immobilised on the bead surface through host-guest complexation (Figure 3.2F-G). The amount of peptide immobilised was calculated to be 0.207 pmol/μm^2 and thus the extent of ternary complexation was 81 %.

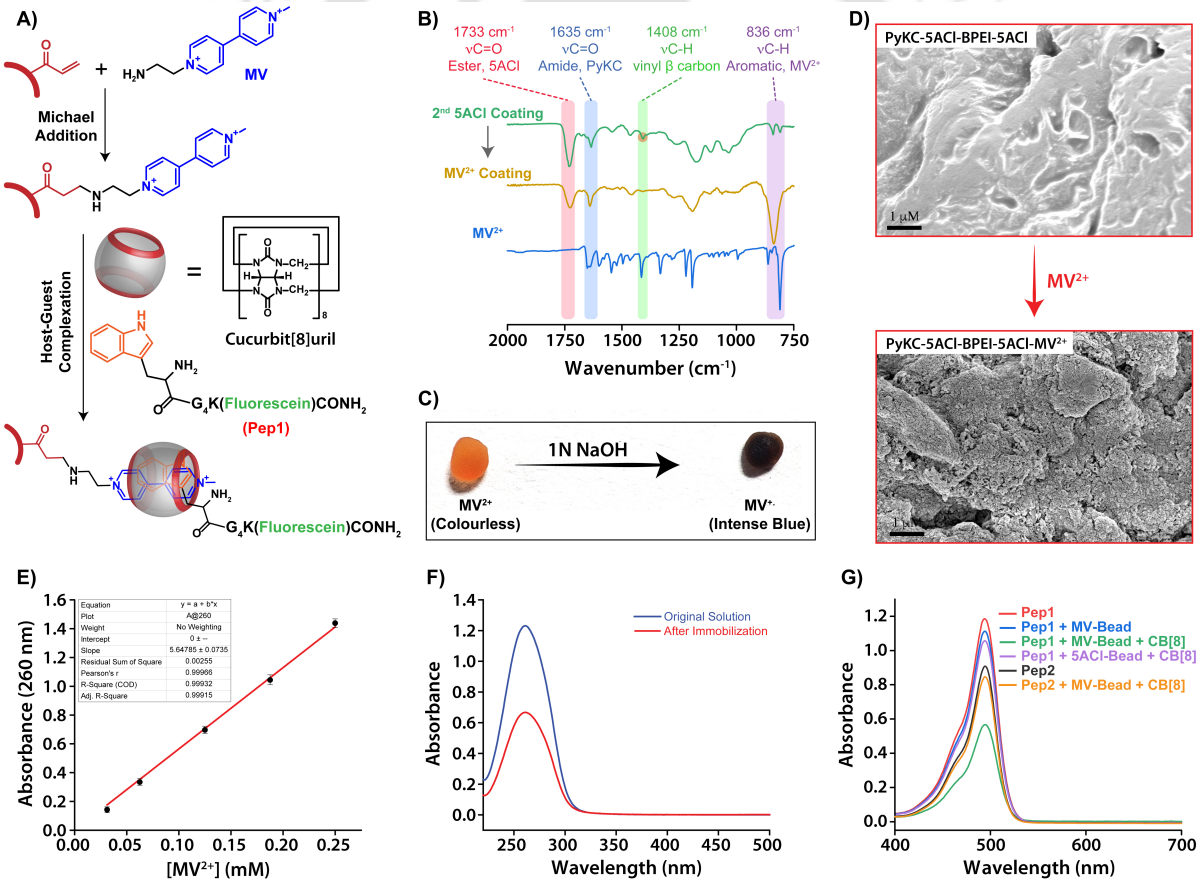

Figure 3.2 A) Schematic representation of ternary complexation on bead surface, B) FTIR spectra showing immobilization of methyl viologen on the surface of 5ACl coated beads through Michael addition reaction, C) Change in the colour of viologen functionalized beads due to the base mediated reduction of colourless MV^{2+} to intense blue coloured $MV^{+\cdot}$ radical cation, D) FESEM images of the 5ACl coated beads before and after the immobilisation of MV^{2+}, E) Calibration plot for MV^{2+} in 1:10 water/methanol mixed solvent, F) Absorption spectra of MV^{2+} in 1:10 water/methanol mixed solvent before and after the functionalisation reaction with the beads, and G) Absorption spectra showing selective attachment of tryptophan containing peptide on the bead surface through Cucurbit[8]uril assisted heteroternary complexation.

To ensure that the loss of the peptide was indeed due to the formation of ternary complex and not due to physical adsorption on the bead surface, few control experiments were performed using the MV-functionalized beads (without CB[8]), and 5ACl functionalized beads (with or without CB[8]). Insignificant loss of peptide in each control experiment confirmed the formation of ternary complex on the surface. Additionally, a control peptide, (Fluorescein)GGK (**Pep-2**) was used in presence of CB[8] and MV-functionalized beads. **Pep-2** did not get immobilized on to the surface of the beads through ternary complexation due to the absence of any tryptophan (second guest for CB[8]). Owing to the high specificity of this binding process, the viologen functionalized beads can serve as an effective platform for highly specific and selective separation of molecules/peptides containing electron-rich guests from a mixture of analytes.[176]

3.2.3 Surface functionalization with macromolecular host (Cyclodextrin)

Another approach to realize host-guest interaction on bead surface is to immobilize host molecules and for this purpose amine functionalised hydrogel beads were treated with Mono-6-tosyl-β-cyclodextrin (TsO-CD) to produce cyclodextrin coated beads via a nucleophilic substitution reaction (Figure 3.3A).[177]

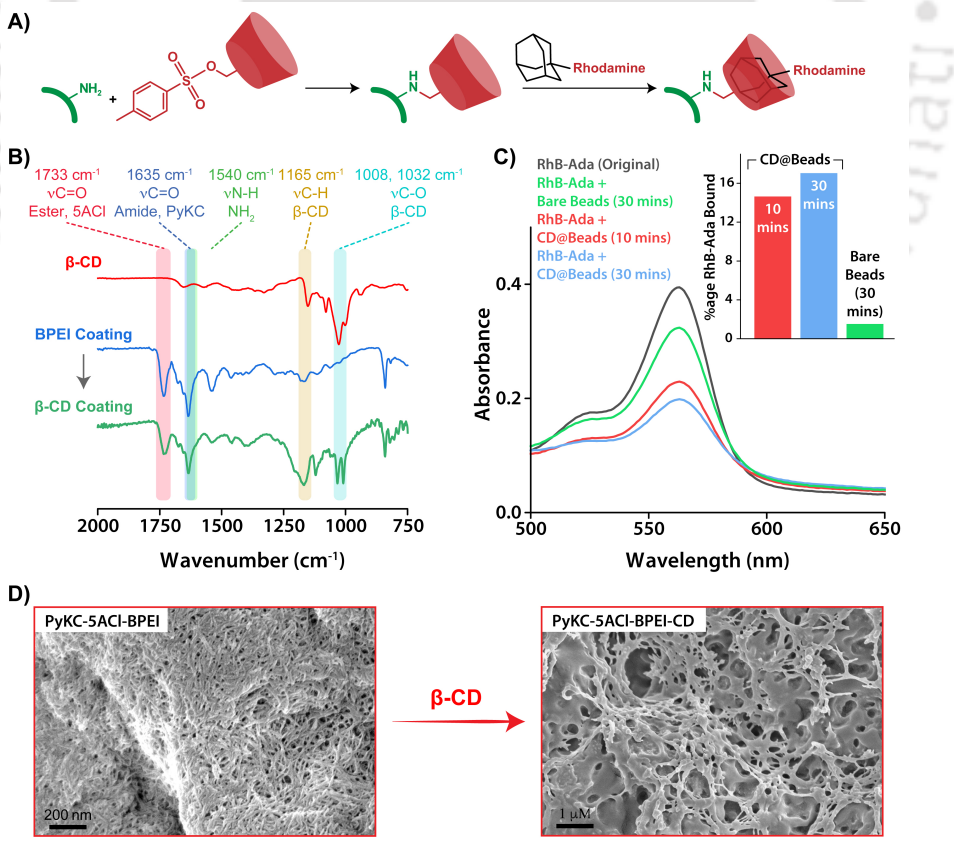

Figure 3.3 Host-guest chemistry on bead surface using cyclodextrin. A) Schematic presentation of the attachment of β-CD on core-shell bead surface, B) FTIR spectra showing immobilization of β-CD on the surface of BPEI coated beads, C) Absorption spectra showing selective attachment of Ada-RhB on the bead surface

through host-guest complexation with β-CD, and D) FESEM images of the BPEI coated beads before and after the immobilization of β-CD.

FTIR analysis of β-cyclodextrin (β-CD) functionalized beads showed characteristic peaks at 1165 cm^{-1} for C-H stretching and 1008, 1032 cm^{-1} for C-O stretching of glycosidic bonds of β-CD, confirming the effective functionalization of β-CD (Figure 3.3B).[178] The surface morphology (as found from the FESEM images, (Figure 3.3D) was also observed to be different from the BPEI coated surface and points toward successful attachment of β-CD.To assess host guest interactions on bead surface, an adamantyl appended rhodamine B derivative (Ada-RhB) was synthesized and it was observed that the beads could effectively bind and remove Ada-RhB from solution, further confirming the presence of β-CD on the surface of the beads (Figure 3.3C). Following similar protocol as in the case of MV-functionalized beads, the amount of RhB-Ada immobilised was calculated to be 0.05 $pmol/\mu m^2$.

3.2.4 Surface functionalization with protein

Next, the beads were tested for their ability to harbour proteins and enzymes on their surface. Enzymes have been found to have improved long-term stability after being covalently immobilised on solid surfaces.[179, 180] As a proof of concept, we chose horseradish peroxidase (HRP) to conjugate on the core-shell bead surface. Amine functionalized beads were treated with HRP in the presence of EDC/NHS under mild agitation (amide coupling reaction) (Figure 3.4A). Attachment of HRP on bead surface was ascertained from FTIR analysis which showed the presence of broad bands at 1635 cm^{-1} and 1540 cm^{-1} corresponding to amide C=O and N-H stretching, respectively arising from the protein (Figure 3.4B). FESEM images and EDX (Energy Dispersive X-Ray) analysis of iron on the surface of the beads also confirmed effective immobilization (Figure 3.4C-D). The amount of HRP immobilised on the beads was calculated using a calibration curve plotted from the peroxidation reaction kinetics of pyrogallol to purpurogallin by known concentrations of free HRP enzyme (for a given concentration of H_2O_2) and was found to be 79.07 $pg/\mu m^2$ (Figure 3.4E-F). HRP immobilization also allowed for easy recovery and reuse of the enzyme for at least up to 10 cycles without any significant loss of activity (Figure 3.4G).

Using an alternative strategy, another protein, Bovine Serum Albumin (BSA), was immobilised on the surface of the beads through glutaraldehyde activation, wherein amine functionalized beads were first activated using glutaraldehyde (5 w/w % in 20 mM pH 7 phosphate buffer) (Figure 3.4A). Free aldehyde groups on the surface of the beads were then connected via a second imine linkage to Lysine units of the enzyme . BSA immobilization was confirmed from FTIR analysis which showed the presence of a broad band at 1635-1680 cm^{-1} indicating the coexistence of C=O, C=N stretching

frequency.[181] Also, broadening of the N-H stretching frequency at 1540 cm^{-1} further confirm the BSA immobilisation on BPEI coated beads (Figure 3.4B).

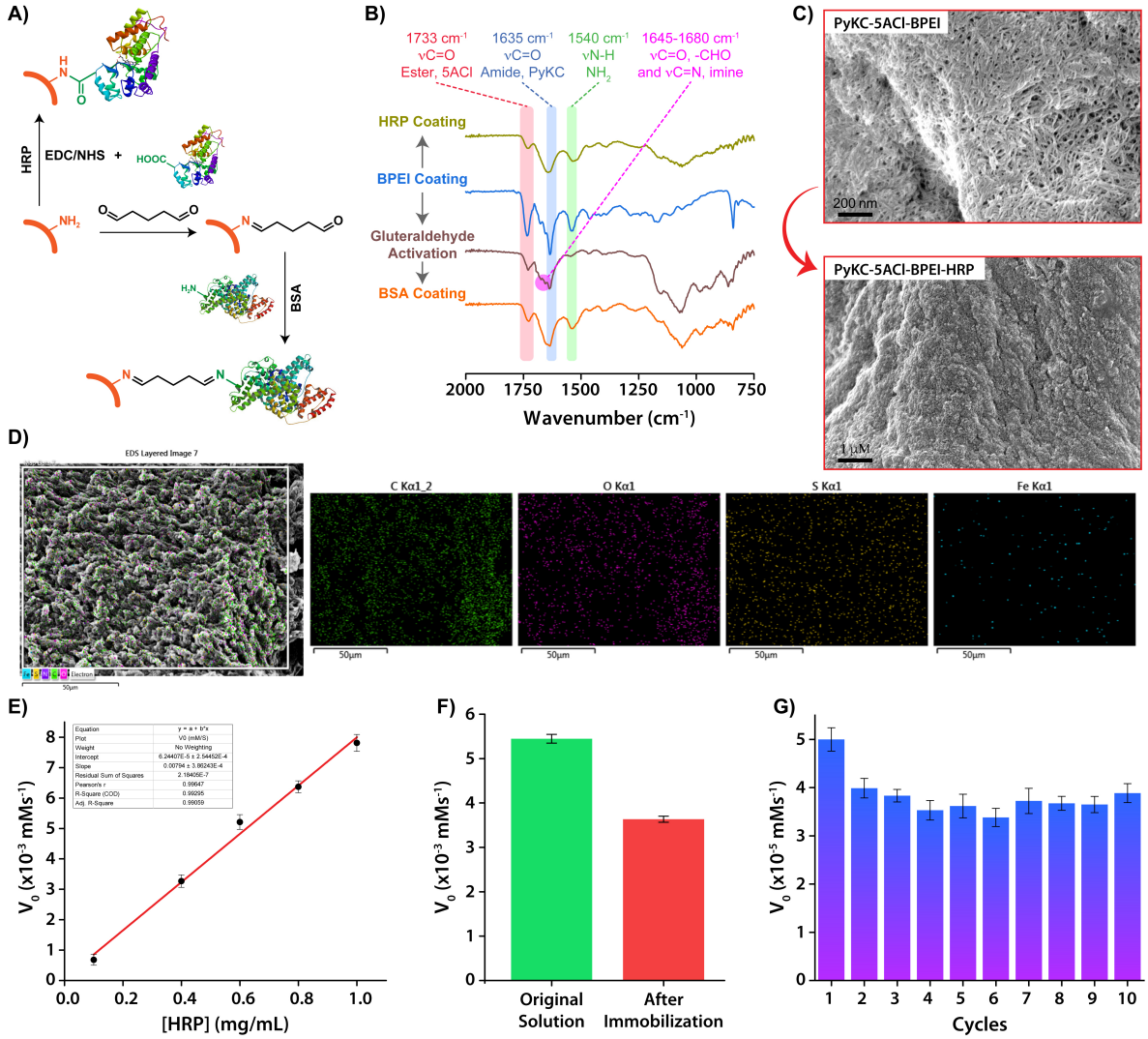

Figure 3.4 Enzyme immobilization on the surface of the core-shell beads. A) Schematic illustration of HRP and BSA immobilization on bead surface, B) FTIR spectra of the HRP and BSA conjugated BPEI coated beads, C) FESEM images of the BPEI coated beads before and after HRP immobilization, D) EDX mapping of HRP functionalised bead, E) Calibration curve for HRP catalysed peroxidase reaction, F) Activity of free HRP in solution before and after immobilization on beads, and G) Rate of peroxidase reaction by the HRP coated bead across ten consecutive cycles.

FESEM images showing rough morphology, which is markedly different from the surface morphology of unfunctionalized beads affirmed effective BSA attachment to the bead surface (Figure 3.5A). Rhodamine B tagged BSA was used to determine the amount of BSA immobilized using UV-visible analysis and was found to be 171 pg/µm^2 (Figure 3.5B-C). The tagged fluorophore also enabled visualizing the BSA functionalized beads through fluorescence microscope (Figure 3.5D). As imine linkages are susceptible to changes in the pH of the medium, attachment of proteins using this strategy might not be effective for applications where the pH varies with time.[182] However,

the pH dependence of the linkages can be taken in to advantage toward application of the system as a smart and responsive material.[183]

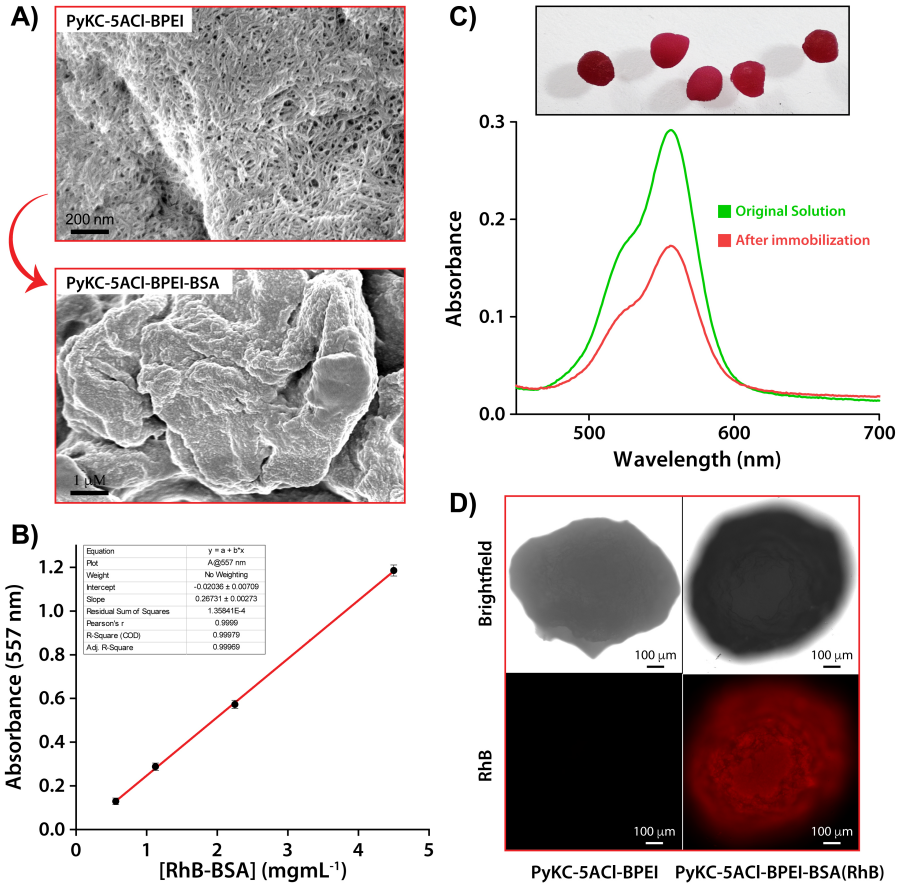

Figure 3.5 A) FESEM images of the BPEI coated beads before and after BSA-RhB immobilization, B) Calibration curve for BSA-RhB in water, C) Photographic images of BSA-RhB coated beads and absorption spectra showing attachment of BSA-RhB on the bead surface, and D) Optical images of the bare and BSA-RhB functionalised beads.

3.2.5 Fabrication of AuNP-embedded catalytic beads

Polyethyleneimine (PEI), both branched and linear, have a high electron density and thus a mild reducing nature due to the presence of several primary, secondary, and tertiary amine groups in close proximity along their polymeric backbone. PEI offers several advantages for the synthesis and stabilization of AuNPs and has been widely employed in the in-situ synthesis of gold nanoparticles (AuNPs).[184-190] This is due to the fact that PEI functions as both a reducing and a capping agent, allowing for the one-step synthesis of AuNPs without the need for additional reducing agents. During the reduction of Au(III) to Au(0), the amine groups in PEI undergo oxidative dehydrogenation, leading to the formation of imine (C=N) linkages and, in some cases, cross-linking between polymer chains.[191] These oxidative transformations contribute to the stabilization of the nanoparticles by forming a more compact polymer network around them. In our system, the imine

vibrations could not be distinctly identified in the FTIR spectra, as they likely overlapped with the amide stretching bands originating from the PyKC hydrogel bead core. The amino groups in PEI also interact electrostatically with the negatively charged AuNP surfaces, forming a stable protective layer that prevents aggregation and maintains catalytic activity and long-term stability. However, despite its benefits, PEI can make the separation and recovery of PEI-capped AuNPs more challenging. Harsh purification methods, such as centrifugation or solvent exchange, can remove PEI coating from the AuNP surface, compromising their stability and properties. In situ synthesis of AuNPs in the BPEI polymeric shell of the core-shell beads will not only provide an environment conducive to catalysis but will also allow for easy recovery and reuse of the beads across many cycles. The AuNP embedded catalytic beads (AuNP@Beads) were synthesised using a convenient and "green" reducing agent-free one-step procedure. Briefly, the BPEI coated beads were agitated in a solution of $HAuCl_4.6H_2O$ (100 mmol) for 3 hours at 90 °C. AuNP formation was also observed at room temperature, however the reaction time was much longer (6-8 days). The AuNP@Beads were then extensively rinsed with water to remove unreacted reagents and loosely attached nanoparticles.

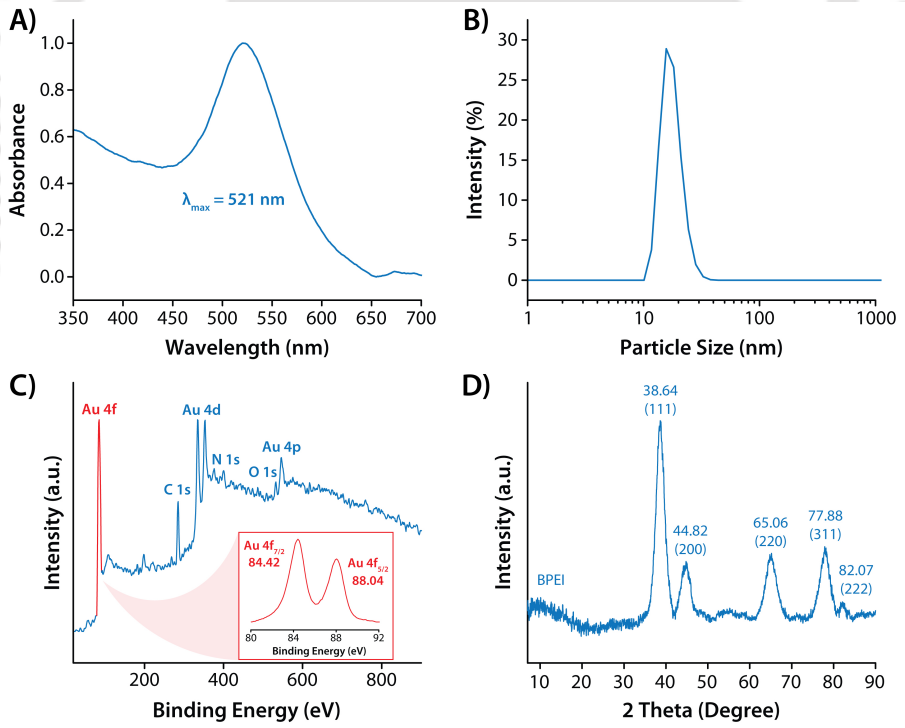

Figure 3.6 In-situ synthesis of gold nanoparticles. A) UV-Visible spectrum, B) Representative plot of the DLS profile, C) XPS pattern (Inset: High resolution XPS pattern of Au 4f), and D) XRD spectrum of the in-situ synthesized gold nanoparticles.

Preliminary investigation of AuNP formation was performed through the UV-Visible and DLS (Dynamic Light Scattering) analysis of an ethanolic suspension of the cryo-ground AuNP@Beads. A

characteristic surface plasmon band at 521 nm (Figure 3.6A) and a hydrodynamic size of 15.7 ± 1.32 nm (Figure 3.6B) indicated the formation of AuNPs.[192] X-ray Photoelectron Spectroscopy (XPS) was then employed to detect changes in the oxidation state of Au as well as the surface elemental composition of the produced AuNPs. The low-resolution spectrum revealed photoelectron peaks for Au (Au 4f, Au 4d, and Au 4p), C 1s, N 1s, and O 1s (Figure 3.6C). The peaks for carbon, nitrogen, and oxygen can be attributed to the BPEI, 5ACl and PyKC. The high-resolution spectrum of the Au 4f peak revealed a distinct doublet composed of the Au $4f_{7/2}$ peak at 84.42 eV and the Au $4f_{5/2}$ peak at 88.04 eV, confirming the presence of Au in its metallic state (Figure 3.6C).[193] The X-Ray Diffraction (XRD) spectrum of cryo-ground AuNP@Beads displayed characteristic diffraction peaks at 38.64°, 44.82°, 65.06°, 77.88°, and 82.07° corresponding to (111), (200), (220), (311) and (222) lattice planes respectively (Figure 3.6D).[194] This reflects the presence of the face-centered-cubic (FCC) crystalline structure of AuNPs embedded in the BPEI polymeric network.

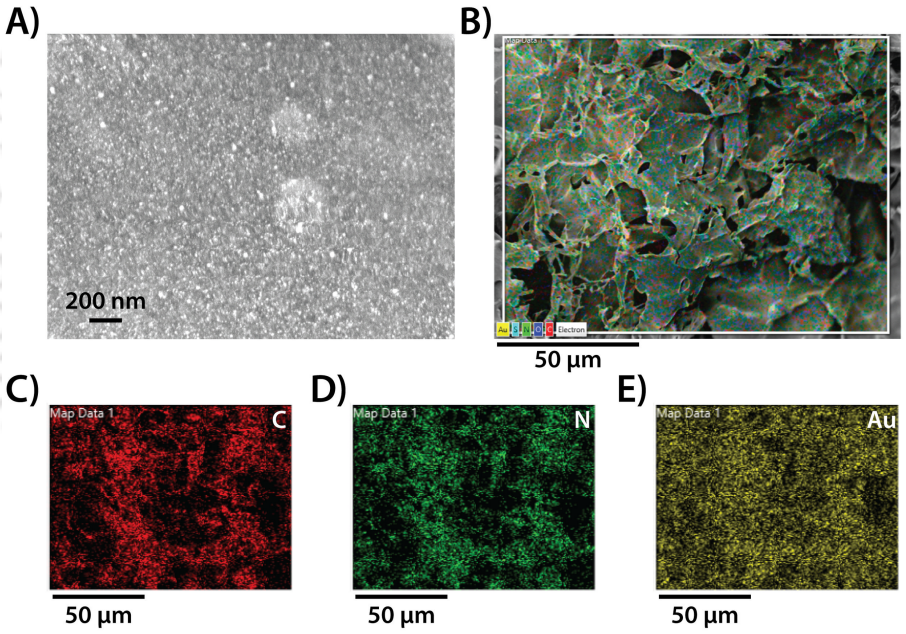

Figure 3.7 A) FESEM image of AuNP embedded surface of the core-shell bead, B-E) EDX elemental mapping of the surface of the AuNP embedded bead.

FESEM and EDX analyses were used to determine the position of AuNPs in the core-shell beads. As expected, the FESEM images revealed a homogeneous distribution of AuNPs in the outer polymeric layer of the bead (Figure 3.7A). Strong interactions between the BPEI polymers and the high concentration of immobilised AuNPs (~28%) presumably resulted in the loss of fibrillar morphology observed in the PyKC-5ACl-BPEI beads. Furthermore, EDX mapping analysis demonstrated extensive localisation of Au on the surface of the beads, corroborating the immobilization of the in situ produced AuNPs on the bead surface (Figure 3.7B-E). Transmission electron microscopy (TEM) analysis of the cryo-ground AuNP@Beads showed the presence of spherical gold nanoparticles with

an average size of 12.05 ± 1.66 nm (Figure 3.8A, D), which is consistent with the size determined from DLS analysis. The selected area electron diffraction (SAED) pattern of the AuNPs revealed that the nanoparticles are polycrystalline in nature.[195] The SAED ring pattern reflected d-spacings of 2.33, 2.02, 1.42, 1.22 and 0.92 Å, which may be attributed to the (111), (200), (220), (311) and (222) reflections of the gold fcc structure, respectively (Figure 3.8B) (JCPDS card No. 04-0784). Furthermore, the HRTEM picture showed the presence of a (111) plane with an inter-planar spacing of 2.37 Å, confirming the formation of fcc gold nanoparticles (Figure 3.8C).[196]

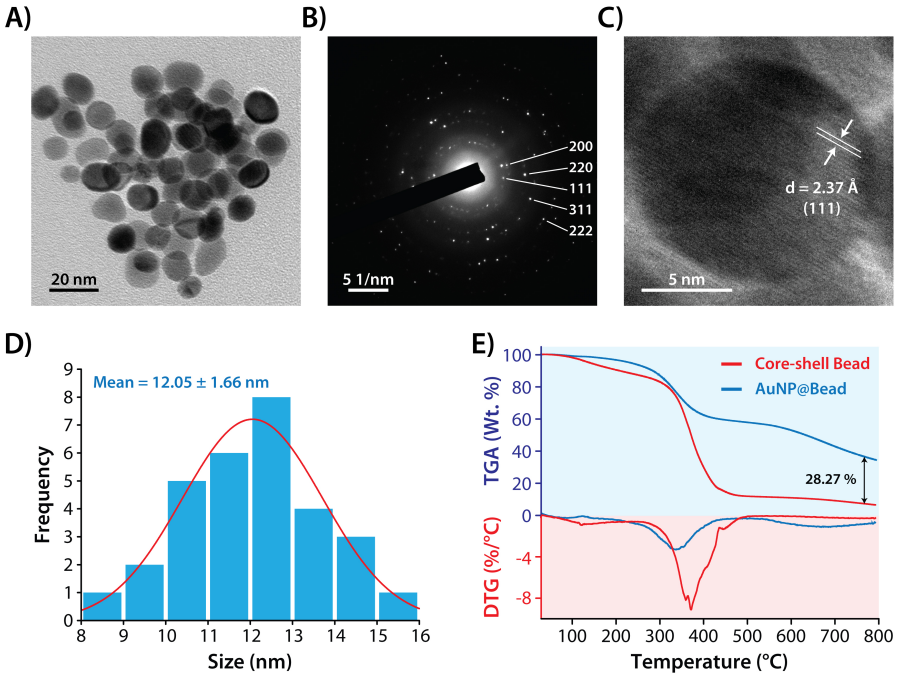

Figure 3.8 A) FETEM image, B) SAED pattern, C) HRTEM image, and D) Size distribution histogram of the in-situ synthesized gold nanoparticles, E) Thermogravimetric and Differential Thermogravimetric plot of the core-shell bead and AuNP embedded bead.

Thermogravimetric analysis (TGA) was performed to assess the thermal stability of the bare and the AuNP loaded beads, as well as to determine the amount of AuNP loading (Figure 3.8E). The initial mass loss of 6 and 1.5% for the bare and the AuNP loaded beads, respectively, up to a temperature of 150 °C may be ascribed to the desorption of moisture and trapped gases. Following that, the bare and AuNP-loaded beads had identical TGA profiles and experienced overall weight losses of 93.8 and 65.5%, respectively, due to the degradation of the peptide and polymeric components of the bead. Thus, AuNPs accounted for approximately ~28 wt% of the dried mass of the catalytic beads.

3.2.6 Catalytic activity of AuNP embedded beads

The catalytic activity of the AuNP-loaded core-shell beads was examined by performing a transfer hydrogenation reaction of *p*-nitrophenol (p-NP) to *p*-aminophenol (p-AP) in water using excess $NaBH_4$ as a hydrogen source. As *p*-nitrophenol is a hazardous chemical that is frequently found in

industrial wastewater and effluents, reducing *p*-nitrophenol using metal nanoparticles has often been adopted as a green strategy for water remediation.[197, 198] This reaction is also widely used as a model reaction for evaluating the activity of metal nanoparticles since it can be easily monitored using UV-Visible spectrophotometry.[198, 199] Under acidic and neutral conditions, p-NP solution has a pale-yellow colour with an absorption peak at 318 nm. With the addition of $NaBH_4$, the absorption peak red-shifted to 400 nm, and the solution became bright yellow, indicating the production of phenolate ions under alkaline conditions (Figure 3.9A). To initiate the reaction, one gold-embedded catalytic bead was introduced to the solution, and the progress of the reaction was monitored using UV-Visible spectrophotometry. A progressive decrease in absorbance at 400 nm, accompanied by the emergence of a band of increasing intensity at 298 nm, suggested catalytic conversion of p-NP to p-AP (Figure 3.9A and 3.10A).[199] The fact that AuNP@Bead resulted in no substantial decline in p-NP absorbance at 400 nm in the absence of $NaBH_4$ over a period of 1 h implies that the consumption of p-NP from the solution is primarily due to catalytic conversion of p-NP rather than adsorption on the bead surface.[199]

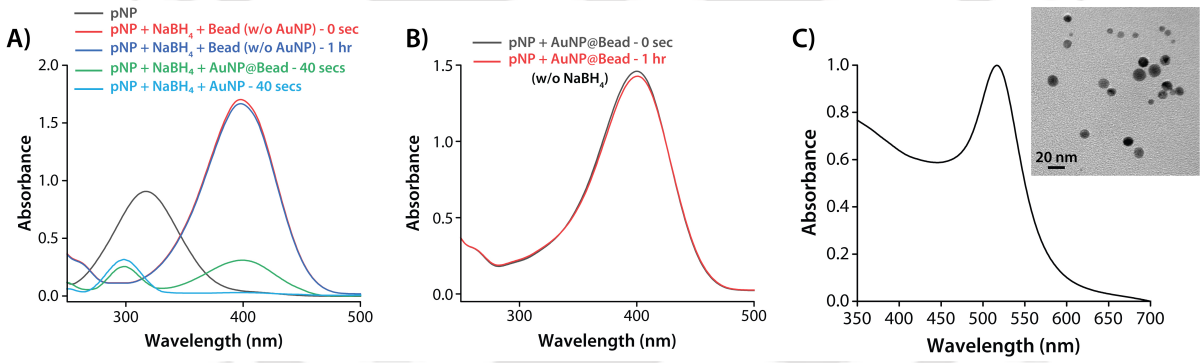

Figure 3.9 Changes in the UV-Visible spectrum of p-NP upon treatment with A) non-catalytic core-shell beads (w/o AuNPs), AuNP loaded catalytic beads (AuNP@Bead) and free AuNPs, in the presence of $NaBH_4$ (20 mM), and B) catalytic AuNP@Bead in alkaline buffer (pH 8), but without $NaBH_4$, C) UV-Visible spectrum and FETEM image of BPEI stabilized free AuNPs.

It is worth mentioning that although reducing p-NP to p-AP with $NaBH_4$ is a thermodynamically feasible process, it is kinetically restricted and exhibits extremely sluggish reaction rates in the absence of a catalyst.[199] This was validated by a control experiment in which $NaBH_4$, in the presence of non-catalytic beads (without AuNPs), was able to reduce only a negligible amount of p-NP over a 1-hour period (Figure 3.9B). To compare the catalytic activity of AuNPs in the free and embedded states, free BPEI-stabilised gold nanoparticles were synthesized and characterised by FETEM and UV-Visible analysis (Figure 3.9C). The higher catalytic activity of AuNPs in the free state compared to those in the embedded form may be explained by the higher surface area-to-volume ratio and mobility of the free nanoparticles. Nonetheless, embedding gold nanoparticles on beads is a beneficial strategy because, while free AuNPs excel in catalytic activity, embedding them on beads

enhances their practicality by facilitating recovery and reuse, making them a versatile and sustainable choice for catalytic applications.

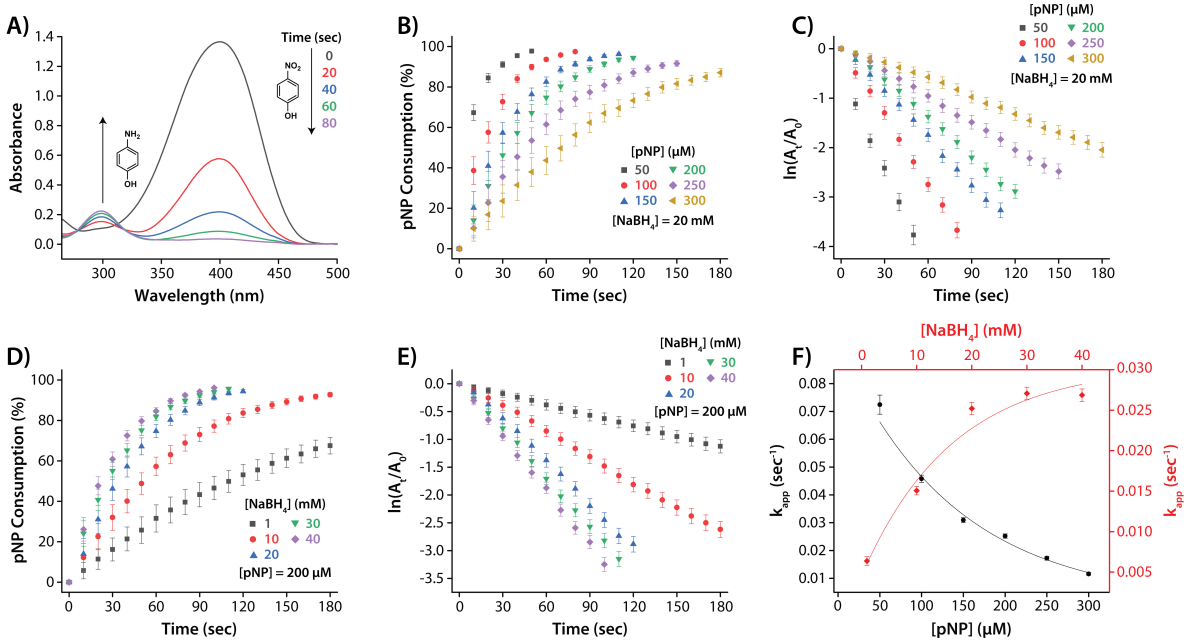

Figure 3.10 Catalytic activity of embedded AuNPs. A) Time-dependent UV-Visible spectrum for the degradation of p-nitrophenol (100 μM), B) Time-dependent consumption, and C) the corresponding plot of $\ln(A_t/A_0)$ vs reaction time for the catalytic degradation of varying concentrations of p-NP in presence of a fixed concentration of $NaBH_4$ (20 mM), D) Time-dependent consumption, and E) the corresponding plot of $\ln(A_t/A_0)$ vs reaction time for the catalytic degradation of a fixed concentrations of p-NP (200 μM) in presence of varying concentrations of $NaBH_4$, F) Dependence of the apparent rate constant on the concentration of p-NP and $NaBH_4$.

Material	Catalyst	[pNP]	[$NaBH_4$]	k (min^{-1})	Ref.
DNA Hydrogel	AuNP	200 μM	1 mM	0.09	200
Reduced Graphene Oxide Aerogel	AuNP	10 mM	5 M	0.19	201
PNIPAAM Hydrogel	AuNP	300 μM	30 mM	0.29	202
Hollow Polymeric Microparticles	Au/Ag NP	-	-	0.126	203
	Pt/Ag NP	-	-	0.276	
Non-woven Fibers	AuNP	1 mM	300 mM	0.204	204
Gelatin Hydrogel	AuNP	500 μM	12.5 mM	0.756	205
Eggshells	AuNP	71.9 mM	1.1 M	0.41	206
Core-Shell Peptide Hydrogel Beads	AuNP	100 μM	20 mM	2.748	This Work

Table 3.1 Comparison of catalytic performance of previously reported macrosized heterogenous catalytic materials for the reduction of *p*-Nitrophenol.

Kinetic analyses of the reduction reactions were carried out by monitoring variations in the absorption intensity of p-NP at 400 nm. As $NaBH_4$ was used in large excess, the apparent rate constant (k_{app}) was calculated employing a pseudo-first order kinetic model from the slope of the

linear correlation between $\ln(A_t/A_0)$ and time, where A_0 and A_t correspond to the absorption intensity of the initial and residual p-NP in the solution at 400 nm at a given time (t).[207] The non-linear relationship between the concentration of the reactants (p-NP or $NaBH_4$) and the apparent rate constant (k_{app}) suggests that the mechanism of catalytic reduction on the surface of the AuNPs can be elucidated using the Langmuir-Hinshelwood model (Figure 3.10B-F).[208] The K_{app} value increases with increasing borohydride ion concentration until it becomes constant beyond a certain point (Figure 3.10F). This is because, increasing concentrations of borohydride ions enrich the surface of AuNPs with surface-hydrogen species. Beyond a certain borohydride concentration, the nanoparticle surface becomes saturated with the hydrogen species, and the k_{app} value plateaus.[209] A high concentration of p-NP, on the other hand, masks the catalytic metal nanoparticle surface, increasing competition between free reactant molecules for adsorption and catalysis on the accessible active sites and therefore slowing the reaction rate (Figure 3.10F). As a result, optimising the reactant concentration is crucial for maximising the catalytic efficiency of the metal nanoparticles. Although heterogeneous catalytic support materials somewhat reduce the effectiveness of embedded catalysts, the AuNP@Beads employed in this study exhibited a notably accelerated rate of catalysis, surpassing the performance of previously reported heterogeneous catalytic support materials (Table 3.1).[200-206]

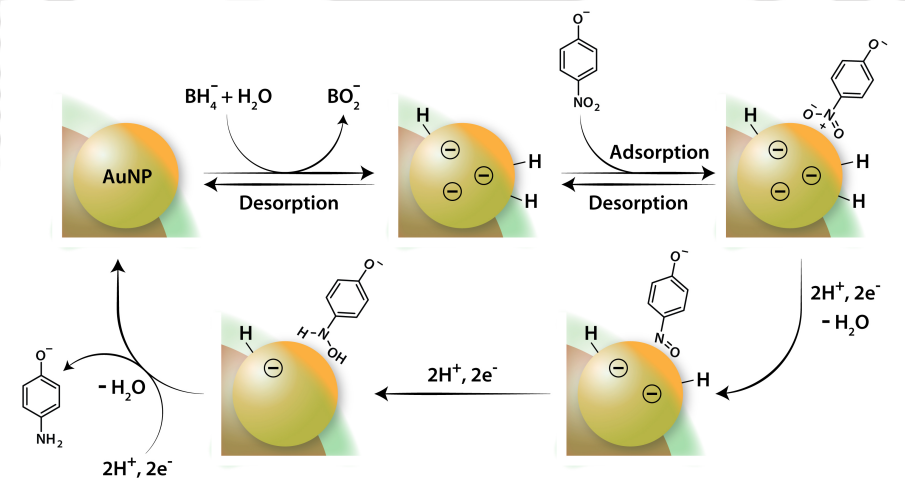

Figure 3.11 Plausible mechanism of degradation of p-NP on the surface of embedded AuNPs.

The catalytic conversion of p-NP to p-AP comprises several stages of hydrodeoxygenation processes (Figure 3.11). Initially, $NaBH_4$ adsorbs and hydrolyses simultaneously on the active sites of the AuNP surface, producing surface-hydrogen ion pairs (H^+/H^-).[210] Concurrently, the p-NP molecule binds to the active sites on the gold surface via weak chemical interactions such as electrostatic forces or coordination bonds. This adsorption allows for close proximity and increased concentration of the reactants, facilitating the subsequent reaction. The borohydride ions then transfer hydrogen and

electron to the nitro group of the adsorbed p-NP via the catalytic gold surface, resulting in the formation of the p-nitrosophenol (p-NO) intermediate through a hydrogenated dehydration reaction. A hydrogen ion pair present on the metal surface then reduces p-NO to 4-hydroxy aminophenol, which then undergoes another stage of hydrogenated dehydration to generate the end product, p-AP.[211] Once formed, p-AP desorbs from the gold nanoparticle surface, making way for new reactant molecules to bind. Throughout the catalytic cycle, p-NP and $NaBH_4$ can diffuse from the surrounding solution to the active sites on the gold nanoparticle surface, ensuring continuous reaction.

3.2.7 Reductive degradation of toxic Nitroaromatics and Azo dyes

The AuNP-loaded beads were tested for their ability to catalytically reduce the nitroaromatic compounds, 4-nitroaniline and picric acid, as well as some azo dyes, congo red (CR), methylene blue (MB), methylene orange (MO), and methylene red (MR)). 4-nitroaniline (p-NA) exhibits a characteristic absorption peak at 380 nm and forms a yellow coloured solution in water (Figure 3.12A).[212] In the presence of excess $NaBH_4$ (20 mM), a 200 µM solution of p-NA in water was completely reduced to 4-phenylenediammine by a single AuNP loaded catalytic bead in ~150 seconds. The change in the colour of the solution from yellow to colourless also confirmed the reduction of p-NA. As previously stated, a pseudo-first order kinetics is assumed to govern the reaction in the presence of excess $NaBH_4$. Therefore, the K_{app} of the reaction was estimated from the slope of the linear plot of $\ln(A_t/A_0)$ vs time, and was found to be 0.00625 sec^{-1} (Figure 3.13A). Here, A_0 is the initial absorption intensity of p-NA at 380 nm and A_t is the absorption intensity at a given time (t). Under identical reaction conditions, picric acid was reduced in ~200 seconds by the AuNP@Bead, as evidenced by the gradual fading of the yellow colour of the solution (Figure 3.12B). The K_{app} for picric acid degradation was found to be 0.00914 sec^{-1} (Figure 3.13B).

The reductive degradation of azo dyes is a process that selectively breaks down the azo bond (-N=N-) present in azo dyes, resulting in the dye being converted into simpler, less toxic compounds. For the degradation of azo dyes, in each case, a 40 µM dye solution was reduced by a single AuNP-embedded bead in the presence of excess $NaBH_4$ (4 mM), and the kinetics of the degradation reactions were tracked by monitoring UV-Visible spectroscopy. Congo Red (CR) has two distinct absorption peaks at 345 and 495 nm, which can be attributed to the azo group's $n - \pi^*$ and $\pi - \pi^*$ transitions, respectively (Figure 3.12C).[213] The gradual decline in the intensity of the characteristic absorption peaks of CR, accompanied by the emergence of new peaks at 257 and 290 nm due to $n - \delta^*$ and $\delta - \delta^*$ transitions respectively, indicated degradation of the diazo bond by the AuNP@Bead.[214] The K_{app} for CR degradation was calculated using variations in absorbance at 495

nm and found to be 0.00401 sec^{-1} (Figure 3.13C). Methylene blue (MB) exhibited a characteristic absorption band at 290 nm due to $\pi - \pi^*$ transition and another band at 662 nm with a shoulder at 613 nm due to $n - \pi^*$ transition (Figure 3.12D).[193] The addition of AuNP@Bead to an aqueous solution of MB and $NaBH_4$ resulted in the rapid decay of the bands at 290 and 662 nm within 10 seconds, alongside the appearance of a new band at 260 nm pertaining to the formation of leuco methylene blue. The K_{app} for the reduction reaction could not be calculated due to the fast degradation of MB.

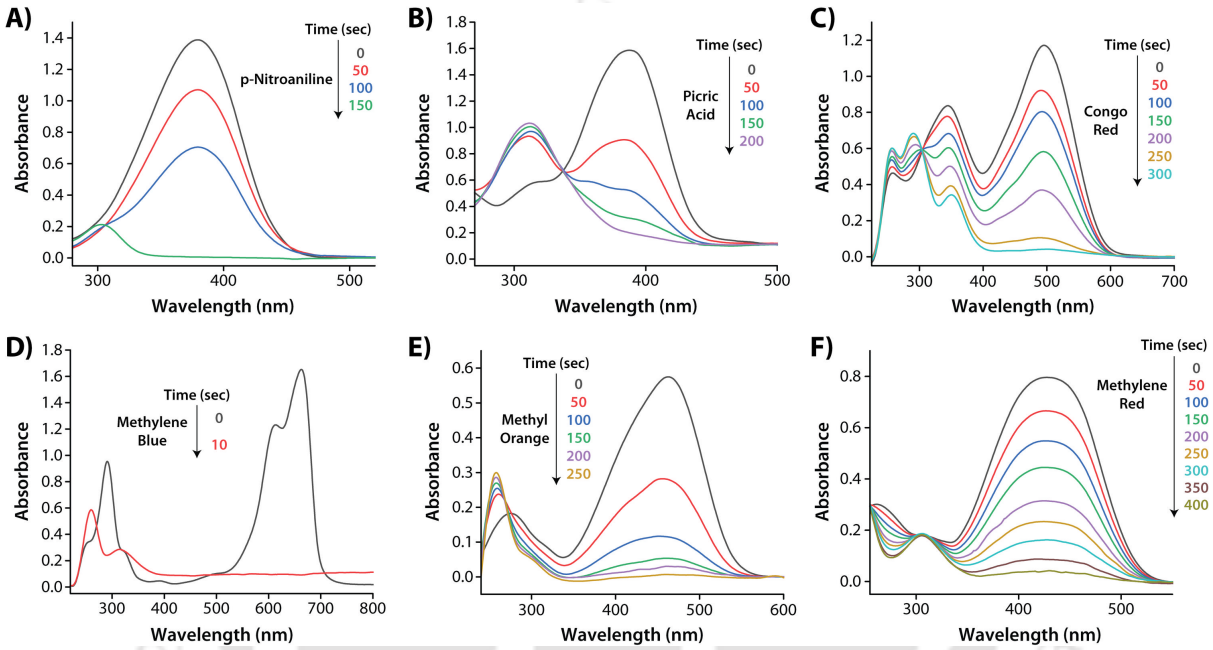

Figure 3.12 Time dependent UV-Visible spectra for the catalytic degradation of A) p-Nitroaniline, B) Picric acid, C) Congo red, D) Methylene blue, E) Methyl orange, and F) Methylene red.

Methyl orange (MO), in an alkaline solution of $NaBH_4$, exhibits a strong absorption peak at 462 nm due to the diazo functional group and a weak band at 275 nm (Figure 3.12E).[193] The catalytic degradation of MO by the AuNP@Bead resulted in the decrease of the absorption band at 462 nm over a period of 250 seconds, with the development of a new band at 258 nm, which can be attributed to the formation of the degradation product, 4-(Dimethylamino)aniline. The K_{app} for the degradation of MO was determined to be 0.01262 sec^{-1} based on the decline in absorption intensity at 462 nm (Figure 3.13D). Under alkaline conditions, methyl red (MR) has a distinct absorption band at 428 nm (Figure 3.12F).[215] The reduction of MR by the AuNP@Bead was ascertained by the decrease in absorption intensity at 428 nm and the emergence of a new band at 306 nm as a result of the generation of the amine degradation product. K_{app} for MR degradation was found to be 0.00362 sec^{-1} (Figure 3.13E). Control experiment using $NaBH_4$ alone revealed no substantial degradation of any of the dyes indicated above, demonstrating the crucial role of the AuNPs in the degradation process (Figure 3.13, Red Symbols).

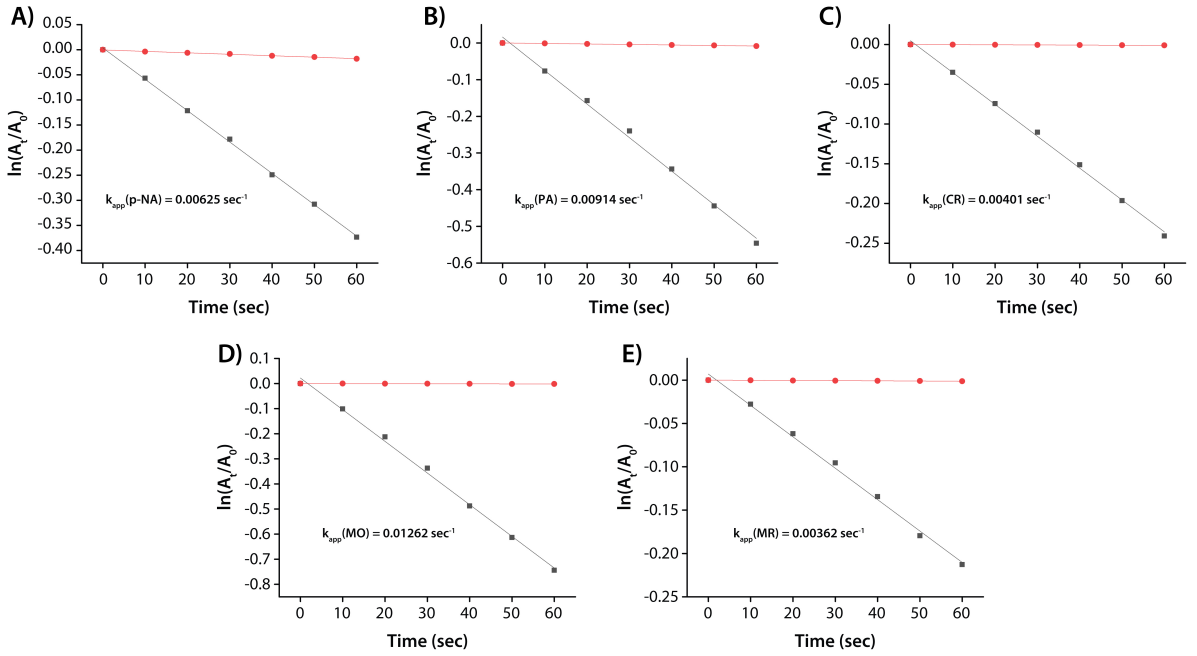

Figure 3.13 ln(A_0/A_t) plot for the catalytic degradation of A) *p*-NA, B) PA, C) CR, D) MO, and E) MR. [*p*-NA] = [PA] = 200 µM, [$NaBH_4$] = 20 mM; [CR] = [MO] = [MR] = 40 µM, [$NaBH_4$] = 4 mM.

3.2.8 Stability and reusability of embedded Gold nanoparticles

AuNPs have been extensively used over the years for catalysing different types of reactions. However, AuNPs can face limitations in terms of stability and reusability in catalytic applications as they are prone to agglomeration, especially under harsh reaction conditions or when exposed to certain solvents. In certain catalytic reactions, AuNPs can undergo leaching, where gold atoms are detached from the nanoparticles and enter the reaction medium. Both these processes lead to a decrease in the available active surface area, reducing catalytic activity. AuNPs often require specific support materials to maintain stability and optimize catalytic performance. However, not all support materials are suitable for embedding AuNPs. Thus, to test the ability of the BPEI coated core-shell beads to sustain the stability of AuNPs, different sets of experiments were performed.

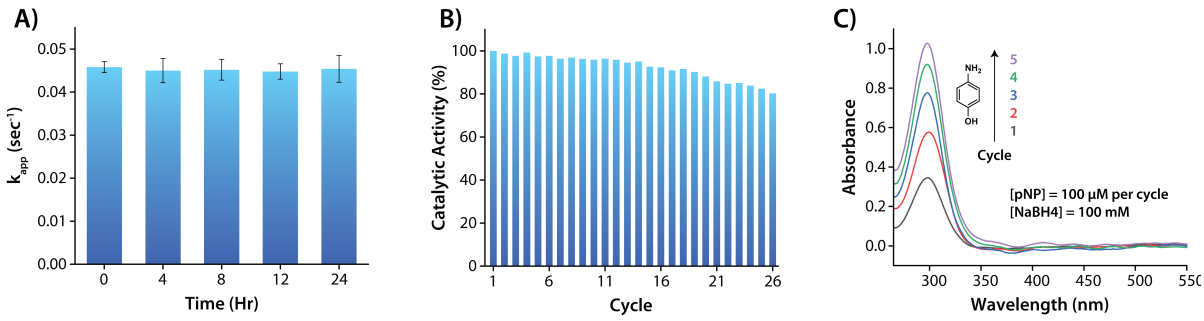

Figure 3.14 Stability and Reusability of the embedded AuNPs. A) Catalytic efficiency of AuNP@Beads at different time intervals of continuous agitation in water, B) Catalytic activity across multiple cycles of p-NP degradation, C) UV-Visible spectra for the complete degradation of five consecutive batches of p-NP in a single vessel. [p-NP] = 100 µM, [$NaBH_4$] = 20 mM and 100 mM for Fig. B and C, respectively.

First, the AuNP@Beads were continuously agitated in water for 24 hours, and their catalytic efficacy was determined every 4 hours (Figure 3.14A). The fact that the activity of the embedded AuNPs did not diminish significantly indicated that the nanoparticles are firmly retained and stabilised in the polymeric shell of the beads and sustain their catalytic activity even under severe conditions. This is corroborated by FESEM and EDX mapping analyses of the AuNP@Bead after catalytic cycles, which revealed uniform distribution of AuNPs on the bead's surface (Figure 3.15A-E). Atomic absorption spectroscopy of the supernatant solution after 24 hours showed that there was negligible gold leaching from the beads into the solution. Second, the catalytic efficiency of the embedded AuNPs was evaluated in 0.1 M KCl solution. A 0.1 M KCl solution is known to cause agglomeration of gold nanoparticles, resulting in complete loss of catalytic activity.[216, 217] However, AuNPs implanted on the bead surface showed no decrease in catalytic activity in 0.1 M KCl as compared to aqueous medium (Figure 3.15F). This is because the covalently immobilised BPEI polymeric layer maintains the colloidal stability of the gold nanoparticles by preventing aggregation of the uniformly dispersed gold nanoparticles on the bead surface, even in the presence of 0.1 M KCl. Finally, the catalytic beads are very simple to handle because they can be simply removed from the reaction vessel, washed with water, and reused in the next catalytic cycle with a fresh batch of reactants. It was observed that the catalytic beads displayed negligible loss of catalytic activity up to 10-12 cycles, and even after 26 cycles, retained ~80 % catalytic activity (Figure 3.14B). Also, in the presence of a large excess of $NaBH_4$, a single AuNP@Bead could completely reduce five successive batches of p-NP (100 µM per batch) in the same reaction vessel (Figure 3.14C). All these experiments highlight the excellent stability and reusability of the AuNP embedded beads which is economically advantageous and contributes to the sustainability of catalytic process.

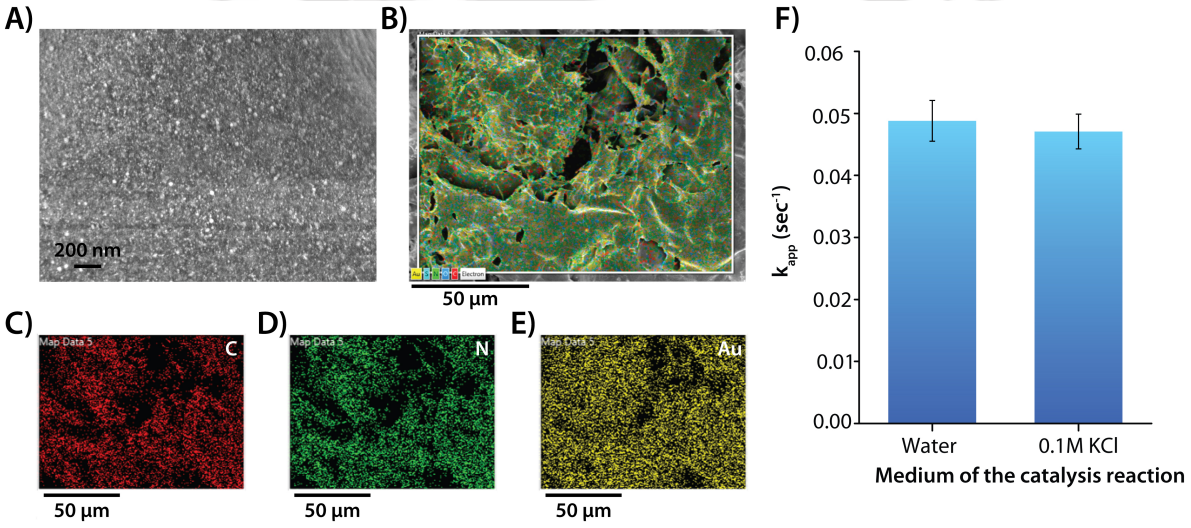

Figure 3.15 A) FESEM image of AuNP embedded surface of the core-shell bead after catalytic cycles, B-E) EDX elemental mapping of the surface of the AuNP embedded bead after catalytic cycles. F) Catalytic efficiency of the AuNP embedded beads in water and 0.1M KCl. [*p*-NP] = 100 µM, [$NaBH_4$] = 20 mM.

3.3 Conclusion

In summary, this chapter presents a comprehensive strategy for the surface engineering of peptide-based core-shell hydrogel beads, enabling diverse functional applications. By systematically modifying the bead surfaces, we achieved superhydrophobicity, enabled host–guest interactions using both guest and host moieties (viologen and β-cyclodextrin), and successfully immobilized biologically relevant macromolecules such as enzymes and proteins. These functionalized surfaces not only retained their structural integrity but also facilitated highly specific molecular interactions and catalytic processes. Notably, in situ synthesis of gold nanoparticles within the BPEI polymeric shell yielded catalytically active beads capable of efficiently reducing nitroaromatic compounds and azo dyes. These AuNP@Beads demonstrated excellent reusability, stability under harsh conditions, and negligible leaching, establishing their potential as sustainable heterogeneous catalysts for water remediation. Kinetic studies confirmed pseudo-first-order behavior and indicated that surface saturation and competitive adsorption govern the reaction mechanism, consistent with the Langmuir–Hinshelwood model. Overall, the modular design, multifunctionality, and robustness of these engineered hydrogel beads underscore their promise as versatile platforms for biocatalysis, molecular recognition, and environmental applications. The convergence of supramolecular chemistry, polymer science, and nanotechnology in this platform opens up new possibilities for the design of responsive, sustainable, and reusable soft materials suitable for real-world applications.

3.4 Experimental Section

3.4.1 Materials and Methods

Dipentaerythritol penta-/hexa-acrylate (5ACl), branched polyethylenimine (BPEI), 5(6)-carboxyfluorescein, 1-adamantylamine, rhodamine B, Rhodamine B Isothiocyanate, Bovine serum albumin (BSA), Hexadecyl amine, and Peroxidase from horseradish (HRP) were purchased from Sigma-Aldrich (USA). Methyl iodide and 2-bromoethylamine hydrobromide were purchased from Spectrochem. 4,4'-bipyridyl, p-toluenesulfonyl chloride and ß-Cyclodextrin were purchased from TCI. Cucurbit[8]uril (CB[8]) was synthesized following a previously published protocol and characterized accordingly.[218] Rink amide MBHA resin, protected amino acids and coupling reagents were purchased from Novabiochem. HPLC-grade dimethylformamide (DMF), dichloromethane (DCM) and acetonitrile (ACN) were procured from Spectrochem (India) and Fisher Scientific (India). Solvents were dried whenever required according to the reported procedures. Milli-Q water with a conductivity of less than 2 $mScm^{-1}$ was used for all sample preparations. 60-120 mesh silica gel (SRL) was used for column chromatography. Chromatographic purifications were performed on a Luna 5 mm (C18) column (Phenomenex) using a Dionex Ultimate 3000 HPLC. ^{1}H NMR and ^{13}C NMR spectra were recorded using a Bruker Ascend 600 MHz (Bruker, Coventry, UK) spectrometer and referenced to deuterated solvents. Coupling constants (J values) are reported in hertz, and chemical shifts are reported in parts per million (ppm). Multiplicities are reported as follows: s (singlet), d (doublet), t (triplet), m (multiplet), and br (broadened).

UV-Visible spectra were recorded on a PerkinElmer Lambda 365+ spectrophotometer, while fluorescence measurements were performed on a Fluoromax 4 Plus spectrophotometer. Bright-field and fluorescence microscopic images were obtained using a ZEISS Axio Vert.A1 inverted microscope with 10X objective. The particle sizes of the AuNPs were obtained at 298 K using a 632.8 nm He–Ne laser using Zetasizer Nano-ZS90 (Malvern). FESEM imaging and Energy Dispersive X-ray (EDX) mapping analysis of freeze-dried samples of different surface functionalised beads were performed on a Gemini SEM 300 (Sigma Zeiss) instrument. The FETEM analysis was performed in JEOL 2100F microscope. DLS analysis was performed at 298 K using a 632.8 nm He–Ne laser using Zetasizer Nano-ZS90 (Malvern). For UV-Visible, FETEM and DLS analysis of the embedded AuNPs, an ethanolic suspension of freeze-dried and ground (henceforth "cryo-ground") AuNP loaded beads was prepared in ethanol through sonication. FTIR spectra for freeze dried samples of different surface functionalised beads were obtained on a PerkinElmer instrument under ambient conditions. The Powder XRD analysis results of the freeze-dried samples were obtained from the Rigaku Smartlab X-ray Spectrophotometer with Cu-Kα (λ = 1.54 Å), source running at a power of 9 KW. The TGA analysis

was performed in Netzsch, STA449F3A00. Atomic Absorption Spectroscopy was performed using Varian AA240.

3.4.2 Synthesis Procedures

3.4.2.1 General synthesis of peptides: PyKC and (fluorescein)GGK (Pep-2)

The peptides were synthesized on Rink amide MBHA resin using standard Fmoc (9-fluorenylmethoxycarbonyl) solid phase peptide synthesis (SPPS) protocol. In a typical coupling, 3 equiv. of a protected amino acid (with respect to the loading of the resin), 3 equiv. of HBTU, and 6 equiv. of DIPEA were taken in 5 mL of DMF (for 0.1 mmol scale with respect to the resin loading) and stirred for 5 minutes prior to the addition of the mixture to the swelled and deprotected resin. The reaction mixture was shaken for 60 min, and the resin was washed several times with DMF. The Fmoc-deprotection was achieved by treatment of the resin three times with 5 ml of 20% piperidine in DMF for 5 minutes, followed by a thorough washing of the resin with DMF and DCM. The Fmoc-deprotection and coupling steps were repeated until the desired peptide sequence was obtained. The resin with the loaded peptide was washed several times with DMF and DCM and dried. The dried resin was then treated with a mixture of freshly prepared mixture of 8.5:1:0.5 (trifluoroacetic acid (TFA)/tetraethylsilane (TES)/H_2O) and stirred for 1 h. The resin was finally washed with DCM several times. The cleavage cocktail and the washings combined were concentrated to a minimum volume on a rotary evaporator. The cleaved peptide was then precipitated from cold dry ether, centrifuged and lyophilized to get the crude peptide. Purification was done in Dionex Ultimate 3000 HPLC using a Luna 5 μm (C18) column (Phenomenex) and using acetonitrile and water (containing 0.1% TFA each) as the mobile phase.

3.4.2.2 Synthesis of WGGGGK(Fluoroscein)G (Pep-1)

At first, Boc-WGGGGK(Mtt)G was synthesised on Rink amide MBHA resin using the aforementioned procedure. The peptide-loaded resin was then agitated for five minutes with a solution of 1% TFA and 0.2% TES in DCM to cleave the (Mtt) protecting group of the lysine side chain. The elimination of the Mtt group as methyltrityl cation was detected by a change in the colour of the solution to yellow. This deprotection procedure was repeated several times until a colourless solution was obtained, ensuring that the (-Mtt) group was completely removed. 5(6)-Carboxyfluorescein (1.5 eqv) was coupled to the free amine group of the lysine side chain via an amide coupling reaction using HBTU (1.5 eqv.) in the presence of DIPEA (3 eqv.). The peptide was then cleaved from the resin surface using the previously described procedure and purified using HPLC.

(Fluorescein)GGK (Pep-2): Yield: 78%. MALDI-TOF: m/z calculated for $C_{31}H_{33}N_5O_9$ [M]: 619.228, found 619.641; HPLC RT = 8.97 min (HPLC Program= 5% Acetonitrile/Water to 100% Acetonitrile in 20 minutes).

WGGGGK(fluorescein)G (Pep-1): Yield: 64%. MALDI-TOF: m/z calculated for $C_{48}H_{53}N_4O_3$ [M]: 976.372, found 976.311; HPLC RT = 19.55 min (HPLC Program= 5% Acetonitrile/Water to 100% Acetonitrile in 25 minutes).

3.4.2.3 Synthesis of 1- (2-aminoethyl)-1′-methyl-[4,4′-bipyriine]-1,1′-diium dihexfluoro-phosphate (C)

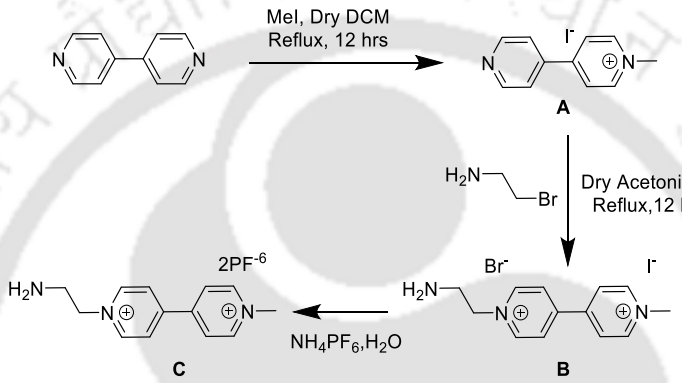

Scheme 3.2 Synthetic route for Viologen analogue used for surface functionalization.

Compound A[168]: Methyl Iodide (896.46 µL, 9.6 mmol, 1.5 eqv.) was added to a solution of 4 4'-bipyridyl (1 g, 6.4 mmol, 1 eqv.) in dry DCM and stirred overnight. The precipitate so obtained was washed with copious amounts of ether to give the product as a yellow solid. Yield =1.7362 g, 90%. ^{1}H NMR (600MHz, D_2O) δ (ppm) 8.86 (d, 2H), 8.72 (d, 2H), 8.34 (d, 2H), 7.86 (d, 1H), 4.40 (s, 3H).

Compound B[219] and C: Compound **A** (500 mg, 1.677 mmol, 1 eqv.) and 2-bromoethylamine hydrobromide (515 mg, 2.515 mmol, 1.5 eqv.) were dissolved in dry acetonitrile and refluxed overnight under an inert atmosphere. The resultant precipitate was filtered and washed multiple times with ether to give the product as an orange-coloured solid. Yield = 605 mg, 85%. The solid was then dissolved in minimum amount of water, and to that was added a saturated solution of ammonium hexafluorophosphate to get a white precipitate. The solid was then separated and washed several times with cold water to get compound **C**. ^{1}H NMR of **B** (600MHz, D_2O) δ (ppm) 9.27 (d, 2H), 9.10 (d, 2H) , 8.68 (d, 2H),8.58 (d, 2H), 5.16 (t, 2H), 4.54 (s, 3H), 3.84 (t, 2H). ESI-MS: m/z calculated for $[C_{13}H_{17}N_3I]^+$: 342.0462, found: 342.0561.

3.4.2.4 Synthesis of Mono-6-Deoxy-6-(p-Toluenesulfonyl)-β-Cyclodextrin[177]

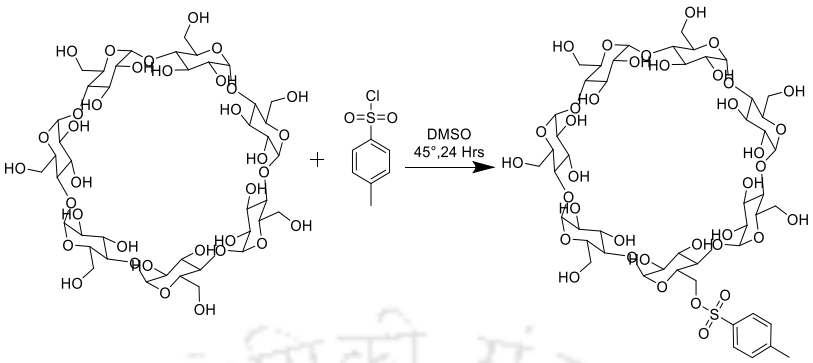

β-Cyclodextrin (1 g, 0.88 mmol, 1 equ.) was suspended in 3 mL DMSO, then p-toluenesulfonyl chloride (1.5 g, 7.86 mmol, 8.9 equ.) in 3 mL DMSO was added dropwise. The solution was stirred for 24 hours at 45 °C. After cooling the solution to room temperature, 30 mL of acetone was added dropwise. A white precipitate appeared quickly, which was filtered and washed three times with precooled acetone to yield the pure product. Yield = 800 mg, 70.5%. ^{1}H NMR (600 MHz, DMSO-d_6) δ (ppm) 7.76-7.72 (m, 2H), 7.44-7.40 (m, 2H), 5.81–5.61 (m, 14H), 4.84–4.74 (m, 7H), 4.52–4.43 (m, 6H), 4.35 (m, 2H), 4.20 (m, 1H), 3.70–3.3.34 (m, 25H), 3.40– 3.15 (m, H2, H4 overlap with water), 2.42 (s, 3H).

3.4.2.5 Synthesis of 2-((1r,3R,5S)-adamantan-1-yl)-3-((2E,4E)-5-(diethylamino)hexa-2,4-dien-2-yl)-3-(4-(diethylamino)phenyl)isoindolin-1-one (Ada-RhB)[220]

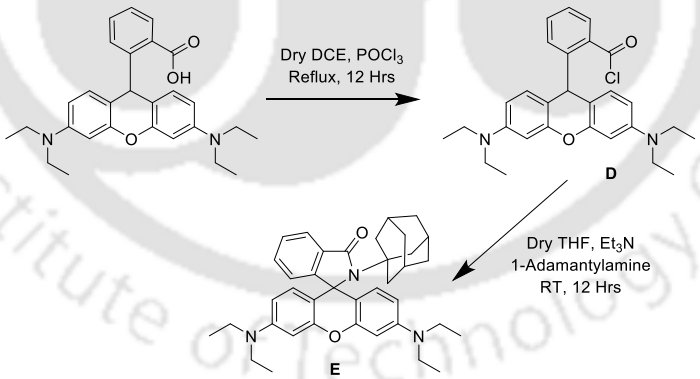

To a solution of rhodamine B (500 mg, 1.12 mmol) in dry 1,2-dichloroethane (10.0 ml) at room temperature, phosphorus oxychloride (0.522 mL) was added dropwise over a period of 5 min. After being refluxed for 12 h, the reaction mixture was cooled and concentrated under vacuum to give rhodamine B acid chloride. Without further purification, the resulting acid chloride was dissolved in dry THF (10 mL), and then was added dropwise to a solution of 1-adamantylamine (1.344 mmol) in dry THF (10 ml) containing triethylamine (0.22 mL). After stirring for 12 h at room temperature, the mixture was concentrated under vacuum and the crude product was purified by column chromatography (CH_2Cl_2) to give the product as a white solid. Yield= 412.5 mg, 72%. ^{1}H NMR

(600MHz, $CDCl_3$) 7.76 (dd, 1H), 7.33 – 7.27 (m, 2H), 6.80 (dd, 1H), 6.63 (d, 2H), 6.34 (d, 2H), 6.27 (dd, J = 8.9, 2.6 Hz, 2H), 3.34 (q, J = 7.1 Hz, 8H), 2.14 (s, 6H), 1.88 (s, 3H), 1.52 – 1.45 (m, 6H), 1.17 (t, 12H).

3.4.3 Rhodamine dye labelling of BSA[221]

BSA (30 mg) was dissolved in 10.0 mL of PBS buffer solution (50 mM, pH = 8.5), and 500 µL of aqueous Rhodamine B Isothiocyanate (RhBITC) solution (1.0 mg/mL) was added dropwise. The mixture was stirred in the dark at room temperature for 6 hours before being purified by dialysis for 24 hours to eliminate unreacted RhBITC. The resulting solution was then freeze-dried to produce a pink powder of BSA-RhB.

3.4.4 Preparation of superhydrophobic beads

For preparing superhydrophobic beads, 5ACl coated beads were agitated in 30 mg/mL solution of hexadecylamine ($C_{16}NH_2$) in ethanol for 3 hours and then washed with copious amounts of ethanol. Significant differences in the FESEM images of the parent 5ACl coated beads and the hydrophobic beads suggested successful surface modification (Figure 3.1A-B).

3.4.5 Immobilization of methyl viologen via Michael addition

5ACl coated beads (10 numbers) were immersed in a solution of MV^{2+} (130 mg MV^{2+} dissolved in 2 ml MeOH containing 200 µl H_2O) and were allowed to react at 50 °C with mild stirring for 48 hrs. Next, the beads were removed from the reaction medium and washed multiple times with MeOH until all the free, and loosely bound MV^{2+} molecules were removed (confirmed through UV). The amount of MV^{2+} immobilised on the bead surface was determined by correlating the absorption of MV^{2+} in the reaction medium before and after treatment with the beads. Quantification was done with the help of calibration curve obtained from solutions of MV^{2+} in the reaction medium. Moreover, FESEM images of the 5ACl-coated beads before and after MV^{2+} immobilisation displayed marked differences, indicating effective surface functionalisation.

3.4.6 CB[8] assisted host-guest ternary complexation on bead surface

To assess the formation of host-guest complex on the surface of the beads, two MV-functionalized beads were shaken with a 1:1 solution of CB[8] and tryptophan containing peptide WG_4K(Fluorescein)$GCONH_2$ (Pep1) of concentration 1 mM each for 10 minutes at room temperature. To prepare 2 mL of 1mM WG_4K(Fluorescein)$GCONH_2$@CB[8] stock solution, 3.5 mg of CB[8] (the overall molecular weight of the used CB[8] was found to be 1730 from the elemental analysis data) and 1.95 mg of peptide were accurately weighed into a 2 mL volumetric flask and 2 mL of pH 7, 20 mM phosphate buffer was added to it. The heterogeneous solution was then sonicated for 1 hour at 298 K. Two MV-functionalized beads were added to 1 ml solution of the

binary complex and subjected to mild shaking for a period of 1 hour. Decrease in the absorption intensity of the peptide in the solution after treatment with beads indicated the attachment of the peptide on the bead surface through host-guest complexation. A control experiment employing Pep1 with CB[8] and a bare 5-ACl coated bead (without MV^{2+}) revealed meagre change in the peptide's absorption intensity. Similarly, treatment of the MV-functionalized beads with CB[8] and the peptide (Fluorescein)GGKCONH$_2$ (Pep2), which lacks a tryptophan unit, resulted in a negligible change in peptide absorption intensity. Both results show that Pep1 attaches to the surface of the MV-functionalized beads via CB[8] assisted heteroternary complexation.

3.4.7 Immobilization of β-cyclodextrin on the bead surface

BPEI functionalised beads (10 numbers) were stirred in an aqueous solution of Mono-6-Deoxy-6-(p-Toluenesulfonyl)-β-Cyclodextrin (150 mg/ml) for 2 days at 50 °C. Thereafter, the beads were separated from the reaction medium and thoroughly washed with water. Change in the surface features of the BPEI-coated beads after reaction with β-Cyclodextrin indicated effective immobilisation.

3.4.8 Cyclodextrin assisted host-guest complexation on bead surface

3 β-cyclodextrin functionalised beads were subjected to mild shaking over a shaker plate in a 250 µM solution of RhB-Ada in water for 30 minutes. The attachment of RhB-Ada on the bead surface was confirmed from UV spectra collected at different time intervals of the immobilization reaction.

3.4.9 Immobilization of HRP on bead surface

HRP immobilization via amide coupling was performed following a previously reported protocol.[222] Two aqueous solutions, containing 15 mg/mL each of EDC.HCl and NHS were prepared separately. 1.4 ml of each solution was taken together, and BPEI-coated beads were added to the solution under continuous shaking. Next, HRP (1.7 mg/mL final concentration) was added to the solution and stirred for 4 hours at room temperature. The beads were then thoroughly washed with water to remove free and loosely bound enzymes.

To determine the amount of HRP immobilised on the bead surface, the peroxidase activity of HRP in the solution before and after treatment with the BPEI-functionalised beads was assessed spectrophotometrically by monitoring the oxidation of pyrogallol to purpurogallin in the presence of H_2O_2. Briefly, 200 µM pyrogallol (2 µL of 1mM stock in ACN) was taken in 1 mL phosphate buffer (20 mM, pH 7.4) in a quartz cuvette of 1 cm path length. To this solution, 1 µL of 10000 times diluted solution of HRP (before as well as after immobilisation on beads) was added. The reaction was then initiated by the addition of 2 mM H_2O_2 (1 µL of 2 M stock in H_2O). The change in absorbance

corresponding to the chromogenic product, purpurogallin was monitored at λ_{max} = 420 nm (ε_{420nm} = 2640 $M^{-1}.cm^{-1}$ in water) over a period of 5 minutes. The difference in the activity of the HRP solution before and after HRP immobilisation gives information about the amount of enzyme immobilised. To quantify the amount of HRP immobilised, a calibration curve was prepared by measuring the activity of varying concentrations of free HRP enzyme for the above-mentioned concentrations of the substrates. The amount of HRP immobilised was found to be 162.89 µg per bead. All the experiments were performed in triplicate. To assess the catalytic activity and reusability of the HRP-functionalised beads, the conversion of pyrogallol to purpurogallin was monitored using the above-mentioned protocol using HRP-coated bead instead of free HRP enzyme . After each catalytic cycle, the beads were washed and the catalysis experiment was repeated with fresh substrates. The cycles could be repeated 10 times without any significant loss of activity. The immobilisation of HRP on the bead surface was also evident from the change in the surface features of the HRP-functionalised beads compared to the unfunctionalized BPEI-coated beads (Figure 3.4). Furthermore, EDX mapping showed the presence of Fe on the bead surface, substantiating the attachment of HRP on the bead surface.

3.4.10 Immobilization of BSA on bead surface

BPEI-coated beads (10 numbers) were immersed in a 5 wt% glutaraldehyde solution (20 mM phosphate buffer pH 7.4) for 4 h.[223] The beads were then washed with a copious amount of water to remove unreacted glutaraldehyde and subsequently agitated in an aqueous solution of BSA-RhB (11 mg/mL) for 4 h for further functionalisation. Finally, the beads were again washed with water to remove the free enzyme. The amount of BSA-RhB immobilised on the bead surface was determined by comparing the absorbance of BSA-RhB in the reaction medium before and after treatment with the beads and quantification was done with the help of a calibration curve of BSA-RhB in water. Optical as well as FESEM images of the BPEI-coated beads before and after BSA-RhB immobilisation displayed marked differences, indicating effective surface functionalisation.

3.4.11 Fabrication of AuNP@Beads

AuNP@Beads were prepared under thermal condition as well as room temperature. Briefly, 15 BPEI functionalised beads were continuously agitated in 1ml aqueous solution of $HAuCl_4$ (100 mM) solution, either for 3 hours at 90 °C, or for 7 days at room temperature. The resultant AuNP@Beads were extensively rinsed with water to remove unreacted and loosely attached nanoparticles. The resulting AuNP@Beads were stored at 4°C before use. The formation of AuNPs in the BPEI polymeric shell was confirmed by various experiments such as UV-Visible, DLS and FETEM analyses.

3.4.12 Fabrication of BPEI stabilised free AuNPs

In a round bottom flask, aqueous solutions of $HAuCl_4$ (2 mM, 714 μL) and BPEI (0.2 mM, 10 mL) were mixed together and stirred at 85 °C. After 30 minutes, the solution turned wine red, and it was allowed to gradually cool to room temperature. To remove free BPEI from the solution, the AuNP suspension was centrifuged, the supernatant was removed and the AuNPs were resuspended in water. The process was repeated multiple times to remove impurities, and the purified AuNP suspension was stored at 4 °C for further use.

Chapter 4

In-Situ Fabricated Gold Nanostars on Hydrogel Beads as Photo-Oxidase Mimic for Rapid and Sustainable POCT of Uric Acid

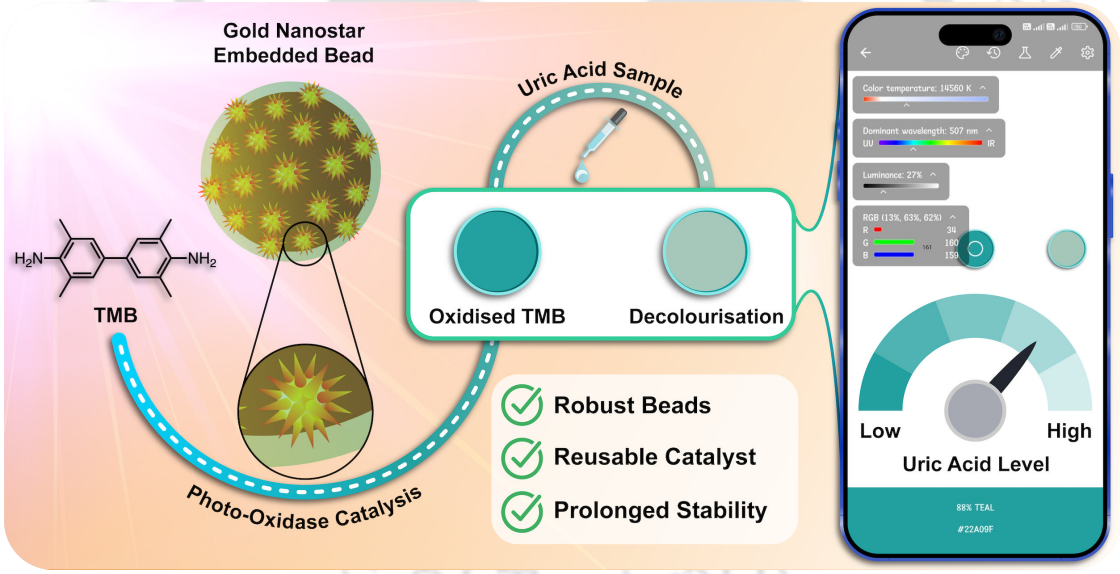

Indian Institute of Technology Guwahati

4.1 Introduction

Enzymes, the biological catalysts responsible for driving countless reactions in living organisms, are remarkable for their high specificity and efficiency. However, their sensitivity to environmental factors such as temperature and pH, coupled with their high cost and limited stability, restricts their use in industrial and biomedical applications.[224] These limitations have fueled the development of synthetic enzyme mimics- engineered molecules and nanostructures designed to replicate the function of natural enzymes without their inherent drawbacks. Synthetic enzymes provide key advantages such as enhanced stability in harsh conditions, ease of modification, and reduced production costs, making them highly appealing for various applications, from biosensing and drug development to catalysis in chemical industries.[225] The most common types of enzyme mimics include small organic molecules,[226, 227] peptides,[169, 179, 183] and metal-based catalysts.[228, 229] Among these, metal-based enzyme mimics, particularly nanostructures of transition metals like palladium (Pd), platinum (Pt) and gold (Au), have garnered significant attention due to their ability to catalyze critical reactions such as hydrogenation and oxidation, which are essential for biosensing and synthetic processes.[230, 231] Gold-based enzyme mimics are lucrative due to their diverse enzyme-like activities, including peroxidase, catalase, superoxide dismutase, and glucose oxidase.[232-234] The catalytic properties of gold nanomaterials are highly dependent on their size, shape, and surface functionalization. Smaller nanoparticles offer higher catalytic efficiency due to their greater surface area, while different shapes affect specific enzyme-mimetic activities.[235, 236] Additionally, surface functionalization with organic ligands or biomolecules can significantly improve their stability, selectivity, and interaction with target substrates.[237] These tunable properties make gold nanomaterials promising for biosensing, drug delivery, environmental monitoring, and catalysis.[238-241]

Metal-based enzyme mimics offer several advantages over small organic molecules and peptide-based mimics, particularly in terms of stability, catalytic versatility, and robustness. However, a major challenge is their tendency to deactivate due to agglomeration. A practical solution to this issue is the immobilization of metal-based nanocatalysts on heterogeneous support materials. Building on our previous work with in-situ synthesis of catalytic gold nanoparticles on hydrogel beads, and recognizing the superior enzyme-mimetic properties of gold nanostars (AuNS) due to their unique structural and optical features, we investigated the in-situ fabrication of AuNS on hydrogel beads coated with branched polyethyleneimine (BPEI).[58, 242-244] The BPEI-stabilized AuNS demonstrated remarkable photo-oxidase-like activity, attributed to their localized surface plasmon resonance (LSPR). This LSPR, originating from the branched structure of the nanostars, enhances light absorption and enables photo-induced catalytic reactions.[242, 243] While gold nanoclusters (AuNCs)

functionalized with bovine serum albumin,[245-247] horseradish peroxidase (HRP),[248] and cysteine[249] have previously been shown to exhibit photo-oxidase mimetic activity, this study represents the first report of AuNS displaying such activity. Furthermore, the hydrogel macro-beads serve as a heterogeneous support that not only stabilizes the nanostars and maintains their catalytic properties but also facilitates their reuse.[49, 250-252]

The unique photo-oxidase activity of gold nanostars was harnessed for the detection and quantification of uric acid, a metabolic byproduct of purine degradation.[253] Purines are metabolized in the liver, with the resulting uric acid typically excreted by the kidneys to maintain a healthy balance. Optimal uric acid levels (3.5-7.2 mg/dL for males and 2.6-6 mg/dL for females) are vital, as uric acid plays both protective and harmful roles in the body. It acts as an antioxidant, shielding cells from oxidative stress,[254, 255] but elevated levels, known as hyperuricemia, can lead to conditions such as gout, cardiovascular diseases, hypertension, and type 2 diabetes.[256, 257] Therefore, it is essential to monitor and manage uric acid levels to prevent associated health risks. Traditional detection methods, such as high-performance liquid chromatography (HPLC),[258, 259] electrochemical analysis,[260, 261] chemiluminescence,[262, 263] fluorescence analysis,[264-267] and colorimetric analysis,[268-270] offer high selectivity and sensitivity. However, their practical use is often limited by expensive reagents, complex instruments, and the need for skilled operators, restricting their accessibility outside laboratory settings. In contrast, colorimetric sensing techniques are well-suited for point-of-care testing (POCT) due to their simplicity, ease of use, and ability to provide quick visual results. They are also cost-effective, requiring minimal equipment, making them more adaptable for a wide range of healthcare applications.

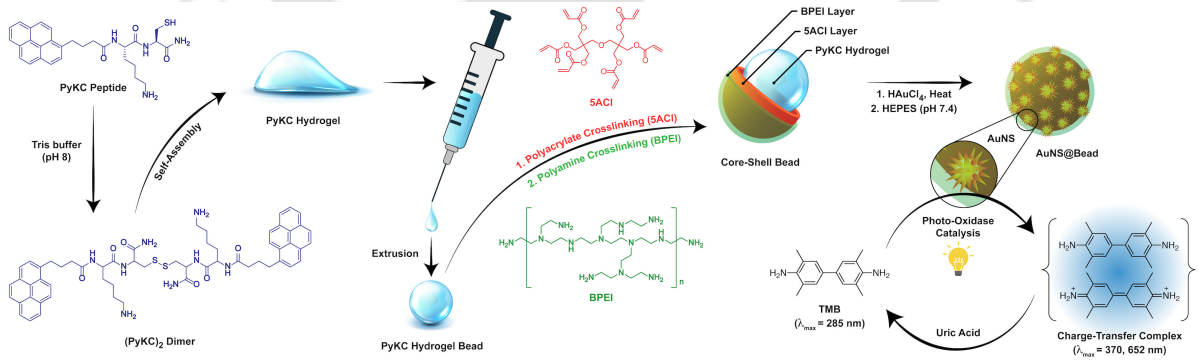

Scheme 4.1 Graphical representation for fabrication of peptide-based core–shell hydrogel beads, and in situ formation of AuNS on the bead surface for uric acid detection via photo-oxidase catalysis.

Colorimetric uric acid sensing commonly employs two primary strategies. The first involves a uricase-peroxidase cascade reaction, where uricase catalyzes the conversion of uric acid into hydrogen peroxide (H_2O_2), which then serves as a substrate for peroxidase to oxidize 3,3',5,5'-

tetramethylbenzidine (TMB) into a colored oxidized-TMB complex. This enables the quantification of uric acid.[271-273] The second strategy involves the oxidation of TMB by a peroxidase enzyme, followed by decolorization upon interaction with uric acid. The degree of decolorization serves as an indirect measure of the uric acid concentration.[274-279] While both approaches are effective, they have limitations, including the poor stability of the enzymes, susceptibility to interference from other biological substances, and the need for strict control of H_2O_2 levels. A more advantageous approach for uric acid detection is using the bead-immobilized photo-oxidase mimetic gold nanostars to directly oxidize TMB, eliminating the need for H_2O_2. This not only streamlines the sensing process but also improves specificity and minimizes potential interference. The sensing mechanism involves the oxidation of the chromogenic substrate TMB by the embedded gold nanostars, followed by reduction of oxidized TMB upon interaction with uric acid, leading to a visible color change. By comparing the color of the TMB solution before and after adding a uric acid sample, it is possible to accurately quantify the uric acid content. Furthermore, since the beads can be reused, this method lowers expenses while enhancing sustainability. Thus, the integration of macro-beads with oxidase-mimetic AuNS presents a robust strategy for reliable and reusable uric acid detection. This approach has also been successfully utilized in smartphone-based POCT of uric acid in blood serum and urine samples.

4.2 Results and Discussion

4.2.1 In-situ fabrication of AuNS on the bead surface

Gold nanostars demonstrate exceptional catalytic performance due to their distinctive structural features.[280] The highly branched morphology results in an augmented surface area, providing numerous active sites for catalysis. The distinctive branched structure of gold nanostars plays a role in generating localized surface plasmon resonance (LSPR), which improves their interaction with light and facilitates photo-catalysis.[281] To harness the catalytic prowess of gold nanostars while ensuring their prolonged stability and reusability, the fabrication of gold nanostars was achieved on the surface of BPEI-coated hydrogel bead (Scheme 4.1). The peptide-based (Pyrene-Lys-Cys, PyKC)[114, 129-131] core-shell hydrogel beads were fabricated through a simple extrusion technique and subsequently coated with a bilayer of dipentaerythritol penta-/Hexa-acrylate (5ACl) and branched polyethylene imine (BPEI) as previously reported by us.[58] Functionalization of the bead surface with 5ACl followed by BPEI was ascertained through FTIR spectroscopy of the freeze-dried beads after subsequent functionalization steps (Figure 4.1A). Change in the surface morphology of the beads after 5ACl and BPEI attachment, as seen by Field Emission Scanning Electron Microscopy (FESEM) (Figure 4.1B-D), further affirmed the effective surface functionalization of the hydrogel beads. The

sequential attachment of 5ACl and BPEI on the bead surface, thus, resulted in a core-shell configuration with the BPEI polymer exposed to the outer surface.

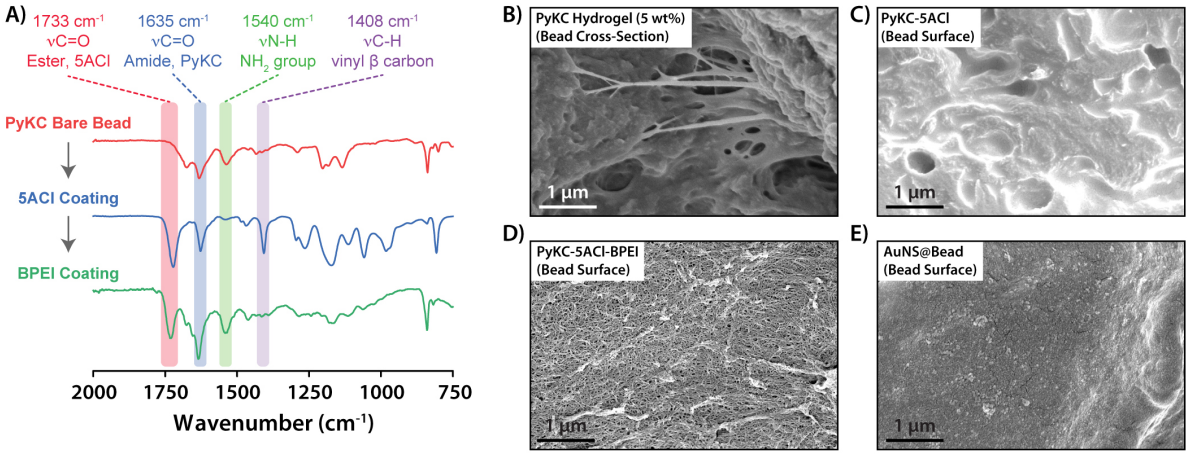

Figure 4.1 A) FTIR spectra of the beads after each successive surface modification step, B-D) FESEM images of the bead surface after each successive surface modification step, and E) FESEM image of AuNS embedded surface of the core-shell bead.

BPEI has a mild reducing nature due to the dense arrangement of primary, secondary, and tertiary amine groups along the polymer backbone.[58] Thus, BPEI exhibits the capability to simultaneously reduce Au(III) to Au(0) and stabilize the produced gold nanoparticles seamlessly in a one-pot setup. In this work, the AuNS were fabricated on the surface of the beads through a two-step process. Initially, BPEI-coated beads of *ca.* 2 mm size were introduced into a solution containing $HAuCl_4$ (100 mM) and heated briefly with continuous stirring. This led to the formation of tiny BPEI-stabilized gold nanoparticles (referred to as gold nanoseeds) on the surface of the beads. Subsequently, HEPES buffer was employed in the second step as a shape-directing agent to induce the growth of branches on the nanoseeds.[282] The in-situ synthesis and immobilization of AuNS on the bead surface was evidenced by a change in the color of the solution from light yellow to greenish-blue and the color of the beads from light brown to dark brown (Figure 4.2A). After thorough rinsing to eliminate excess reagents and stabilizers, the resulting gold nanostar-loaded beads (AuNS@Bead) were stored at 4 °C for further use.

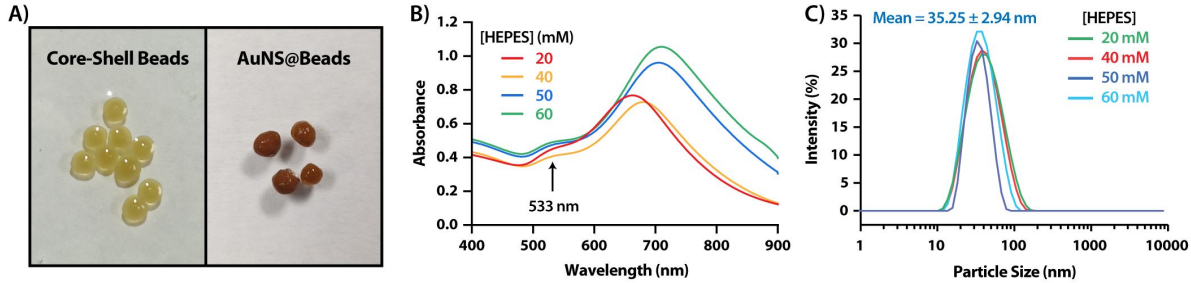

Figure 4.2 In-situ synthesis of gold nanostars. A) Images of the core-shell beads before and after in-situ fabrication of AuNS, B) UV-Visible spectra for AuNS synthesized using varying concentrations of HEPES buffer, and C) Representative plot of the DLS profile of the in-situ synthesized AuNSs.

To assess the impact of HEPES on the extent of anisotropic growth of the AuNS, the in-situ synthesis of AuNS on bead surfaces was conducted by systematically varying the HEPES concentration while keeping the $HAuCl_4$ concentration constant (100 mM). UV–Visible and Dynamic Light Scattering (DLS) analyses of an ethanolic suspension of the cryo-ground AuNS@Beads were then performed to get a preliminary insight into the morphology of AuNS. Two distinct plasmon bands were observed, including a high-frequency band at 533 nm associated with the inner core and a low-frequency band indicative of individual tips of the nanostars (Figure 4.2B).[283] Notably, a red shift in the lower-energy plasmon band suggested an increase in tip length with increasing HEPES concentration.[283] Despite this variation in tip length, DLS measurements indicated identical overall sizes of ~ 35 nm for the nanostars (Figure 4.2C). Considering the potential association of longer nanostar tips with enhanced photo-catalytic properties, unless otherwise stated, 50 mM HEPES buffer was used for the fabrication of AuNS@Beads for all subsequent experiments.

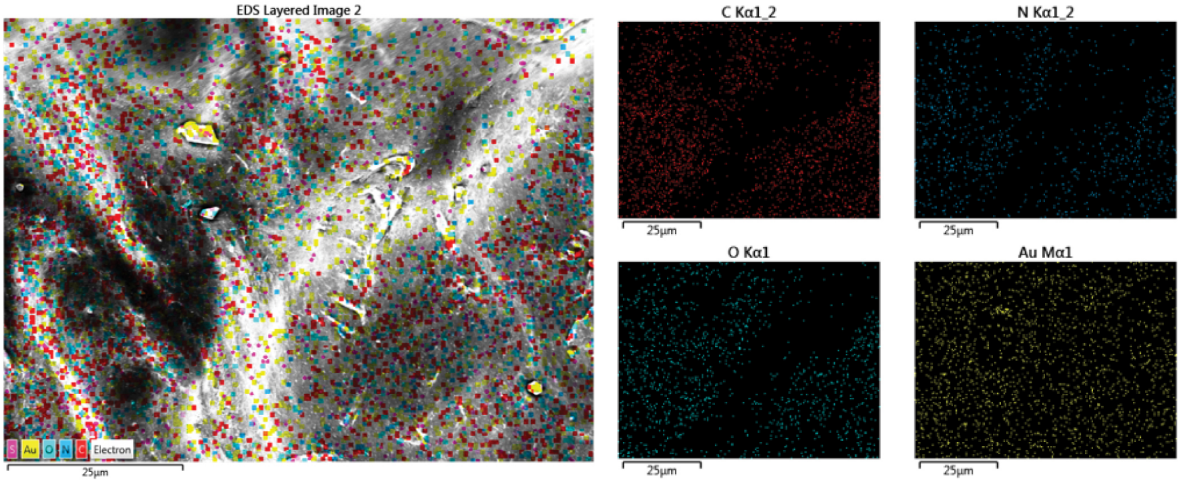

Figure 4.3 EDX elemental mapping of the surface of the AuNS embedded bead.

The formation of gold nanostars on the surface of beads was substantiated through a comprehensive analysis. The distribution of gold nanostars (AuNSs) on the core-shell beads was determined using FESEM and Energy-Dispersive X-ray (EDX) analyses. The FESEM images of the BPEI-coated unfunctionalized beads revealed a fibrous surface morphology (Figure 4.1D and 4.3). However, following the in-situ fabrication of gold nanostars, a noticeable transformation in the surface morphology was observed (Figure 4.1E). This alteration is likely attributable to the robust interaction between the positively-charged BPEI polymers on the bead surface and the negatively-charged immobilized gold nanostars.[58] Complementing this observation, EDX mapping analysis demonstrated a uniform distribution of gold throughout the bead surface (Figure 4.3). This indicated the successful in situ fabrication of gold nanostars on the bead surface. Transmission Electron Microscopy (TEM) images of the cryo-ground AuNS@Beads revealed distinct star-shaped

configurations with well-defined branches, confirming the successful formation of AuNS (Figure 4.4A). The size distribution of the AuNS, as determined by TEM analysis, closely aligns with the size calculated through DLS analysis and was found to be ~30 nm (measured from tip to tip across the nanostar) (Figure 4.4B).

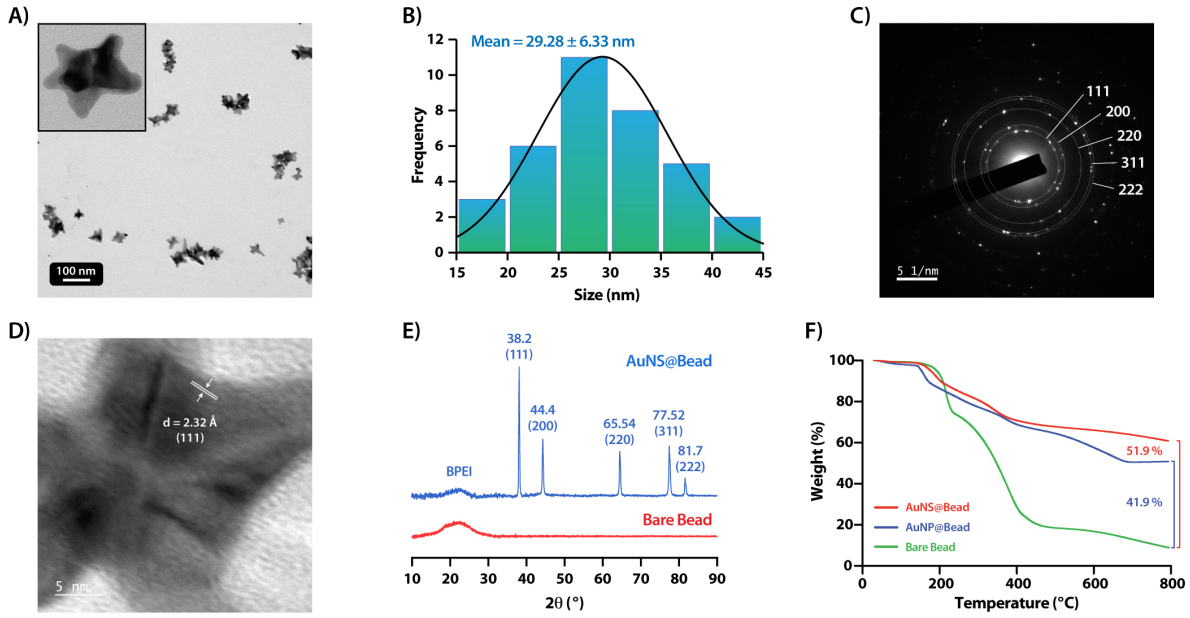

Figure 4.4 In-situ synthesis of gold nanostars. A) FETEM image, B) Size distribution histogram, C) SAED pattern, and D) HRTEM image of the in-situ synthesized AuNS, E) XRD spectrum of the bare and AuNS-embedded core shell beads, F) TGA profiles of the bare, AuNS-embedded, and AuNP-embedded core shell beads.

Selected Area Electron Diffraction (SAED) patterns revealed the polycrystalline nature of the nanostars, displaying characteristic d- spacings of 2.35, 2.03, 1.42, 1.23 and 1.17 Å, corresponding to the (111), (200), (220), (311) and (222) reflections, respectively of the face-centered cubic (FCC) structure of gold (Figure 4.4C) (JCPDS card No. 04–0784).[195] Moreover, the HRTEM image revealed the existence of a (111) plane featuring an inter-planar distance of 2.37 Å, thus verifying the creation of fcc gold nanostars (Figure 4.4D).[196] X-ray Diffraction (XRD) analysis further corroborated the face-centered-cubic (FCC) crystalline nature of the nanostars, with diffraction peaks at 38.2°, 44.4°, 65.54°, 77.52°, and 81.7° aligning with the expected lattice planes (111), (200), (220), (311) and (222), respectively (Figure 4.4E).[284] Furthermore, the thermal stability and loading efficiency of the AuNS and AuNP (characterized through FETEM and UV-Visible spectrophotometry, Figure 4.5A-B) on the surface of the beads were compared using Thermogravimetric Analysis (TGA) (Figure 4.4F). The desorption of moisture and trapped gases resulted in a negligible mass loss up to a temperature of 150 °C. After that, the bare and AuNS/AuNP loaded beads displayed an overall mass loss of 91.1 %, 39.2 %, and 49.2 %, respectively. This mass loss may be attributed to the thermal breakdown of the bead's organic components. This also showed that the nanoparticles made up about 42% of the

dried bead mass, while the nanostars accounted for a substantial 52% of the dried bead weight. The greater degree of AuNS immobilization on the bead surface could be attributed to stronger interactions between the BPEI polymer and the asymmetrically structured AuNS.

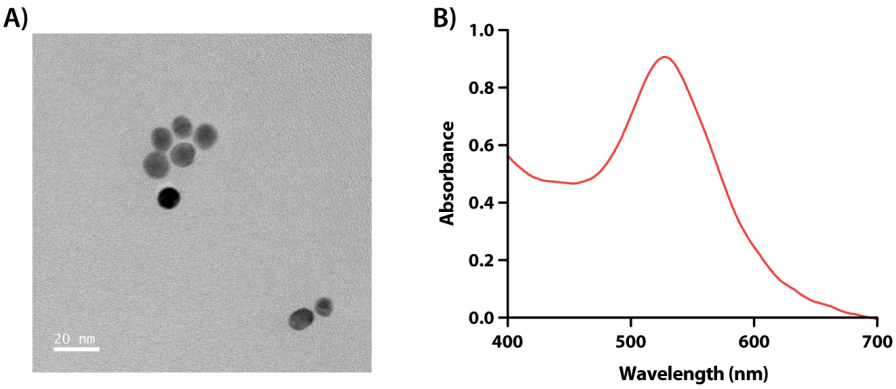

Figure 4.5 A) FETEM image, and B) UV-Visible spectrum of cryo-ground ethanolic suspension of AuNP@Beads.

4.2.2 Photo-oxidase like activity of the AuNS

To assess the catalytic activity of gold nanostars embedded on the bead surface, the oxidation of the chromogenic substrate TMB was systematically analyzed. Remarkably, under visible light irradiation at pH 7, the gold nanostar-embedded beads exhibited the ability to oxidize TMB even in the absence of hydrogen peroxide (H_2O_2), as evidenced by the time-dependent UV-Visible spectra (Figure 4.6A). The spectra revealed a progressive increase in the absorbance band at 652 nm, indicative of TMB oxidation. This observation signified the manifestation of photocatalytic oxidase like activity by the gold nanostars. Notably, the oxidase like activity of the gold nanostars displayed a pH-dependent behavior, with a pronounced catalytic efficacy observed in the pH range of 3 to 6 (Figure 4.6B). In stark contrast, both the unfunctionalized beads and the gold nanoparticle-embedded beads exhibited negligible catalytic activity across the entire pH spectrum. The limited photocatalytic performance of gold nanoparticles, as opposed to the gold nanostars, is likely due to the higher band gap energy of the gold nanoparticles (2.12 eV) compared to the gold nanostars (1.52 eV) (Figure 4.6C-D). The lower band gap of the gold nanostars makes them particularly effective for photocatalysis under visible light, emphasizing their unique and superior photocatalytic properties. The light-induced oxidase-like activity was further substantiated by Michaelis-Menten kinetics analysis, which revealed that the embedded AuNS had negligible catalytic activity in the absence of light (V_{max} = 1.1×10^{-5} mMs^{-1}, K_m = 3.125 mM, Figure 4.7A) but a significant increase in catalytic efficiency was observed in the presence of light (V_{max} = 11.3×10^{-5} mMs^{-1}, K_m = 1.768 mM). Additionally, the catalytic affinity of gold nanostars towards a diverse range of substrates was explored using ortho-phenylenediamine (OPD) and 2,2'-azino-bis(3-

ethylbenzothiazoline-6-sulfonic acid) (ABTS) as chromogenic substrates (Figure 4.6E-F) . As anticipated, both substrates were efficiently oxidized to their colored forms in the presence of light, affirming the broad catalytic potential of the gold nanostars.

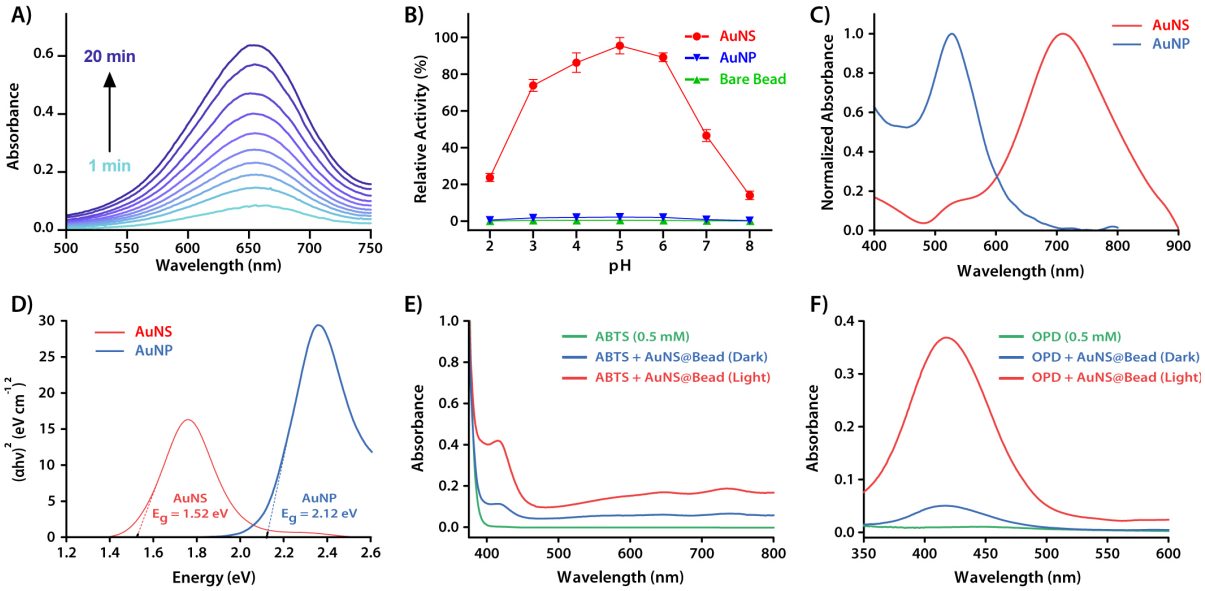

Figure 4.6 Catalytic activity of the embedded AuNS A) Time-dependent UV–Visible spectrum for the photo-oxidation of TMB (0.5 mM) by the AuNS@Bead in pH 7 buffer, B) Comparison of pH dependent catalytic of the AuNS-embedded, AuNP-embedded and bare hydrogel beads, C) Normalized UV-Visible spectra, and D) Tauc's plot for the band gap energy of the AuNS and AuNP; UV-Visible spectra showing light-activated photo-oxidation of E) ABTS, and F) OPD, by the AuNS@Beads.

Gold nanostars are recognized for their capacity to generate reactive oxygen species (ROS) under light irradiation, a phenomenon crucial for their oxidase-like activity.[285] In efforts to elucidate the catalytic mechanism of AuNS, a scavenger assay was conducted to identify the specific ROS responsible for the catalysis (Fig. 4.7B). When AuNS-embedded beads were incubated with various ROS scavengers and then treated with TMB, significant decreases in TMB absorbance were observed with the scavengers for singlet oxygen (NaN_3,[286] and histidine[287]), superoxide radicals (BQ i.e. p-benzoquinone[288]), and photogenerated holes (KI[289] and EDTA[290]). However, hydroxyl radical scavengers, Isopropyl alcohol (IPA)[291] and tert-Butyl alcohol (t-BuOH),[292] had no effect on TMB absorbance. This indicates that singlet oxygen, superoxide radicals, and photogenerated holes are the active species in the oxidation reaction. To better understand the oxidase-like catalysis mechanism, additional assays were conducted using the hydroxyl radical probe, terephthalic acid (TA) and the singlet oxygen probe, 3,3′-diaminobenzidine (DAB). TA reacts with hydroxyl radicals to produce 2-hydroxy terephthalic acid, which has a characteristic fluorescence peak at 435 nm.[279] The absence of a noticeable emission band at 435 nm when AuNS@Beads were treated with TA and H_2O_2 under light irradiation suggested that AuNS do not have peroxidase-like activity (Figure 4.7C).

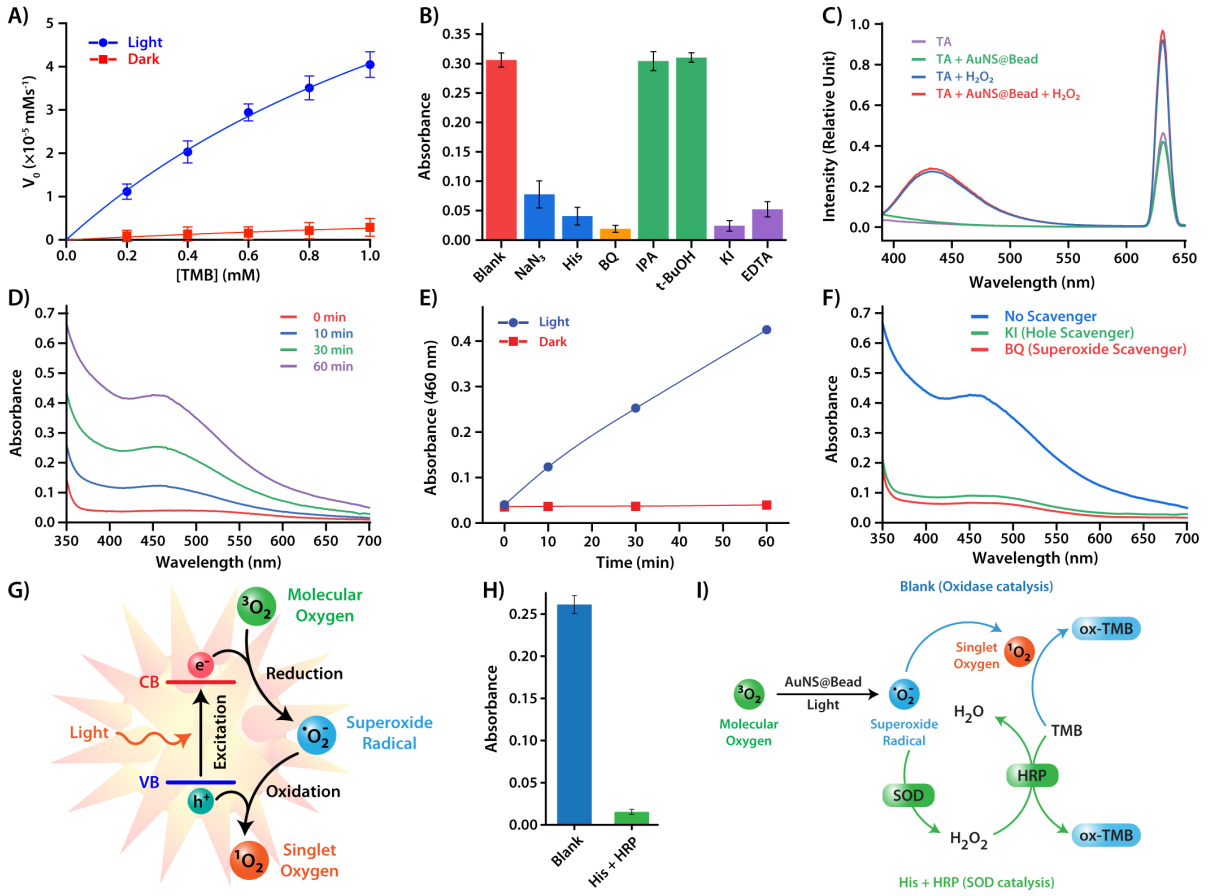

Figure 4.7 A) Michaelis-Menten kinetics of the AuNS@Bead catalyzed oxidation reaction under visible light irradiation and in dark, B) Effect of scavengers on the photo-oxidation of TMB by the AuNS@Bead, C) Fluorescence spectra of the TA assay for detecting hydroxyl radicals, D) UV-Visible spectra of the DAB assay for detecting singlet oxygen, and E) Comparison of the DAB assay under light and dark conditions, F) DAB absorption spectra for detecting AuNS@Bead-catalyzed singlet oxygen generation in the presence of KI (positive holes scavenger), BQ (superoxide radicals scavenger), and in the absence of any scavenger, G) Proposed mechanism for the photo-oxidase activity of the AuNS, H) Comparison of absorbance intensity of oxidized-TMB charge-transfer complex at 652 nm upon oxidation of TMB through photo-oxidase catalysis (Blank) and peroxidase catalysis by HRP using H_2O_2 generated via SOD catalysis (His + HRP), and I) Schematics showing the oxidation of TMB via oxidase catalysis, and SOD catalysis.

DAB oxidizes in the presence of singlet oxygen, resulting in a characteristic absorption band centered at 460 nm.[246] When DAB was treated with AuNS@Beads under light irradiation, there was a significant increase in absorbance at 460 nm, whereas no such increase was observed in the dark (Figure 4.7D-E). This confirmed that AuNS exhibit light-activated oxidase-mimetic behavior. Furthermore, DAB demonstrated negligible oxidation and weak absorption bands when photo-oxidation was carried out in the presence of KI or BQ, suggesting that both photogenerated holes and superoxide radicals are required for the generation of singlet oxygen (Figure 4.7F). Thus, the probable mechanism of photo-oxidase catalysis in gold nanostars involves light-induced excitation of electrons from the valence band to the conduction band, resulting in the formation of positive holes (Figure 4.7G).[293] The high energy electrons in the conduction band then oxidize the adsorbed

molecular oxygen, generating superoxide radicals. The superoxide radicals then interact with the highly reactive holes and undergo reduction to form singlet oxygen. This rationale underscores the active role of light, positive holes, and superoxide radicals in producing singlet oxygen, which drives the photo-oxidase activity of the AuNS. Since superoxide radicals are generated during photocatalysis, the AuNS were also tested for superoxide dismutase (SOD) mimetic activity. To evaluate this, the oxidation of TMB by AuNS@Bead under light irradiation was tested in the presence of histidine and HRP (Figure 4.7H-I). Histidine acts as a singlet oxygen scavenger, preventing TMB oxidation by singlet oxygen, while HRP was included to utilize any H_2O_2 generated through SOD catalysis to oxidize TMB and produce a colorimetric response. The absence of blue coloration indicated that the AuNS do not exhibit SOD-mimetic activity, and exclusively display photo-oxidase activity.

4.2.3 Colorimetric detection of uric acid

In this study, the inherent antioxidant properties of uric acid have been harnessed to devise a highly sensitive and selective colorimetric assay for the detection of uric acid. The methodology revolves around the redox interaction between uric acid and oxidized-TMB solution, wherein the blue-colored oxidized form of TMB is efficiently reduced back to its colorless neutral state. This color change serves as a measure for uric acid concentration, forming the basis for its detection.

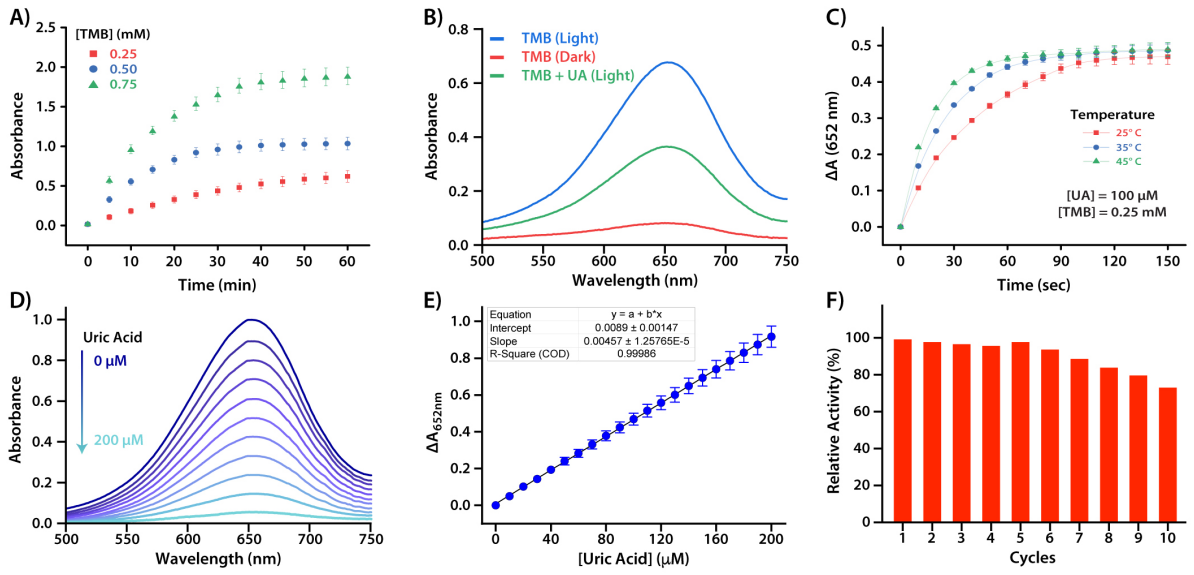

Figure 4.8 Uric acid detection A) Time-dependent change in the absorbance of oxidised-TMB charge-transfer complex at 652 nm during photo-oxidation across varying concentrations of TMB substrate, B) UV-visible spectra showing the photo-oxidation of TMB (0.5 mM) by the AuNS@Bead under dark conditions, after exposure to visible light, and in the presence of uric acid (100 µM), C) Time-dependent variation in the absorbance intensity of oxidized TMB charge-transfer complex at 652 nm following the addition of uric acid at varying temperatures, D) UV-Visible spectra of oxidized-TMB solution following sequential addition of uric acid, E) Change in the absorbance of oxidized-TMB at 652 nm as a function of uric acid concentration (From Fig. 4.8D), and F) Catalytic activity across multiple cycles of TMB oxidation.

To attain optimal uric acid sensing performance, crucial experimental parameters such as pH, irradiation time, and TMB concentration were systematically optimized. The pH value was set at 5, as the AuNS@Beads exhibited maximum photo-oxidase like activity under this condition. Notably, a positive correlation between TMB concentration and absorbance of oxidized-TMB at 650 nm was observed during the oxidase catalysis, with absorbance values surpassing 1.5 at higher TMB concentrations (Figure 4.8A). Given the importance of maintaining sample absorbance near 1 in sensing applications to optimize spectrophotometer linearity, sensitivity, and signal-to-noise ratio for reliable measurements, a judicious selection of a 0.5 mM TMB solution was made for the spectrophotometric analysis. Furthermore, it was found that the absorbance of oxidized TMB increased proportionally with the duration of light irradiation, reaching a plateau at 25 minutes, beyond which the solution-maintained color stability for extended periods (Figure 4.8A). Consequently, the oxidation reaction was performed for a duration of 30 minutes prior to initiating the spectrophotometric analysis.

Material	Linear Range (µM)	LOD (µM)	Reference
Histidine-doped porphyrin covalent organic framework nanozyme	5-100	5	[294]
Upconversion-nanoparticle-functionalized janus micromotors	100-5000	1.59	[295]
Hemin-graphene oxide (H-GO)/Uricase-based photoacoustic device	100-2000	36	[296]
Hemin-functionalized microfluidic chip	1-1000	0.41	[295]
MXene-$Ti_3C_2T_x$ based electrochemical microfluidic biosensor	30-500	5	[297]
Prussian blue nanoparticles	0.5-50	0.9	[298]
TABB-BDB COF	29.74–951.76	21.24	[299]
Gold nanostars embedded hydrogel beads	10-200	0.9	This work

Table 4.1 Comparison of catalytic performance of previously reported catalytic materials for the sensing of uric acid

UV-Visible analysis revealed that a 0.5 mM solution of TMB in pH 5 buffer was efficiently oxidized by AuNS@Bead in the absence of uric acid under light irradiation, resulting in a characteristic absorption band with maxima at 652 nm (Figure 4.8B). However, in the presence of uric acid (100 µM), under identical conditions, a noticeable reduction in the intensity of the absorption band was

observed. The rate of change in the absorbance intensity was found to be temperature-dependent. After adding uric acid, the absorbance change of oxidized TMB at 652 nm (ΔA) reached a plateau in approximately 2 minutes at 25°C, while decolorization occurred in about 1 minute at higher temperatures (Figure 4.8C). Although elevated temperatures led to faster decolorization, assays at high temperatures were avoided to prevent any inadvertent effects on the sensing process. Therefore, all subsequent assays were conducted at ambient temperature. The degree of color fading was found to correlate with uric acid concentration in a linear fashion over the range of 0-200 μM, with a limit of detection (LOD, 3σ/k, where σ is the standard deviation of the response, and k is the slope of the calibration curve) of 0.9 μM (Figure 4.8D-E). This LOD is at par with most reported colorimetric methods, underscoring the sensitivity of the proposed assay (Table 4.1).

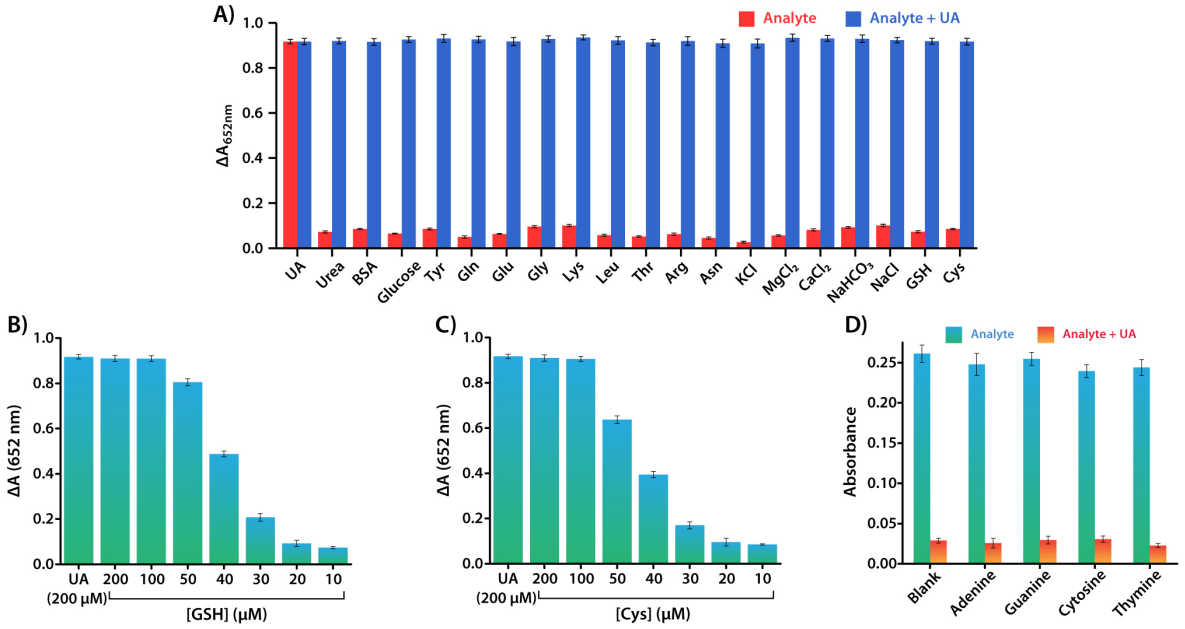

Figure 4.9 A) Response of the sensing platform towards various potential interfering species, [UA] = 200 μM, [GSH] = [Cys] = 20 μM, Concentration of all other analytes = 500 μM; Comparison of change in absorbance intensity of oxidized-TMB charge-transfer complex at 652 nm upon addition of varying concentrations of B) GSH, and C) L-Cysteine, and D) Comparison of absorbance intensity of oxidised-TMB charge-transfer complex at 652 nm upon addition of various purine and pyrimidine bases, both in the absence and presence of uric acid. [TMB] = 0.5 mM, [UA] = 200 μM, Concentration of the analytes = 500 μM

To assess selectivity, the sensing system's absorbance responses were measured in the presence of potential interfering species found in biological fluids, including L-tyrosine (Tyr), L-glutamic acid (Glu), L-glutamine (Gln), L-glycine (Gly), L-lysine (Lys), L-leucine (Leu), L-threonine (Thr), L-arginine (Arg), L-aspargine (Asn), K^+, Mg^{2+}, Ca^{2+}, Na^+, Cl^-, HCO_3^-, urea, glucose, BSA, GSH and L-cysteine (Cys) (Figure 4.9A). Remarkably, uric acid (200 μM) caused significant color fading, whereas most other interfering species had a negligible impact on oxidized-TMB absorbance, even at higher concentrations (500 μM). However, both GSH and Cys (200 μM) did cause significant color fading,

likely due to their antioxidant properties (Figure 4.9B-C). A concentration-dependent decolorization analysis revealed that at concentrations of 20 μM or less, GSH and Cys have no discernible impact on oxidized-TMB absorbance. Fortunately, GSH and Cys concentrations in biofluids are around 3.4 μM[300] and 9.7 μM[301], respectively, which is significantly lower than the concentration of uric acid. Also, purine and pyrimidine bases, which share structural similarities with uric acid, had minimal influence on the absorbance of oxidized TMB, likely due to their relatively weaker antioxidant properties compared to uric acid (Figure 4.9D). Thus, the colorimetric analysis of real samples would not be affected by any of the aforementioned interfering species. Moreover, uric acid retained its ability to decolorize the oxidized-TMB solution even when these interfering species were present, demonstrating the high selectivity of this colorimetric method for uric acid detection without significant interference from other common biological components.

4.2.4 Stability and reusability of the catalytic beads

While homogenous catalysts display high sensitivity and selectivity, and have extensively been employed in sensing applications, heterogeneous catalysts stand out for their recoverability and reusability.[58, 179] Their cost-effectiveness, sustainability, and ease of handling make them superior choices, addressing economic and environmental concerns in analytical processes. This work presents an innovative approach for improving and sustaining the stability and catalytic effectiveness of photo-oxidase mimetic gold nanostars through their immobilization onto a heterogeneous support material. Gold-based nanocatalysts are prone to aggregation and deactivation in aqueous medium.[302, 303] However, the gold nanostars embedded on the bead surface demonstrated exceptional stability, maintaining catalytic activity despite continuous agitation in water for 24 hours (Figure 4.10A). Furthermore, even after the beads underwent prolonged incubation in aqueous medium for 60 days, the embedded gold nanostars continued to demonstrate sustained catalytic activity (Figure 4.10B). This consistent performance across numerous cycles and an extended duration underscores the robust retention and stabilization of gold nanostars within the polymeric bead surface. This stability is further supported by EDX mapping analyses, revealing a uniform distribution of gold nanostars on the bead's surface even after three catalytic cycles (Figure 4.10C). Moreover, atomic absorption spectroscopy confirmed negligible gold leaching from the beads into the solution, affirming their suitability for sustained catalytic applications. The easily retrievable and washable catalytic beads showcased resilient performance across numerous cycles, with minimal activity loss observed through five cycles (Figure 4.8F). Remarkably, even after 10 cycles, they retained ~ 70% catalytic efficiency. This underscores

the enduring catalytic prowess and reusability of the beads, establishing their practicality, efficiency and cost-effectiveness in the sensing processes.

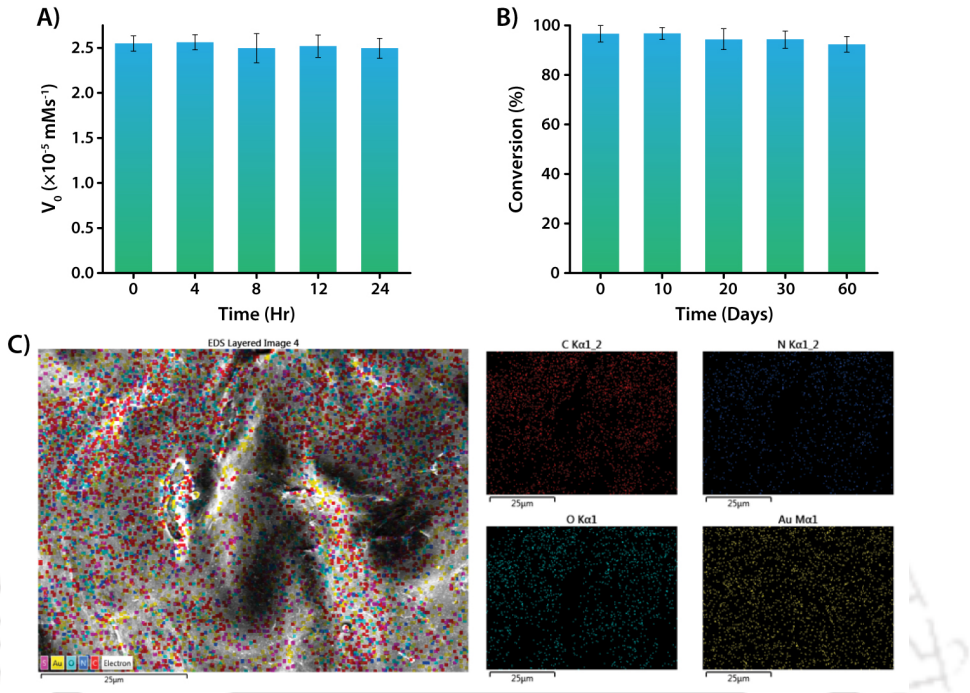

Figure 4.10 A and B) Catalytic activity of AuNS@Beads at different time intervals of continuous agitation in water, C) EDX elemental mapping of the surface of the AuNS embedded bead after catalytic cycles.

4.2.5 Smartphone-based POCT application

The system presented herein showcased exceptional sensitivity and specificity in its calorimetric response to varying uric acid concentrations, prompting the development of a smartphone-based point-of-care testing (POCT) platform for convenient and on-site uric acid detection. Using the installed "Color Picker" application, the smartphone can read the image color signals and translate them into digital values that represent the red (R), green (G), and blue (B) color channels. To avoid extraneous interferences, a homemade setup was devised in which the sample was placed in a chamber and the smartphone was kept at a constant distance from the sample (Figure 4.11A). The sample was illuminated with the camera's LED flash light, and its color was analyzed using the smartphone's color picker application. The color intensities of the samples were calculated using the formula, $I = 0.3R + 0.59G + 0.11B$,[304] where *I* represents intensity. The difference in the intensity of the oxidized-TMB solution before and after the addition of uric acid sample, *ΔI*, allowed for the quantification of the uric acid concentration. To optimize the TMB concentration for the POCT setup, TMB solutions of three different concentrations (2.5, 5, and 7.5 mM) were oxidized by an AuNS@Bead over a 30-minute period. Subsequently, images of the colored oxidized-TMB solutions, containing varying concentrations of uric acid (0-200 µM), were captured and analyzed using the smartphone

Color Picker application (Figure 4.11B). Notably, a linear colorimetric response across a wide uric acid concentration range was achieved with the 0.5 mM TMB solution (Figure 4.11C).

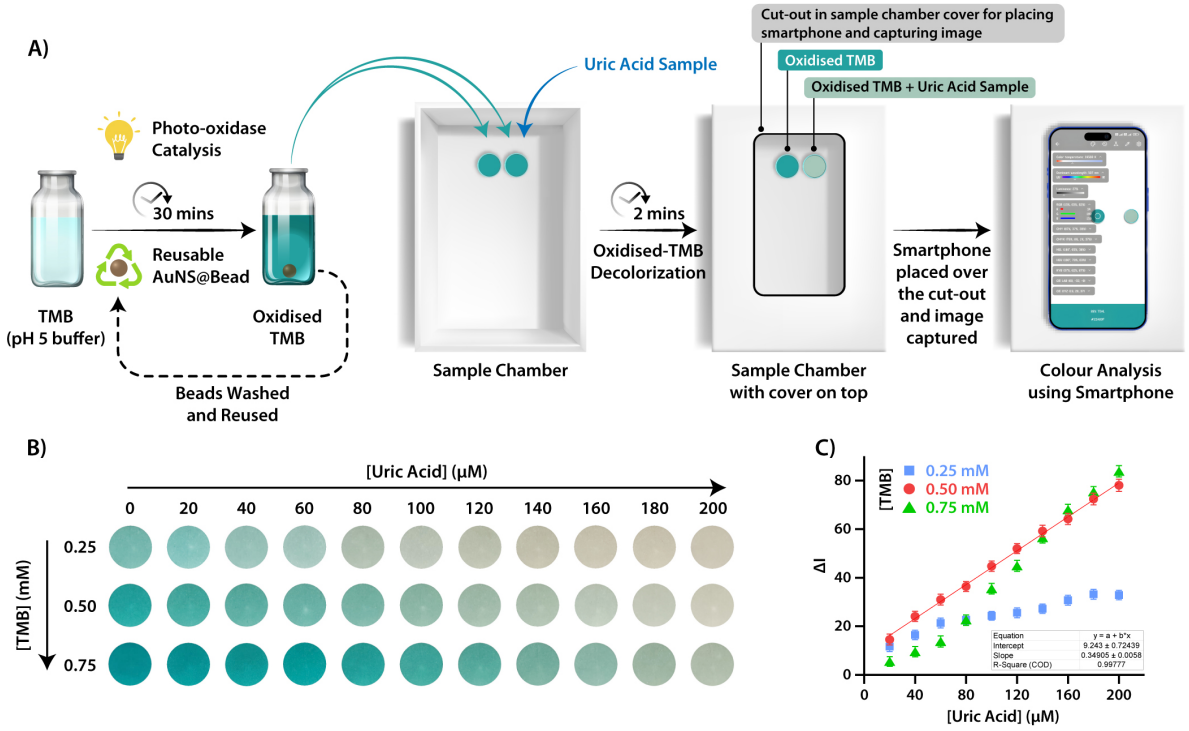

Figure 4.11 Designing POCT platform. A) Schematics demonstrating operation of the smartphone-based POCT setup, B) Images showing color of oxidized TMB solutions upon addition of increasing concentrations of uric acid, and C) Variation of ΔI with increasing concentrations of uric acid.

Sample No.	Pathology Lab Determined (μM)[a]	Uric Acid Added (μM)	Spectrometric Determination (μM)	Recovery (%)	RSD (%, n=3)	POCT Determination (μM)	Recovery (%)	RSD (%, n=3)
Sample **1**[b] Blood Serum	327.2	0	33.1 ± 0.9	-	2.8	32.3 ± 1.0	-	3.2
		10	43.9 ± 1.4	101.8	3.1	43.4 ± 1.2	102.6	2.8
		30	61.9 ± 1.3	98.1	2.1	63.1 ± 1.8	101.3	2.9
		50	81.3 ± 2.0	97.8	2.5	80.9 ± 1.7	98.3	2.1
Sample **2**[b] Blood Serum	345.0	0	33.5 ± 1.1	-	3.2	33.8 ± 0.9	-	2.8
		10	43.3 ± 1.2	97.4	2.8	43.5 ± 1.3	99.3	3.1
		30	65.3 ± 1.4	101.3	2.1	64.8 ± 1.7	101.5	2.6
		50	86.3 ± 2.5	102.1	2.9	86.1 ± 2.3	102.7	2.7
Sample **3**[c] Urine	-	0	50.8 ± 1.4	-	2.7	49.9 ± 1.2	-	2.5
		10	60.0 ± 1.1	98.7	1.9	58.3 ± 1.8	97.3	3.1
		30	78.5 ± 1.6	97.2	2.1	78.5 ± 2.2	98.2	2.8
		50	103.2 ± 2.4	102.4	2.3	101.3 ± 1.9	101.4	1.9
Sample **4**[c] Urine	-	0	74.5 ± 1.3	-	1.8	76.7 ± 1.6	-	2.1
		10	83.3 ± 1.9	98.6	2.3	88.1 ± 2.4	101.6	2.7
		30	101.6 ± 2.1	97.2	2.1	104.9 ± 3.1	98.3	3.0
		50	126.6 ± 2.4	101.7	1.9	129.7 ± 3.2	102.4	2.5

Table 4.2 Determination of uric acid content in blood serum and urine samples using spectrophotometric and POCT-based methods. [a] Data supported by the affiliated hospital of IIT Guwahati; [b] 10-fold diluted sample; [c] 50-fold diluted sample.

The limit of detection (LOD, 3σ/k) of this POCT setup was found to be 6.2 μM. To assess the feasibility of this POCT system, uric acid concentration in blood serum and urine samples was assessed using both the spectrophotometric approach and the smartphone-based POCT platform (Table 4.2). The uric acid levels obtained using both techniques were in excellent agreement with the results of pathological analyses, demonstrating high accuracy and precision with minimal relative errors and relative standard deviations (RSD, n = 3). Additionally, uric acid sensing was conducted in spiked samples to reaffirm the effectiveness of both methods. The spiked recoveries ranged from 97.2 % to 102.7 %, with RSDs below 3.2 %, confirming the practical utility of both methods for quantifying uric acid levels in serum samples. These comprehensive findings highlight the gold nanostar-based sensor's robustness and reliability in detecting uric acid levels, underscoring its tremendous potential for practical applications in diverse real-world scenarios.

4.3 Conclusion

In summary, this study unveils, for the first time, the unique photo-oxidase like activity exhibited by BPEI-stabilized gold nanostars, synthesized in situ on the surface of a core-shell hydrogel bead. The utilization of these gold nanostars as oxidase mimics offered a new avenue for the sensitive and specific colorimetric detection of uric acid. By embedding the nanostars on the surface of hydrogel beads, stability, reusability, and cost-effectiveness are achieved, distinguishing this system from conventional methods. Furthermore, the incorporation of smartphone technology for point-of-care testing improved accessibility and convenience, enabling rapid and accurate on-site quantification of uric acid in blood serum and urine samples. This innovative approach not only streamlines early detection and monitoring of uric acid-related conditions but also harbors the potential to transform personalized healthcare management. Also, the sensing mechanism described herein can be extended for detecting and quantifying a broader spectrum of antioxidant analytes, making it a versatile tool for comprehensive antioxidant analysis.

4.4 Experimental Section

4.4.1 Materials and Methods

Dipentaerythritol penta-/hexa-acrylate (5ACl), branched polyethylenimine (BPEI), 1-pyrenebutyric acid, 4-(2-Hydroxyethyl)piperazine-1-ethanesulfonic acid (HEPES), and Tetrachloroauric(III) acid ($HAuCl_4$) were purchased from Sigma-Aldrich (USA). 3,3′,5,5′-Tetramethylbenzidine (TMB), 2,2′-azinobis(3-ethylbenzothiazoline-6-sulfonic acid (ABTS), o-Phenylenediamine (OPD), Terephthalic acid (TA), and 3,3′-diaminobenzidine (DAB) were purchased from TCI, Japan. Rink amide MBHA resin, protected as well as unprotected amino acids, and coupling reagents were purchased from Novabiochem. HPLC-grade dimethylformamide (DMF), dichloromethane (DCM) and acetonitrile (ACN) were procured from Spectrochem (India) and Fisher Scientific (India). Solvents were dried whenever required according to the reported procedures. Milli-Q water with a conductivity of less than 2 μScm^{-1} was used for all sample preparations.

UV–Visible spectra were recorded on a PerkinElmer Lambda 365+ spectrophotometer, while fluorescence measurements were performed on a Horiba Fluoromax 4 Plus spectrophotometer. The particle sizes of the AuNSs were obtained at 298 K using a 632.8 nm He – Ne laser using Zetasizer Nano- ZS90 (Malvern). FESEM imaging and Energy Dispersive X-ray (EDX) mapping analysis of freeze-dried samples were performed on a Gemini SEM 300 (Sigma Zeiss) instrument. The FETEM analyses were performed in JEOL 2100F microscope. For UV–Visible, FETEM and DLS analysis of the embedded AuNSs (and/or AuNPs), an ethanolic suspension of freeze-dried and ground (henceforth "cryo-ground") AuNS loaded beads was prepared in ethanol through sonication. FTIR spectra for freeze dried samples of the beads were obtained on a PerkinElmer instrument under ambient conditions. The Powder XRD analysis results of the freeze-dried samples were obtained from the Rigaku Smartlab X-ray Spectrophotometer with Cu-Kα (λ =1.54 Å), source running at a power of 9 KW. The TGA analysis was performed in Netzsch, STA449F3A00. Atomic Absorption Spectroscopy was performed using Varian AA240.

4.4.2 Synthesis of PyKC Peptide

The peptide was synthesized on Rink amide MBHA resin using standard Fmoc (9-fluorenylmethoxycarbonyl) solid phase peptide synthesis (SPPS) protocol. In a typical coupling, 3 equiv. of a protected amino acid (with respect to the loading of the resin), 3 equiv. of HBTU, and 6 equiv. of DIPEA were taken in 5 mL of DMF (for 0.1 mmol scale with respect to the resin loading) and stirred for 5 minutes prior to the addition of the mixture to the swelled and deprotected resin. The reaction mixture was shaken for 60 min, and the resin was washed several times with DMF. The Fmoc-deprotection was achieved by treatment of the resin three times with 5 ml of 20% piperidine

in DMF for 5 minutes, followed by a thorough washing of the resin with DMF and DCM. The Fmoc-deprotection and coupling steps were repeated until the desired peptide sequence was obtained. The resin with the loaded peptide was washed several times with DMF and DCM and dried. The dried resin was then treated with a mixture of freshly prepared mixture of 8.5:1:0.5 (trifluoroacetic acid (TFA)/tetraethylsilane (TES)/H_2O) and stirred for 1 h. The resin was finally washed with DCM several times. The cleavage cocktail and the washings combined were concentrated to a minimum volume on a rotary evaporator. The cleaved peptide was then precipitated from cold dry ether, centrifuged and lyophilized to get the crude peptide. Purification was done in Dionex Ultimate 3000 HPLC using a Luna 5 μm (C18) column (Phenomenex) and using acetonitrile and water (containing 0.1% TFA each) as the mobile phase.

^{1}H-NMR (DMSO-d_6, 400 MHz): δ (ppm) 8.39 (d, 1H), 8.28 (m, 2H), 8.23 (m, 2H), 8.14 (d, 2H), 8.07 (t, 1H), 7.97 (t, 2H), 7.66 (s, 3H), 7.29 (s, 1H), 7.20 (s,1H), 4.39 – 4.21 (m, 2H), 2.90 – 2.66 (m, 4H), 2.29 (m, 3H), 2.03 (p, 2H), 1.69 (m, 1H),1.55 (m, 3H), 1.35 (d, 2H).

MALDI-TOF: m/z calculated for $C_{29}H_{34}N_4O_3S$ $[M+H]^+$: 519.27, found: 519.23

HPLC R_T = 12.5 min (HPLC Program: 5% Acetonitrile/Water to 100% Acetonitrile in 20 minutes.)

4.4.3 Preparation of Core-Shell Beads

The core-shells beads were fabricated following our previously reported 2-step protocol.[1]

Step 1: Typically, a 5 wt% solution of PyKC (20 mM Tris buffer, pH 8) was prepared in a 1 mL syringe fitted with a 26G needle and was left undisturbed at room temperature for a period of 24 h to allow the formation of the hydrogel. The hydrogel in the syringe was then forced out through the fine needle orifice using gentle mechanical pressure. Owing to the shear thinning property of PyKC hydrogel, the sol emerging out of the needle immediately hardened into small spherical hydrogel droplets which were dropped into an ethanolic solution of 5ACl (1 g/mL) for surface functionalization. The beads were allowed to react with 5ACl for 15 min with gentle shaking and subsequently washed several times with copious amounts of ethanol to remove the unreacted and loosely bound 5ACl molecules from the surface.

Step 2: The beads, surface-functionalized with acrylate groups, were then treated with an ethanolic solution of BPEI (20 mg/ml) over a shaker for 15 min, followed by washing with ethanol to remove any unreacted BPEI. This led to the cross-linking of the surface of the beads and generated an amine functionalized surface.

4.4.4 Fabrication of Gold Nanostar-Embedded Beads (AuNS@Beads)

The AuNS@Beads were synthesized through a 2-step seeded growth process. Initially, gold nanoseeds were synthesized in situ on the surface of the beads under thermal conditions.

Specifically, 20 BPEI-coated beads were continuously agitated in a 1ml aqueous solution of $HAuCl_4$ (100 mM) for 30 minutes at 90 °C, followed by an additional 20 minutes at room temperature. Subsequently, 50 µL of 1M HEPES buffer at pH 7.4 was introduced, and agitation continued for an additional 4 hours. The colour of the solution transitioned from yellow to bluish-green, indicating the formation of gold nanostars, while the colour of the beads changed from light brown to deep reddish-brown, signifying successful in situ fabrication of gold nanostructures on their surface. The resulting AuNS@Beads were thoroughly rinsed with water to eliminate unreacted reagents and loosely attached nanostars before being stored at 4 °C. Confirmation of AuNS formation within the BPEI polymeric shell was achieved through various analyses including UV-Visible, DLS, and FETEM.

4.4.5 Fabrication of Gold Nanoparticles-Embedded Beads (AuNP@Beads)

The AuNP@Beads were synthesized under thermal conditions following a previously established protocol.[58] Specifically, 15 BPEI-functionalized beads were continuously agitated in a 1ml aqueous solution of $HAuCl_4$ (100 mM) for 3 hours at 90 °C. Subsequently, the resulting AuNP@Beads were thoroughly rinsed with water to eliminate unreacted reagents and loosely attached nanoparticles. The AuNP@Beads were then stored at 4°C until further use. Confirmation of AuNP formation within the BPEI polymeric shell was attained through various analyses including UV-Visible and FETEM examinations.

4.4.6 Assessment of Oxidase-Like Activity

The oxidase activity of the AuNS@Beads was evaluated by spectrophotometrically monitoring the oxidation process of the chromogenic substrate, TMB. In a typical procedure, 0.5 mM TMB (1 µL of 0.5 M stock solution in DMSO) was taken in 1 mL of pH 7 phosphate buffer (20 mM) in a quartz cuvette with a path length of 1 cm. To initiate the reaction, one AuNS@Bead was inserted into the cuvette, the solution was thoroughly mixed, and the solution was exposed to visible light irradiation (20 W white-light LED bulb; $\lambda \geq 420$ nm). UV-Visible spectra of the solution were recorded at 2-minute intervals for a duration of 20 minutes. The gradual emergence of an absorbance band at 652 nm, corresponding to the charge-transfer complex of oxidized-TMB, provided evidence for the oxidase activity of the AuNS@Beads. Similarly, the oxidation of ABTS and OPD (0.5 mM each) by the AuNS@Beads further confirmed the oxidase activity of the gold nanostars.

4.4.7 Assessment of pH Dependent Oxidase-Like Activity

The pH-dependent oxidase activity of AuNS@Beads was assessed by spectrophotometrically monitoring the oxidation of TMB across various buffers ranging from pH 2 to pH 8 (20 mM). In a typical procedure, 0.5 mM TMB (1 µL from a 0.5 M stock solution in DMSO) was dissolved in 1 mL of

the corresponding buffer solution in a quartz cuvette with a 1 cm path length. The reaction was initiated by adding a single AuNS@Bead into the cuvette, followed by thorough mixing. After a 10-minute incubation period under visible light irradiation, UV-Visible spectra of the solutions were recorded. Catalysis experiments were conducted in triplicate, and the intensity of the absorption spectra at 652 nm was utilized to evaluate the relative oxidase activity of the AuNS@Beads under varying pH conditions.

4.4.8 Kinetic Analysis of the Oxidase-Like Catalysis

The oxidase activity of AuNS@Beads under visible light irradiation and in the absence of light at pH 5 was evaluated by spectrophotometrically monitoring the oxidation of TMB. In brief, a single AuNS@Bead was placed in 1 mL of pH 5 acetate buffer (20 mM) within a quartz cuvette of 1 cm path length and varying amounts of TMB (1 µL of 0.2, 0.4, 0.6, 0.8, and 1.0 M stock solutions in DMSO used to attain final concentrations of 0.2, 0.4, 0.6, 0.8, and 1.0 mM, respectively) were added to the solution. Following mixing, the solutions were allowed to sit in darkness or exposed to visible light for five minutes. After that, the absorbance of the oxidized TMB charge-transfer complex at λ_{max} = 652 nm (with $\varepsilon_{652\,nm}$ = 39000 $M^{-1}.cm^{-1}$ in water) was measured. Catalysis experiments were conducted in triplicate, and the kinetics of the reactions at different pH values were determined via nonlinear regression using GraphPad Prism 9 software, assuming Michaelis-Menten kinetics.

4.4.9 Band Gap Analysis of AuNS/AuNP

The band gap was extracted by converting the UV-visible spectral data into a Tauc plot using Tauc's equation for direct band gap materials[305]:

$$(\alpha h\upsilon)^2 = k(h\upsilon - E_g)$$

where α is the absorption constant, hυ is the photon energy, E_g is the band gap energy, and k is a constant. This equation can also be expressed as

$$(2.303 \times A \times 1240/\lambda)^2 = k(1240/\lambda - E_g)$$

where A represents absorbance and λ is the wavelength derived from the UV-Visible spectra of the AuNS and AuNP. Plotting this equation results in a graph (Fig. S9B), where. the tangent of the curve corresponds to the band gap energy of the AuNS and AuNP.

4.4.10 ROS Scavenger Study

To investigate the generation of various reactive oxygen species (ROS) within the system, a ROS scavenger study was conducted. In this experiment, a single AuNS@Bead was incubated with different scavengers (1 mM NaN_3, 0.4 mM histidine, 10 mM BQ, 10 mM IPA, 20 mM t-BuOH, 5 mM KI, and 1 mM EDTA) in 1 mL of pH 5 acetate buffer under visible light irradiation for 30 minutes.

Subsequently, 0.5 mM TMB was introduced into the solution, followed by further incubation for 5 minutes. The UV-Visible spectrum was then recorded to assess the impact of the scavengers on the oxidation reaction.

4.4.11 3,3′ -Diaminobenzidine (DAB) Assay

3,3′-diaminobenzidine (DAB) serves as a probe for detecting singlet oxygen generation in aqueous systems. To assess the production of singlet oxygen, 1 mM DAB was introduced into a 1 ml solution of pH 5 acetate buffer (20 mM) containing one AuNS@Bead, and DAB oxidation was monitored by UV-Visible spectrophotometry at fixed time intervals under both light and dark conditions. In order to assess the impact of photogenerated holes and superoxide radicals on the process of generating singlet oxygen, DAB oxidation was also observed in the presence of 5 mM KI (positive holes scavenger) and 10 mM BQ (superoxide radical scavenger).

4.4.12 Terephthalic Acid (TA) Assay

Terephthalic acid acts as a probe to capture hydroxyl radicals, leading to the formation of a highly fluorescent product known as 2-hydroxyterephthalic acid. In this experiment, a solution containing 0.5 mM TA in 1 mL of pH 5 acetate buffer (20 mM) was subjected to a one-hour incubation period under light irradiation, in the presence of H_2O_2, AuNS@Bead, and a combination of both. Following incubation, the fluorescence spectra of the solutions were monitored at 435 nm using an excitation wavelength of 315 nm. The absence of a prominent emission band at 435 nm in presence of AuNS@Bead and H_2O_2 indicates that the system does not generate hydroxyl radicals.

4.4.13 Assessment of Superoxide Dismutase (SOD)-Like Activity

To evaluate the SOD-like activity of AuNS@Beads, the generation of H_2O_2 was indirectly analysed by spectrophotometrically monitoring the oxidation of the chromogenic substrate TMB by HRP, utilizing the H_2O_2 produced through SOD catalysis. In this assay, a single AuNS@Bead was incubated with 0.4 mM histidine in 1 mL of pH 5 acetate buffer under visible light irradiation for 30 minutes. Following this, 0.5 mM TMB and 10 units/mL HRP was added to the solution, and the mixture was incubated for an additional 5 minutes. The UV-Visible spectrum was then recorded to determine H_2O_2 generation via SOD catalysis. In this setup, histidine acts as a scavenger for singlet oxygen, preventing TMB oxidation via oxidase catalysis.

4.4.14 Colorimetric Detection of Uric Acid

Initially, a solution containing 0.5 mM TMB in 1 mL of pH 5 acetate buffer (20 mM) was subjected to oxidation by a single AuNS@Bead under light irradiation for a duration of 30 minutes. Following this, the bead was extracted using a pair of forceps, and incremental concentrations of uric acid were

introduced into the coloured oxidized-TMB solution. The change in the colour of the solution upon each successive addition of uric acid was monitored via UV-Visible spectrophotometry. The absorbance difference, ΔA_{652nm} (the difference in absorption intensity at 652 nm before and after the uric acid addition), served as the basis for constructing the calibration curve and facilitated the determination of uric acid concentrations.

4.4.15 Smartphone-Assisted Detection of Uric Acid

In a vial, a solution containing 0.5 mM of TMB in pH 5 acetate buffer (20 mM) was oxidised by a single AuNS@Bead under light irradiation for 30 minutes. Subsequently, the bead was carefully removed, and a 100 µL aliquot of the oxidized-TMB solution was transferred to an inverted vial cap with a diameter of 0.5 cm. This vial cap was positioned within a self-constructed sample chamber measuring 20 cm (L) x 15 cm (W) x 10 cm (H). A digital image of the coloured solution was captured using a smartphone camera, positioned 10 cm away from the sample, with illumination provided by the smartphone's LED flashlight. Following this, increasing concentrations of uric acid were added to the oxidized-TMB solution in the vial. Following each addition, a 100 µL aliquot of the solution was isolated, and its digital image was recorded. All captured images were analysed using the "Color Picker" app and processed to determine the R, G, and B parameters. The colour intensities of the samples were calculated using the formula, $I = 0.3R + 0.59G + 0.11B$, where I represents intensity. The difference in intensity of the oxidized-TMB solution before and after the addition of uric acid, denoted as ΔI, was utilized to establish the calibration curve, enabling the precise determination of uric acid concentrations.

For assessing the uric acid content in real samples, two 90 µL aliquots of the oxidized-TMB solution were dispensed into separate inverted vial caps, each with a diameter of 0.5 cm. To one of these aliquots, 10 µL of the uric acid sample (either undiluted blood serum or five-fold diluted urine) was added, while the other aliquot received 10 µL of pH 5 acetate buffer. Subsequently, the colour intensities of the two aliquots were measured using a smartphone camera, and the concentration of uric acid in the samples was determined by referencing the obtained intensities to the calibration curve previously established. The blood and urine samples were obtained from donors with written consent and no ethics committee approval was necessary for these samples.

4.4.16 FTIR Analysis of surface functionalisation

Functionalization of the bead surface with 5ACl followed by BPEI was ascertained through FTIR spectroscopy of the freeze-dried beads after subsequent functionalization steps (Figure S1). Appearance of new peaks at 1408 and 1735 cm^{-1} corresponding to the asymmetric stretching vibration of the vinyl group and stretching vibration of ester carbonyl groups, respectively, affirmed

the successful attachment of 5ACl on the surface of the peptide hydrogel beads.[58] As the peptide amide bonds remain unaffected during surface functionalization, taking the amide carbonyl stretching band at 1635 cm^{-1} as an internal standard, a relative decrease in the amine stretching band at 1540 cm^{-1} following 5ACl functionalization indicated the free lysine amine groups on the surface of the beads underwent Michael addition reaction with the 5ACl molecules. Also, as the ester groups of 5ACl do not participate in subsequent functionalization reaction, a relative decrease in the peak intensity at 1408 cm^{-1} for C-H stretching of the vinyl groups compared to the carbonyl stretching of 5ACl ester groups at 1735 cm^{-1} indicated the Michael addition of BPEI with the residual 5ACl acrylate moieties on the bead surface.

Indian Institute of Technology Guwahati

Chapter 5

Non-Plasmonic Oxidase-Like Gold Nanocatalysts on Hydrogel Beads for Broad-Spectrum Water Decontamination

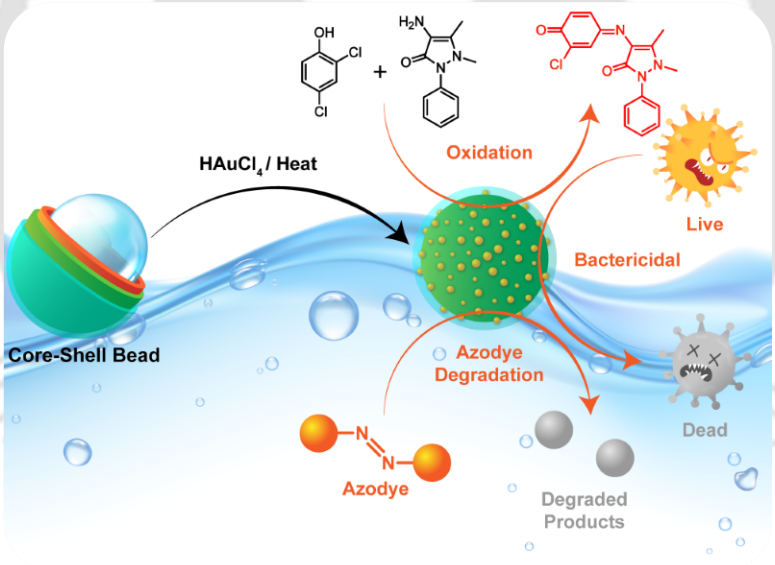

Indian Institute of Technology Guwahati

5.1 Introduction

The accelerating pace of industrialization and urban development has significantly intensified the release of untreated or inadequately treated wastewater from industrial, agricultural, and domestic sources.[306] This widespread discharge has led to the pervasive contamination of global freshwater resources with a complex array of pollutants. These contaminants include both organic and inorganic species, such as heavy metals, synthetic dyes, pharmaceutical residues, endocrine-disrupting chemicals (EDCs), phenolic compounds, surfactants, nitrates, and diverse microbial pathogens.[307] Such multifaceted pollution poses severe environmental and public health risks, including ecosystem disruption, bioaccumulation, toxicity in aquatic organisms, and the emergence of antibiotic-resistant bacteria.[308, 309] Although conventional water treatment techniques, such as biochemical processes, chemical coagulation and precipitation, membrane filtration, activated carbon adsorption, and electrochemical oxidation are routinely employed, each method suffers from intrinsic limitations.[310] Biochemical treatments are often ineffective against non-biodegradable or toxic compounds and are sensitive to fluctuations in environmental parameters. Coagulation and precipitation can result in the generation of large volumes of sludge and may involve hazardous chemical additives. Membrane-based methods are energy-intensive and prone to fouling, while activated carbon, despite its high adsorption capacity, requires frequent regeneration or replacement, thereby increasing operational costs. Furthermore, most of these technologies are pollutant-specific, necessitating multi-step treatment schemes for comprehensive remediation.

In this context, advanced oxidation processes (AOPs) have emerged as powerful strategies for the degradation of a broad spectrum of waterborne contaminants.[311] AOPs operate through the in-situ generation of highly reactive oxygen species (ROS), including hydroxyl radicals (•OH), superoxide anions (O_2•$^-$), and singlet oxygen ($^1O_2$) that can non-selectively oxidize and mineralize organic pollutants into benign end-products.[312-317] Within the AOP framework, oxidase mimetic nanocatalysts offer a particularly attractive approach due to their ability to utilize molecular oxygen as the terminal oxidant under mild conditions, without requiring additional chemical reagents.[318] Recent studies have demonstrated that nanomaterials composed of noble and transition metals, such as gold (Au), silver (Ag), palladium (Pd), platinum (Pt), TiO_2, Mn_3O_4, CeO_2, and Fe_3O_4 can emulate the catalytic activity of natural oxidase enzymes by activating molecular oxygen for the oxidative transformation of organic substrates.[230, 231, 318] The catalytic efficiency of these nanozymes is strongly influenced by their morphology, size, and surface chemistry, particularly the presence of functional ligands or polymeric coatings that modulate electronic properties and enhance substrate accessibility.[319, 320] However, a major limitation of many reported oxidase-mimetic systems, especially those based on plasmonic metals like gold and silver, is their dependence on external

light irradiation.[245, 247-249, 321] These photocatalytic systems typically rely on localized surface plasmon resonance (LSPR) to generate energetic electron-hole pairs, which facilitate ROS production.[293, 322] While effective under controlled illumination, the practical application of such light-dependent systems in water treatment is constrained by several factors: limited light penetration in turbid media, high energy demands of artificial lighting, and sensitivity to environmental variables such as temperature, pH, and interfering chromophores. These limitations underscore the urgent need for light-independent catalytic systems capable of ROS generation through alternative, non-plasmonic mechanisms.

In our prior work, we reported the fabrication of branched polyethylenimine (BPEI)-coated core-shell hydrogel beads functionalized with in situ synthesized gold nanostars.[59] These nanostar-embedded beads exhibited robust oxidase-like activity under light irradiation, driven by the LSPR effect. In contrast, when isotropic gold nanoparticles were synthesized on the same BPEI-coated surface, no photocatalytic activity was observed, emphasizing the pivotal role of nanostructured morphology and anisotropy in dictating catalytic behavior. These findings highlighted the importance of surface engineering and structural design in modulating redox activity. Building on these insights, we sought to investigate the impact of surface ligand chemistry by modifying the polymeric coating of the hydrogel beads. In the present study, we introduce sulfobetainized BPEI (SO_4-BPEI) as a new negatively charged surface coating on the core-shell hydrogel beads. Remarkably, gold nanoparticles synthesized in situ on this sulfonate-enriched matrix demonstrated intrinsic oxidase-mimetic activity even in the absence of light irradiation. This unforeseen observation prompted an in-depth exploration of the ligand-mediated catalytic mechanism. Unlike conventional light-activated plasmonic systems, our catalyst operates via a non-plasmonic, radiation-less mechanism, wherein the sulfonate ligands alter the electronic environment of the gold nanoparticles, thereby promoting the activation of molecular oxygen into singlet oxygen under ambient, dark conditions. Crucially, in contrast to traditional porous or colloidal catalytic architectures, the gold nanoparticles in our system are localized exclusively on the outer surface of the hydrogel beads. This surface-confined configuration eliminates internal mass transfer resistance and diffusion limitations, enabling rapid and efficient substrate interaction with the catalytic sites.[58, 59] Additionally, the hydrogel bead provides mechanical integrity, inhibits nanoparticle leaching or aggregation, and facilitates easy catalyst recovery and reuse.[49, 61, 250-252] The heterogeneous nature and structural robustness of the system enhance its environmental compatibility and scalability, making it well-suited for practical implementation. To validate the multifunctional utility of our nanocatalyst-embedded hydrogel beads, we evaluated their performance against a range of representative water pollutants, encompassing both abiotic (chemical) and biotic (biological) contaminants. The catalyst

exhibited excellent activity toward the oxidation of phenolic compounds, which are known for their environmental persistence and toxicity. It also enabled the efficient degradation of azo dyes, widely used in textile industries and recognized for their mutagenic and carcinogenic potential. Furthermore, the beads displayed pronounced antibacterial activity against common waterborne pathogens, demonstrating their effectiveness in microbial load reduction and disinfection. Taken together, the broad-spectrum catalytic performance, operational simplicity, reusability, and heterogeneity of the system underscore its promise as a versatile platform for sustainable water remediation. By addressing multiple classes of contaminants within a single catalytic framework, this work advances a holistic approach toward the development of field-deployable, low-maintenance water purification technologies.

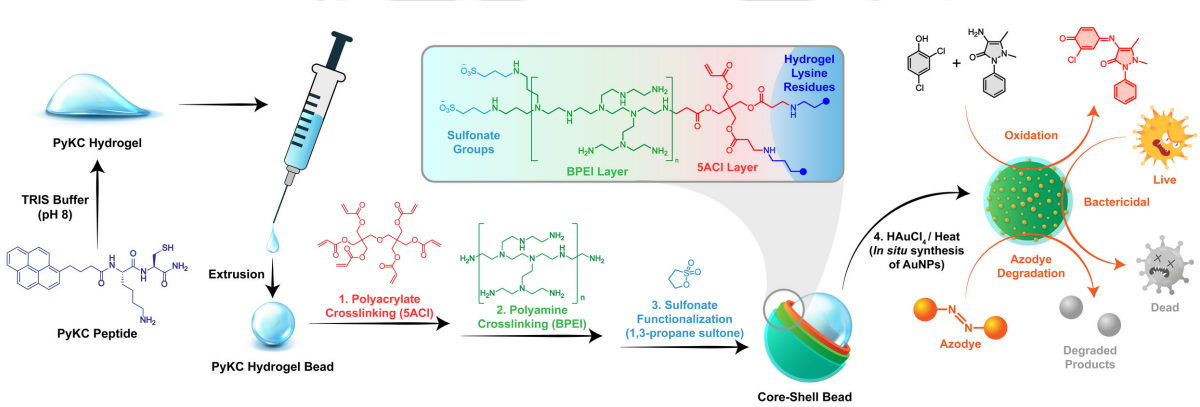

Scheme 5.1 Graphical illustration depicting the fabrication of peptide-based core–shell hydrogel beads and the subsequent *in-situ* formation of gold nanoparticles on their surface, enabling the oxidation of phenolic compounds, degradation of azo dyes, and antibacterial activity through oxidase-like catalysis.

5.2 Results and Discussion

5.2.1 Localized growth of gold nanostructures on hydrogel beads

Surface modifications and the nature of the surrounding polymeric matrix highly influence the catalytic performance of gold nanoparticles (AuNPs).[237] In particular, the physicochemical interactions between AuNPs and their support materials can significantly modulate nanoparticle size, dispersion, oxidation state, and catalytic efficiency. Building on our previous works[58, 59] involving the in-situ fabrication of catalytically active Au nanostructures on hydrogel beads coated with positively charged branched polyethyleneimine (BPEI), we sought to explore the impact of negatively charged functionalization on the growth and surface characteristics of AuNPs. In the present study, peptide-based core-shell hydrogel beads were employed as heterogeneous scaffolds for nanoparticle growth. These beads were synthesized using a low molecular weight peptide, Pyrene-Lysine-Cysteine (PyKC),[114, 130, 133, 323, 324] through a simple and reproducible extrusion technique.

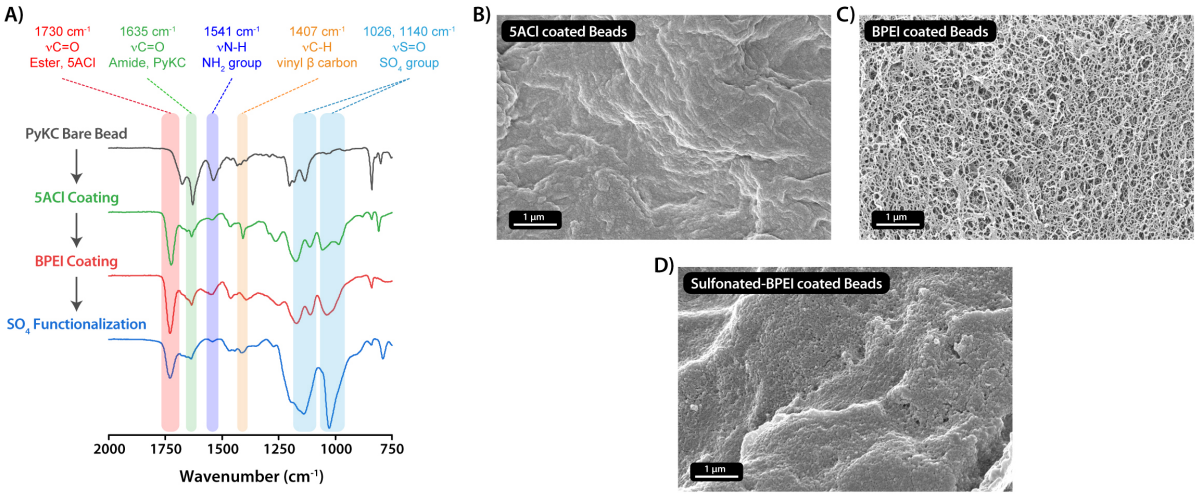

Figure 5.1 A) FTIR spectra of the beads after each successive surface modification step, B-D) FESEM images of the bead surface after each successive surface modification step.

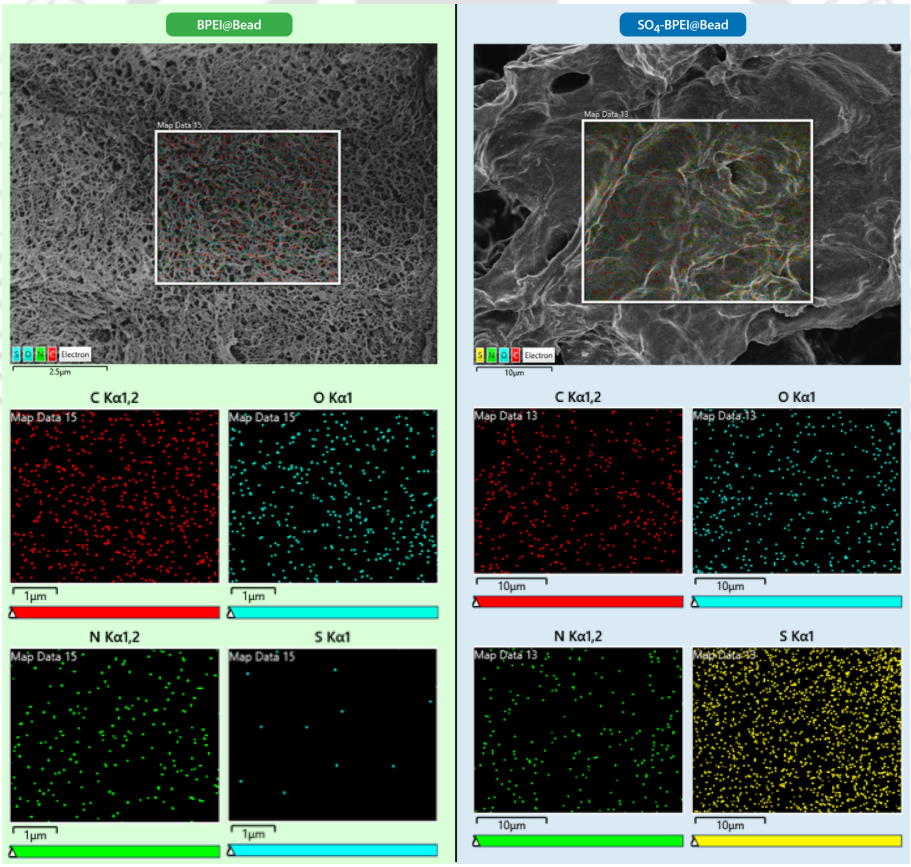

Figure 5.2 EDX elemental mapping of the surfaces of BPEI-functionalized (BPEI@Bead) and sulfonated BPEI-functionalized (SO_4-BPEI@Bead) core–shell beads.

Following gelation, the beads were sequentially coated with dipentaerythritol penta-/hexa-acrylate (5ACl) and BPEI to form a bilayered shell, as established in our earlier work.[58, 59] To introduce negatively charged moieties, the surface-exposed BPEI layer was treated with 1,3-propane sultone,

which resulted in the formation of sulfonate-functionalized hydrogel beads (Scheme-5.1).[325] The stepwise surface functionalization was confirmed by Fourier-transform infrared (FTIR) spectroscopy of freeze-dried beads after each modification step. FTIR signatures corresponding to sulfonate stretching vibrations indicated the successful grafting of sulfonate groups (Figure 5.1A).[326] Furthermore, Field Emission Scanning Electron Microscopy (FESEM) revealed notable changes in surface morphology after the sequential application of 5ACl, BPEI, and 1,3-propane sultone (Figure 5.1B-D). In contrast to the initial nanofibrillar network observed in the BPEI-coated beads, the sulfonated beads displayed a distinctly smoother, granular surface morphology, suggesting the successful surface engineering of the core-shell system. Moreover, EDX mapping analysis revealed significant localization of sulfur on the bead surfaces, confirming the effective grafting of sulfonate groups onto the beads (Figure 5.2).

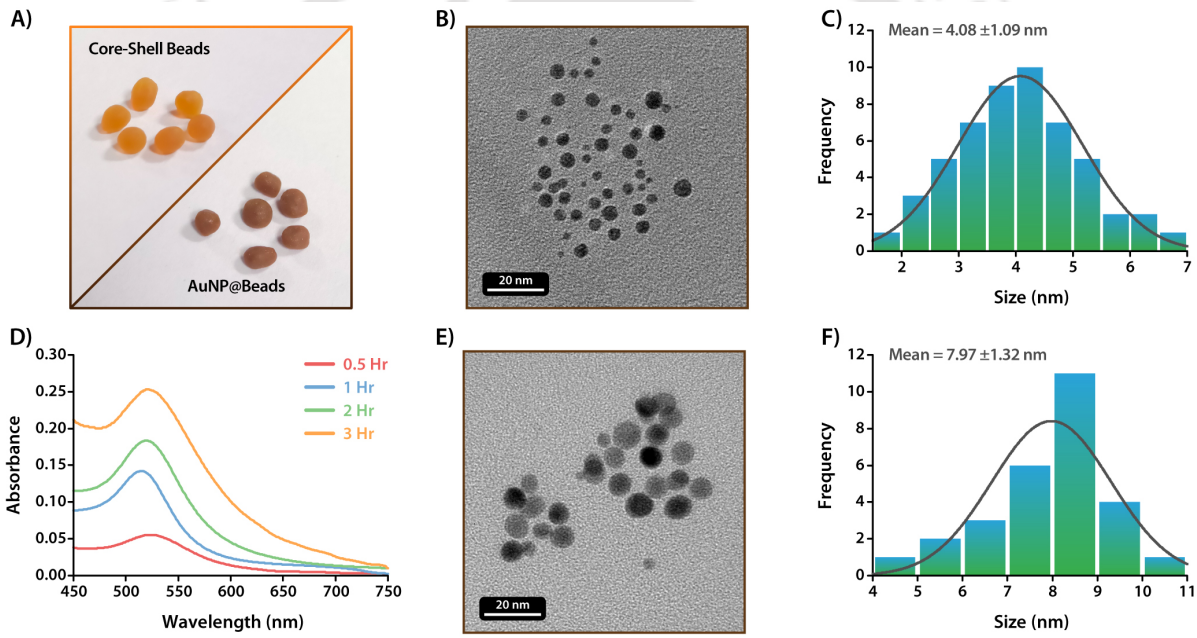

Figure 5.3 In situ synthesis of gold nanoparticles on core-shell hydrogel beads. A) Photographs of the beads before and after AuNP deposition; B) FETEM image, and C) Size distribution histogram of the AuNPs synthesized over a duration of 1 hour, D) UV-visible spectra of AuNPs synthesized over varying reaction durations, E) FETEM image, and C) Size distribution histogram of the AuNPs synthesized over a duration of 2.5 hours.

Both BPEI and sulfonate-containing polymers are known to possess mild reducing capabilities.[58, 327] BPEI contains densely packed amine functionalities which can reduce metal ions under suitable conditions. Similarly, sulfonated polymer such as chondroitin sulfate have demonstrated dual roles as reducing and stabilizing agents during metal nanoparticle formation.[327] As expected, the sulfonated BPEI surface facilitated the simultaneous reduction of Au(III) to Au(0) and provided stabilization to the in-situ formed gold nanoparticles. For nanoparticle fabrication, sulfonated

hydrogel beads (~2 mm diameter) were introduced into an aqueous $HAuCl_4$ solution (100 mM) and gently heated under continuous stirring. The *in-situ* reduction process led to a visible color change from light brown to dark brown, indicating the formation of AuNPs (Figure 5.3A). The resulting AuNP-loaded beads (AuNP@Beads) were thoroughly washed to remove unbound reagents and stored at 4 °C for further use.

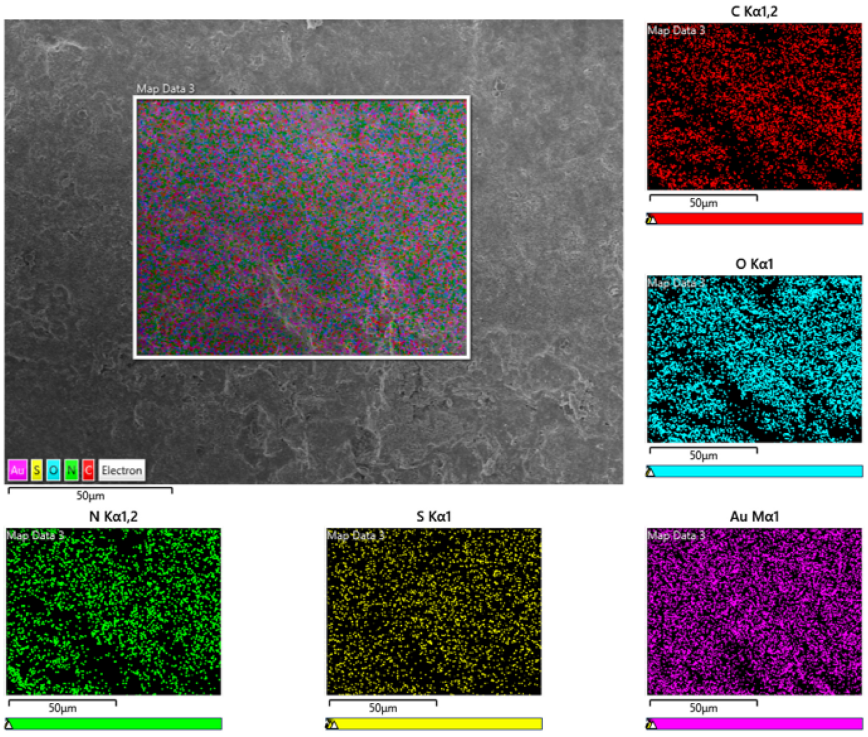

Figure 5.4 EDX elemental mapping of the surface of the AuNP embedded bead.

To evaluate the influence of reaction time on AuNP growth, the in-situ synthesis was performed for varying durations ranging from 0.5 to 3 hours. UV–Visible analysis of ethanolic suspensions of cryo-ground AuNP@Beads revealed a weak surface plasmon resonance (SPR) band at 0.5 hours (Figure 5.3D). With longer reaction times, the SPR band intensified and exhibited a slight red shift from 515 nm (at 1 hour) to 521 nm (at 3 hours), indicating progressive growth and stabilization of AuNPs over time.[328] The formation of AuNPs was further confirmed by FESEM and Energy-Dispersive X-ray (EDX) analysis. FESEM images of the sulfonated beads before gold loading showed a uniform granular surface, which transformed significantly after AuNP deposition (Figure 5.5A-B). This morphological change is attributed to electrostatic interactions between the anionic sulfobetainized BPEI and the deposited gold nanoparticles.[58, 59] EDX elemental mapping confirmed the homogeneous distribution of gold across the bead surface (Figure 5.4). Transmission Electron Microscopy (TEM) analyses of cryo-ground beads synthesized at different time points showed spherical gold nanoparticles (Figure 5.3B, E). At 1 hour, the average nanoparticle size was determined to be 4.08 ±

1.09 nm (Figure 5.3B-C). Extending the reaction time to 2.5 hours resulted in larger particles with an average diameter of 7.97 ± 1.32 nm (Figure 5.3E-F). These findings highlight a clear time-dependent nucleation and growth mechanism of AuNPs on the hydrogel bead surface. High-resolution TEM (HRTEM) images further confirmed the crystalline nature of the nanoparticles, showing a distinct lattice fringe corresponding to the (111) plane with an interplanar spacing of 2.36 Å (Figure 5.5C).[196] X-ray diffraction (XRD) patterns of the cryo-ground AuNP@Beads exhibited characteristic peaks at 38.6°, 44.8°, 64.9°, 77.9°, and 82.1°, corresponding to the (111), (200), (220), (311), and (222) planes, respectively, confirming the face-centered cubic (FCC) structure of the embedded gold nanoparticles (Figure 5.5D).[194]

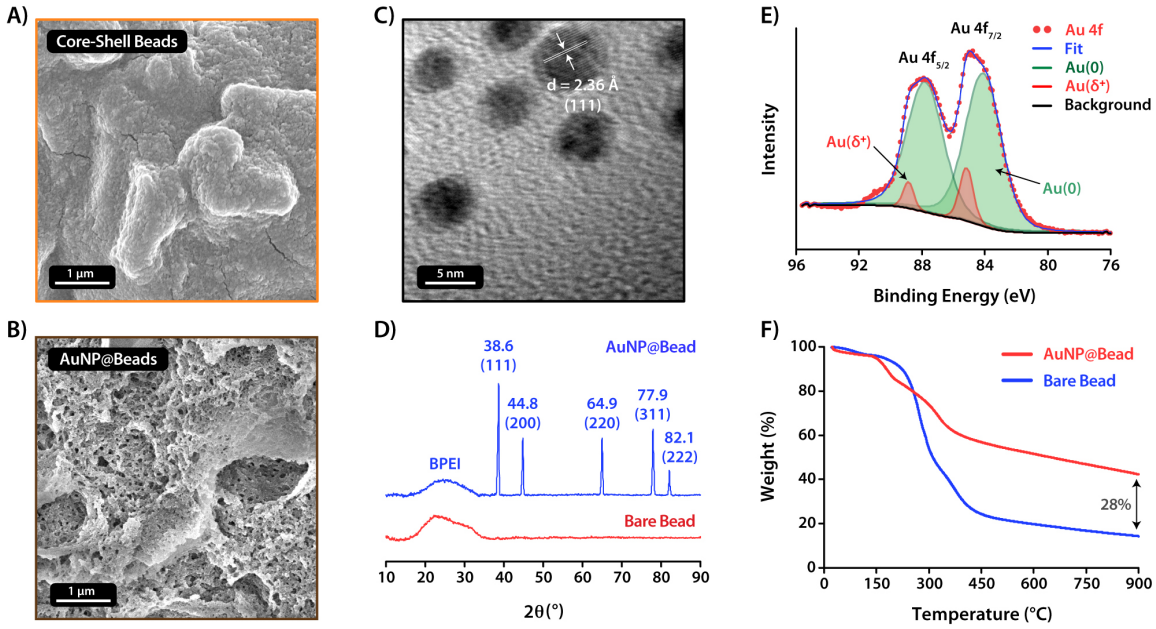

Figure 5.5 FESEM images showing surface morphology changes of the beads A) Before, and B) After AuNP formation, C) HRTEM image of the AuNP synthesized over a duration of 1 hour, D) XRD patterns of bare and AuNP-embedded beads, E) High-resolution XPS spectra of Au 4f, and F) TGA profiles of the bare and AuNP-embedded core shell beads.

X-ray Photoelectron Spectroscopy (XPS) was conducted to probe the oxidation states of the surface-bound gold species (Figure 5.5E). The high-resolution Au 4f spectrum exhibited a spin-orbit doublet at 84.1 eV and 87.8 eV, attributable to metallic gold (Au^0).[329, 330] However, the spectral profile could not be adequately modeled with a single doublet, indicating the coexistence of multiple oxidation states. A second doublet, with peaks at 85.2 eV and 88.9 eV, was observed and attributed to partially oxidized gold species ($Au^{\delta+}$).[331] This partial oxidation is likely induced by the strong electron-withdrawing nature of sulfonate groups in the BPEI matrix, which can deplete electron density from surface Au^0 atoms, shifting their binding energies to higher values.[332] Quantitative integration of the peak areas revealed that Au^0 and $Au^{\delta+}$ comprised 90.9% and 9.1% of the total gold content,

respectively. The coexistence of metallic and partially oxidized species may influence the electronic structure and catalytic behavior of the AuNPs. Finally, Thermogravimetric Analysis (TGA) was performed to assess the thermal stability and AuNP loading efficiency (Figure 5.5F). Minimal mass loss occurred up to 140 °C due to the release of moisture and trapped gases. Beyond this, the total mass loss for the unmodified and AuNP-loaded beads was found to be 85.7% and 57.7%, respectively. This indicates that the gold nanoparticles accounted for approximately 28% of the total dry mass of the AuNP@Beads, further supporting the successful and substantial incorporation of AuNPs onto the sulfonated hydrogel support.

5.2.2 The non-plasmonic oxidase-like activity of the AuNP

To evaluate the catalytic performance of gold nanoparticles (AuNPs) embedded on the surface of the core-shell hydrogel beads, the oxidation of the chromogenic substrate 3,3′,5,5′-tetramethylbenzidine (TMB) to 3,3',5,5'-tetramethylbenzidine diimine was systematically investigated by monitoring the emergence of its characteristic absorption peak at 652 nm using UV-visible spectroscopy.[59, 333] The AuNPs were fabricated in-situ on the bead surface over different growth durations to optimize their catalytic properties. As anticipated, control beads lacking AuNPs showed no catalytic activity, confirming the essential role of the embedded Au-nanostructures (Figure 5.6A; Beads without AuNP growth (0 hours) are referred to as control beads). In contrast, beads bearing AuNPs grown for at least 1 hour exhibited pronounced catalytic activity, capable of oxidizing TMB in the absence of both hydrogen peroxide (H_2O_2) and external light illumination (Figure 5.6A). This observation indicates the presence of intrinsic oxidase-like activity in the AuNP@Beads system. Interestingly, a marginal decline in catalytic efficiency was observed when the AuNP growth period was extended beyond 1 hour, up to 3 hours. This decline is likely attributable to the previously noted increase in nanoparticle size, which leads to a lower surface-to-volume ratio and, consequently, fewer accessible catalytic sites.[235] Consequently, beads with AuNPs grown for 1 hour were selected for all subsequent experiments to ensure optimal catalytic performance. Recognizing the critical role of pH in regulating the catalytic activity of metal-based nanocatalysts, the oxidase-like behavior of the AuNP@Beads was further examined across a wide range of pH (2-10, Figure 5.6B). The system exhibited a clear pH-dependent activity profile, with optimal catalytic performance observed in the mildly acidic range of pH 4–5. Time-dependent UV–Visible spectral analysis in a buffer of pH 5 demonstrated a pronounced and progressive increase in absorbance at 652 nm, corresponding to the oxidized TMB product (Figure 5.6C). This result underscores the robust oxidase-like catalytic activity of the AuNP@Beads under mildly acidic conditions. To probe the substrate versatility of the catalytic system, the oxidation of other chromogenic substrates,

including ortho-phenylenediamine (OPD) and 2,2′-azino-bis(3-ethylbenzothiazoline-6-sulfonic acid) (ABTS), was assessed (Figure 5.6D). In both cases, efficient oxidation to their respective colored products was observed, highlighting the broad substrate affinity and catalytic competence of the embedded AuNPs. The catalytic performance of the AuNP@Beads was quantitatively analyzed using Michaelis–Menten kinetics, resulting in a maximum reaction rate (V_{max}) of 5.07 × 10^{-4} mM·s^{-1} and a Michaelis constant (K_m) of 1.86 mM (Figure 5.6E). These values are comparable to, and in some cases exceed, those reported for other oxidase-mimetic nanocatalysts (comparison table, Table 5.1), thereby underscoring the promising catalytic potential of the present system.

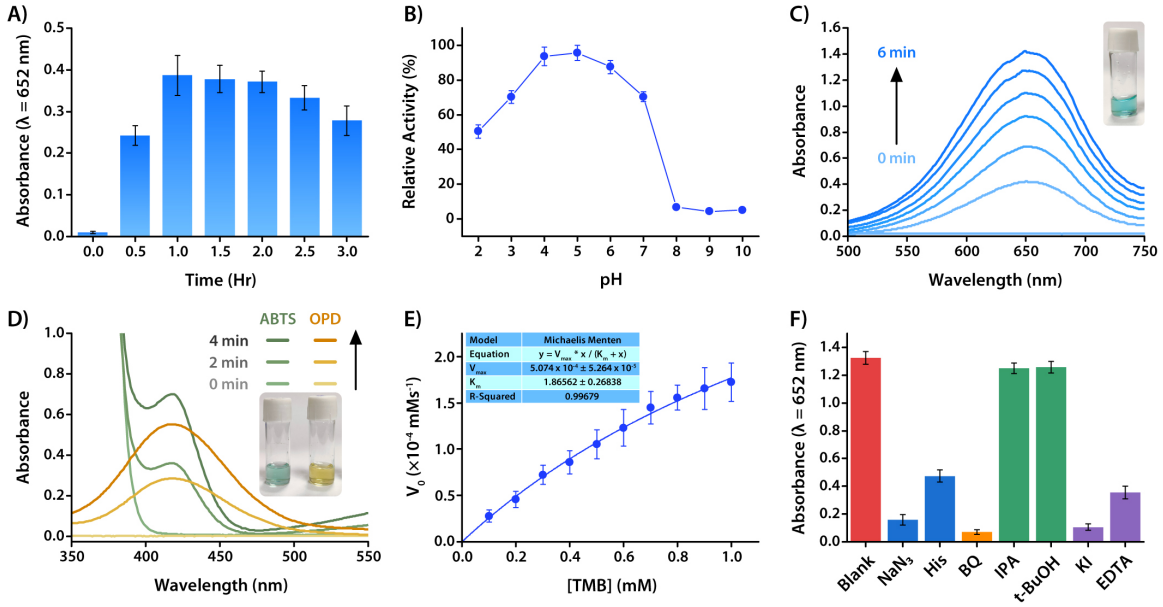

Figure 5.6 Evaluation of the oxidase-like catalytic activity of AuNP-embedded hydrogel beads. A) Comparison of the absorbance intensity at 652 nm for the oxidized TMB charge-transfer complex, generated by the oxidation of TMB using AuNP@Beads synthesized via in situ growth of AuNPs on the bead surface over varying reaction times, B) pH-dependent variation in catalytic activity, C) Time-resolved UV–Vis spectra for the oxidation of TMB (1 mM), and D) Oxidation of OPD and ABTS by AuNP@Beads in pH 5 buffer. Inset: Photographs of the vials showing the final colors after the oxidation of the respective substrates, E) Michaelis–Menten kinetic analysis of the catalytic oxidation, and F) Influence of various reactive oxygen species scavengers on TMB oxidation.

The oxidase-like catalytic behavior of the AuNPs is primarily attributed to their ability to generate reactive oxygen species (ROS).[334] To gain deeper insights into the underlying mechanism, a series of targeted scavenger assays was carried out to identify the specific ROS responsible for TMB oxidation (Figure 5.6F). A notable decrease in the absorbance of oxidized TMB was observed when singlet oxygen scavengers such as sodium azide (NaN_3)[286] and histidine[287] were introduced, indicating the involvement of singlet oxygen ($^1O_2$). Similarly, *p*-benzoquinone (BQ),[288] which selectively scavenges superoxide radicals ($O_2•^-$), and potassium iodide (KI)[289] and ethylenediaminetetraacetic acid (EDTA),[290] which quench positive holes, also significantly inhibited the catalytic reaction. In contrast,

the inclusion of hydroxyl radical(•OH) scavengers like isopropyl alcohol (IPA)[291] and tert-butyl alcohol (t-BuOH)[292] had negligible influence on the oxidation of TMB. These results collectively suggest that singlet oxygen, superoxide radicals, and positive holes are the principal reactive species responsible for driving the oxidase-like activity of the AuNP-embedded hydrogel beads.

Catalytic Material	V_{max} ($M.s^{-1}$)	K_m (mM)	Reference
CeO_2 NPs (5 nm)	7.00×10^{-7}	3.8	*Angew. Chem. Int. Ed.,* 2009, **48**, 2308-2312
Se NPs	5.10×10^{-8}	8.3	*J. Nanopart. Res.,* 2016, **18**, 74
Fe-N-C SAzymes	6.10×10^{-8}	1.81	*Small,* 2019, **15**, 1903108
Nanoceria	1.00×10^{-7}	0.42	*Chem. Commun.,* 2019, **55** (16), 2285-2288
Pd-Cage	7.08×10^{-8}	0.24	*J. Am. Chem. Soc.,* 2020, **142**, 18981- 18989
Heme-AuNP/Al^{3+}	6.93×10^{-8}	1.83	*ACS Sustain. Chem. Eng.,* 2022, **10**, 16670–16680
Gold nanostars embedded hydrogel beads (Previous Work)	1.13×10^{-7}	1.77	*J. Mater. Chem. B,* 2025,**13**, 1079-1088
Gold nanoparticles embedded hydrogel beads	5.07×10^{-7}	1.86	This work

Table 5.1 Comparison of catalytic performance of previously reported oxidase-mimetic catalytic materials.

To further substantiate the proposed catalytic mechanism, a series of probe-based fluorescence and UV–Vis absorption assays were employed. Terephthalic acid (TA), a well-established fluorescent probe for hydroxyl radicals (•OH), emits a characteristic fluorescence at 435 nm upon interaction with •OH species.[279] When TA was incubated with AuNP@Beads in the presence of hydrogen peroxide (H_2O_2), no fluorescence emission was observed, effectively excluding the generation of hydroxyl radicals and thereby ruling out peroxidase-like catalytic behavior (Figure 5.7A). In contrast, the singlet oxygen ($^1O_2$)-specific probe 3,3′-diaminobenzidine (DAB) exhibited a marked increase in absorbance at 460 nm upon exposure to AuNP@Beads, clearly indicating the production of $^1O_2$ (Figure 5.7B).[321] Additionally, when DAB oxidation was carried out in the presence of KI and BQ, scavengers of positive holes and superoxide radicals, respectively, a substantial decrease in absorbance was recorded (Figure 5.7C). This strongly suggests that both positive holes and superoxide radicals are critically involved in the generation of singlet oxygen during the catalytic process.

Although the scavenger studies highlight the roles of $O_2^{\bullet -}$ and positive holes in the catalytic cycle, the observed singlet oxygen generation, even in dark conditions, excludes the involvement of a plasmon-mediated mechanism based on light-induced electron-hole pair formation. Instead, the oxidase-like activity of the AuNP@Beads originates from their unique surface electronic structure, modulated by the sulfonate-rich polymeric shell of the hydrogel beads. The electron-withdrawing sulfonate ($-SO_3^-$) ligands anchored on the polymer scaffold partially oxidize surface Au^0 atoms, resulting in the formation of positively charged $Au^{\delta+}$ species (Figure 5.7D).[332] These electron-deficient sites introduce catalytically active surface defects that promote redox activity.[335] This ligand-induced electronic modulation facilitates the transfer of electrons from the AuNP surface to adsorbed molecular oxygen, generating superoxide radicals ($O_2^{\bullet -}$).[336, 337] A redox recombination process then occurs on the nanoparticle surface, wherein $Au^{\delta+}$ sites (serving as hole equivalents) accept electrons from $O_2^{\bullet -}$, culminating in the formation of singlet oxygen ($^1O_2$).[59] The negatively charged polymeric shell not only enhances electron transfer but also enriches local concentrations of both oxygen and organic substrates around the AuNP surface, thus amplifying catalytic efficiency. This mechanism enables effective oxidase-like catalysis under ambient, light-independent conditions.

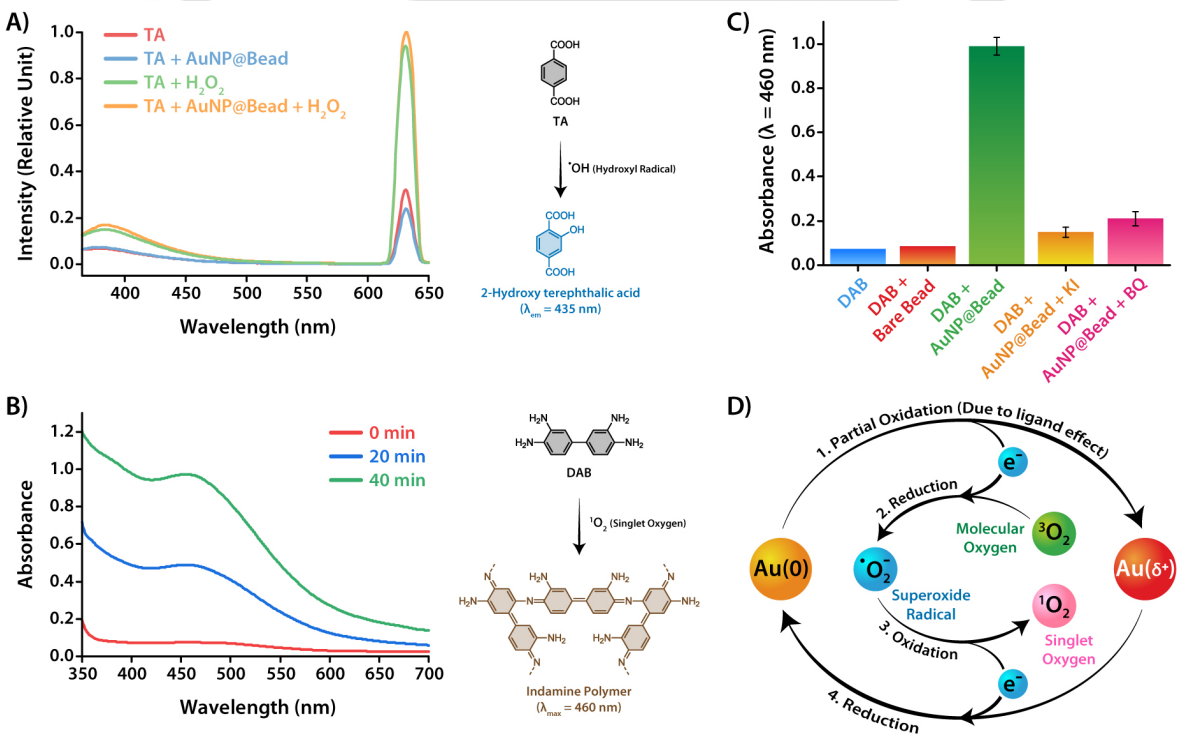

Figure 5.7 A) Fluorescence spectra of the TA assay for detecting hydroxyl radicals, B) UV-Visible spectra of the DAB assay for detecting singlet oxygen, and B) Comparison of the DAB assay under light and dark conditions, C) Comparison of the DAB absorbance intensity at 460 nm for evaluating singlet oxygen generation by control bare beads and catalytically active AuNP@Beads, in the presence of KI (positive holes scavenger), BQ

(superoxide radical scavenger), and in the absence of any scavenger, and D) Schematic representation of the proposed mechanism underlying the oxidase-like activity of AuNPs.

5.2.3 Oxidative degradation of phenolic pollutants and dyes

Phenolic derivatives, frequently found in industrial effluents, are persistent and toxic pollutants that threaten both ecosystems and human health. Consequently, devising stable and efficient catalytic methods for the oxidative degradation of phenolic pollutants is a key focus in advancing sustainable environmental remediation technologies. In this study, we leveraged the oxidase-mimetic catalytic activity of gold nanoparticle-embedded core-shell hydrogel beads (AuNP@Beads) to oxidize a wide range of phenolic compounds. For spectrophotometric and visual monitoring, the reactions were carried out in the presence of 4-amino antipyrine (4-AP), which forms a red quinone-imine chromophore upon reacting with the oxidized phenolic intermediates (Figure 5.8A). The resulting complex exhibits a distinct absorbance peak at 510 nm, enabling convenient monitoring of the oxidation process. For initial assessment, 2,4-dichlorophenol (2,4-DP) was chosen as a model substrate to assess the oxidase-like catalytic activity of the AuNP@Beads under mildly acidic conditions (pH 5). Although neither 2,4-DP nor 4-AP absorb in the visible region, time-resolved UV–Visible spectroscopy revealed a gradual emergence of the 510 nm peak upon exposure to the catalyst, signifying the formation of the oxidation product (Figure 5.8B). The kinetic parameters obtained from Michaelis–Menten analysis ($V_{max} = 3.25 \times 10^{-4}$ mM·s^{-1}; $K_m = 0.73$ mM) suggest that the embedded gold nanoparticles exhibit a high catalytic efficiency (Figure 5.8C).

Encouraged by these results, the catalytic platform was further tested against a diverse set of phenolic compounds. Oxidation efficiency was evaluated by measuring the absorbance at 510 nm for various concentrations of substrates (Figure 5.8D). While the AuNP@Beads effectively catalyzed oxidation of all tested phenolic compounds, namely 4-methoxyphenol (4-MP), hydroquinone (HQ), 1-naphthol, phenol, pyrogallol, 2-aminophenol (2-AP), and 4-nitrophenol (4-NP), compounds bearing electron-donating substituents were oxidized more readily than those with electron-withdrawing groups, consistent with the electronic effects on the oxidation potential.[338] These findings emphasize the robustness and versatility of the AuNP@Beads as a heterogeneous catalyst for treating phenol-based organic pollutants.

Given their promising oxidase-mimetic activity, we next explored the potential of AuNP@Beads for colorimetric detection of biologically significant catecholamines, namely dopamine (DA) and epinephrine (EP), both of which possess redox-active catechol moieties. DA plays a critical role as a neurotransmitter, with dysregulation implicated in conditions such as attention-deficit hyperactivity disorder (ADHD), schizophrenia, depression, and neurodegenerative diseases like Parkinson's and Alzheimer's.[339] EP is an essential hormone and neurotransmitter used in clinical

management of asthma, cardiac arrest, anaphylaxis, and bleeding disorders.[340] Upon exposure to AuNP@Beads, colorless aqueous solutions of both DA and EP underwent oxidation, leading to a visible dark brown color. Time-resolved UV–Vis analysis demonstrated progressive increases in absorbance at 475 nm for DA (Figure 5.8E) and 485 nm for EP (Figure 5.8G). Quantification revealed a linear correlation between absorbance and analyte concentration over the range of 0–0.2 mM, with limits of detection (LOD) of 2.79 μM for DA (Figure 5.8F) and 5.55 μM for EP (Figure 5.8H), calculated based on the 3σ/k method (where σ is the standard deviation of the response, and k is the slope of the linear fit). The sensitivity and operational simplicity of this method demonstrate its suitability for point-of-care (PoC) diagnostic applications.

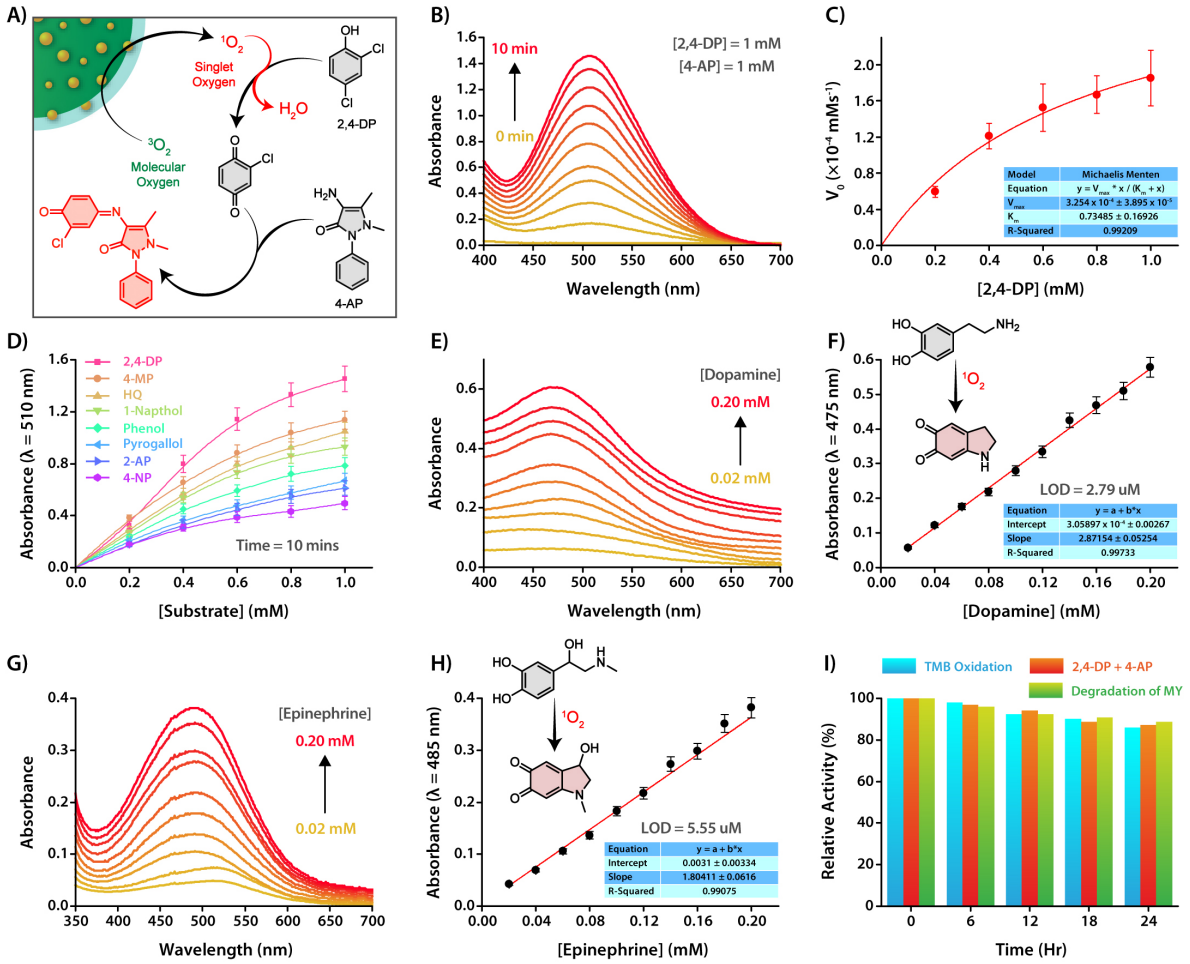

Figure 5.8 Singlet oxygen-mediated catalytic oxidation by AuNP@Beads. A) Schematic illustration of the reaction mechanism, B) Time-resolved UV–Vis spectra, and C) Michaelis–Menten kinetic analysis for the AuNP@Bead-catalyzed oxidative coupling of 2,4-DP (1 mM) with 4-AP (1 mM), D) Oxidation of various phenolic substrates tracked via quinone imine formation at 510 nm; lines are provided as a visual aid, E and F) Catalytic oxidation of dopamine by AuNP@Beads, showing a concentration-dependent increase in absorbance at 475 nm, G and H) Epinephrine oxidation showing a linear relationship between absorbance at 485 nm and epinephrine concentration, and I) Catalytic performance of AuNP@Beads in pH 5 buffer for TMB oxidation, 2,4-DP/4-AP coupling, and methyl orange (MO) degradation after subjecting the beads to continuous agitation in water for varying time durations.

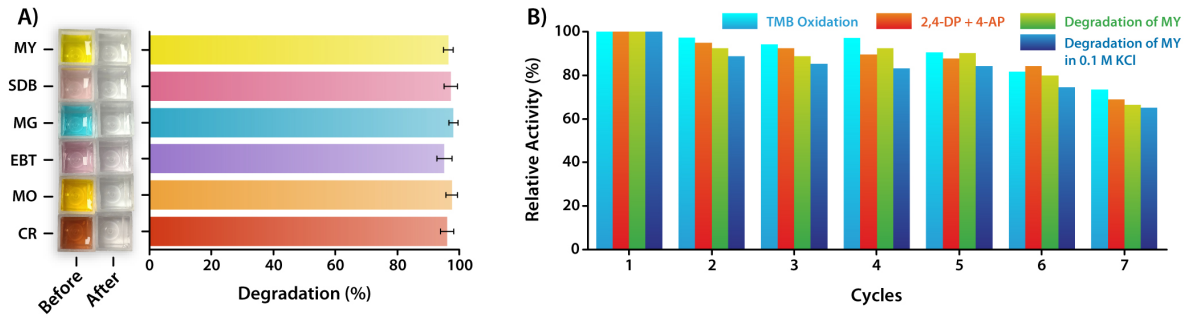

Figure 5.9 A) Photographs and corresponding degradation efficiency plots of different dyes (40 μM solution in 1 mL pH 5 buffer) treated with AuNP@Beads for 1 hour, and B) Recyclability study showing catalytic performance over multiple cycles for TMB oxidation, 2,4-DP/4-AP coupling, and methyl orange (MY) degradation in pH 5 buffer, with and without 0.1 M KCl.

To further demonstrate the environmental remediation potential of this catalytic platform, AuNP@Beads were used to degrade structurally diverse azo and triarylmethane dyes, including Metanil Yellow (MY), Solochrome Dark Blue (SDB), Malachite Green (MG), Eriochrome Black T (EBT), Methyl Orange (MO), and Congo Red (CR). Each dye, prepared as a 40 μM solution in 1 mL pH 5 buffer, was individually treated with a single AuNP@Bead, and all six structurally diverse dyes exhibited efficient oxidative degradation upon treatment (Figure 5.9A). The degradation process was further examined using time-resolved UV–Visible spectroscopy (Figure 5.10). Prior to oxidation, each dye displayed a distinct absorption band in the visible region, characteristic of its extended conjugated π-system. Following catalytic treatment, a gradual decrease in absorbance associated with these chromophores was observed, indicating cleavage or disruption of the conjugated backbone and effective decolorization. Simultaneously, the appearance of new absorption bands at shorter wavelengths (typically below 300 nm) was observed, attributable to the formation of lower molecular weight, less-conjugated aromatic degradation products.[341, 342]

Among the tested dyes, Eriochrome Black T (EBT) exhibited the fastest decolorization, completing within just 1 minute. Solochrome Dark Blue (SDB) and Metanil Yellow (MY) followed, with complete degradation observed at 8 and 16 minutes, respectively. Methyl Orange (MO) and Malachite Green (MG) required slightly longer durations of 25 and 30 minutes, while Congo Red (CR) showed the slowest response, achieving full decolorization in 35 minutes. The ability of the AuNP@Bead to catalyze the oxidative degradation of a wide range of dyes under ambient conditions highlights its broad-spectrum oxidase-like activity and potential utility in wastewater treatment and environmental remediation. Control experiments using bare beads without gold nanoparticles showed negligible changes in dye absorbance even after one hour, confirming that the observed decolorization stemmed from catalytic activity rather than passive adsorption (Figure 5.11).[58]

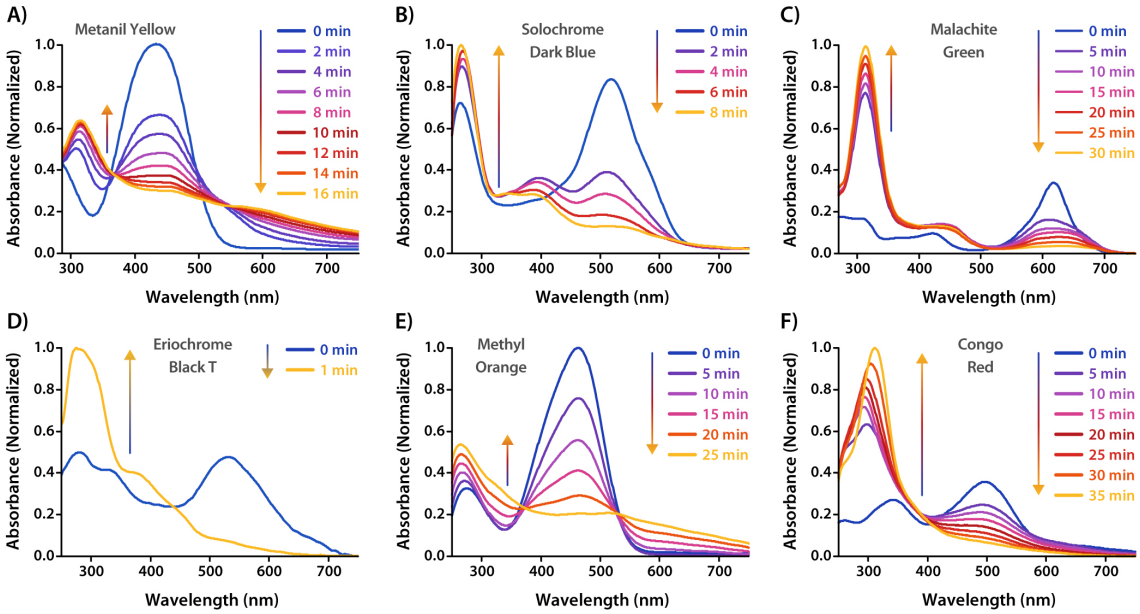

Figure 5.10 Time dependent UV–Visible spectra for the catalytic degradation of A) Metanil Yellow, B) Solochrome Dark Blue, C) Malachite Green, D) Eriochrome Black T, E) Methyl Orange, and F) Congo Red.

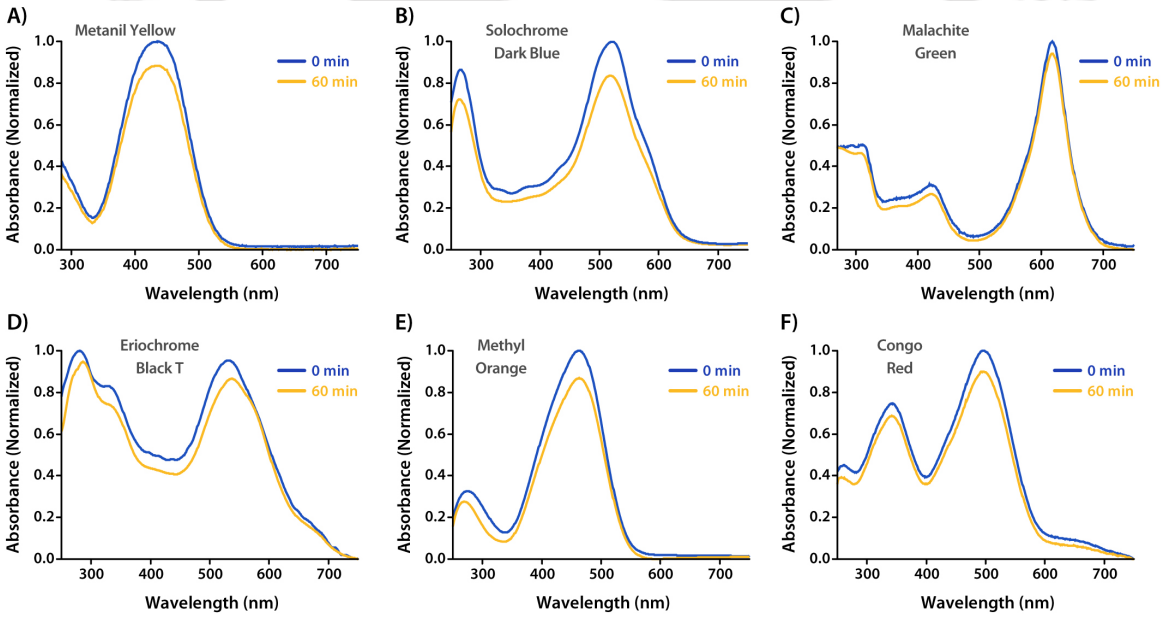

Figure 5.11 Comparison of the UV–visible spectra of A) Metanil Yellow, B) Solochrome Dark Blue, C) Malachite Green, D) Eriochrome Black T, E) Methyl Orange, and F) Congo Red after 1-hour treatment with bare, unfunctionalized SO_4-BPEI beads.

Despite the well-documented catalytic potential of AuNPs, their practical application is often hindered by issues such as aggregation, leaching, and poor reusability under harsh conditions. To assess the stability of the embedded nanoparticles, several durability studies were performed. Continuous agitation of AuNP@Beads in water for 24 hours showed a negligible loss in catalytic activity, suggesting strong immobilization of the nanoparticles within the polymer matrix (Figure

5.8I). FESEM and EDX analyses after multiple catalytic cycles confirmed the uniform distribution of AuNPs on the bead surface (Figure 5.12). Furthermore, atomic absorption spectroscopy of the post-reaction solution detected minimal gold leaching, reaffirming the structural integrity of the catalyst. The beads also offered practical advantages in terms of reusability. They could be easily recovered, rinsed with water, and reused for successive catalytic cycles. The beads retained consistent activity over five cycles for the oxidation of TMB, 2,4-DP, and MY degradation, and retained over 70% activity even after seven cycles (Figure 5.9B). Furthermore, to examine colloidal stability under ionic stress, catalytic activity was tested in 0.1 M KCl, a condition known to induce nanoparticle aggregation.[216, 217] Remarkably, AuNP@Beads retained their catalytic function with negligible activity loss compared to aqueous conditions, even after multiple cycles (Figure 5.9B). This resilience is attributed to the covalently grafted sulfonated BPEI polymeric layer that prevents nanoparticle aggregation and secures them firmly onto the bead surface. Together, these results highlight the superior stability, reusability, and catalytic efficiency of AuNP@Beads, making them a highly promising platform for sustainable environmental remediation and biosensing applications.

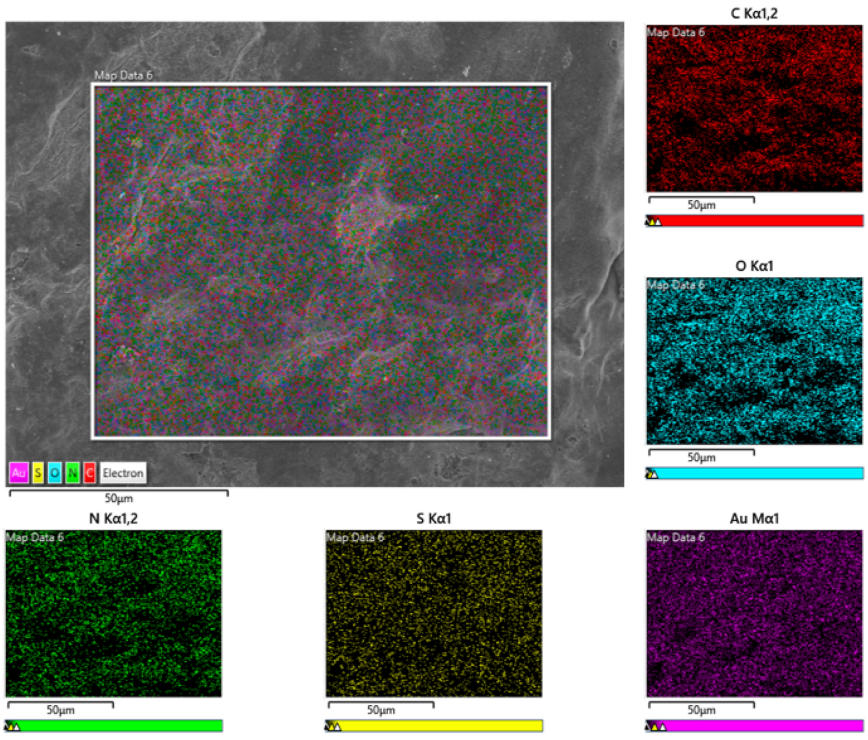

Figure 5.12 EDX elemental mapping of the surface of the AuNP embedded bead after catalytic cycles.

5.2.4 ROS-induced bacterial inactivation

Several antimicrobials are known to exert their bactericidal effects through a ROS-mediated pathway.[234, 343] Given the strong ROS generation capability of the AuNP@Beads, their antibacterial potential was systematically evaluated. To assess their broad-spectrum bactericidal efficacy,

representative Gram-negative and Gram-positive bacterial strains, *Escherichia coli (E. coli)* and *Staphylococcus aureus (S. aureus)*, respectively, were selected for the study. Initially, the antibacterial performance was evaluated using an agar well diffusion assay.[60] AuNP@Beads were introduced into wells on agar plates inoculated with bacterial cultures, followed by incubation at 37 °C for 24 hours. Clear and prominent zones of inhibition measuring approximately 1.5 cm and 1.0 cm in diameter were observed surrounding the AuNP@Beads against both *E. coli* (Figure 5.13A) and *S. aureus* (Figure 5.13H), respectively, indicating effective bactericidal activity. In contrast, no inhibition zones were detected in the presence of BPEI-coated beads or SO_4-BPEI-coated beads (Figure 5.13B, 5.13I) under identical experimental conditions, suggesting that the antimicrobial effect was specifically attributable to the embedded AuNPs.

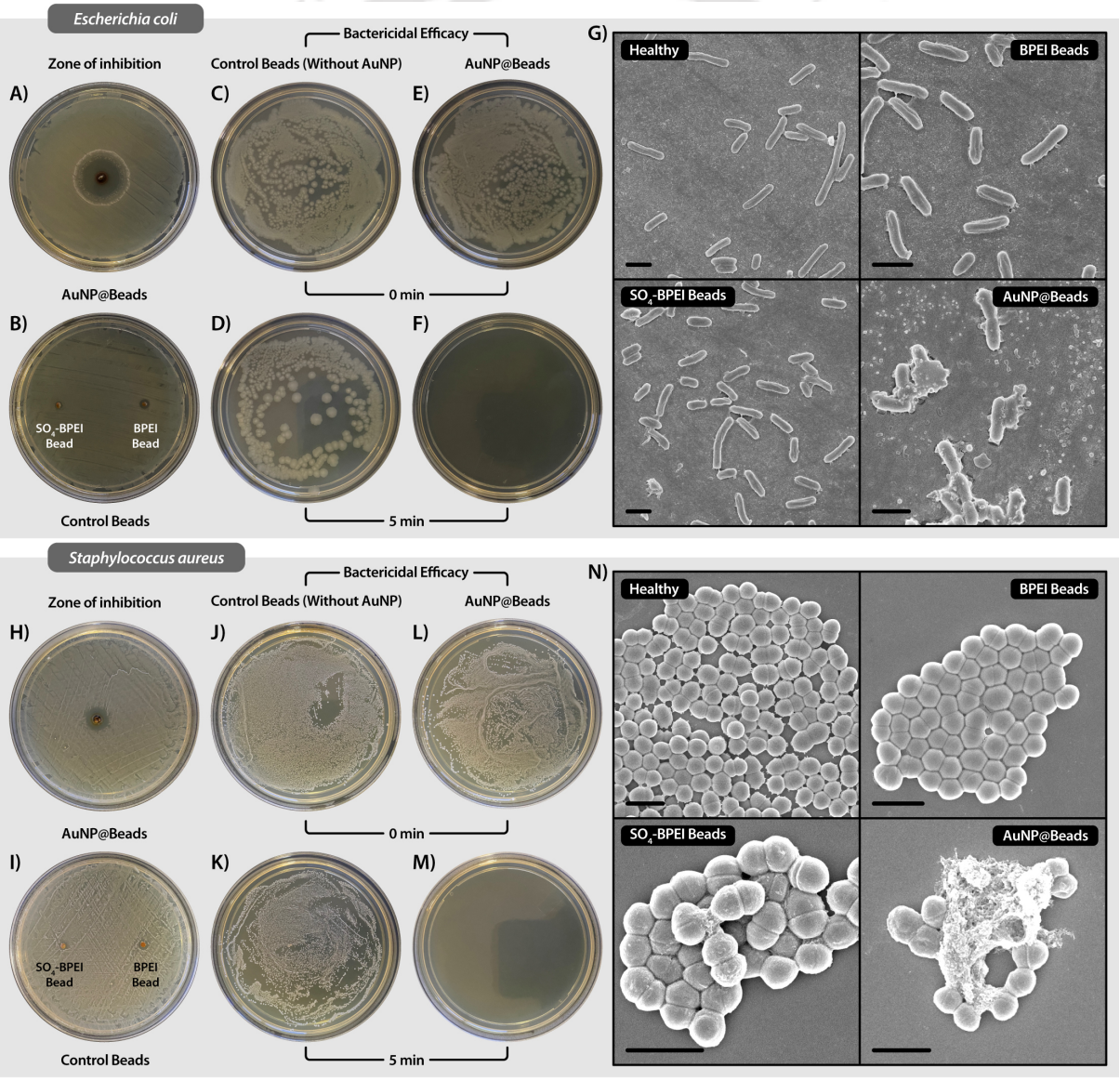

Figure 5.13 Antibacterial Efficacy of AuNP@Beads. Digital images illustrating: (A, H) Antibacterial activity of AuNP@Beads against *E. coli* and *S. aureus*, showing visible zones of inhibition; (B, I) Control beads showing no antibacterial effect; (C–F, J–M) *E. coli* and *S. aureus* inactivation studies using control and AuNP@Beads before

and after 5 minutes of incubation; (G, N) FESEM images of *E. coli* and *S. aureus* cells treated with control and catalytic beads. Scale for FESEM images: 2 µm

To further substantiate the bactericidal potential of the AuNP@Beads, their efficacy was tested in a bacterial suspension system mimicking contaminated water.[344] Simulated bacterial solutions containing ~10^5 cfu/mL of *E. coli* and *S. aureus* were prepared in phosphate-buffered saline (PBS), and treated separately with the different bead formulations. Upon treatment with BPEI-coated or SO_4-BPEI-coated control beads, negligible changes were observed in bacterial concentrations even after extended exposure, indicating their inert nature (Figure 5.13C-D, 5.13J-K, and 5.14A-B). However, upon treatment with AuNP@Beads, an almost complete reduction in viable bacterial count was recorded within 5 minutes for both strains (Figure 5.13E-F, 5.13L-M, and 5.14C). Notably, when tested under light illumination, the AuNS@Beads (reported in Chapter 4) exhibited a similar bactericidal effect, rapidly eliminating both bacterial strains through photocatalytic ROS generation (Figure 5.14C). This rapid and efficient inactivation of both *E. coli* and *S. aureus* highlights the robust antimicrobial capability of the AuNP-embedded beads, attributed to the oxidative stress induced by the catalytically generated ROS, particularly singlet oxygen ($^1O_2$).

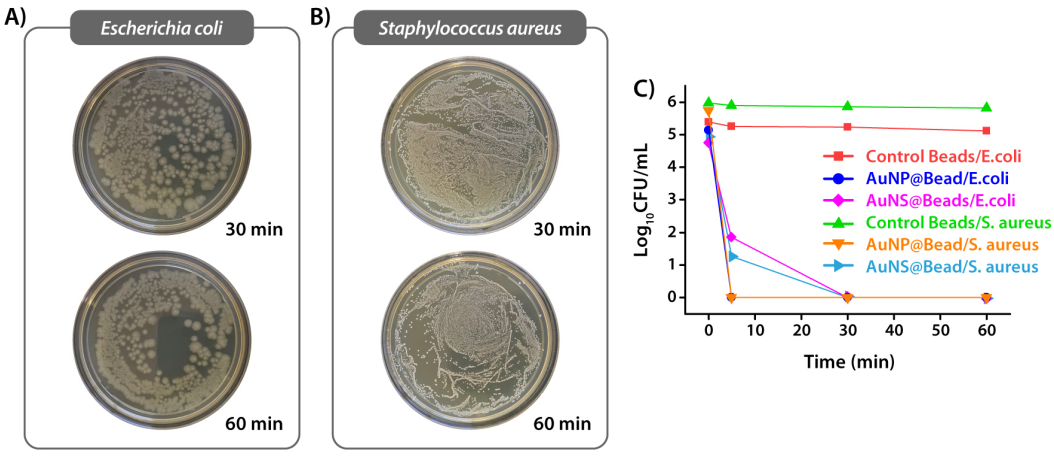

Figure 5.14 Digital images showing the effects of control beads against A) *E. coli* and B) *S. aureus*, following extended incubation for 30 and 60 minutes, C) Time-dependent bactericidal kinetics of control beads, AuNP@Beads and AuNS@Beads against *E. coli* and *S. aureus.*

To corroborate the bactericidal effect visually, FESEM was employed to examine the morphological state of the bacterial cells post-treatment. Untreated *E. coli* cells in PBS appeared healthy, exhibiting typical elongated rod-shaped morphology with smooth surfaces and intact membranes (Figure 5.13G). Similar morphology was retained following treatment with either BPEI-coated or SO_4-BPEI-coated beads, confirming their non-toxic nature. In stark contrast, *E. coli* cells treated with AuNP@Beads displayed severely deformed and irregularly shaped surfaces, accompanied by partial wrinkling and membrane disruption. These structural damages are consistent with extensive oxidative damage induced by ROS, leading to compromised membrane integrity and leakage of

intracellular contents, ultimately causing bacterial cell death. Analogous morphological disruption was also observed in *S. aureus* cells treated with AuNP@Beads, corroborating the broad-spectrum antibacterial activity of the catalytic beads (Figure 5.13N). These findings collectively underscore the strong oxidative bactericidal effect of the AuNP@Beads, mediated by the generation of singlet oxygen through their intrinsic oxidase-like activity. The demonstrated ability of these beads to rapidly and effectively inactivate pathogenic bacteria in aqueous systems highlights their potential as promising candidates for application in bacterial decontamination and water purification technologies.

5.2.5 Phyto-compatibility assessment of remediated wastewater

To evaluate the practical utility of AuNP@Beads in real-life wastewater decontamination, a study was conducted using a simulated wastewater system containing a mixture of phenolic pollutants and synthetic dyes. This model wastewater was designed to replicate the complexity of industrial effluents that frequently contain multiple classes of organic contaminants. An aqueous solution containing four representative phenolic compounds namely phenol, p-nitrophenol, 2-aminophenol and 4-methoxyphenol, along with three representative dyes namely Methyl Orange, Eriochrome Black T and Congo Red, was prepared. The simulated wastewater was divided into two equal portions: one was directly used for plant cultivation studies (Figure 5.15A), and the other was subjected to catalytic treatment using AuNP@Beads for 3 hours before being employed for plant cultivation.

Following the catalytic treatment, a significant fading of color was observed in the treated solution, visually indicating the catalytic degradation of the dyes and phenolic compounds (Figure 5.15B). This observation was a clear preliminary confirmation of the efficacy of AuNP@Beads in breaking down toxic organic components via catalytic oxidation. The decontaminated water was then repurposed for irrigation, and its phyto-compatibility was evaluated by comparing the growth of green gram (*Vigna radiata*) sprouts cultivated in both treated and untreated wastewater samples under identical growth conditions. After two days of incubation, a significant difference in plant morphology was observed. Sprouts grown using the decontaminated water reached an average height of approximately 10 cm, demonstrating healthy and accelerated growth (Figure 5.15C). In stark contrast, the sprouts grown in untreated wastewater showed negligible development, with an average height of only around 3 cm. Over a 5-day period, this disparity became even more evident. Plants grown in decontaminated water exhibited robust growth, achieving heights of up to 17 cm and showing vigorous shoot development. Meanwhile, those irrigated with the contaminated water continued to display stunted growth, reaching only about 6 cm in height. These results indicated

that the decontaminated water was not only non-toxic but also phyto-compatible, supporting healthy plant development.

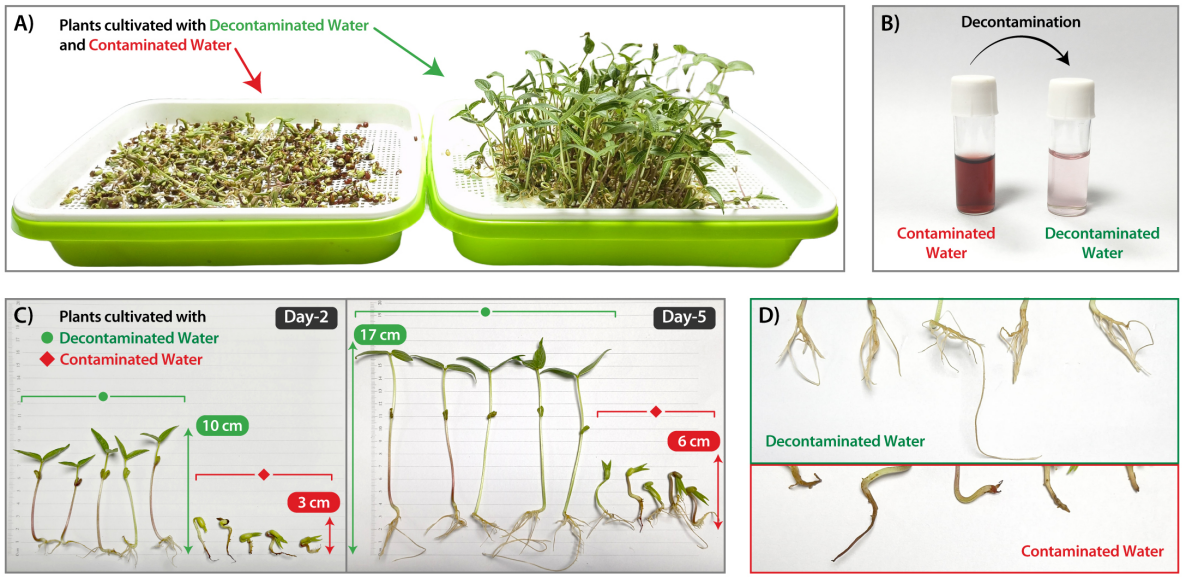

Figure 5.15 Phyto-compatibility Studies. Digital images showing: (A) Plants cultured with contaminated (left) and decontaminated (right) water; (B) The color of simulated wastewater (left) and decontaminated water (right); (C) Plant growth (length) after 2 and 5 days using contaminated and decontaminated water; (D) Root development of plants after 5 days of cultivation with contaminated and decontaminated water.

In addition to shoot growth, root development was also significantly affected by water quality. After 5 days, plants irrigated with the purified water had developed long and healthy roots, indicative of efficient nutrient uptake and a favorable growth environment (Figure 5.15D). In contrast, the roots of plants exposed to untreated wastewater were short and exhibited a reddish coloration due to dye absorption, suggesting the detrimental impact of phenolic and dye pollutants on plant metabolism and root development. These findings suggest that phenolic pollutants and synthetic dyes in wastewater can severely impede plant development by introducing toxic stress, limiting nutrient absorption, and adversely affecting root morphology. In contrast, water treated with AuNP@Beads, free from such toxicants, provided a significantly cleaner and safer medium for plant cultivation, thereby enhancing both shoot and root development.

5.3 Conclusion

This study presents an effective approach to sustainable water purification using a non-plasmonic gold nanocatalyst embedded in peptide-based core-shell hydrogel beads. This system operates efficiently under ambient, dark conditions, eliminating the need for external light sources typically required for plasmonic photocatalysis. The sulfonate-functionalized surface of the hydrogel modifies the electronic environment of the gold nanoparticles, enabling intrinsic oxidase-like activity that can degrade various organic pollutants, including phenolic compounds and azo dyes

commonly found in industrial wastewater. The localized growth of gold nanoparticles on the hydrogel surface ensures efficient catalytic interactions while minimizing nanoparticle leaching. The hydrogel's mechanical stability and ease of recovery contribute to its reusability over multiple cycles without significant loss of activity. Additionally, the system's antimicrobial properties help treat both chemical and biological contaminants, providing a comprehensive solution for water treatment.

With a simple fabrication process, operational robustness, and adaptability to complex wastewater, this platform offers a scalable, environmentally friendly solution for water remediation. Its broad-spectrum activity, stability, and reusability make it suitable for use in resource-limited settings. This research supports the development of efficient, sustainable water purification technologies that can improve global clean water access and environmental health.

5.4 Experimental Section

5.4.1 Materials and Methods

Dipentaerythritol penta-/hexa-acrylate (5ACl), branched polyethylenimine (BPEI), 1-pyrenebutyric acid, 1,3-Propanesultone, and Tetrachloroauric(III) acid ($HAuCl_4$) were purchased from Sigma-Aldrich (USA). TMB, ABTS, OPD, TA, DAB, MY, Solochrome Dark Blue (SDB), MG, EBT, MO, CR, 4-MP, HQ, 1-naphthol, phenol, pyrogallol, 2-AP, and 4-NP were purchased from TCI, Japan. Rink amide MBHA resin, protected as well as unprotected amino acids, and coupling reagents were purchased from Novabiochem. HPLC-grade dimethylformamide (DMF), dichloromethane (DCM) and acetonitrile (ACN) were procured from Spectrochem (India) and Fisher Scientific (India). Solvents were dried whenever required according to the reported procedures. Milli-Q water with a conductivity of less than 2 μScm^{-1} was used for all sample preparations.

UV–Visible spectra were recorded using a PerkinElmer Lambda 365+ spectrophotometer, while fluorescence measurements were conducted on a Horiba Fluoromax 4 Plus spectrophotometer. Field Emission Scanning Electron Microscopy (FESEM) imaging and Energy Dispersive X-ray (EDX) mapping of freeze-dried samples were carried out using a Gemini SEM 300 (Sigma Zeiss) instrument. Field Emission Transmission Electron Microscopy (FETEM) analyses were performed using a JEOL 2100F microscope. For UV–Visible and FETEM analysis of the embedded AuNPs, an ethanolic suspension of freeze-dried and ground (hereafter referred to as "cryo-ground") AuNP-loaded beads was prepared via sonication. FTIR spectra of the freeze-dried beads were recorded on a PerkinElmer instrument under ambient conditions. Powder X-ray Diffraction (XRD) analysis of the freeze-dried samples was performed using a Rigaku SmartLab diffractometer with a Cu-Kα radiation source (λ = 1.54 Å) operating at 9 kW. X-ray Photoelectron Spectroscopy (XPS) was conducted using a PHI 5000 Versa Probe III system (ULVAC-PHI Inc., Japan), equipped with a monochromatic Al Kα radiation source. Thermogravimetric analysis (TGA) was carried out on a Netzsch STA449F3A00 instrument. Atomic Absorption Spectroscopy (AAS) was performed using a Varian AA240 system.

5.4.2 Synthesis of PyKC

The peptide was synthesized on Rink amide MBHA resin following our previously reported protocol.[129, 131]

5.4.3 Fabrication of core-shell beads

The core-shell hydrogel beads were fabricated following our previously reported two-step protocol,[58, 59] with a third step added for further surface functionalization. Step 1: A 5 wt% solution of PyKC was prepared in 20 mM Tris buffer (pH 8) and loaded into a 1 mL syringe fitted with a 26G

needle. The syringe was left undisturbed at room temperature for 24 hours to allow hydrogel formation. The hydrogel was then extruded through the needle using gentle mechanical pressure. Due to the shear-thinning behavior of the PyKC hydrogel, the material emerging from the needle immediately re-gelled into spherical hydrogel droplets, which were collected directly into an ethanolic solution of 5ACl (1 g/mL) for surface functionalization. The beads were allowed to react with 5ACl for 15 minutes under gentle shaking at room temperature, then washed thoroughly with ethanol to remove unreacted or loosely bound 5ACl. Step 2: The acrylate-functionalized beads were treated with an ethanolic solution of branched polyethyleneimine (BPEI, 20 mg/mL) under shaking at room temperature for 15 minutes. Afterward, the beads were washed with ethanol to remove unreacted BPEI. This step enabled cross-linking at the surface and introduced primary amine functionalities. Step 3: The amine-functionalized beads were further treated with an aqueous solution of 1,3-propanesultone (50 mg/mL) under shaking at room temperature for 24 hours. The beads were then washed thoroughly with ethanol to remove any excess or residual reagents. This step introduced negatively charged sulfonic acid groups onto the bead surface.

5.4.4 XPS spectrum analysis

XPS spectra were analyzed using CasaXPS software (Version 2.3.23PR1.0, CasaSoftware Ltd., Teignmouth, UK). To account for any potential energy shifts, the energy scale of each spectrum was calibrated by aligning the C 1s peak maximum with the reference value of 284.8 eV, corresponding to the pure carbon substrate.[345] In accordance with standard procedures, peak fitting was performed without smoothing. A Shirley-type background was subtracted, and the peaks were fitted using a mixed Gaussian–Lorentzian profile with weighting factors of 70% Gaussian and 30% Lorentzian.[346] The percentage of Au(0) and Au(δ^+) was determined by integrating the area under their respective Au 4f doublets. Using the known $4f_{7/2}$ to $4f_{5/2}$ intensity ratio (4:3),[345] the relative abundance was calculated as the ratio of each doublet's area to the total Au 4f peak area.

5.4.5 FTIR analysis of surface functionalisation

The functionalization of the bead surface with 5ACl, followed by BPEI and 1,3-propane sultone, was confirmed using FTIR spectroscopy of the freeze-dried beads after each functionalization step (Figure S1). The appearance of new peaks at 1407 cm^{-1} and 1730 cm^{-1}, corresponding to the asymmetric stretching vibration of the vinyl group and the stretching vibration of ester carbonyl groups, respectively, confirmed the successful attachment of 5ACl to the peptide hydrogel beads.[58, 59] As the peptide amide bonds remained unaffected during surface functionalization, the amide carbonyl stretching band at 1635 cm^{-1} was used as an internal standard. A relative decrease in the amine stretching band at 1541 cm^{-1} after 5ACl functionalization indicated that the free lysine amine

groups on the bead surface underwent a Michael addition reaction with the 5ACl molecules. Furthermore, since the ester groups of 5ACl do not participate in the subsequent functionalization reactions, a relative decrease in the peak intensity at 1407 cm^{-1} (C-H stretching of the vinyl groups) compared to the carbonyl stretching at 1730 cm^{-1} for the 5ACl ester groups indicated the Michael addition of BPEI with the residual 5ACl acrylate groups on the bead surface. Lastly, following the modification of BPEI polymers on the bead surface with 1,3-propanesultone, the intensity of the S=O peaks at 1030 and 1148 cm^{-1} increased significantly, indicating the successful functionalization of the bead surface with negatively charged sulfonate groups.[326]

5.4.6 In-situ formation of AuNPs on beads (fabrication of AuNP@Beads)

The AuNP@Beads were synthesized under thermal conditions following a previously reported protocol.[59] Briefly, 25 sulfonate-modified beads were continuously agitated in 1 mL of an aqueous $HAuCl_4$ solution (100 mM) at 70 °C for 1 hour. During the reaction, the bead color transitioned from light brown to deep brown, indicating the successful in situ formation of gold nanostructures on their surface. The resulting AuNP@Beads were then thoroughly washed with water to remove any residual reagents and loosely bound nanoparticles. Finally, the beads were stored at 4 °C for future use. The formation of gold nanoparticles within the BPEI-based polymeric shell was confirmed through a combination of UV–Visible spectroscopy and FETEM analysis.

5.4.7 Evaluation of pH-dependent oxidase activity

The pH-dependent oxidase-like activity of AuNP@Beads was evaluated by monitoring the oxidation of TMB using UV–Visible spectroscopy across a pH range of 2 to 10, using 20 mM buffer solutions. In a typical experiment, 1 µL of a 1 M TMB stock solution in DMSO (final concentration: 1 mM) was added to 1 mL of the respective buffer in a quartz cuvette (1 cm path length). The reaction was initiated by introducing a single AuNP@Bead into the cuvette, followed by thorough mixing. After a 3-minute incubation, UV–Vis spectra were recorded. All catalytic reactions were performed in triplicate, and the absorbance at 652 nm was used to quantify the relative oxidase activity of the AuNP@Beads under different pH conditions.

5.4.8 Spectrophotometric evaluation of oxidase-mimetic Activity

The oxidase-like activity of AuNP@Beads was assessed by spectrophotometrically tracking the oxidation of the chromogenic substrate TMB. Typically, 1 µL of a 1 M TMB stock solution in DMSO (final concentration: 1 mM) was added to 1 mL of 20 mM acetate buffer (pH 5) in a quartz cuvette (1 cm path length). The reaction was initiated by introducing a single AuNP@Bead into the solution, followed by thorough mixing. UV–Visible spectra were recorded at 1-minute intervals over a period

of 6 minutes. The progressive development of an absorbance band at 652 nm—characteristic of the oxidized TMB charge-transfer complex—confirmed the oxidase-mimetic activity of the beads. Similarly, the ability of AuNP@Beads to oxidize ABTS and OPD (1 mM each) further validated their intrinsic oxidase-like catalytic behaviour.

5.4.9 Kinetic evaluation of oxidase-mimetic catalysis

The oxidase-like activity of AuNP@Beads at pH 5 was assessed by spectrophotometrically monitoring the oxidation of TMB. Briefly, a single AuNP@Bead was placed into 1 mL of 20 mM acetate buffer (pH 5) in a quartz cuvette with a 1 cm path length. Varying amounts of TMB (1 µL of 0.2, 0.4, 0.6, 0.8, and 1.0 M stock solutions in DMSO, resulting in final concentrations of 0.2, 0.4, 0.6, 0.8, and 1.0 mM, respectively) were added to the solution. After thorough mixing, the mixture was allowed to equilibrate for one minute. The absorbance of the oxidized TMB charge-transfer complex was then measured at λ_{max} = 652 nm (with $\varepsilon_{652\ nm}$ = 39,000 $M^{-1}{\cdot}cm^{-1}$ in water). Catalytic experiments were conducted in triplicate, and the reaction kinetics were analyzed using nonlinear regression with GraphPad Prism 9 software, assuming Michaelis-Menten kinetics.

5.4.10 ROS scavenger study

To explore the generation of various reactive oxygen species (ROS) in the system, a ROS scavenger study was performed. In this experiment, a single AuNP@Bead was incubated with different scavengers (1 mM NaN_3, 0.4 mM histidine, 10 mM BQ, 10 mM IPA, 20 mM t-BuOH, 5 mM KI, and 1 mM EDTA) in 1 mL of pH 5 acetate buffer for 30 minutes. Following this, 1 mM TMB was added to the solution, and the mixture was incubated for an additional 5 minutes. The UV-Visible spectrum was then recorded to evaluate the effect of the scavengers on the oxidation process.

5.4.11 3,3' -Diaminobenzidine (DAB) assay

3,3'-Diaminobenzidine (DAB) was used as a probe to detect the generation of singlet oxygen in aqueous systems. To evaluate singlet oxygen production, 1 mM DAB was added to 1 mL of pH 5 acetate buffer (20 mM) containing a single AuNP@Bead. DAB oxidation was then monitored using UV-Visible spectrophotometry at regular time intervals. Additionally, to investigate the influence of positive holes and superoxide radicals on singlet oxygen generation, DAB oxidation was also observed in the presence of 5 mM KI (a positive hole scavenger) and 10 mM BQ (a superoxide radical scavenger).

5.4.12 Terephthalic Acid (TA) Assay

Terephthalic acid (TA) serves as a probe for capturing hydroxyl radicals, resulting in the formation of the highly fluorescent product, 2-hydroxyterephthalic acid. In this experiment, a 0.5 mM TA solution

in 1 mL of pH 5 acetate buffer (20 mM) was incubated for one hour in the presence of H_2O_2, AuNP@Bead, or a combination of both. After incubation, the fluorescence spectra of the solutions were recorded at 435 nm with an excitation wavelength of 315 nm. The absence of a significant emission band at 435 nm when both AuNP@Bead and H_2O_2 were present suggests that hydroxyl radicals are not generated in this system.

5.4.13 Chromogenic Assay of Phenol Oxidation

The oxidation of phenolic pollutants by AuNP@Beads at pH 5 was demonstrated using a chromogenic reaction involving 4-aminoantipyrine (4-AP) and 2,4-dichlorophenol (2,4-DP). In a typical experiment, 1 µL each of 1 M stock solutions of 2,4-DP and 4-AP (both prepared in DMSO, yielding final concentrations of 1 mM) were added to 1 mL of 20 mM acetate buffer (pH 5) in a quartz cuvette (1 cm path length). The reaction was initiated by introducing a single AuNP@Bead, followed by thorough mixing. UV–Vis spectra were recorded at 1-minute intervals over a 10-minute period. A gradual increase in absorbance at 510 nm, characteristic of the red-coloured quinone-imine chromophore, confirmed the oxidation of 2,4-DP by the AuNP@Beads.

For kinetic analysis of phenolic compound oxidation, the same chromogenic reaction between 4-AP and 2,4-DP was systematically studied. A single AuNP@Bead was introduced into 1 mL of 20 mM acetate buffer (pH 5) in a quartz cuvette (1 cm path length). Various concentrations of 2,4-DP (0.2–1.0 mM, prepared by adding 1 µL of 0.2, 0.4, 0.6, 0.8, or 1.0 M stock solutions in Isopropanol) were added along with a fixed 1 mM concentration of 4-AP. After mixing, the reaction mixture was allowed to equilibrate for two minutes, and the absorbance was measured at 510 nm ($\varepsilon_{510\,nm}$ = 13.6 $mM^{-1}{\cdot}cm^{-1}$ in water). All catalytic assays were performed in triplicate, and the kinetic data were analyzed using nonlinear regression based on the Michaelis–Menten model with GraphPad Prism 9. The catalytic oxidation of other phenolic substrates, including 4-methoxyphenol (4-MP), hydroquinone (HQ), 1-naphthol, phenol, pyrogallol, 2-aminophenol (2-AP), and 4-nitrophenol (4-NP), was similarly evaluated in 20 mM acetate buffer (pH 5). Reactions were carried out by treating 1 mM 4-AP with varying concentrations (0.2–1.0 mM) of each phenolic compound in the presence of AuNP@Beads for 10 minutes. The emergence of a characteristic absorbance peak at 510 nm, with increasing intensity correlating with substrate concentration, indicated efficient catalytic oxidation by the AuNP@Beads.

5.4.14 Spectrophotometric detection of dopamine and epinephrine

To detect the catecholamines dopamine and epinephrine, varying concentrations (0.02–0.2 mM) of each were prepared in 1 mL of 20 mM phosphate buffer (pH 7) and subjected to oxidation using a single AuNP@Bead for 1 hour. The absorbance of the oxidized dopamine and epinephrine solutions

was then measured at 475 nm and 485 nm, respectively. These values were used to construct calibration curves for the quantitative determination of dopamine and epinephrine. The limit of detection (LOD) was calculated using the formula 3σ/slope, where σ represents the standard deviation of three blank measurements.

5.4.15 Dye degradation

Stock solutions (1.0 mM) of various dyes including Metanil Yellow (MY), Solochrome Dark Blue (SDB), Malachite Green (MG), Eriochrome Black T (EBT), Methyl Orange (MO), and Congo Red (CR), were prepared in water. For visual assessment of dye degradation, each dye (40 µM in 1 mL of pH 5 acetate buffer) was incubated with a single AuNP@Bead for 1 hour. The percentage of dye degradation was then evaluated based on the change in absorbance of the respective dye. For spectrophotometric analysis, 10 µM of each dye was treated with a single AuNP@Bead, and the UV–Visible spectra were recorded at regular intervals until complete decolorization was observed.

5.4.16 Reusability and stability assessment of the catalytic beads

The reusability of the AuNP@Beads was evaluated by performing multiple catalytic cycles involving the oxidation of TMB and 2,4-dichlorophenol (2,4-DP), as well as the degradation of Metanil Yellow (MY). For TMB oxidation, a single AuNP@Bead was added to the TMB solution (1 mM) and allowed to react for 2 minutes. After each cycle, the bead was removed using forceps, thoroughly washed with water to eliminate residual reactants, and reused in fresh TMB solutions. The catalytic efficiency across successive cycles was monitored by measuring the absorbance of oxidized TMB at 652 nm. Similarly, the reusability of the beads for 2,4-DP oxidation and MY degradation was assessed by repeating the reaction cycles and recording the UV–Visible spectra after each cycle. To further evaluate the robustness of the system under challenging conditions, the degradation of MY was also conducted in the presence of 0.1 M KCl. The stability and sustained catalytic activity of the AuNP@Beads under these conditions were confirmed through spectrophotometric analysis.

5.4.17 Antibacterial activity (Agar well diffusion assay)

The antibacterial activity of the AuNP@Beads was assessed using the agar well diffusion assay. Briefly, *Escherichia coli* (DH5α) and *Staphylococcus aureus* were seeded onto YPD agar and BHI agar petri plates, respectively, from a mid-log phase grown bacterial culture (10^8 CFU/ml). Wells were made in the agar plates using a pipette tip. Beads were placed into the wells and were left to incubate at 37°C for 24 hours. SO_4-BPEI beads and BPEI beads were also used as controls. After 24 hours, the zone of inhibition was measured for each bead. The experiment was conducted in triplicate.

5.4.18 Time-dependent inactivation of bacterial cells

Catalytic inactivation of *Escherichia coli* and *Staphylococcus aureus* was carried out in a 96-well plate. The mid-log phase of the bacterial strain was obtained from an overnight grown culture. Cells were centrifuged at 6000 g for 6 minutes and were washed thrice in PB buffer (pH 7.4). The washed cells were resuspended in the same buffer and diluted to make a bacterial suspension of 10^5 CFU/ml. A 100 µL aliquot of this suspension was incubated with AuNP@Beads in a 96-well plate and incubated at 37°C. A 10 µL aliquot was taken out at different time intervals and spread onto YPD agar plates (*Escherichia coli*) and BHI agar plates (*Staphylococcus aureus*). The plates were then kept for incubation at 37°C for 24 hours, followed by colony counting. Similarly, cells with control beads (SO_4-BPEI beads and BPEI beads) were also tested using the same procedure to test the inactivation of bacterial cells. The experiment was done in triplicate.

5.4.19 FESEM analysis of the bacterial cells

1 mL of a mid-log phase grown bacterial culture of *Escherichia coli* and *Staphylococcus aureus* was taken and washed thrice in PB buffer (pH 7.4). The cells were resuspended in the same buffer and diluted to a concentration of 10^5 CFU/ml. The cells were incubated with AuNP@Beads, SO_4-BPEI beads, and BPEI beads for 6 hours. After incubation, 2.5% glutaraldehyde was added to fix the cells. The cells were then washed twice with autoclaved water, drop casted on a clean cover slip, and left to dry. The dried coverslips were taken for FESEM analysis.

5.4.20 Plant growth experiment

Green gram (*Vigna radiata*) seeds were chosen as the model system for this study. The seeds were thoroughly cleaned, and damaged or defective ones discarded. Healthy seeds were soaked in water for 12 hours to facilitate germination. Two solutions were prepared: untreated wastewater and treated (degraded) water. The untreated wastewater was an aqueous mixture containing dyes (Methyl Orange, Eriochrome Black T, Congo Red) and phenolic contaminants (phenol, *p*-nitrophenol, 2-aminophenol, 4-methoxyphenol), each at 0.5 mM. The treated water was obtained by processing this mixture with AuNP@Beads for 3 hours. These solutions were poured into separate trays, each with a perforated grid tray on top. Equal numbers of pre-soaked seeds were evenly placed on the grids without overlap. To maintain moisture, seeds were misted with water and covered with seedling paper, which was removed once seedlings reached ~1 cm. Plant growth and root development were monitored and recorded on the 2nd and 5th days in both control (treated water) and test (untreated wastewater) groups. All experiments were conducted at room temperature under ambient natural light.

Outlook and Future Perspectives

The PyKC-based core–shell hydrogel beads developed in this work present a modular and multifunctional platform that may find broad relevance in biomedical, catalytic, and environmental domains. A promising future direction involves the scalable and controlled fabrication of these beads using microfluidic techniques, which allow the continuous generation of highly uniform core–shell architectures with precise control over size and shell thickness. This approach is expected to ensure reproducibility, enable quality control, and facilitate transition from laboratory-scale synthesis to industrial production.

One of the most important physicochemical features of these beads is their slow and sustained dissolution in acidic environments, such as those present in gastric fluids. Owing to this property, the beads may serve as oral delivery vehicles for therapeutic agents that benefit from pH-triggered, gradual release. Sensitive payloads such as peptides, enzymes, or probiotics could be protected and released over an extended period in the stomach, potentially improving therapeutic efficacy and patient compliance in chronic treatment regimens.

In the area of catalysis, the robust and impermeable nature of the core–shell structure may allow for the immobilization of catalytic species including nanoparticles, enzymes, or small-molecule catalysts. These beads could be used to carry out multistep tandem reactions in a one-pot setup, simplifying complex syntheses while enabling catalyst separation and reuse. Their integration into packed bead columns may support continuous flow processes for chemical synthesis, pollutant degradation, or biotransformations, where high surface area, efficient mass transfer, and mechanical resilience are critical.

The chemically tunable surface of the PyKC shell further adds to the versatility of this system. Through functionalization with macrocyclic receptors such as Cucurbit[n]urils, Cyclodextrins, or Calixarenes, the beads may be tailored for molecular recognition and selective capture. This could lead to the development of molecular fishing systems capable of isolating small molecules, toxins, or biologically relevant targets from complex mixtures. Such systems may find applications in diagnostics, targeted biosensing, affinity purification, or environmental monitoring.

Overall, the PyKC-based core–shell hydrogel beads hold significant promise. Their combination of structural robustness, responsive behaviour, and adaptability, paired with scalable microfluidic fabrication, may open new pathways for their deployment in next-generation drug delivery, catalytic systems, and molecular recognition technologies.

References

(1) Lee, S. C.; Kwon, I. K.; Park, K. *Adv. Drug Deliv. Rev.* **2013**, *65* (1), 17-20.

(2) Hardy, W. B.; Neville, F. H. *Proc. R. Soc. Lond.* **1997**, *66* (424-433), 95-109.

(3) Wichterle, O.; LÍM, D. *Nature* **1960**, *185* (4706), 117-118.

(4) Zhang, Y. S.; Khademhosseini, A. *Science* **2017**, *356* (6337), eaaf3627.

(5) Ribeiro, M. M.; Simões, M.; Vitorino, C.; Mascarenhas-Melo, F. *Coord. Chem. Rev.* **2025**, *542*, 216868.

(6) Yadav, P.; Singh, S.; Jaiswal, S.; Kumar, R. *Int. J. Biol. Macromol.* **2024**, *280*, 136126.

(7) Chen, G.; Yang, Z.; Pan, H.; Zhang, J.; Guo, Y.; Zhou, Z.; Zheng, J.; Zhang, Z.; Cao, R.; Hou, K.; et al. *Chem. Rev.* **2025**.

(8) Sawahata, K.; Hara, M.; Yasunaga, H.; Osada, Y. *J. Control. Release* **1990**, *14* (3), 253-262.

(9) Fujita, H.; Ninomiya, K.; Homma, T. *Bull. Chem. Soc. Jpn.* **1952**, *25* (6), 374-378.

(10) Takigawa, T.; Kasihara, H.; Masuda, T. *Polym. Bull.* **1990**, *24* (6), 613-618.

(11) Peppas, N. A. *Makromol. Chem.* **1977**, *178* (2), 595-601.

(12) Abe, T.; Egawa, H.; Ito, H.; Nitta, A. *J. Appl. Polym. Sci.* **1990**, *40* (7-8), 1223-1235.

(13) Warren, T. C.; Prins, W. *Macromolecules* **1972**, *5* (4), 506-512.

(14) Solari, M. *J. Intell. Mater. Syst. Struct.* **1994**, *5* (3), 295-304.

(15) Chiarelli, P.; De Rossi, D. *J. Intell. Mater. Syst. Struct.* **1992**, *3* (3), 396-417.

(16) Jianqi, F.; Lixia, G. *Eur. Polym. J.* **2002**, *38* (8), 1653-1658.

(17) Jin, X.; Hsieh, Y.-L. *Polymer* **2005**, *46* (14), 5149-5160.

(18) Alarcón, C. d. l. H.; Pennadam, S.; Alexander, C. *Chem. Soc. Rev.* **2005**, *34* (3), 276-285.

(19) Lim, J. Y. C.; Lin, Q.; Xue, K.; Loh, X. J. *Mater. Today Adv.* **2019**, *3*, 100021.

(20) Pramanik, B. Short Peptide-Based Smart Thixotropic Hydrogels. In *Gels*, 2022; Vol. 8, p 569.

(21) Yin, H.; Liu, F.; Abdiryim, T.; Liu, X. *ACS Mater. Lett.* **2023**, *5* (7), 1787-1830.

(22) Xu, X.; Liu, Y.; Fu, W.; Yao, M.; Ding, Z.; Xuan, J.; Li, D.; Wang, S.; Xia, Y.; Cao, M. Poly(N-isopropylacrylamide)-Based Thermoresponsive Composite Hydrogels for Biomedical Applications. In *Polymers*, 2020; Vol. 12, p 580.

(23) Tian, B.; Liu, J. *Int. J. Biol. Macromol.* **2023**, *235*, 123902.

(24) Kocak, G.; Tuncer, C.; Bütün, V. *Polym. Chem.* **2017**, *8* (1), 144-176.

(25) Correa, S.; Grosskopf, A. K.; Lopez Hernandez, H.; Chan, D.; Yu, A. C.; Stapleton, L. M.; Appel, E. A. *Chem. Rev.* **2021**, *121* (18), 11385-11457.

(26) Lee, K. Y.; Mooney, D. J. *Chem. Rev.* **2001**, *101* (7), 1869-1880.

(27) Liang, Y.; He, J.; Guo, B. *ACS Nano* **2021**, *15* (8), 12687-12722.

(28) Qin, C.; Wang, H.; Zhao, Y.; Qi, Y.; Wu, N.; Zhang, S.; Xu, W. *Eur. Polym. J.* **2024**, *219*, 113376.

(29) Zhou, R.; Cai, R.; Chen, Y.; Qiao, J.; Ding, K.; Tan, X.; Ding, M.; Chen, Y. *Chem. Eng. Res. Des.* **2025**, *216*, 1-24.

(30) Yang, J.; Dong, Z.; Liu, H.; Tian, Y. *Chem. Eng. J.* **2025**, *512*, 162743.

(31) Jia, R.; Wei, C.; Ma, B.; Li, L.; Yang, C.; Wang, B.; Tan, L.; Feng, J. *Adv. Funct. Mater.* **2025**, *35* (12), 2417498.

(32) Adams, D. J. *J. Am. Chem. Soc.* **2022**, *144* (25), 11047-11053.

(33) Das, S.; Das, D. *Front. Chem.* **2021**, *9*, 770102.

(34) Gao, Y.; Peng, K.; Mitragotri, S. *Adv. Mater.* **2021**, *33* (25), 2006362.

(35) Ihara, H.; Takafuji, M.; Kuwahara, Y. *Polym. J.* **2016**, *48* (8), 843-853.

(36) Wang, T.; Turhan, M.; Gunasekaran, S. *Polym. Int.* **2004**, *53* (7), 911-918.

(37) Wang, G.; Wang, X.; Huang, L. *Biotechnol. Biotechnol. Equip.* **2017**, *31* (4), 766-773.

(38) Rickett, T. A.; Amoozgar, Z.; Tuchek, C. A.; Park, J.; Yeo, Y.; Shi, R. *Biomacromolecules* **2011**, *12* (1), 57-65.

(39) Broguiere, N.; Isenmann, L.; Zenobi-Wong, M. *Biomaterials* **2016**, *99*, 47-55.

(40) Gelain, F.; Bottai, D.; Vescovi, A.; Zhang, S. *PLoS One* **2006**, *1* (1), e119.

(41) Matyash, M.; Despang, F.; Ikonomidou, C.; Gelinsky, M. *Tissue Eng. Part C Methods* **2013**, *20* (5), 401-411.

(42) Lu, Y.; Wang, D.; Li, T.; Zhao, X.; Cao, Y.; Yang, H.; Duan, Y. Y. *Biomaterials* **2009**, *30* (25), 4143-4151.

(43) Koyama, M.; Helbert, W.; Imai, T.; Sugiyama, J.; Henrissat, B. *Proc. Natl. Acad. Sci. U.S.A.* **1997**, *94* (17), 9091-9095.

(44) George, J.; Hsu, C.-C.; Nguyen, L. T. B.; Ye, H.; Cui, Z. *Biotechnol. Adv.* **2020**, *42*, 107370.

(45) Hennink, W. E.; van Nostrum, C. F. *Adv. Drug Deliv. Rev.* **2002**, *54* (1), 13-36.

(46) Wang, H.; Heilshorn, S. C. *Adv. Mater.* **2015**, *27* (25), 3717-3736.

(47) Rumon, M. M. H.; Rahman, M. S.; Akib, A. A.; Sohag, M. S.; Rakib, M. R. A.; Khan, M. A. R.; Yesmin, F.; Shakil, M. S.; Rahman Khan, M. M. *Discov. Mater.* **2025**, *5* (1), 5.

(48) Hoare, T. R.; Kohane, D. S. *Polymer* **2008**, *49* (8), 1993-2007.

(49) Albino, M.; Burden, T. J.; Piras, C. C.; Whitwood, A. C.; Fairlamb, I. J. S.; Smith, D. K. *ACS Sustain. Chem. Eng.* **2023**, *11*, 1678-1689.

(50) Barry Iii, R. A.; Shepherd, R. F.; Hanson, J. N.; Nuzzo, R. G.; Wiltzius, P.; Lewis, J. A. *Adv. Mater.* **2009**, *21* (23), 2407-2410.

(51) Hong, S.; Sycks, D.; Chan, H. F.; Lin, S.; Lopez, G. P.; Guilak, F.; Leong, K. W.; Zhao, X. *Adv. Mater.* **2015**, *27* (27), 4035-4040.

(52) Gao, Q.; He, Y.; Fu, J.-z.; Liu, A.; Ma, L. *Biomaterials* **2015**, *61*, 203-215.

(53) Chandra, D.; Taylor, J. A.; Yang, S. *Soft Matter* **2008**, *4* (5), 979-984.

(54) Miller, J. S.; Stevens, K. R.; Yang, M. T.; Baker, B. M.; Nguyen, D.-H. T.; Cohen, D. M.; Toro, E.; Chen, A. A.; Galie, P. A.; Yu, X.; et al. *Nat. Mater.* **2012**, *11* (9), 768-774.

(55) Haque, M. A.; Kurokawa, T.; Gong, J. P. *Soft Matter* **2012**, *8* (31), 8008-8016.

(56) Piras, C. C.; Kay, A. G.; Genever, P. G.; Fitremann, J.; Smith, D. K. *Chem. Sci.* **2022**, *13* (7), 1972-1981.

(57) Lopez-Vince, E.; Simon-Yarza, T.; Wilhelm, C. *Sci. Rep.* **2025**, *15* (1), 4213.

(58) Das, T.; Das, S.; Das, D. *Chem. Eng. J.* **2023**, *477*, 147105.

(59) Das, T.; Das, S.; Das, D. *J. Mater. Chem. B* **2025**, *13*, 1079-1088.

(60) Piras, C. C.; Mahon, C. S.; Smith, D. K. *Chem. Eur. J.* **2020**, *26*, 8452-8457.

(61) Smith, D. K. *Angew. Chem. Int. Ed.* **2025**, *64* (24), e202502053.

(62) Xu, X.; Kentish, S. E.; Martin, G. J. O. *ACS Sustain. Chem. Eng.* **2021**, *9* (29), 9698-9706.

(63) Tan, W. H.; Takeuchi, S. *Adv. Mater.* **2007**, *19* (18), 2696-2701.

(64) Amiri, M.; Khazaeli, P.; Salehabadi, A.; Salavati-Niasari, M. *Adv. Colloid Interface Sci.* **2021**, *288*, 102316.

(65) Piras, C. C.; Slavik, P.; Smith, D. K. *Angew. Chem. Int. Ed.* **2020**, *59*, 853-859.

(66) Cha, C.; Oh, J.; Kim, K.; Qiu, Y.; Joh, M.; Shin, S. R.; Wang, X.; Camci-Unal, G.; Wan, K.-t.; Liao, R.; et al. *Biomacromolecules* **2014**, *15* (1), 283-290.

(67) Kim, S.; Oh, J.; Cha, C. *Colloids Surf. B Biointerfaces* **2016**, *147*, 1-8.

(68) Lai, W.-F.; Susha, A. S.; Rogach, A. L. *ACS Appl. Mater. Interfaces* **2016**, *8* (1), 871-880.

(69) Patel, P.; Thareja, P. *Eur. Polym. J.* **2022**, *163*, 110935.

(70) McClements, D. J. *Adv. Colloid Interface Sci.* **2017**, *240*, 31-59.

(71) Farjami, T.; Madadlou, A. *Food Hydrocoll.* **2017**, *62*, 262-272.

(72) Beldengrün, Y.; Aragon, J.; Prazeres, S. F.; Montalvo, G.; Miras, J.; Esquena, J. *Langmuir* **2018**, *34* (33), 9731-9743.

(73) Butstraen, C.; Salaün, F. *Carbohydr. Polym.* **2014**, *99*, 608-616.

(74) Zou, L.; Zhang, Z.; Zhang, R.; Liu, W.; Liu, C.; Xiao, H.; McClements, D. J. *J. Food Eng.* **2016**, *178*, 81-89.

(75) Zheng, C.; Huang, Z. *Colloids Surf. A Physicochem. Eng. Asp.* **2015**, *468*, 327-332.

(76) Daniel-da-Silva, A. L.; Ferreira, L.; Gil, A. M.; Trindade, T. *J. Colloid Interface Sci.* **2011**, *355* (2), 512-517.

(77) Yan, Y.-Z.; An, Q.-D.; Xiao, Z.-Y.; Zhai, S.-R.; Zhai, B.; Shi, Z. *J. Mater. Chem. A* **2017**, *5* (32), 17073-17087.

(78) Hu, X.; Islam, M. A.; Khalili, A.; Aghaei, A.; Cho, J.-Y.; Sadrzadeh, M. *RSC Sustain.* **2025**, *3* (5), 2255-2272.

(79) Georgouvelas, D.; Abdelhamid, H. N.; Edlund, U.; Mathew, A. P. *Nanoscale Adv.* **2023**, *5* (21), 5892-5899.

(80) Ramsheh, N. A.; Dogari, H.; Mosaffa, E.; Akhgari, M.; Ghafuri, H.; Banerjee, A. *ACS Appl. Polym. Mater.* **2023**, *5* (4), 3148-3160.

(81) Yin, S.; Xu, Y.; Wang, Z.; Wei, Z.; Xu, T.; Zhao, W.; Zhao, C. *J. Mater. Chem. B* **2022**, *10* (14), 2534-2543.

(82) Yang, J.; Geng, N.; Li, Y.; Wu, L.; Chang, T.; Shi, H.; Ahmad, Z.; Jiang, M.; Qu, J.; Zhang, H.; et al. *Adv. Funct. Mater.* **2025**, *35* (14), 2418340.

(83) Gokhale, D.; Stathatou, P. M.; Athanasiou, C. E.; Doyle, P. S. *RSC Sustain.* **2024**, *2* (6), 1761-1772.

(84) Karunarathna, M. H. J. S.; Bailey, K. M.; Ash, B. L.; Matson, P. G.; Wildschutte, H.; Davis, T. W.; Midden, W. R.; Ostrowski, A. D. *ACS Omega* **2020**, *5* (36), 23009-23020.

(85) Chang, X.; Li, S.; Li, N.; Wang, S.; Li, J.; Guo, C.; Yu, L.; Murto, P.; Xu, X. *J. Mater. Chem. A* **2022**, *10* (35), 18170-18184.

(86) Baruah, M.; Gogoi, R.; Borgohain, A.; Karak, T.; Saikia, J. *ACS Appl. Polym. Mater.* **2024**, *6* (21), 13238-13252.

(87) Shaheen, A.; Zargar, M. I.; Dar, A. A. *Soft Matter* **2023**, *19* (23), 4237-4253.

(88) Yang, J.; Hu, Z.; Rao, W.; Xie, Y.; Yu, C. *Langmuir* **2024**, *40* (28), 14245-14256.

(89) Harris, C. G.; Gedde, H. K.; Davis, A. A.; Semprini, L.; Rochefort, W. E.; Fogg, K. C. *RSC Sustain.* **2024**, *2* (4), 1101-1117.

(90) Jawed, A.; Rizvi, A.; Çitoğlu, S.; Azeem, I.; Maclean, M.; Golder, A. K.; Pandey, L. M.; Duran, H.; Davidson, C. M.; Lau, K. H. A. *ACS Sustain. Chem. Eng.* **2025**, *13* (19), 7212-7222.

(91) Li, Q.; Wang, D.; Wang, X.; Wang, D.; Xu, Z.; Wu, M.; Zou, K.; Wang, B.; Tang, X. *ACS ES&T Eng.* **2025**, *5* (6), 1462-1476.

(92) Wang, D.-E.; Wang, Y.; Tian, C.; Zhang, L.; Han, X.; Tu, Q.; Yuan, M.; Chen, S.; Wang, J. *J. Mater. Chem. A* **2015**, *3* (43), 21690-21698.

(93) Mohammed, N.; Baidya, A.; Murugesan, V.; Kumar, A. A.; Ganayee, M. A.; Mohanty, J. S.; Tam, K. C.; Pradeep, T. *ACS Sustain. Chem. Eng.* **2016**, *4* (11), 6167-6176.

(94) Helwa, Y.; Dave, N.; Froidevaux, R.; Samadi, A.; Liu, J. *ACS Appl. Mater. Interfaces* **2012**, *4* (4), 2228-2233.

(95) Al Sulaiman, D.; Chang, J. Y. H.; Ladame, S. *Angew. Chem. Int. Ed.* **2017**, *56* (19), 5247-5251.

(96) Kim, S.; Kim, H.; Qiao, T.; Cha, C.; Lee, S. K.; Lee, K.; Ro, H. J.; Kim, Y.; Lee, W.; Lee, H. *ACS Appl. Mater. Interfaces* **2019**, *11* (15), 14354-14361.

(97) Chen, J.; Yang, Y.; Lin, B.; Wei, X.; Lin, Z.; Hong, G. *ACS Appl. Nano Mater.* **2021**, *4* (10), 10287-10295.

(98) Yang, X.; Yao, L.; Yu, S.; Mu, T.; Hu, Y.; He, X.; Cheng, Y.; Xu, Z. *Anal. Chem.* **2024**, *96* (39), 15598-15607.

(99) Huang, S.; Xiao, Z.; Zhai, S.; Zhai, B.; Zhang, F.; An, Q. *RSC Adv.* **2014**, *4* (105), 60460-60466.

(100) Li, Q.; Gao, R.; Zhang, Y.; Zhang, Y.; Liu, T.; He, Y.-C.; Zheng, M.-M. *Green Chem.* **2023**, *25* (19), 7764-7773.

(101) Moriyama, J.; Yoshimoto, M. *ACS Omega* **2021**, *6* (9), 6368-6378.

(102) Xu, X.; Appel, E. A.; Liu, X.; Parker, R. M.; Scherman, O. A.; Abell, C. *Biomacromolecules* **2015**, *16* (9), 2743-2749.

(103) Wu, T.; Yu, S.; Lin, D.; Wu, Z.; Xu, J.; Zhang, J.; Ding, Z.; Miao, Y.; Liu, T.; Chen, T.; et al. *ACS Appl. Bio Mater.* **2020**, *3* (5), 3057-3065.

(104) Piras, C. C.; Patterson, A. K.; Smith, D. K. *Chem. Eur. J.* **2021**, *27*, 13203-13210.

(105) Piras, C. C.; Kay, A. G.; Genever, P. G.; Smith, D. K. *Chem. Sci.* **2021**, *12*, 3958-3965.

(106) Chen, Y.; Song, H.; Huang, K.; Guan, X. *Food Funct.* **2021**, *12* (19), 9165-9177.

(107) Sagar, P.; Singh, V.; Gupta, R.; Kaul, S.; Sharma, S.; Kaur, S.; Bhunia, R. K.; Kondepudi, K. K.; Singhal, N. K. *ACS Appl. Bio Mater.* **2021**, *4* (10), 7467-7484.

(108) Jeong, Y.; Han, X.; Vyas, K.; Irudayaraj, J. *ACS Appl. Mater. Interfaces* **2024**, *16* (22), 28093-28103.

(109) Felip-León, C.; Cejudo-Marín, R.; Peris, M.; Galindo, F.; Miravet, J. F. *Langmuir* **2017**, *33* (39), 10322-10328.

(110) Torres-Martínez, A.; Angulo-Pachón, C. A.; Galindo, F.; Miravet, J. F. *Soft Matter* **2019**, *15* (17), 3565-3572.

(111) Bai, S.; Debnath, S.; Gibson, K.; Schlicht, B.; Bayne, L.; Zagnoni, M.; Ulijn, R. V. *Small* **2014**, *10* (2), 285-293.

(112) Bai, S.; Pappas, C.; Debnath, S.; Frederix, P. W. J. M.; Leckie, J.; Fleming, S.; Ulijn, R. V. *ACS Nano* **2014**, *8* (7), 7005-7013.

(113) Chivers, P. R. A.; Smith, D. K. *Nat. Rev. Mater.* **2019**, *4* (7), 463-478.

(114) Singha, N.; Srivastava, A.; Pramanik, B.; Ahmed, S.; Dowari, P.; Chowdhuri, S.; Das, B. K.; Debnath, A.; Das, D. *Chem. Sci.* **2019**, *10*, 5920-5928.

(115) Hamzah, Y. B.; Hashim, S.; Rahman, W. A. W. A. *J. Polym. Res.* **2017**, *24*, 134.

(116) Dasgupta, A.; Mondal, J. H.; Das, D. *RSC Adv.* **2013**, *3*, 9117-9149.

(117) Zhang, Z. P.; Zhang, R. J.; Zou, L. Q.; McClements, D. J. *Food Hydrocoll.* **2016**, *58*, 308-315.

(118) Das, P.; Das, D. Peptide Amphiphile Nanomaterials. In *Peptide Bionanomaterials: From Design to Application*, Elsawy, M. A. Ed.; Springer International Publishing, 2023; pp 145-194.

(119) Felip-León, C.; Cejudo-Marín, R.; Peris, M.; Galindo, F.; Miravet, J. F. *Langmuir* **2017**, *33*, 10322-10328.

(120) Torres-Martínez, A.; Angulo-Pachón, C. A.; Galindo, F.; Miravet, J. F. *Soft Matter* **2019**, *15*, 3565-3572.

(121) Bai, S.; Debnath, S.; Gibson, K.; Schlicht, B.; Bayne, L.; Zagnoni, M.; Ulijn, R. V. *Small* **2014**, *10*, 285-293.

(122) Aviño, F.; Matheson, A. B.; Adams, D. J.; Clegg, P. S. *Org. Biomol. Chem.* **2017**, *15*, 6342-6348.

(123) Bai, S.; Pappas, C.; Debnath, S.; Frederix, P. W. J. M.; Leckie, J.; Fleming, S.; Ulijn, R. V. *ACS Nano* **2014**, *8*, 7005-7013.

(124) Sheehan, F.; Sementa, D.; Jain, A.; Kumar, M.; Tayarani-Najjaran, M.; Kroiss, D.; Ulijn, R. V. *Chem. Rev.* **2021**, *121*, 13869-13914.

(125) Du, X.; Zhou, J.; Shi, J.; Xu, B. *Chem. Rev.* **2015**, *115*, 13165-13307.

(126) Piras, C. C.; Smith, D. K. *Chem. Eur. J.* **2021**, *27*, 14527-14534.

(127) Piras, C. C.; Mahon, C. S.; Genever, P. G.; Smith, D. K. *ACS Biomater. Sci. Eng.* **2022**, *8*, 1829-1840.

(128) Dasgupta, A.; Das, D. *Langmuir* **2019**, *35*, 10704-10724.

(129) Singha, N.; Das, B. K.; Pramanik, B.; Das, S.; Das, D. *Chem. Sci.* **2019**, *10*, 10035-10039.

(130) Chowdhuri, S.; Ghosh, M.; Adler-Abramovich, L.; Das, D. *Pharmaceutics* **2021**, *13*, 1602.

(131) Chowdhuri, S.; Das, S.; Kushwaha, R.; Das, T.; Das, B. K.; Das, D. *Chem. Eur. J.* **2023**, *29* (24), e202203820.

(132) Das, B. K.; Pramanik, B.; Chowdhuri, S.; Scherman, O. A.; Das, D. *Chem. Commun.* **2020**, *56* (23), 3393-3396.

(133) Islam, M. M.; Chivu, A.; AbuSamra, D. B.; Saha, A.; Chowdhuri, S.; Pramanik, B.; Dohlman, C. H.; Das, D.; Argüeso, P.; Rajaiya, J.; et al. *Sci. Rep.* **2022**, *12* (1), 9108.

(134) Rather, A. M.; Manna, U. *Chem. Mater.* **2016**, *28*, 8689-8699.

(135) Farrer, R. A.; LaFratta, C. N.; Li, L.; Praino, J.; Naughton, M. J.; Saleh, B. E. A.; Teich, M. C.; Fourkas, J. T. *J. Am. Chem. Soc.* **2006**, *128*, 1796-1797.

(136) Shome, A.; Das, A.; Manna, U. *Chem. Mater.* **2021**, *33*, 8941-8959.

(137) Borbora, A.; Manna, U. *Chem. Commun.* **2021**, *57*, 2110-2123.

(138) Tong, W.; Song, X.; Gao, C. *Chem. Soc. Rev.* **2012**, *41*, 6103-6124.

(139) Pramanik, B.; Ahmed, S.; Singha, N.; Das, B. K.; Dowari, P.; Das, D. *Langmuir* **2019**, *35*, 478-488.

(140) Yan, C.; Pochan, D. J. *Chem. Soc. Rev.* **2010**, *39*, 3528-3540.

(141) Chowdhuri, S.; Saha, A.; Pramanik, B.; Das, S.; Dowari, P.; Ukil, A.; Das, D. *Langmuir* **2020**, *36*, 15450-15462.

(142) Ahmed, S.; Mondal, J. H.; Behera, N.; Das, D. *Langmuir* **2013**, *29*, 14274-14283.

(143) Singha, N.; Gupta, P.; Pramanik, B.; Ahmed, S.; Dasgupta, A.; Ukil, A.; Das, D. *Biomacromolecules* **2017**, *18*, 3630-3641.

(144) Haris, P. I.; Chapman, D. *Biopolymers* **1995**, *37* (4), 251-263.

(145) Shome, A.; Rather, A. M.; Ghosal, A.; Bhunia, B. K.; Mandal, B. B.; Manna, U. *ACS Sustain. Chem. Eng.* **2019**, *7*, 7502-7509.

(146) Dhar, M.; Das, A.; Shome, A.; Borbora, A.; Manna, U. *Mater. Horiz.* **2021**, *8* (10), 2717-2725.

(147) Curtis, K. A.; Miller, D.; Millard, P.; Basu, S.; Horkay, F.; Chandran, P. L. *PLoS One* **2016**, *11* (9).

(148) Skirtach, A. G.; Yashchenok, A. M.; Möhwald, H. *Chem. Commun.* **2011**, *47*, 12736-12746.

(149) Kim, H. C.; Park, W. H. *Int. J. Biol. Macromol.* **2019**, *135*, 1217-1221.

(150) Jiang, L.; Li, X.; Liu, L.; Zhang, Q. *Int. J. Nanomed.* **2013**, *8* (1), 1825-1834.

(151) Kunc, F.; Nirmalananthan-Budau, N.; Rühle, B.; Sun, Y.; Johnston, L. J.; Resch-Genger, U. *Anal. Chem.* **2021**, *93*, 15271-15278.

(152) Lima, A. L.; Gratieri, T.; Cunha-Filho, M.; Gelfuso, G. M. *Methods* **2022**, *199*, 54-66.

(153) Kojima, R.; Hidaka, S.; Taira, M.; Kohri, M.; Taniguchi, T.; Kishikawa, K.; Karatsu, T.; Okabe, E.; Kondo, F. *J. Colloid Interface Sci.* **2020**, *563*, 122-130.

(154) Feoktistova, N.; Rose, J.; Prokopović, V. Z.; Vikulina, A. S.; Skirtach, A.; Volodkin, D. *Langmuir* **2016**, *32*, 4229-4238.

(155) Li, B.; Yang, X.; Xia, L.; Majeed, M. I.; Tan, B. *Sci. Rep.* **2013**, *3*, 2128.

(156) Borbora, A.; Manna, U. *Chem. Commun.* **2020**, *56*, 7853-7856.

(157) Shao, H.; Ding, Y.; Hong, X.; Liu, Y. *Analyst* **2018**, *143* (2), 409-414.

(158) Lakhani, P.; Bhanderi, D.; Modi, C. K. *Discov. Catal.* **2024**, *1* (1), 2.

(159) Huang, Y.; Li, P.; Zhao, R.; Zhao, L.; Liu, J.; Peng, S.; Fu, X.; Wang, X.; Luo, R.; Wang, R.; et al. *Biomed. Pharmacother.* **2022**, *151*, 113053.

(160) Satchanska, G.; Davidova, S.; Petrov, P. D. Natural and Synthetic Polymers for Biomedical and Environmental Applications. In *Polymers*, 2024; Vol. 16.

(161) Materón, E. M.; Miyazaki, C. M.; Carr, O.; Joshi, N.; Picciani, P. H. S.; Dalmaschio, C. J.; Davis, F.; Shimizu, F. M. *Appl. Surf. Sci. Adv.* **2021**, *6*, 100163.

(162) Du, H.; Shi, S.; Liu, W.; Teng, H.; Piao, M. *Environ. Sci. Pollut. Res.* **2020**, *27* (12), 12967-12994.

(163) Wang, X.; Wang, Q. *Acc. Chem. Res.* **2021**, *54* (5), 1274-1287.

(164) Guo, Y.; Bae, J.; Fang, Z.; Li, P.; Zhao, F.; Yu, G. *Chem. Rev.* **2020**, *120* (15), 7642-7707.

(165) Shome, A.; Rather, A. M.; Manna, U. *Nanoscale Adv.* **2019**, *1* (5), 1746-1753.

(166) Barrow, S. J.; Kasera, S.; Rowland, M. J.; del Barrio, J.; Scherman, O. A. *Chem. Rev.* **2015**, *115*, 12320-12406.

(167) Das, D.; Scherman, O. A. *Isr. J. Chem.* **2011**, *51*, 537-550.

(168) Dowari, P.; Das, S.; Pramanik, B.; Das, D. *Chem. Commun.* **2019**, *55* (94), 14119-14122.

(169) Das, S.; Das, P.; Dowari, P.; Das, B. K.; Das, D. *J. Colloid Interface Sci.* **2022**, *614*, 172-180.

(170) Singh, P.; Sieger, M.; Fiedler, J.; Su, C. Y.; Kaim, W. *Dalton Trans.* **2008**, (7), 868-873.

(171) Zhu, D.; Li, W.; Wen, H. M.; Zhang, J. R.; Zhu, J. J. *Anal. Methods* **2013**, *5*, 4321-4324.

(172) Pramanik, B.; Mondal, J. H.; Singha, N.; Ahmed, S.; Mohanty, J.; Das, D. *ChemPhysChem* **2017**, *18*, 245-252.

(173) Ahmed, S.; Singha, N.; Pramanik, B.; Mondal, J. H.; Das, D. *Polym. Chem.* **2016**, *7*, 4393-4401.

(174) Jiao, D.; Geng, J.; Loh, X. J.; Das, D.; Lee, T.-C.; Scherman, O. A. *Angew. Chem. Int. Ed.* **2012**, *51*, 9633-9637.

(175) Bush, M. E.; Bouley, N. D.; Urbach, A. R. *J. Am. Chem. Soc.* **2005**, *127*, 14511-14517.

(176) Chen, X.; Huang, Z.; Sala, R. L.; McLean, A. M.; Wu, G.; Sokolowski, K.; King, K.; McCune, J. A.; Scherman, O. A. *J. Am. Chem. Soc.* **2022**, *144*, 8474-8479.

(177) Ding, W. Y.; Zheng, S. D.; Qin, Y.; Yu, F.; Bai, J. W.; Cui, W. Q.; Yu, T.; Chen, X. R.; Bello-Onaghise, G.; Li, Y. H. *Front. Chem.* **2018**, *6*, 657.

(178) Mosivand, S.; Kazeminezhad, I. *CrystEngComm* **2016**, *18* (3), 417-426.

(179) Dowari, P.; Kumar Baroi, M.; Das, T.; Kanti Das, B.; Das, S.; Chowdhuri, S.; Garg, A.; Debnath, A.; Das, D. *J. Colloid Interface Sci.* **2022**, *618*, 98-110.

(180) Wang, S.; Fang, H.; Wen, Y.; Cai, M.; Liu, W.; He, S.; Xu, X. *RSC Adv.* **2015**, *5*, 57286-57292.

(181) Aybastıer, Ö.; Şahin, S.; Işık, E.; Demir, C. *Anal. Methods* **2011**, *3* (10), 2289-2297.

(182) Pramanik, B.; Das, D. *J. Phys. Chem. C* **2018**, *122*, 3655-3661.

(183) Das, S.; Das, T.; Das, P.; Das, D. *Chem. Sci.* **2022**, *13*, 4050-4057.

(184) Sharma, A. K.; Shankhwar, S.; Gaur, M. S. *J. Exp. Nanosci.* **2014**, *9* (9), 892-905.

(185) Kim, K. M.; Nam, Y. S.; Lee, Y.; Lee, K. B. *J. Anal. Methods Chem.* **2018**, *2018*, 1206913.

(186) Wen, S.; Zheng, F.; Shen, M.; Shi, X. *Colloids Surf. A Physicochem. Eng. Asp.* **2013**, *419*, 80-86.

(187) Thomas, M.; Klibanov, A. M. *Proc. Natl. Acad. Sci. U.S.A.* **2003**, *100* (16), 9138-9143.

(188) Zhang, Y.; Wen, S.; Zhao, L.; Li, D.; Liu, C.; Jiang, W.; Gao, X.; Gu, W.; Ma, N.; Zhao, J.; et al. *Nanoscale* **2016**, *8* (10), 5567-5577.

(189) Zhou, B.; Xiong, Z.; Wang, P.; Peng, C.; Shen, M.; Shi, X. *Langmuir* **2018**, *34* (29), 8701-8707.

(190) Mulens-Arias, V.; Nicolás-Boluda, A.; Gehanno, A.; Balfourier, A.; Carn, F.; Gazeau, F. *Nanoscale* **2019**, *11* (7), 3344-3359.

(191) Bali, K.; Bak, M.; Szarka, K.; Juhász, G.; Sáfrán, G.; Pécz, B.; Mihály, J.; Mészáros, R. *J. Mol. Liq.* **2021**, *322*, 114559.

(192) López-Muñoz, G. A.; Pescador-Rojas, J. A.; Ortega-Lopez, J.; Salazar, J. S.; Balderas-López, J. A. *Nanoscale Res. Lett.* **2012**, *7* (1), 423.

(193) Cavuslar, O.; Nakay, E.; Kazakoglu, U.; Abkenar, S. K.; Ow-Yang, C. W.; Acar, H. Y. *Mater. Adv.* **2020**, *1* (7), 2407-2417.

(194) Maye, M. M.; Zheng, W.; Leibowitz, F. L.; Ly, N. K.; Zhong, C.-J. *Langmuir* **2000**, *16* (2), 490-497.

(195) Shankar, S. S.; Rai, A.; Ankamwar, B.; Singh, A.; Ahmad, A.; Sastry, M. *Nat. Mater.* **2004**, *3* (7), 482-488.

(196) Castillo-López, D. N.; Pal, U. *J. Nanopart. Res.* **2014**, *16* (8), 2571.

(197) Tchieno, F. M. M.; Tonle, I. K. *Rev. Anal. Chem.* **2018**, *37* (2), 20170019.

(198) Aditya, T.; Pal, A.; Pal, T. *Chem. Commun.* **2015**, *51* (46), 9410-9431.

(199) Saha, S.; Pal, A.; Kundu, S.; Basu, S.; Pal, T. *Langmuir* **2010**, *26* (4), 2885-2893.

(200) Zinchenko, A.; Miwa, Y.; Lopatina, L. I.; Sergeyev, V. G.; Murata, S. *ACS Appl. Mater. Interfaces* **2014**, *6* (5), 3226-3232.

(201) Cao, X.; Yan, S.; Hu, F.; Wang, J.; Wan, Y.; Sun, B.; Xiao, Z. *RSC Adv.* **2016**, *6* (68), 64028-64038.

(202) Gancheva, T.; Virgilio, N. *ACS Appl. Mater. Interfaces* **2018**, *10* (25), 21073-21078.

(203) Park, S. H.; Kim, J.; Hur, S. H.; Kim, D. H.; Kim, M. H. *Chem. Eng. J.* **2018**, *348*, 46-56.

(204) Ullah, N.; Odda, A. H.; Li, D.; Wang, Q.; Wei, Q. *Colloids Surf. A Physicochem. Eng. Asp.* **2019**, *571*, 101-109.

(205) Ozay, H.; Tarımeri, N.; Gungor, Z.; Demirbakan, B.; Özcan, B.; Sezgintürk, M. K.; Ozay, O. *ChemistrySelect* **2020**, *5* (29), 9143-9152.

(206) Bhatt, C. S.; Parimi, D. S.; Bollu, T. K.; H. U, M.; Jacob, N.; Korivi, R.; Ponugoti, S. S.; Mannathan, S.; Ojha, S.; Klingner, N.; et al. *ACS Appl. Mater. Interfaces* **2022**, *14* (46), 51855-51866.

(207) Liu, J.; Yu, H.; Wang, L. *Appl. Catal. A Gen.* **2020**, *599*, 117605.

(208) Hervés, P.; Pérez-Lorenzo, M.; Liz-Marzán, L. M.; Dzubiella, J.; Lu, Y.; Ballauff, M. *Chem. Soc. Rev.* **2012**, *41* (17), 5577-5587.

(209) Wunder, S.; Polzer, F.; Lu, Y.; Mei, Y.; Ballauff, M. *J. Phys. Chem. C* **2010**, *114* (19), 8814-8820.

(210) Strachan, J.; Barnett, C.; Masters, A. F.; Maschmeyer, T. *ACS Catal.* **2020**, *10* (10), 5516-5521.

(211) Corma, A.; Concepción, P.; Serna, P. *Angew. Chem. Int. Ed.* **2007**, *46* (38), 7266-7269.

(212) Kumar, M.; Deka, S. *ACS Appl. Mater. Interfaces* **2014**, *6* (18), 16071-16081.

(213) Iqbal, S.; Zahoor, C.; Musaddiq, S.; Hussain, M.; Begum, R.; Irfan, A.; Azam, M.; Farooqi, Z. H. *Ecotoxicol. Environ. Saf.* **2020**, *202*, 110924.

(214) Shah, L. A.; Haleem, A.; Sayed, M.; Siddiq, M. *J. Environ. Chem. Eng.* **2016**, *4* (3), 3492-3497.

(215) Francis, S.; Joseph, S.; Koshy, E. P.; Mathew, B. *New J. Chem.* **2017**, *41* (23), 14288-14298.

(216) Frens, G. *Nat. Phys. Sci.* **1973**, *241* (105), 20-22.

(217) Alzahrani, H. A. H.; Buckingham, M. A.; Wardley, W. P.; Tilley, R. D.; Ariotti, N.; Aldous, L. *Chem. Commun.* **2020**, *56* (8), 1263-1266.

(218) Kim, J.; Jung, I.-S.; Kim, S.-Y.; Lee, E.; Kang, J.-K.; Sakamoto, S.; Yamaguchi, K.; Kim, K. *J. Am. Chem. Soc.* **2000**, *122* (3), 540-541.

(219) Kumar, R.; Jalani, K.; George, S. J.; Rao, C. N. R. *Chem. Mater.* **2017**, *29* (22), 9751-9757.

(220) Yuan, L.; Lin, W.; Feng, Y. *Org. Biomol. Chem.* **2011**, *9* (6), 1723-1726.

(221) Chen, H.; Li, W.; Lin, Y.; Wang, L.; Liu, X.; Huang, X. *Angew. Chem. Int. Ed.* **2020**, *59* (39), 16953-16960.

(222) Dahili, L. A.; Kelemen-Horváth, I.; Feczkó, T. *Process Biochem.* **2015**, *50* (11), 1835-1842.

(223) Wu, Q.; Xu, Z.; Duan, Y.; Zhu, Y.; Ou, M.; Xu, X. *RSC Adv.* **2017**, *7* (45), 28114-28123.

(224) Reetz, M. T. *Chem. Rec.* **2016**, *16* (6), 2449-2459.

(225) Kuah, E.; Toh, S.; Yee, J.; Ma, Q.; Gao, Z. *Chem. Eur. J.* **2016**, *22* (25), 8404-8430.

(226) Makam, P.; Yamijala, S. S. R. K. C.; Bhadram, V. S.; Shimon, L. J. W.; Wong, B. M.; Gazit, E. *Nat. Commun.* **2022**, *13* (1), 1505.

(227) Wang, Q.; Yang, Z.; Zhang, X.; Xiao, X.; Chang, C. K.; Xu, B. *Angew. Chem. Int. Ed.* **2007**, *46* (23), 4285-4289.

(228) Liu, Q.; Zhang, A.; Wang, R.; Zhang, Q.; Cui, D. *Nano-Micro Lett.* **2021**, *13* (1), 154.

(229) Pietrzak, M.; Ivanova, P. *Sens. Actuators B Chem.* **2021**, *336*, 129736.

(230) Fu, Q.; Wei, C.; Wang, M. *ACS Nano* **2024**, *18* (19), 12049-12095.

(231) Zhang, D.; Chen, Q.; Ren, Q.; Zhong, W.; Zhang, H.; Wang, G.; Zhang, Y. *Coord. Chem. Rev.* **2024**, *508*, 215771.

(232) Lin, Y.; Ren, J.; Qu, X. *Adv. Mater.* **2014**, *26* (25), 4200-4217.

(233) Sharifi, M.; Hosseinali, S. H.; Yousefvand, P.; Salihi, A.; Shekha, M. S.; Aziz, F. M.; JouyaTalaei, A.; Hasan, A.; Falahati, M. *Mater. Sci. Eng. C* **2020**, *108*, 110422.

(234) Azharuddin, M.; Zhu, G. H.; Das, D.; Ozgur, E.; Uzun, L.; Turner, A. P. F.; Patra, H. K. *Chem. Commun.* **2019**, *55* (49), 6964-6996.

(235) Liang, C.; Cheong, J. Y.; Sitaru, G.; Rosenfeldt, S.; Schenk, A. S.; Gekle, S.; Kim, I. I. D.; Greiner, A. *Adv. Mater. Interfaces* **2022**, *9* (4), 2100867.

(236) Ishida, T.; Murayama, T.; Taketoshi, A.; Haruta, M. *Chem. Rev.* **2020**, *120* (2), 464-525.

(237) Zhou, B.; Guo, X.; Yang, N.; Huang, Z.; Huang, L.; Fang, Z.; Zhang, C.; Li, L.; Yu, C. *J. Mater. Chem. B* **2021**, *9* (28), 5583-5598.

(238) Zhang, Q.; Hou, D.; Wen, X.; Xin, M.; Li, Z.; Wu, L.; Pathak, J. L. *Mater. Today Bio* **2022**, *15*, 100333.

(239) Yu, L.; Song, Z.; Peng, J.; Yang, M.; Zhi, H.; He, H. *TrAC Trends Anal. Chem.* **2020**, *127*, 115880.

(240) Su, S.; Wu, W.; Gao, J.; Lu, J.; Fan, C. *J. Mater. Chem.* **2012**, *22* (35), 18101-18110.

(241) Lin, Y.; Ren, J.; Qu, X. *Acc. Chem. Res.* **2014**, *47* (4), 1097-1105.

(242) Hao, F.; Nehl, C. L.; Hafner, J. H.; Nordlander, P. *Nano Lett.* **2007**, *7* (3), 729-732.

(243) Nehl, C. L.; Liao, H.; Hafner, J. H. *Nano Lett.* **2006**, *6* (4), 683-688.

(244) Lim, B.; Xia, Y. *Angew. Chem. Int. Ed.* **2011**, *50* (1), 76-85.

(245) Wang, G.-L.; Jin, L.-Y.; Dong, Y.-M.; Wu, X.-M.; Li, Z.-J. *Biosens. Bioelectron.* **2015**, *64*, 523-529.

(246) Yu, P.-Y.; Chen, Y.-S.; Yu, H.-H.; Chen, F.-I.; Chen, Z.-W.; Liu, C.-P. *J. Photochem. Photobiol. A* **2022**, *432*, 114063.

(247) Ni, P.; Liu, S.; Wang, B.; Chen, C.; Jiang, Y.; Zhang, C.; Chen, J.; Lu, Y. *J. Hazard. Mater.* **2021**, *411*, 125106.

(248) Cao, G.-X.; Wu, X.-M.; Dong, Y.-M.; Li, Z.-J.; Wang, G.-L. *Microchim. Acta* **2016**, *183* (1), 441-448.

(249) Borghei, Y. S.; Hosseini, M.; Ganjali, M. R. *Sens. Actuators B Chem.* **2018**, *273*, 1618-1626.

(250) Slavík, P.; Kurka, D. W.; Smith, D. K. *Chem. Sci.* **2018**, *9* (46), 8673-8681.

(251) Slavik, P.; Smith, D. K. *Tetrahedron* **2020**, *76* (31), 131344.

(252) Slavík, P.; Trowse, B. R.; O'Brien, P.; Smith, D. K. *Nat. Chem.* **2023**, *15* (3), 319-325.

(253) Maiuolo, J.; Oppedisano, F.; Gratteri, S.; Muscoli, C.; Mollace, V. *Int. J. Cardiol.* **2016**, *213*, 8-14.

(254) Ames, B. N.; Cathcart, R.; Schwiers, E.; Hochstein, P. *Proc. Natl. Acad. Sci. U.S.A.* **1981**, *78* (11), 6858-6862.

(255) Becker, B. F. *Free Radic. Biol. Med.* **1993**, *14* (6), 615-631.

(256) Otani, N.; Hoshiyama, E.; Ouchi, M.; Takekawa, H.; Suzuki, K. *Front. Neurol.* **2023**, *14*, 1164756.

(257) Saito, Y.; Tanaka, A.; Node, K.; Kobayashi, Y. *J. Cardiol.* **2021**, *78* (1), 51-57.

(258) Dai, X.; Fang, X.; Zhang, C.; Xu, R.; Xu, B. *J. Chromatogr. B* **2007**, *857* (2), 287-295.

(259) Li, Q.; Qiu, Y.; Han, W.; Zheng, Y.; Wang, X.; Xiao, D.; Mao, M.; Li, Q. *RSC Adv.* **2018**, *8* (45), 25808-25814.

(260) Lakshmi, D.; Whitcombe, M. J.; Davis, F.; Sharma, P. S.; Prasad, B. B. *Electroanalysis* **2011**, *23* (2), 305-320.

(261) Liang, X.-H.; Yu, A.-X.; Bo, X.-J.; Du, D.-Y.; Su, Z.-M. *Coord. Chem. Rev.* **2023**, *497*, 215427.

(262) Kong, M.; Wei, W.; Wang, W.; Chen, H.; He, J. *Spectrochim. Acta A Mol. Biomol. Spectrosc.* **2021**, *257*, 119773.

(263) Mostafa, I. M.; Halawa, M. I.; Chen, Y.; Abdussalam, A.; Guan, Y.; Xu, G. *Analyst* **2020**, *145* (7), 2709-2715.

(264) Kumari, C.; Sain, D.; Dey, S. *Sens. Actuators B Chem.* **2018**, *264*, 208-215.

(265) Pang, X.; Yan, R.; Li, L.; Wang, P.; Zhang, Y.; Liu, Y.; Liu, P.; Dong, W.; Miao, P.; Mei, Q. *Anal. Chim. Acta* **2022**, *1199*, 339571.

(266) Zhang, Q.; Du, S.; Tian, F.; Long, X.; Xie, S.; Tang, S.; Bao, L. *Molecules* **2022**, *27* (14), 4586.

(267) Wang, F.; Chai, X.; Fu, X.; Mao, G.; Wang, H. *New J. Chem.* **2022**, *46* (32), 15367-15372.

(268) Ma, Z.; Yang, L.; Wang, Y.; Wang, M.; Qi, W.; He, Z. *Chem. Eng. J.* **2021**, *416*, 129149.

(269) Qin, X.; Yuan, C.; Geng, G.; Shi, R.; Cheng, S.; Wang, Y. *Sens. Actuators B Chem.* **2021**, *333*, 129638.

(270) Qu, S.; Li, Z.; Jia, Q. *ACS Appl. Mater. Interfaces* **2019**, *11* (37), 34196-34202.

(271) Wang, X.; Yao, Q.; Tang, X.; Zhong, H.; Qiu, P.; Wang, X. *Anal. Bioanal. Chem.* **2019**, *411* (4), 943-952.

(272) Lu, J.; Xiong, Y.; Liao, C.; Ye, F. *Anal. Methods* **2015**, *7* (23), 9894-9899.

(273) Liang, X.; Chen, Y.; Wen, K.; Han, H.; Li, Q. *J. Mater. Chem. B* **2021**, *9* (34), 6811-6817.

(274) Peng, Z.; Tang, X.; Xu, P.; Qiu, P. *ACS Appl. Mater. Interfaces* **2024**, *16* (1), 54-65.

(275) Kang, Q.; Xu, Y.; Chen, X. *Sensors* **2023**, *23* (8), 3881.

(276) Pal, J.; Pal, T. *RSC Adv.* **2016**, *6* (87), 83738-83747.

(277) Farshchi, F.; Saadati, A.; Hasanzadeh, M.; Seidi, F. *RSC Adv.* **2021**, *11* (44), 27298-27308.

(278) Tripathi, A.; Harris, K. D.; Elias, A. L. *ACS Omega* **2020**, *5* (16), 9123-9130.

(279) Liu, J.; An, T.; Chen, Z.; Wang, Z.; Zhou, H.; Fan, T.; Zhang, D.; Antonietti, M. *J. Mater. Chem. A* **2017**, *5* (19), 8933-8938.

(280) Ma, T.; Yang, W.; Liu, S.; Zhang, H.; Liang, F. *Catalysts* **2017**, *7* (2), 38.

(281) Barbosa, S.; Agrawal, A.; Rodríguez-Lorenzo, L.; Pastoriza-Santos, I.; Alvarez-Puebla, R. A.; Kornowski, A.; Weller, H.; Liz-Marzán, L. M. *Langmuir* **2010**, *26* (18), 14943-14950.

(282) Becerril-Castro, I. B.; Calderon, I.; Pazos-Perez, N.; Guerrini, L.; Schulz, F.; Feliu, N.; Chakraborty, I.; Giannini, V.; Parak, W. J.; Alvarez-Puebla, R. A. *Anal. Sens.* **2022**, *2* (3), e202200005.

(283) Spedalieri, C.; Szekeres, G. P.; Werner, S.; Guttmann, P.; Kneipp, J. *Nanoscale* **2021**, *13* (2), 968-979.

(284) Cui, Q.; Xia, B.; Mitzscherling, S.; Masic, A.; Li, L.; Bargheer, M.; Möhwald, H. *Colloids Surf. A Physicochem. Eng. Asp.* **2015**, *465*, 20-25.

(285) Deveci, P. *J. Incl. Phenom. Macrocycl. Chem.* **2021**, *99* (1), 23-31.

(286) Bancirova, M. *Luminescence* **2011**, *26* (6), 685-688.

(287) Matheson, I. B. C.; Etheridge, R. D.; Kratowich, N. R.; Lee, J. *Photochem. Photobiol.* **1975**, *21* (3), 165-171.

(288) Yang, W.; Fei, J.; Xu, W.; Jiang, H.; Sakran, M.; Hong, J.; Zhu, W.; Zhou, X. *Colloids Surf. B Biointerfaces* **2022**, *212*, 112347.

(289) Ma, R.; Wang, X.; Huang, J.; Song, J.; Zhang, J.; Wang, X. *Vacuum* **2017**, *141*, 157-165.

(290) Chi, Y.; Wang, W.; Zhang, Q.; Yu, H.; Liu, M.; Ni, S.; Gao, B.; Xu, S. *Chemosphere* **2021**, *285*, 131323.

(291) An, C.; Wang, J.; Qin, C.; Jiang, W.; Wang, S.; Li, Y.; Zhang, Q. *J. Mater. Chem.* **2012**, *22* (26), 13153-13158.

(292) Gao, Z.; Zhang, D.; Jun, Y.-S. *Environ. Sci. Technol.* **2021**, *55* (15), 10442-10450.

(293) Nosaka, Y.; Nosaka, A. Y. *Chem. Rev.* **2017**, *117* (17), 11302-11336.

(294) Zhong, C.; Hu, C.; Ouyang, D.; Dan, A.; Zhong, Y.; Cai, Z.; Lin, Z. *Chem. Eng. J.* **2023**, *477*, 146979.

(295) Zhao, P.; Liu, Y.; Chen, Y.; Yang, M.; Zhao, S.; Qi, N.; Wang, Y.; Huo, D.; Hou, C. *ACS Appl. Mater. Interfaces* **2022**, *14*, 41369-41378.

(296) Zhang, Y.-J.; Guo, L.; Yu, Y.-L.; Wang, J.-H. *Anal. Chem.* **2020**, *92* (24), 15699-15704.

(297) Liu, J.; Jiang, X.; Zhang, R.; Zhang, Y.; Wu, L.; Lu, W.; Li, J.; Li, Y.; Zhang, H. *Adv. Funct. Mater.* **2019**, *29* (6), 1807326.

(298) Hou, B.; Guo, X.; Zhang, Y.; Zhang, L.; Zhang, D.; Wu, Z.; Zhang, J.; Hao, Z. *ACS Sustain. Chem. Eng.* **2023**, *11* (16), 6211-6219.

(299) Liu, C.-X.; Zhou, Z.-W.; Yu, Y.; Wei, Y.-J.; Cai, C.-X.; Wang, N.; Yu, X.-Q. *Small Struct.* **2023**, *4* (9), 2200321.

(300) Michelet, F.; Gueguen, R.; Leroy, P.; Wellman, M.; Nicolas, A.; Siest, G. *Clin. Chem.* **1995**, *41* (10), 1509-1517.

(301) Donald, D.; Gatautis, V.; Green, R.; Robinson, K.; Savon, S.; Secic, M.; Otto, J.; Taylor, L. *Clin. Chem.* **1994**, *40*, 873-881.

(302) Corma, A.; Garcia, H. *Chem. Soc. Rev.* **2008**, *37* (9), 2096-2126.

(303) Mikami, Y.; Dhakshinamoorthy, A.; Alvaro, M.; García, H. *Catal. Sci. Technol.* **2013**, *3* (1), 58-69.

(304) Yue, J.-Y.; Song, L.-P.; Wang, Y.-T.; Yang, P.; Ma, Y.; Tang, B. *Anal. Chem.* **2022**, *94* (41), 14419-14425.

(305) Ekennia, A. C.; Uduagwu, D. N.; Nwaji, N. N.; Oje, O. O.; Emma-Uba, C. O.; Mgbii, S. I.; Olowo, O. J.; Nwanji, O. L. *J. Inorg. Organomet. Polym. Mater.* **2021**, *31* (2), 886-897.

(306) Holt, M. S. *Food Chem. Toxicol.* **2000**, *38*, S21-S27.

(307) Morin-Crini, N.; Lichtfouse, E.; Liu, G.; Balaram, V.; Ribeiro, A. R. L.; Lu, Z.; Stock, F.; Carmona, E.; Teixeira, M. R.; Picos-Corrales, L. A.; et al. *Environ. Chem. Lett.* **2022**, *20* (4), 2311-2338.

(308) Amoatey, P.; Baawain, M. S. *Water Environ. Res.* **2019**, *91* (10), 1272-1287.

(309) Larsson, D. G. J.; Flach, C.-F. *Nat. Rev. Microbiol.* **2022**, *20* (5), 257-269.

(310) Crini, G.; Lichtfouse, E. *Environ. Chem. Lett.* **2019**, *17* (1), 145-155.

(311) O'Shea, K. E.; Dionysiou, D. D. *J. Phys. Chem. Lett.* **2012**, *3* (15), 2112-2113.

(312) Chen, Y.-d.; Duan, X.; Zhou, X.; Wang, R.; Wang, S.; Ren, N.-q.; Ho, S.-H. *Chem. Eng. J.* **2021**, *409*, 128207.

(313) Li, Z.; Yang, Z.; Meng, L.; Jing, L. *ChemSusChem* **2025**, e202500903.

(314) Liu, Y.; Liu, G.; Chen, L.; Hong, S. *ChemSusChem* **2024**, *17* (22), e202400252.

(315) Yang, T.; Chen, M.; Li, J.; Feng, Z.; Zou, S.; Mao, S.; Tian, Z.; Zhao, H. *Environ. Sci. Technol.* **2025**, *59* (16), 8155-8166.

(316) Yang, X. D.; Pan, Y.; Ding, L. L.; Wang, J. F.; Niu, S. Y.; Xia, X. Y.; Ren, H. Q. *Environ. Sci. Technol.* **2025**, *59* (25), 13063-13072.

(317) Yu, W.; Yin, M.; Nie, S.; Xiao, X.; Chu, C.; Chen, B. *Environ. Sci. Technol.* **2025**, *59* (25), 12692–12702.

(318) Masood, Z.; Ikhlaq, A.; Akram, A.; Qazi, U. Y.; Rizvi, O. S.; Javaid, R.; Alazmi, A.; Madkour, M.; Qi, F. *Catalysts* **2022**, *12* (7), 741.

(319) Hou, L.; Jiang, G.; Sun, Y.; Zhang, X.; Huang, J.; Liu, S.; Lin, T.; Ye, F.; Zhao, S. *Catalysts* **2019**, *9* (12), 1057.

(320) Huang, Y.; Ren, J.; Qu, X. *Chem. Rev.* **2019**, *119* (6), 4357-4412.

(321) He, X.; Feng, Y.; Xu, F.; Chen, F.-F.; Yu, Y. *J. Chem. Eng.* **2022**, *450*, 137927.

(322) Linic, S.; Christopher, P.; Ingram, D. B. *Nat. Mater.* **2011**, *10* (12), 911-921.

(323) Halder, S.; Das, T.; Kushwaha, R.; Misra, A. K.; Jana, K.; Das, D. *Mater. Horiz.* **2025**, *12*, 987-1001.

(324) Singha, N.; Das, D. Peptide-Based Water Insoluble Molecular Hydrogel. India Indian Patent Number 417150, 2023.

(325) Bui, H. L.; Chen, Y.-L.; Chuang, Y.-C.; Ou, K.; Tsai, Y.-C.; Huang, C.-J. *Langmuir* **2023**, *39*, 13169-13177.

(326) Sahiner, N.; Demirci, S. *Mater. Sci. Eng. C* **2017**, *77*, 642-648.

(327) Cho, H.-J.; Oh, J.; Choo, M.-K.; Ha, J.-I.; Park, Y.; Maeng, H.-J. *Int. J. Biol. Macromol.* **2014**, *63*, 15-20.

(328) Njoki, P. N.; Lim, I. I. S.; Mott, D.; Park, H.-Y.; Khan, B.; Mishra, S.; Sujakumar, R.; Luo, J.; Zhong, C.-J. *J. Phys. Chem. C* **2007**, *111* (40), 14664-14669.

(329) Martín-Barreiro, A.; Soto, R.; Chiodini, S.; García-Serrano, A.; Martín, S.; Herrer, L.; Pérez-Murano, F.; Low, P. J.; Serrano, J. L.; de Marcos, S.; et al. *Adv. Mater. Interfaces* **2021**, *8* (18), 2100876.

(330) Zhang, Y.; Huang, Y.; Chen, H.; Luo, X.; Zhang, J.; Wang, H.; Zou, Q.; Wang, S. *Mater. Adv.* **2022**, *3* (23), 8438-8448.

(331) Nasrallah, H. O.; Min, Y.; Lerayer, E.; Nguyen, T.-A.; Poinsot, D.; Roger, J.; Brandès, S.; Heintz, O.; Roblin, P.; Jolibois, F.; et al. *JACS Au* **2021**, *1* (2), 187-200.

(332) Liu, Z.; Tan, H.; Li, B.; Hu, Z.; Jiang, D.-e.; Yao, Q.; Wang, L.; Xie, J. *Nat. Commun.* **2023**, *14* (1), 3374.

(333) Zhang, X.; Yang, Q.; Lang, Y.; Jiang, X.; Wu, P. *Anal. Chem.* **2020**, *92* (18), 12400-12406.

(334) Feng, M.; Li, X.; Zhang, X.; Huang, Y. *TrAC Trends Anal. Chem.* **2023**, *166*, 117220.

(335) Kessler, A.; Hedberg, J.; Blomberg, E.; Odnevall, I. *Nanomaterials* **2022**, *12* (11), 1922.

(336) Pan, M.-M.; Ouyang, Y.; Song, Y.-L.; Si, L.-Q.; Jiang, M.; Yu, X.; Xu, L.; Willner, I. *Small* **2022**, *18* (23), 2200548.

(337) Wu, J.; Wang, X.; Wang, Q.; Lou, Z.; Li, S.; Zhu, Y.; Qin, L.; Wei, H. *Chem. Soc. Rev.* **2019**, *48* (4), 1004-1076.

(338) Xu, X.; Wang, J.; Huang, R.; Qi, W.; Su, R.; He, Z. *Catal. Sci. Technol.* **2021**, *11* (10), 3402-3410.

(339) Juárez Olguín, H.; Calderón Guzmán, D.; Hernández García, E.; Barragán Mejía, G. *Oxid. Med. Cell. Longev.* **2016**, *2016* (1), 9730467.

(340) Williams, C. A.; Fairley, H. E.; Tran, Q. K.; Pourmand, A. *Medicina* **2024**, *60* (11), 1904.

(341) Al-Zahrani, S. A.; Patil, M. B.; Mathad, S. N.; Patil, A. Y.; Al Otaibi, A.; Masood, N.; Mansour, D.; Khan, A.; Gupta, V.; Topare, N. S.; et al. *Crystals* **2023**, *13* (4), 577.

(342) Saroyan, H.; Kyzas, G. Z.; Deliyanni, E. A. *Processes* **2019**, *7* (1), 40.

(343) Vaishampayan, A.; Grohmann, E. *Microorganisms* **2022**, *10* (1), 61.

(344) Jiang, X.; Liu, S.; Wang, W.; Shi, S.; Zeng, Z.; Chen, C. *Appl. Surf. Sci.* **2022**, *575*, 151769.

(345) John F Moulder, W. F. S., Peter E Sobol, Kenneth D Bomben. *Handbook of X-ray Photoelectron Spectroscopy: A Reference Book of Standard Spectra for Identification and Interpretation of XPS Data*; Eden Prairie, 1992.

(346) Hepperle, P.; Herman, A.; Khanbabaee, B.; Baek, W. Y.; Nettelbeck, H.; Rabus, H. *Part. Part. Syst. Charact.* **2022**, *39* (9), 2200070.

List of Publications

1. **Tanushree Das**, Maitery Yadav, Saurav Das, Gargi Mondal, Sunanda Chatterjee, Debapratim Das*; Non-Plasmonic Oxidase-Like Gold Nanocatalysts on Hydrogel Beads for Broad-Spectrum Water Decontamination; *Langmuir* **2025**, *41, 37*, 25439–25453
2. Priyam Das, Sampurna Routray, Malay Kumar Baroi, **Tanushree Das**, Debapratim Das*; An Aggregation-Induced Room Temperature Phosphorescence Probe for the Efficient and Selective Detection of Heparin and Protamine; *Anal. Chem.* **2025**, *97,* 10628-10637
3. **Tanushree Das**, Saurav Das, Debapratim Das*; In-Situ Fabricated Gold Nanostars on Hydrogel Beads as Photo-Oxidase Mimic for Rapid and Sustainable POCT of Uric Acid; *J. Mater. Chem. B.* **2025**, *13*, 1079-1088
4. Satyajit Halder, **Tanushree Das**, Ritvika Kushwaha, Anup Kumar Misra, Kuladip Jana, Debapratim Das*; Targeted and Precise Drug Delivery Using a GSH-Responsive Ultra-Short Peptide-Based Injectable Hydrogel for Breast Cancer Cure; *Mater. Horiz.* **2025**, *12*, 987-1001
5. Priyam Das, **Tanushree Das**, Suprotim Koley, Malay Kumar Baroi, Saurav Das, Jyotirmayee Mohanty, Debapratim Das*; Time-Encoded Information Encryption with pH Clock Guided Broad-Spectrum Emission by Dynamic Assemblies; *Angew. Chem. Int. Ed.* **2024**, *64*, e202414239
6. Saurav Das, **Tanushree Das**, Shreya Debnath, Oren A. Scherman, Debapratim Das*; pH Clock Guided Dynamic Broad Spectrum Multi-Color Fluorescence Modulation in Size-Oscillatory Vesicles; *Adv. Optical. Mater.* **2024**, *12*, 2301422
7. **Tanushree Das**, Saurav Das, Debapratim Das*; Fabrication of core-shell beads, hollow capsules, and AuNP-embedded catalytic beads from an ultrasmall peptide hydrogel; *Chem. Eng. J.* **2023**, *477*, 147105
8. Sumit Chowdhuri; Saurav Das; Ritvika Kushwaha; **Tanushree Das**; Basab Kanti Das; Debapratim Das*; Cumulative Effect of pH and Redox Triggers on Highly Adaptive Transient Coacervates; *Chem. Eur. J.* **2023**, *29*, e202203820
9. Payel Dowari; Malay Kumar Baroi; **Tanushree Das**; Basab Kanti Das; Saurav Das; Sumit Chowdhuri; Avinash Garg; Ananya Debnath and Debapratim Das*; Development of a hydrolase mimicking peptide amphiphile and its immobilization on silica surface for stereoselective and enhanced catalysis; *J. Colloid Interface Sci.,* **2022**, *618*, 98-110
10. Saurav Das; **Tanushree Das**; Priyam Das and Debapratim Das*; Controlling the lifetime of cucurbit[8]uril based self-abolishing nanozymes; *Chem. Sci.,* **2022**, *13*, 4050-4057.